UNIVERSITY OF SOUTHAMPTON

FACULTY OF ENGINEERING AND PHYSICAL SCIENCES

School of Engineering

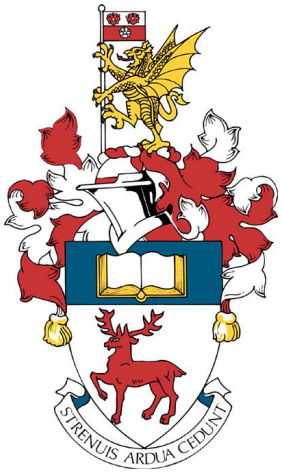

DEVELOPMENT OF IMAGE-BASED INERTIAL IMPACT TESTS FOR CHARACTERISING THE HIGH-STRAIN-RATE INTERLAMINAR PROPERTIES OF COMPOSITES

doi: 10.5258/SOTON/D0561
doi: 10.5258/SOTON/D0192
doi: 10.5258/SOTON/D0193

by

JARED VAN BLITTERSWYK

ORCID: 0000-0003-1186-2944

Thesis for the degree of Doctor of Philosophy

Supervisors: Prof. Fabrice Pierron and Dr. Lloyd Fletcher

November, 2019

UNIVERSITY OF SOUTHAMPTON

ABSTRACT

FACULTY OF ENGINEERING AND PHYSICAL SCIENCES

School of Engineering

Doctor of Philosophy

DEVELOPMENT OF IMAGE-BASED INERTIAL IMPACT TESTS FOR CHARACTERISING THE HIGH-STRAIN-RATE INTERLAMINAR PROPERTIES OF COMPOSITES

Jared Van Blitterswyk

Reliable measurement of interlaminar properties at high strain rates ($\sim 10^3$ s^{-1}) is very challenging with existing test methods due to inertia generated by dynamic loading. With the emergence of ultra-high-speed cameras has come the opportunity to use full-field measurements to quantify the high-strain-rate behaviour of materials and directly measure constitutive properties. This project explored the design and experimental validation of two image-based inertial impact (IBII) tests to measure the interlaminar elastic modulus, shear moduli, and tensile failure stress of fibre-reinforced polymer composite materials at high strain rates. A new set of special optimised virtual fields were developed as part of this work for the direct identification of the elastic and shear moduli from full-field maps of strain and acceleration. Synthetic image deformation routines were used to rigorously quantify the error introduced on the identification of stiffness by experimental factors (contrast and noise), and post-processing parameters (temporal and spatial smoothing). The potential of the IBII tension/compression tests was demonstrated by successfully identifying the interlaminar elastic modulus and tensile failure stress at 3-5$\times 10^3$ s^{-1}. Back-to-back, surface measurements made with synchronised ultra-high-speed cameras were used to analyse the assumption that the IBII tension/compression test is 2D. It was found that out-of-plane loading has a relatively small effect on stiffness identification (bias of 4% on average), but has a large effect on failure stress estimates (bias of up to 30% on average). Finally, the IBII shear test developed in this work demonstrated that the interlaminar shear modulus can be characterised with remarkable consistency at 1.5×10^3 s^{-1}. Overall, this project clearly demonstrates that the IBII method is an excellent tool for interlaminar material property identification at high strain rates. In the future, camera technology will improve increasing the efficacy of the IBII methods developed in this work.

Contents

List of Figures

List of Tables

UNIVERSITY OF Southampton

Academic Thesis: Declaration Of Authorship

I, Jared Van Blitterswyk declare that this thesis and the work presented in it are my own and has been generated by me as the result of my own original research.

Development of image-based inertial impact tests for characterising the high-strain-rate interlaminar properties of composites

I confirm that:

1. This work was done wholly or mainly while in candidature for a research degree at this University;
2. Where any part of this thesis has previously been submitted for a degree or any other qualification at this University or any other institution, this has been clearly stated;
3. Where I have consulted the published work of others, this is always clearly attributed;
4. Where I have quoted from the work of others, the source is always given. With the exception of such quotations, this thesis is entirely my own work;
5. I have acknowledged all main sources of help;
6. Where the thesis is based on work done by myself jointly with others, I have made clear exactly what was done by others and what I have contributed myself;
7. Either none of this work has been published before submission, or parts of this work have been published as: [please list references below]:

   J. Van Blitterswyk, L. Fletcher, F. Pierron, Interlaminar mechanical properties of polymer matrix fibre composites at high strain rates: a review, Advanced Experimental Mechanics; 2, pp. 3-28, 2017, doi: 10.11395/aem.2.0_3

   J. Van Blitterswyk, L. Fletcher, F. Pierron, Image-based inertial impact test for composite interlaminar tensile properties, Journal of Dynamic Behavior of Materials; 4, pp. 543-572, 2019, doi: 10.1007/s40870-018-0175-1

Signed: .....

Date: .....

Acknowledgements

Firstly, I would like to thank my supervisors, Prof. Fabrice Pierron and Dr. Lloyd Fletcher. I have learned so much from both of you and I am very grateful for your dedication to my training. Your scientific diligence, insights and vision were always inspiring. I feel fortunate to have had many opportunities to travel and make connections at conferences. Last but not least, I am truly grateful for your patience and understanding with my personal situation and management of the challenges of long distance from my family.

A sincere thanks also goes to my examiners: Prof. Janice Barton, Prof. Ole Thomsen, and Prof. Clive Siviour who dedicated time to critically review my work during internal and final examinations. Their insightful comments have enriched this thesis and the publications that resulted from this work. Thank you to EPSRC and the US Air Force for funding this work.

The PhD has been very rewarding, but has undoubtedly been one of the most difficult challenges I have faced. This thesis would not have materialised without the unwavering love and support from my wife Jen, and my friends and family in Canada. To Jen, thank you for your patience, for always lifting my spirits in challenging times, and your inspiring mental toughness over the past three years. Thank you for reminding me that dedication and a strong work ethic will pay off in the end. To my friends and family, I am truly grateful for your encouragement and the efforts you made to come and visit while I lived in Southampton and the unforgettable memories we made during our travels together.

The group of friends that I formed during my three years in Southampton played a massive part in my success as a PhD student. Thank you to Simon and my teammates for welcoming me onto the Southampton Spitfires. The friendships, experiences and memories from playing hockey in the UK will be something I always cherish. A special thanks goes to Geir Ólafsson for being an incredible friend and flatmate. Thank you for introducing me to Scottish culture, rugby, and some of the hidden gems in the greatest city in the world. Thank you for being a sounding board and a constant source of encouragement over the past three years. I also thank my other fellow PhD students and friends for their support and our discussions that undoubtedly improved aspects of this research.

Disclaimer

This material is based on research sponsored by the Air Force Research Laboratory, under grant number 516841101. The U.S. Government is authorized to reproduce and distribute reprints for Governmental purposes notwithstanding any copyright notation thereon. The views and conclusions contained herein are those of the authors and should not be interpreted as necessarily representing the official policies or endorsements, either expressed or implied, of the Air Force Research Laboratory or the U.S. Government.

Nomenclature

A	Average field illumination [grey level]/gauge area [m^2]
a	Acceleration component (x,y) [$m{\cdot}s^{-2}$]
$\boldsymbol{a}$	Acceleration vector [$m{\cdot}s^{-2}$]
c	Wave speed [$m\ {\cdot}s^{-1}$]
e	Specimen thickness [m]
e_R, e_S, e_T	Normalised identification error [%]
E	Young's modulus [Pa]
E	Expected value
f	Spatial frequency of grid pattern [m^{-1}]
F	Force [N]
G	Shear modulus [Pa]
$\boldsymbol{G}$	Strain minimisation matrix (special optimised virtual fields)
H	Specimen height [m]
H_P	Projectile diameter [m]
H_S	Sabot diameter [m]
H_T	Total height of IBII shear test specimen [m]
H_{WG}	Wave guide diameter [m]
L	Specimen length [m]
L_P	Projectile length [m]
L_S	Sabot length [m]
L_{WG}	Wave guide length [m]
m	mesh density/polynomial order (x-direction)
N	Number of measurement points/number of noise copies
n	mesh density/polynomial order (y-direction), noise [grey level]
$\boldsymbol{n}$	Unit normal vector
p	Grid pitch [m]
Q	Stiffness parameter [Pa]
S	Surface area [m^2]
s	Light intensity at any location in the synthetic images [grey level]
$\boldsymbol{T}$	Surface traction [Pa]
t	Time [s]
u	Displacement component (x,y) [m]
$\boldsymbol{u}$	Displacement vector [m]
$\tilde{u}^*$	Virtual displacement degrees of freedom
u^*	Virtual displacement
V	Variance
V	Volume [m^3]
V_P	Projectile velocity [$m{\cdot}s^{-2}$]

$\boldsymbol{Y}^*$	Vector of virtual mesh degrees of freedom
x, y, z	Image coordinate system
1,2,3	Material coordinate system
β	Stiffness proportional damping coefficient [s]
γ	Strain noise amplitude/grey level noise amplitude/synthetic image pattern contrast amplitude
γ_{xy}	Shear strain
$\dot{\gamma_{xy}}$	Shear strain rate [s^{-1}]
δl	Line boundary on which tractions applied
δS	Surface boundary on which tractions applied
Δx, Δy	Translation required to translate back-face measurements to front-face coordinates [m]
ϵ	Strain component (x,y)
$\boldsymbol{\epsilon}$	Strain vector
$\dot{\epsilon}$	Strain rate [s^{-1}]
ϵ^*	Virtual strain
ν	Poisson's ratio
Π	Gaussian noise distribution
ρ	Density [kg·m^{-3}]
σ	Stress [Pa]
$\boldsymbol{\sigma}$	Stress matrix [Pa]
ϕ	Phase [rad]
ω	Rotation [rad]

List of Abbreviations

'BSI'	Back-side illuminated
'CCD'	Charged-coupled device
'CMOS'	Complimentary metal oxide semiconductor
'CPS4R'	Plane stress four-node reduced integration element (ABAQUS)
'C3D8R'	Eight-node reduced integration brick element (ABAQUS)
'DIC'	Digital image correlation
'fps'	Frames per second
'$frng$'	2π periodic function
'FE'	Finite element
'FEMU'	Finite element model updating
'FRP'	Fibre-reinforced polymer
'FT'	Fourier transform
'FTCMOS'	Frame-transfer complimentary metal oxide semiconductor
'GFRP'	Glass fibre-reinforced polymer
'HSR'	High-strain-rate
'IBII'	Image-based inertial impact
'ISIS-CCD'	In-situ image sensor charged-coupled device
'Mfps'	Million frames per second
'SHPB'	Split-Hopkinson pressure bar
'UHS'	Ultra-high-speed
'VFM'	Virtual fields method
'WFT'	Windowed Fourier transform

Chapter 1

Introduction

Traditionally, polymer-matrix composites have been integrated into applications where they can be modelled as thin plates according to classical lamination theory. In these cases the thickness is much smaller than the in-plane dimensions, and thus it is assumed that the interlaminar stresses are negligible compared to the in-plane stresses. Due to high specific stiffness and strength characteristics, there is an increasing desire to use thicker composite structures as lightweight alternatives to their metallic counterparts. This is particularly true in the aerospace industry for components such as brackets, wing spar box, *etc.*, which must support complex three-dimensional stress states [1–4]. Large structures with relatively simple geometries or those primarily subjected to in-plane loading may also see complex stresses locally due to design features such as ply drops and manufacturing defects like out-of-plane fibre waviness. In these cases, the interlaminar stresses become important to consider due to the relatively low strength and stiffness in these material planes, which leads to increased susceptibility to micro-cracking or delaminations, and premature failure of the material. Moreover, these structures are often subjected to dynamic loading (*e.g.*: blast, crash, foreign object strike, *etc.*) where significant interlaminar stresses can develop over a range of strain rates [5–7]. Therefore, the reliability of numerical simulations hinges on the accuracy of models for the strain-rate sensitivity of interlaminar constitutive properties, which must be established experimentally. Since interlaminar properties are matrix-dominated, literature suggests that the stiffness and strength should exhibit a strain rate dependency [8–13]. However, the effects of strain rate above a few 100 s^{-1} are still not well understood, largely due to the lack of specific test methods for the interlaminar planes, and limitations inherent to existing test methods. This is shown by the scarcity and inconsistency in studies attempting to measure high-strain-rate (HSR) properties in the interlaminar directions [13].

Obtaining material properties for composites in the through-thickness direction is a long outstanding problem. At high strain rates there are numerous factors that make testing particularly challenging for the interlaminar planes, some of which include: issues with gripping the sample, sensitivity to manufacturing and machining defects, and volume effects. For instance, introducing a tensile load generally requires gripping of the specimen. Often this causes premature failure due to eccentric loading (bending stresses) or stress concentrations at the grips. This is especially problematic for through-thickness testing due to the small specimen dimensions. Manufacturing and machining quality, and specimen geometry can also have a significant influence on the failure behaviour [14]. For thick specimens formed by bonding several smaller laminates, failure can occur near the bond interface, resulting in failure strengths that are not representative of an original laminate [15]. Composites also show a strong volume effect. Void

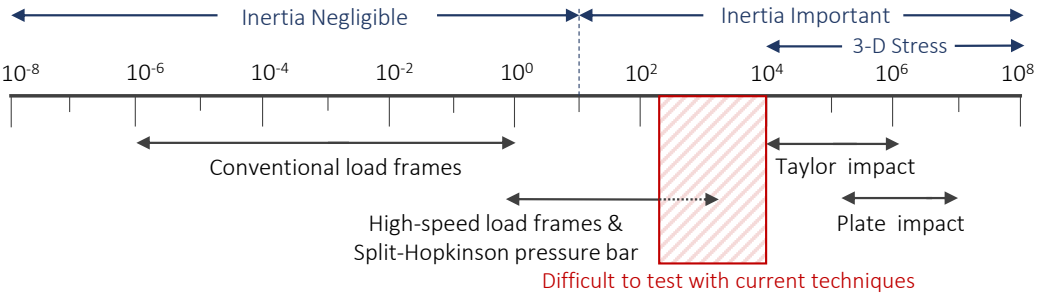

Figure 1.1: Schematic diagram of strain rate regimes illustrating applicability of existing test methods and where inertial effects become significant. Adapted from [25]

content from manufacturing increases with volume causing a degradation of matrix properties and reduced tensile and shear strengths [16, 17]. Pre-defects are especially critical as failure can initiate prematurely from voids or micro cracks caused by the machining process. All of these issues have created a notable sensitivity of material properties to test method [18–20].

The largest issue with testing composites at high strain rates is the management of inertial effects, which becomes important at strain rates above 10^1 s^{-1} (Fig. 1.1). This is particularly problematic for many existing techniques, which make use of limited information and rely on a number of assumptions to quantify the material's response. The best example of this is the split-Hopkinson pressure bar (SHPB), which acts as a dynamic load cell under the key assumptions of one-dimensional wave propagation and quasi-static equilibrium conditions. The latter assumption become critical for HSR loading since this condition is not satisfied until the inertia in the sample dampens out. This occurs after several reverberations of the pulse within the sample, and the time required for this to occur is dependent on the wave speed of the material being tested [21, 22]. For lower wave speed materials, such as polymer-matrix composites in the interlaminar planes, it is generally accepted that the SHPB apparatus is not able to provide a true measurement of the initial stiffness [9, 22–24]. If the strain rate is high enough then the inertial effects may also persist throughout the entire duration of the test, which may render strength measurements unreliable in composites where failure strains are small. Inertia is thought to be the largest contributor to the high amounts of scatter in reported measurements of stiffness and strength in the literature as discussed in Chapter 2 and the review paper in [13].

A number of recent experimental studies have demonstrated the advantages of using ultra-high-speed imaging (UHS) with full-field measurement techniques for HSR material characterisation [26–36]. In these studies, full-field maps of acceleration were processed using the virtual fields method (VFM) to directly identify the properties of the material. In doing so, the specimen acted as a load cell, and stress was reconstructed without needing to measure force externally. Full-field measurements remove the requirement of quasi-static stress equilibrium, and thus allow for a significant increase in strain rates at which materials can be tested. Prior to the commencement of this project, the idea of using full-field measurements and the VFM for HSR testing was initially explored by Moulart *et al.* [26] and Pierron & Forquin [27], and later used for characterising the in-plane properties of composites [28, 29] and concrete [27]. Concurrently with this project, the idea was formalised as a new test principle called the image-based inertial impact (IBII) test, and was demonstrated for testing ceramics [32] and measuring transverse in-plane properties of composites [31, 37]. The prospect of an image-based test method for material characterisation in the interlaminar planes is particularly attractive as it removes the need to grip the material, and issues with inertia are avoided by using the acceleration as a

load cell. Therefore, the overall aim of this project was to explore the design space of IBII tests for characterising the HSR constitutive behaviour of a carbon fibre-reinforced epoxy laminate in interlaminar tension/compression and shear. The project was structured according to three main aims as described in the following section.

1.1 Aims and Objectives

The overall intention of this project was to design and assess the feasibility of a new set of IBII tests for HSR characterisation of interlaminar stiffness and failure stress. The first aim was to design a test to measure the HSR interlaminar elastic modulus and failure stress in tension. The second aim was to verify the assumption of through-thickness uniformity for the interlaminar test configuration developed in the first part of the project [38] using back-to-back, UHS imaging. Finally, the third aim was to develop a new HSR test to measure the interlaminar shear modulus, and explore the design space for extending the IBII test method for populating failure envelopes for the interlaminar planes. The objectives for each aim of the project are described in detail in the following sections.

1.1.1 Image-based inertial impact (IBII) test for interlaminar tensile properties

The first objective was to develop and assess the feasibility of an IBII test configuration for tension/compression loading. A design study using explicit dynamics simulations was performed to select optimal projectile length and impact speed. An 18 mm thick laminate (MTM45-1/AS4-145) supplied by Material Sciences Corp. was used to validate the test procedure using direct imaging on the sample. The linear-elastic behaviour also provided a relatively simple case to validate processing and identification procedures. The full orthotropic version of the special optimised virtual fields [28, 29] was not well suited to identifying the interlaminar stiffness (Q_{33}) since the remaining in-plane stiffness parameters were weakly activated (Q_{11}, Q_{13}, and G_{13}) and introduced noise into the identification. Therefore, a new set of special optimised virtual fields was developed in this work to isolate the Q_{33} term. Simulations were also used to generate a set of kinematic fields based on a known input constitutive behaviour to verify the VFM identification routines. In the case of dynamics there is a need to apply spatial and temporal smoothing to the experimental images. The choice of these parameters is important as they will interact differently with the VFM procedures. Therefore, a key objective was to develop an image deformation framework for the IBII test based on the work in [39, 40]. Finite element displacement fields were imposed on a set of synthetic grid images that include effects from lighting intensity, imaging resolution, frame rate, and camera grey-level noise. These images were processed using a range of spatial and temporal smoothing parameters to identify the optimal amount of smoothing for minimal error on measured stiffness parameters. The final objective was the experimental validation of the proposed test for the 1-3 and 2-3 interlaminar planes.

1.1.2 Experimental verification of test assumptions

Typically IBII tests are performed with a single camera and therefore, to use surface measurements for material property identification it is necessary to assume that: 1) kinematic fields are uniform through the thickness dimension of the sample; and 2) the specimen can be considered

to be in a state of plane stress. These assumptions are difficult to validate experimentally as the effects are embedded within the surface measurements. The main objective was to use UHS imaging to simultaneously measure the response on the front and back faces of a sample tested using the configuration developed in the first part of the project [38] to evaluate the assumption of uniform loading through-thickness. The interlaminar specimens provide the most challenging test case for this assumption as they are more difficult to align, and the samples are generally less slender compared to the in-plane tests in [37]. Since most experiments will be performed with a single camera, an additional objective of this work was to establish diagnostics for single-sided measurements to identify when measurement assumptions are not well satisfied.

1.1.3 IBII test for measuring the interlaminar shear modulus

The final aim of the project was to develop a new HSR test to measure the interlaminar shear modulus, and explore the design space for extending the IBII test method for interlaminar shear strength measurements. Characterisation of the shear modulus with existing test methods is very challenging since inertial effects contaminate the determination of stress, and the necessity to assume that the material is in a state of uniform shear stress. Uniform shear can only be achieved using tubular specimens, which are difficult to machine, and are not representative of most laminates. These assumptions are lifted in this work by using the VFM to identify the interlaminar shear modulus directly from heterogeneous deformation maps. Given the constraints on specimen size for the interlaminar samples, and to minimise the likelihood of introducing machining defects, it was desired to develop a test configuration requiring limited specimen machining. A similar specimen geometry to the short-beam-shear test was adopted to activate the shear behaviour. Full-field measurements and the VFM were used to directly identify the interlaminar shear modulus from maps of strain and acceleration similar to that in quasi-statics by [41–43]. The shear loading with this specimen configuration causes the sample and grid to rotate with respect to the camera sensor. Since the phase (displacement) maps from the grid method are made with respect to the camera coordinates, grid rotation causes a systematic bias in the identified shear modulus. Therefore, a separate image deformation framework was developed to quantify this effect on the identification of the shear modulus, and to select optimal spatial and temporal smoothing parameters for minimal identification bias. The final objective of this phase was to experimentally validate the measurement of the interlaminar shear modulus using the proposed test configuration.

The following section describes the novel contributions resulting from the project for the advancement of the IBII test methodology and HSR characterisation of composite materials.

1.2 Novelty

This work represents the first exploration of an inertia-based test method for interlaminar characterisation of polymer-matrix fibre composites in tension/compression and shear. This project resulted in many key contributions towards establishing the IBII test method for characterisation of composites at strain rates where existing test methods are unreliable (greater than a few hundred s^{-1}). This section will describe the novelty associated with each of the three main objectives of the project.

The first aim of this work resulted in the development of a complete experimental design procedure for interlaminar IBII tests. Simulated kinematic fields were also used to validate a new set of special optimised virtual fields for the direct identification of the interlaminar elastic modulus from full-field maps of strain and acceleration. An image deformation framework specific to the interlaminar IBII tests was created to rigorously analyse the propagation of errors introduced from the imaging setup and post-processing routines. This was the first implementation of this framework for dynamic testing in the interlaminar planes. An experimental validation study showed that the proposed IBII test provided remarkably consistency measurements of the interlaminar modulus (coefficient of variation (COV) of 3.5%) at strain rates on the order of $2{\times}10^3$ s^{-1}. This represents a vast improvement over reported values in the literature which are highly scattered at similar strain rates [10, 13, 44, 45]. A set of rigid-body virtual fields were developed concurrently with the in-plane IBII test [37] to reconstruct a linear approximation of the stress field across the height of the sample for more accurate estimation of the tensile failure stress at strain rates on the order of 3-5$\times10^3$ s^{-1}.

The second phase of this project represents the first time that synchronised back-to-back, UHS cameras have been used to evaluate the validity of full-field measurement assumptions for the IBII test. This study developed a set of rigorous experimental diagnostics to determine if the key assumptions of the through-thickness uniformity is valid from single-sided measurements. The use of rigid-body virtual fields was extended in a novel way to address the under-estimation of failure stress from in-plane acceleration in the presence of out-of-plane loading. Key improvements were made to the alignment procedure to significantly mitigate out-of-plane loading effects, which resulted in improved measurement consistency for stiffness and failure stress measurements. The advancement in our understanding of the importance of alignment will benefit all IBII tests, and in particular those on brittle materials where out-of-plane bending can significantly influence measured properties (*i.e.*: ceramics, concrete, *etc.*).

The final phase of this project resulted in the design and experimental validation of a new IBII test for measuring the interlaminar shear modulus from heterogeneous deformation fields. A new sets of special optimised virtual fields were developed for the direct identification of the shear modulus from full-field maps of strain and acceleration. A separate image deformation framework was successfully implemented to quantify the uncertainty associated with the identification of the shear modulus from limited camera spatial resolution, smoothing, and grid rotation. Measurements of the interlaminar shear modulus were made with impressive consistency (COV $\leq$ 3%) at strain rates on the order of $1.5{\times}10^3$ s^{-1}, which is beyond the capabilities of existing tests methods.

1.3 Structure of the Thesis

This thesis begins with a summary of the literature on test methods and reported interlaminar properties at intermediate and high strain rates (Chapter 2). Also included in Chapter 2 is a review of full-field measurement techniques, inverse identification procedures and UHS imaging technologies, as these are the essential tools of the IBII method. The relevant theory for implementing the VFM for the interlaminar IBII tests is presented in Chapter 3. The focus of Chapter 4 is the design and experimental implementation of the IBII tension/compression test to measure the HSR interlaminar elastic modulus and the tensile failure stress. Chapter 4 also describes the implementation of an image deformation framework for smoothing parameter selection and uncertainty quantification for stiffness identifications. Chapter 5 describes the experimental studies conducted with back-to-back cameras to address the effect of out-of-plane

loading on stiffness and failure stress identifications made using the IBII test. The development of a new type of IBII test to measure the interlaminar shear modulus is presented in Chapter 6. This includes the derivation and validation of a new set of special optimised virtual fields for identifying the interlaminar shear modulus from strain and acceleration maps. The image deformation framework used to quantify the effects of grid rotation and smoothing is also presented. Finally, Chapter 7 discusses the limitations of the new interlaminar IBII tests developed in this project, possible directions for future work, and key conclusions from this project.

Chapter 2

Literature Review

2.1 Overview

This chapter provides a detailed review of the literature on HSR interlaminar properties of fibre-reinforced polymer composites in tension, compression and shear. First, a review of the SHPB and challenges associated with testing in the interlaminar planes is provided. This is followed by a review of reported strain rate sensitivities of stiffness and strength in tension, compression and shear. Also included is a discussion on the state-of-the-art in ultra-high-speed imaging technology, and an overview of full-field measurement techniques. An overview of inverse identification methods are provided for extracting constitutive properties from experimental measurements. The final section of this chapter discusses the concept of using of inverse techniques, combined with full-field measurements and ultra-high-speed imaging to develop new test methods for HSR material characterisation.

2.2 Split-Hopkinson pressure bar (SHPB) Test

The SHPB has played an invaluable role in obtaining information on the high strain rate response of FRP composites in the through-thickness direction [9–11, 46, 47]. Most efforts have focused on obtaining the dynamic compressive properties of composites in the through-thickness direction due to the relative simplicity of implementing the test [25]. In this configuration, a specimen is subjected to a compressive loading pulse while being sandwiched between two elastic bars, denoted as the incident and transmitter bars (Fig. 2.1a). In this configuration, a striker is used to impact the incident bar and induce a compressive pulse. The specimen may also be loaded by direct impact (Fig. 2.1b); however, this approach is less common due to issues with alignment and pulse transmission. In the two-bar configuration, the pulse from the striker propagates towards the specimen, with the input pulse recorded via the strain gauge on the bar. Once the pulse reaches the specimen, some of the compressive pulse is transmitted through the specimen into the transmitter bar, and some is reflected back through the incident bar at the specimen interface. The amount of the pulse which is reflected or transmitted is dependent on the impedance mismatch between the bars and the specimen. Under specific conditions, the pulses measured on the incident and transmitter bars can be used to deduce the stress state within the specimen using one-dimensional wave theory. In these cases, the portion of the wave transmitted through the specimen describes the stress in the specimen, while the reflected pulse describes the strain rate [10]. The compression SHPB test has been adapted

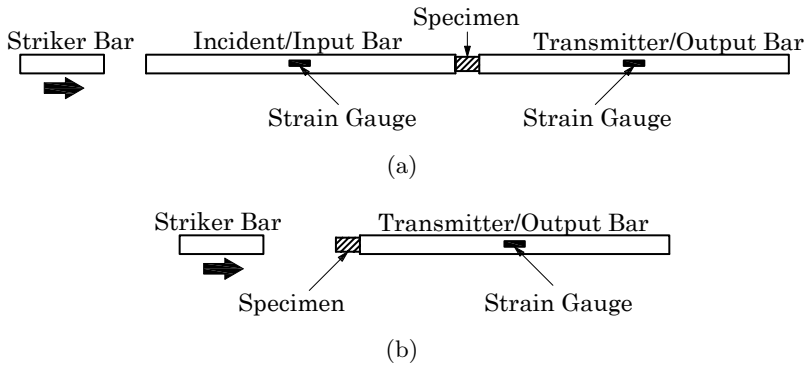

Figure 2.1: Schematic of two typical configurations of the Hopkinson bar apparatus. Adapted from [24]

to permit high rate testing of materials in tension, shear, torsion, bending, and combined load states [10, 24, 46, 48], as described next.

The principles of a tensile SHPB are similar to compression. In the case of tensile loading, the main differences lie in the means of generating the pulse, typical specimen geometries, and gripping/attachment to the input and transmitter bars [23]. Tensile pulses are most commonly applied to the incident bar using a direct impact on a flange attached to the bar, or through the release of a static tensile load [49]. Tensile pulses may also be applied using a top hat specimen and hollow transmitter bars, or using the reflected pulse from the transmitter bar with a collar used to protect the specimen in compression. The reader is referred to reference [49] for further details. U-shaped striker bars have also been considered as a means of generating longer pulses and extending the range of achievable strain rates [50].

For direct tensile loading, the specimen is generally attached to the incident and transmitted bars using threaded inserts or adhesives [21]. The need to grip the sample is disadvantageous as the grips introduce stress concentrations or eccentric loading (heterogeneous stress state). Mechanical inserts also have the disadvantage of creating additional reflections and dispersion of the wave, affecting the accuracy of the measurement using SHPB theory [49, 51]. Specimen geometry must also be considered carefully in tensile testing to ensure failure occurs in the gauge section. A waisted cylindrical specimen is commonly used to ensure failure occurs within the gauge section [23, 52], however, the variable cross-section complicates the calculation of strain using one-dimensional wave theory [52].

An alternative approach for tensile loading is the single bar spalling test [53]. In this case, the specimen is attached on one side to the end of the input bar and the transmitter bar is removed so one edge of the specimen is free. The specimen in loaded in tension after the compressive pulse reflects off of the free edge. The spall test is useful for materials which have a greater strength in compression than in tension, which allows the input pulse to be tailored such that no damage is caused during compressive loading, but the reflected tensile wave causes failure. Strain gauge measurements and point-wise laser Doppler velocimetry may be used to infer the tensile strength of the material. This is accomplished using an analytical solution for the specimen stress state based on the assumption of one-dimensional wave propagation [53]. While this removes the need to grip the material, it requires corrections for dispersion and one must assume one-dimensional wave propagation through the bar and specimen, which is difficult to verify in this configuration using point measurements.

The SHPB has also been used in two different configurations to measure interlaminar shear

properties: 1) using a single or double lap shear joint loaded in compression [44, 45], and 2) using thin-walled tubular specimens in a torsion configuration [10, 54]. This arrangement is very similar to the compression SHPB, with the exception that a shear wave is induced by applying a torque pre-load on the incident bar.

As discussed above, the SHPB apparatus offers versatility for testing in compression, tension and shear. However, the usefulness of these configurations for material characterisation hinges on the ability to satisfy a number of underlying assumptions. These assumptions are explained in detail in the following section along with discussions on the relevance and specific challenges to testing in the interlaminar planes of FRP composites.

2.2.1 Assumptions and limitations associated with the SHPB

A number of assumptions are required for strain gauge measurements on the bars to be used to infer the stress and strain states in the specimen for a SHPB test. The assumptions are briefly summarised below, and the interested reader is referred to the paper by Gama *et al.* [24] for a more in-depth review. The assumptions to be satisfied for a valid test include:

1. one-dimensional stress wave propagation in the incident and transmission bars (*i.e.*: negligible wave dispersion);
2. interfaces between the specimen and bars remain planar at all times;
3. loading satisfies quasi-static stress equilibrium (*i.e.*, the forces exerted at both specimen ends are equal in magnitude and opposite in sign), and;
4. friction effects at the specimen-bar interfaces can be neglected.

Tests suffering from high amounts of dispersion (violating assumption 1) exhibit a non-linear initial region of the stress-strain curve, followed by oscillations about the straight line that would exist for a bar free of distortion [24]. An example is shown in the work by Gerlach *et al.* [47], where the stress-strain response at high strain rate exhibits an oscillatory behaviour (Fig. 2.2). A number of corrective approaches have been developed [24] but, the effects of dispersion are never completely removed. Pulse shaping is a common approach to reduce the amount of dispersion by smoothing and limiting high frequency content in the compressive pulse [24, 55]. Pulse shaping is generally achieved by modifying the shape of the impactor or placing a thin layer of low impedance material, or plastically deforming metal, between the striker and input bar. This, however, limits the strain rate that the tested specimen will experience.

The second assumption is generally satisfied for FRP composites in the through-thickness direction due to the relatively low acoustic impedance compared to the bars. This condition is more problematic for harder materials that may cause local deformation of the bars [24].

The critical limitation is the necessity for quasi-static equilibrium loading conditions(assumption 3). The importance of this assumption has been studied extensively in the literature [22, 24, 56]. The concept is explained here by considering an anvil type specimen of constant thickness e, in a SHPB test as shown in Fig. 2.3. The specimen is subjected to two time varying end loads from the reactions at the incident and transmitter bar interfaces. Assuming the loads are applied normal to the specimen end faces, the local equilibrium for this specimen has the form of Eq. (2.1),

$$F_1(t) + F_2(t) = \rho e \int_0^L \int_{-H/2}^{H/2} a_x(x, y, t) dx dy \tag{2.1}$$

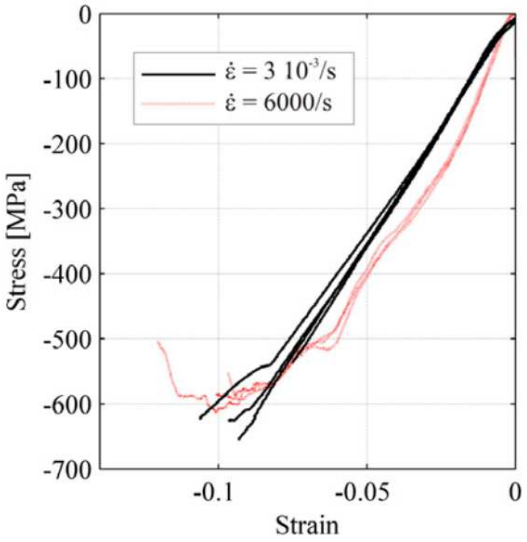

Figure 2.2: Compression stress-strain curve highlighting the influence of wave dispersion effects on the linear response measured using a SHPB at a strain rate of $6{\times}10^3$ s^{-1} [47]. Cubic specimens, 10 mm thick, carbon/epoxy 3D weave

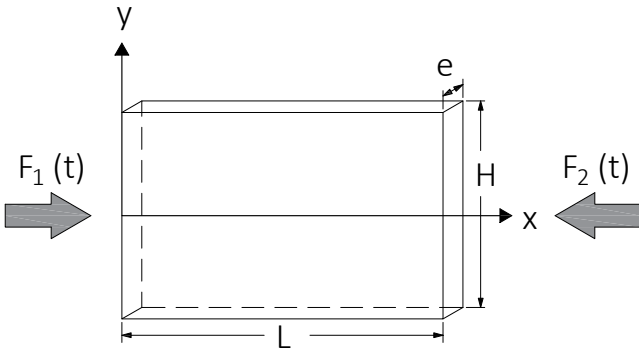

Figure 2.3: Schematic of anvil-type specimen subjected to arbitrary end loads

where $F_1(t)$ and $F_2(t)$, denote the forces at the incident and transmitter bar interfaces, L, H and e denote the specimen length, height and thickness, respectively, ρ is the density of the material (assumed constant here), and a_x is the local acceleration in the x direction.

Stress equilibrium assumes that the force at the incident bar-specimen interface is equivalent to that at the transmitter bar-specimen interface (*i.e.*: acceleration is neglected and $F_1 = F_2$). When the pulse reaches the specimen the input force generates a stress wave in the specimen (*i.e.*: inertial effects caused by transient acceleration). This stress wave travels through the specimen to the output bar where some is transmitted and some reflects and reverberates in the specimen. When the stress wave initially travels through the specimen, a heterogeneous stress state results, violating the assumption of quasi-static equilibrium (condition 3). Depending on the strain rate, stresses arising from inertial effects can be large and may mask the true mechanical response until the waves eventually damp out [21, 22]. For through-thickness tests, this condition is generally not satisfied until late in the test, as illustrated by the work of Gama *et al.* [57] (Fig. 2.4). A general criterion is that quasi-static stress equilibrium occurs after approximately three or four reverberations of the pulse through the specimen [22, 56]. Rather than counting reverberations, Gillespie *et al.* [46] used an 'R criterion', based on the difference between incident and transmitted signals, to assess the validity of a test. Regardless of the technique used to determine when quasi-static stress equilibrium conditions have been

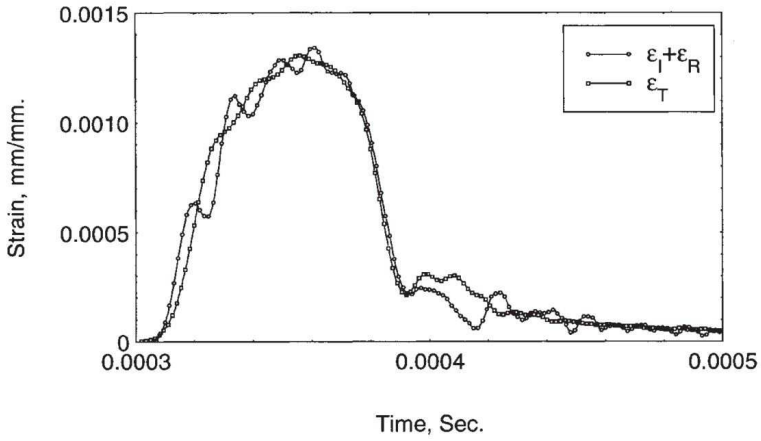

Figure 2.4: Verification of quasi-static stress equilibrium for a through-thickness compression test at an average strain rate of 1.1×10^3 s^{-1} [57]. Cubic specimens, 12.7 mm thick, plain weave S-2 glass/vinyl ester composite

achieved, this assumption is always a source of discussion [24]. However, it is generally accepted that the SHPB is unreliable for measuring stiffness of low wave speed materials [9, 22–24].

The problem with inertia is exacerbated for FRP composites by the low wave speed, and the low signal to noise ratio, and quasi-brittle behaviour [12, 54]. Low strains at failure means that a state of quasi-static stress equilibrium may not be achieved before the test is complete. Short specimens and pulse shaping may be used to reduce the time to achieve quasi-static equilibrium and improve the uniformity of strain rate [22, 24, 58]; however, quasi-static equilibrium still may not be achieved prior to failure and short specimens may suffer from larger friction effects [21]. For tensile tests there is a minimum specimen length due to the need to grip the material, which prolongs the time required for inertial effects to dampen out. Softer materials also suffer from low signal-to-noise levels in the reflected pulse [21]. Efforts to improve this include reducing the cross-section and stiffness of the input bars, using more sensitive strain gauges, using polymer bars [59], or direct force measurement [21]. Unfortunately, these approaches generally suffer from higher levels of wave dispersion and inertial ringing, making reliable force measurement more challenging using SHPB theory.

The assumptions and limitations described above create issues with obtaining reliable measurements of the interlaminar properties at high strain rate, as described in the next section.

2.3 Review of Interlaminar Properties at High Strain Rates

A review of current literature reporting on the sensitivity of through-thickness properties to strain rate will now be discussed. A compilation of references for compression, tension and shear properties is presented in Appendix A in Tables A.1, A.2 and A.3, respectively. It must be noted that the following discussion focusses on relative trends between quasi-static and HSR properties. This is a result of the inconsistency in the literature regarding material composition (fibre and matrix materials, fibre volume fraction, reinforcement architecture, etc.), which makes direct comparison of quoted properties uninformative. Also, failure strain rate is defined inconsistently in the literature with some reporting an average strain rate and others reporting instantaneous strain rates. Defining a failure strain rate using a SHPB is difficult and not necessarily reliable due to the dependency on damage progression in composite materials. Therefore, no attempt is made to convert reported strain rates to an equivalent metric across

all studies.

2.3.1 Strain rate effects on compressive properties

Elastic modulus under compressive loading

As discussed in the previous section, effects from inertia tend to mask the initial behaviour of the material under dynamic loading using a SHPB. Therefore, measurements of the modulus using the SHPB can only be regarded as 'apparent'. The degree to which inertia influences the measurement of strain is difficult to resolve using strain measurements on the incident and transmitter bars. This may contribute to the lack of general agreement in the literature regarding the sensitivity of the elastic modulus to strain rate.

A summary of relative change in compressive elastic modulus as a function of strain rate is shown in Fig. 2.5. The majority of studies report an increase in apparent modulus with increasing strain rate [9, 58, 60–63]. This behaviour is expected for a matrix-dominated behaviour as reported for thermoset resins tested without reinforcing fibres [12]. The relative increase in modulus is highly variable among studies, with increases ranging between 60% [58, 63] and 150% at strain rates around 10^3 s^{-1} [9]. According to the tests performed by Yokoyama and Nakai [9], the level of sensitivity appears to be more dependent on the reinforcement architecture (*i.e.*: cross-ply versus plain weave) compared to reinforcement material (glass versus carbon fibres). Despite having a lower compressive strength, the cross-ply laminates absorbed more energy compared to the plain weave composites. No physical explanation is provided for this behaviour. This may be a result of the increased void content for the plain weave architecture. In the work by Hosur *et al.* [64], the only other study to consider cross-ply laminates, the elastic modulus was higher compared to quasi-static values, but decreased with increasing strain rate. No physical explanation was offered by the authors for this trend.

The influence of fibre architecture is unclear, as very few studies consider pre-preg laminates, as illustrated in Fig. 2.5. Considering only studies that analyse plain weave architectures [47, 57, 58, 61–63, 65–68], the magnitude of strain rate sensitivity is difficult to discern due to large scatter in reported measurements (see Table A.1). For example, Song *et al.* [58] and Akil *et al.* [62] report increases in stiffness ranging from 75% to 115% (for strain rates near $1{\times}10^3$ s^{-1}), where as Shen *et al.* [61] report a mean increase of 350% at $1.2{\times}10^3$ s^{-1}. The unrealistically high effect of strain rate on the modulus measured by Shen *et al.* [61] suggests that specimens are unlikely to be in stress equilibrium. Alternatively, a number of studies on plain weave composites [47, 65–67] show negligible variations of the modulus over a similar range of strain rates.

It is not surprising that many studies using the SHPB report an increase in compressive elastic modulus. In the early stages of a test, the reaction force on the input bar does not equal the force on the transmitter bar due to a significant contribution from acceleration (see Eq. (2.1)). As a result, the strains measured by the input bar are lower, and stress in the specimen, computed using the force on the transmitter bar, is higher. This leads to a perceived stiffening of the material. This effect is likely to increase with increasing strain rate as a greater portion of the impact force is expended in accelerating the material. The degree to which inertia affects a test is dependent on several factors, which is thought to contribute to the scatter in reported values of strain rate sensitivity.

In general, a review of the literature indicates that the compressive elastic modulus is matrix dominated and probably increases with increasing strain rate. The magnitude of this sensitivity

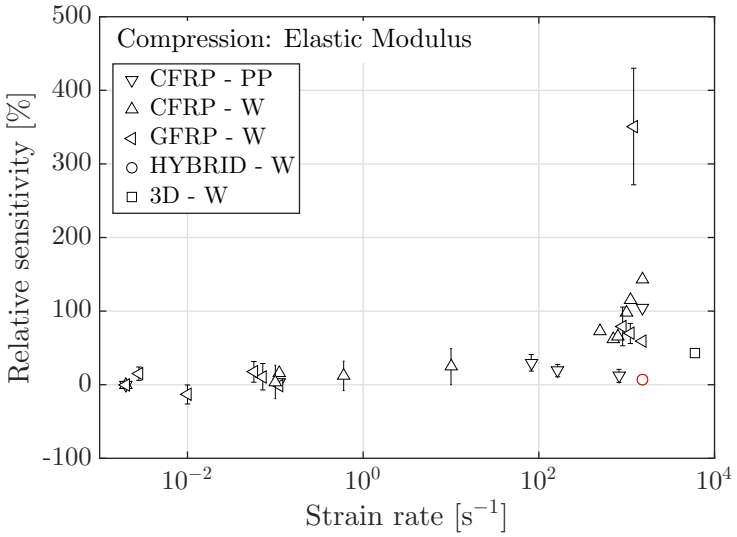

Figure 2.5: Summary of relative strain rate sensitivity for compressive modulus from the literature. 'PP' and 'W' denote pre-preg and plain weave reinforcement, respectively. Red symbol outline denotes that values are quoted with respect to modulus at lowest strain rate considered (1.3×10^3 s^{-1} for [67]). Error bars denote the range of reported sensitivity and not standard deviation. Data taken from [9, 47, 58, 60, 64, 67]

is uncertain due to high scatter in the literature.

Compressive strength

A summary of relative change in compressive strength as a function of strain rate is shown in Fig. 2.6. From Fig. 2.6 it is clear that there is high variability associated with the magnitude of change in strength with increasing strain rate. The trend at intermediate strain rates appears much more defined, showing a near linear positive sensitivity. There is a small group of studies that report a moderate and positive increase in strength for strain rates below 1×10^3 s^{-1} [9, 60–62, 66]. Reported increases vary between 6% and 23% for both CFRP and GFRP. The remaining studies report large relative increases in strength compared to quasi-static values: 33% [57] (reaching a near asymptotic value at 7×10^2 s^{-1}), 46% [67], 56% [63], 80% (between 1-1.9×10^3 s^{-1}) [68] and 180% [65]. The large increase in strength at high strain rates reported by Woo *et al.* [68] (80%) was attributed to high energy absorption by the kevlar fibres. However, the maximum strain rate achievable by Woo *et al.* [68] was limited by low pulse transmission (as low as 10%) through the specimen. In the study by Pankow *et al.* [65], the stress-strain response was highly non-linear and was heavily contaminated by dispersion. This introduces uncertainty when attempting to determine ultimate properties. In contrast to these results, Gerlach *et al.* [47] reported that failure strength remains approximately constant with increasing strain rate (quoted up to 6×10^3 s^{-1}).

A small number of studies report mixed trends for strength at high strain rates [9, 58, 64]. Hosur *et al.* [64] reported a positive sensitivity to strain rate, but peak stresses that are below quasi-static values. The specimens were loaded to failure under quasi-static conditions; however, at 8.2×10^1 s^{-1} and 1.6×10^2 s^{-1} the compressive input pulse was not strong enough to damage the specimens. Therefore, comparisons made by the authors between peak stress at these strain rates and quasi-static strength are not equivalent. Only measurements collected at 8.2×10^2 s^{-1} can be used to assess the effect of strain rate on compressive strength. From this case, strain rate causes a decrease in strength by 37%. The authors attributed this to a progressive change in failure mechanism from splitting and crushing at 1.6×10^2 s^{-1} to crushing

and shearing at 8.2×10^2 s^{-1}. The instability of compressive loading tends to cause the specimen to fail in shear according to the strength of the matrix. Therefore, the change in failure mode is unlikely to be an intrinsic property of the material and more a result of the experimental setup (structural behaviour). Song *et al.* [58] reported lower strengths at strain rates up to 8×10^2 s^{-1} compared to quasi-static values. At higher strain rates ($> 1\times10^3$ s^{-1}), the dynamic strength exceeds the quasi-static one. The authors offer no explanation for this behaviour. Similar to the compression modulus, Yokoyama & Nakai [9] found that compressive strength was sensitive to reinforcement architecture. The woven glass/epoxy laminate exhibited a positive strain rate sensitivity, whereas the carbon/epoxy cross-ply pre-preg and plain weave laminates had a negative sensitivity. This was attributed to the properties of the fibres, however, the carbon/epoxy laminates had 15-20% higher fibre volume fractions. The potential dependency on reinforcement architecture (*i.e.*: pre-preg., weave, *etc.*) is difficult to ascertain since the majority of studies focus on one type of reinforcement and have large scatter.

Other factors contributing to scatter include specimen geometry and uncertainty associated with quasi-static values. All studies in the literature use cubic or cylindrical specimens. A study by Tagarielli *et al.* [69] showed that the compressive strength and strain is highly sensitive to specimen geometry. For the same contact surface area, cylindrical specimens were found to fail at lower stress and strain compared to cubic specimens. As the volume of the cylindrical specimens was larger, this may indicate a volume effect. In any case, there appears to be a sensitivity to geometry and/or volume, which differs between studies in the literature. Another complication with comparing studies is that some work do not report quasi-static values at the same strain rates. Considering relative changes in strength over the high strain rate tests only, the values range between -5% and +30% compared to the range of -40% to +40%, when compared against quasi-static values, as shown in Fig. 2.6. This does not necessarily imply better accuracy, and instead suggests that high strain rate tests are reasonably repeatable under different conditions.

Compressive strength is heavily dominated by structural failure due to the inherent instability of the loading condition. Specimens will tend to fail in shear, which is determined by the strength of the resin. Some authors report a change in failure mode, which is attributed to strain rate sensitivity [60, 61, 65]. This highlights the challenge associated with measuring compressive strength and is likely a strong contributor to scatter in the literature. The intrinsic instability of the test makes the measured strength highly sensitive to variations in manufacturing, fibre volume fraction, defects, void content, specimen geometry, specimen preparation (flat contact surfaces) and alignment.

In summary, the literature suggests that there is likely a positive sensitivity of compression strength to strain rate but the magnitude is uncertain. The sensitivity to fibre material and architecture is also difficult to determine as a consequence of limited studies and high scatter.

Ultimate compressive strain

As with strength and stiffness, the influence of strain rate on failure strain is uncertain. Many authors report a slight decrease (less than 14%) or negligible influence of strain rate on failure strains as shown in Fig. 2.7 [9, 60, 62, 63, 65, 66]. Song *et al.* [58] reported a negative sensitivity, but one that is much stronger than reported by most (-62%). Pankow *et al.* [65], Shah Khan *et al.* [60] and Gama *et al.* [57] reported a negligible sensitivity to strain rate. In the study by Shah Khan *et al.* [60], only strain rates up to 10 s^{-1} were considered. The results from

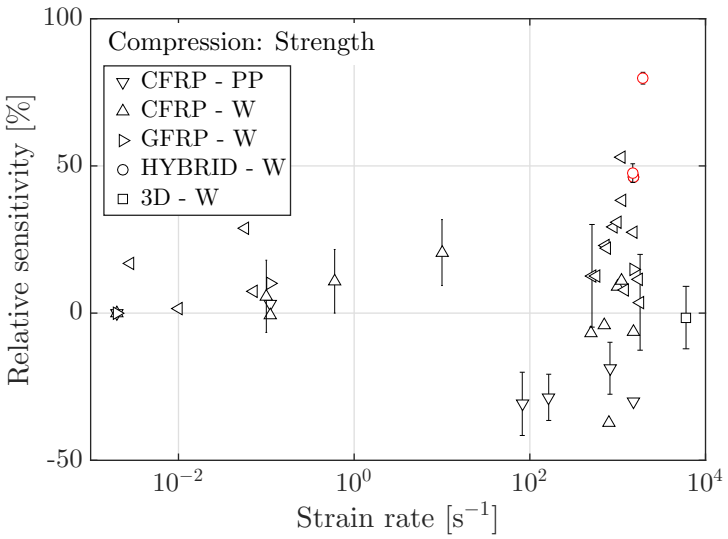

Figure 2.6: Summary of relative strain rate sensitivity for compressive strength from the literature. 'PP' and 'W' denote pre-preg and plain weave reinforcement, respectively. Red symbol outline denotes that values are quoted with respect to strength at lowest strain rate considered (1.3×10^3 s^{-1} for [67]). Error bars denote the range of reported sensitivity and not standard deviation. Data taken from [9, 47, 57, 58, 60–68]

Gama *et al.* [57] and Pankow *et al.* [65] illustrate the effects of dispersion. Both studies show oscillations in the initial portion of the stress-strain curve. Further, strain measurements with 2D DIC by Pankow *et al.* [65] showed significant heterogeneity throughout the entire test. This was attributed to the coarse textile architecture and local variations in wave speed within the material. However, the reliability of this conclusion is questionable due to the poor spatial and temporal resolution of the measurements.

The studies mentioned above report an opposite effect of strain rate to the positive sensitivity reported by Gerlach *et al.* [12] for an RTM-6 resin tested without reinforcement. A positive sensitivity was also established by Naik *et al.* [67] (+34% between 1.3×10^3 s^{-1} and 1.5×10^3 s^{-1}) and Gama *et al.* [57] (up to +108% at 1.2×10^3 s^{-1}). The notably higher sensitivity from Gama *et al.* [57] is likely unreliable due to significant contamination from dispersion. However, the magnitude of this sensitivity is similar to that reported by Kapoor *et al.* [70] for a Kevlar 29/polypropylene (PP) 2D woven composite (+134% up to 4.3×10^3 s^{-1}). A larger magnitude of sensitivity is to be expected for the through-thickness behaviour that is dominated by a ductile thermoplastic matrix due to the stronger molecule mobility. Hosur *et al.* [64] found that failure strains increased with increasing strain rate due to a change in failure mode. Further, the strain rate sensitivity cannot be assessed for intermediate strain rates in that study since the specimens did not fail. Song *et al.* [58] reported a decrease in ultimate strain between 5×10^2 s^{-1} and 8×10^2 s^{-1}, followed by an increase at strain rates above 1×10^3 s^{-1}. No explanation was provided by the authors for this behaviour.

In general, the effect of strain rate on ultimate strains has yet to be established. A number of studies reveal that the effects of dispersion may still have significant influence on the measurement of ultimate properties, which may contribute to the high levels of disparity of conclusions reported within the literature.

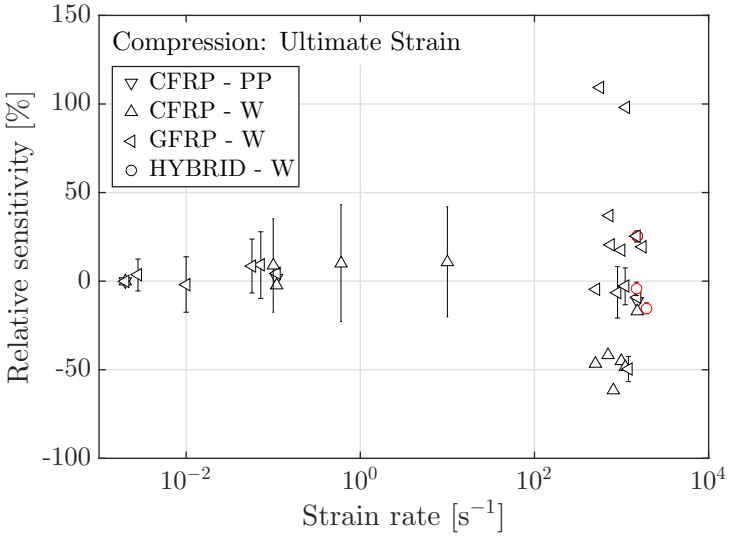

Figure 2.7: Summary of relative strain rate sensitivity for ultimate compressive strain from the literature. 'PP' and 'W' denote pre-preg and plain weave reinforcement, respectively. Red symbol outline denotes that values are quoted with respect to strain at lowest strain rate considered (1.3×10^3 s^{-1} for [67] and 1×10^3 s^{-1} for [68]). Error bars denote the range of reported sensitivity and not standard deviation. Data taken from [9, 57, 58, 60–68]

2.3.2 Strain rate effects on tensile properties

Comparatively fewer studies are available on the strain rate dependency of tensile interlaminar properties. This is because testing in tension is more complicated than it is in compression. As described in Sec. 2.2, additional challenges are introduced with specimen gripping, alignment and sensitivity to stress concentrations. Studies on resin strength in tension are also very limited and the majority of available studies are of little benefit since tensile specimens loaded with a SHPB commonly fail outside of the gauge region and thus have high scatter [12]. All of these issues tend to impose additional restrictions on the attainable strain rates using a tensile SHPB.

Elastic modulus under tensile loading

Very few studies have reported measurements of high strain rate elastic modulus [11, 12, 48, 66, 71, 72]. A summary of findings from the literature is provided in Fig. 2.8. Lifshitz and Leber [71] used a tensile SHPB to test carbon/epoxy pre-preg and glass/epoxy woven composites. They reported a greater increase in modulus for the pre-preg (+40%) compared to the woven composite (+18%) for strain rates up to 2×10^2 s^{-1}. Similar trends were reported by Medina and Harding [72] at strain rates up to 9.5×10^2 s^{-1} (+31% for carbon/epoxy pre-preg, -13% for glass/epoxy weave). At such high strain rates, it is likely that inertia has significant influence on the apparent modulus. Dispersion may also act to mask the true mechanical response. This is shown in longitudinal and transverse strain measurements within the specimen, which exhibit oscillations throughout the duration of the test (Fig. 3 in [72]). Comparison of carbon and glass epoxy weaves show that the tensile modulus appears to be insensitive to fibre material. Nakai and Yokoyama [11, 48] noted a substantial increase in the 'apparent' modulus, which was thought to be a result of the viscoelastic modulus of the resin. This explanation is in agreement with studies on the tensile properties of epoxy resins, which show a marked increase in apparent modulus at high strain rates [12].

Hufenbach *et al.* [73] used direct tensile loading in a two-bar SHPB configuration to test two

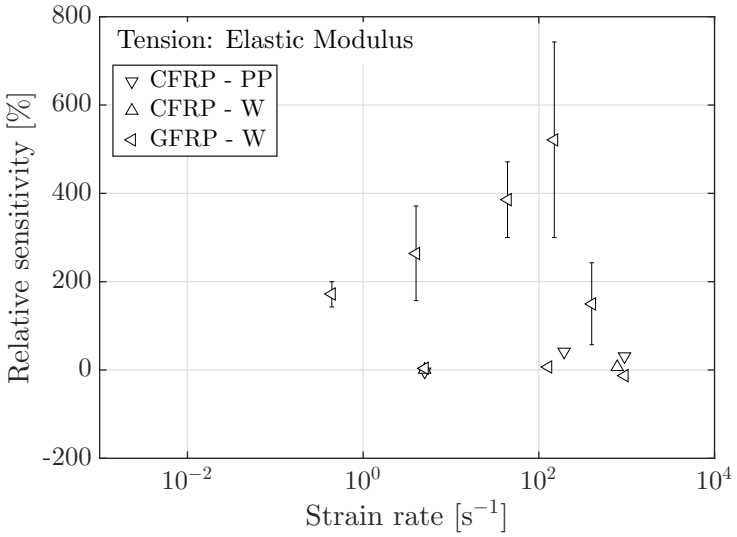

Figure 2.8: Summary of relative strain rate sensitivity for tensile modulus from the literature. 'PP' and 'W' denote pre-preg and plain weave reinforcement, respectively. Error bars denote the range of reported sensitivity and not standard deviation. Data taken from [71–73]

glass/polypropylene woven composites. A very large sensitivity to strain rate (up to +500%) and considerable scatter was observed. The large scatter led to the conclusion that the SHPB technique was unsuitable for studying coarse reinforcement architectures [73]. Hufenbach *et al.* [73] also comment on the influence of manufacturing on the measured tensile modulus. Compaction levels were reported to be much higher for L-shaped beam specimens compared to the dog bone specimens used with the SHPB. This resulted in a much higher modulus for the L-shaped beams.

In summary, measurements of the elastic modulus under tensile loading is scarcely reported in the literature. There is some indication of a positive sensitivity to strain rate but high scatter and the lack of studies makes this difficult to say with any certainty.

Tensile strength

The majority of studies which focus on tensile strength utilise some form of a tensile SHPB, with strain rates generally lower than $4{\times}10^2$ s^{-1} [11, 48, 51, 71, 73–75]. A summary of relative strain rate sensitivity reported in the literature is provided in Fig. 2.9. While most studies report an increase in strength at high strain rates, the magnitude is unclear due to high inter and intra study scatter. Some report moderate increases in strength of around 30% compared to quasi-static values [71, 72], while others report much more significant increases of up to several hundred percent [11, 48, 74]. In the case of Naik *et al.* [74], it appears that the reaction forces on the specimen are not equal for much of the test (not in quasi-static stress equilibrium). This is difficult to confirm due to poor sampling of strain gauge signals from the incident and transmitter bars. In the studies by Nakai and Yokoyama [11, 48], where much lower strain rates are considered, it appears that quasi-static stress equilibrium is obtained. Those studies report large increases in strength, which is expected for a matrix-dominated property based on studies of an unreinforced epoxy resin [12].

Studies by Gerlach *et al.* [47] and Govender *et al.* [66] report higher strain rates up to $1.1{\times}10^4$ s^{-1} and $1.8{\times}10^3$ s^{-1}, respectively. In the case of Gerlach *et al.* [47], tensile loading was induced using a customised fixture to load an overlapping joint, or 'cross' specimen, using a compressive SHPB. In that study, it is unclear how strain rate was defined, or how the

effects of the custom loading fixture were accounted for. Govender *et al.* [66] used a spall test configuration to measure the tensile failure strength of a woven glass fibre-vinyl ester composite. Pulse time-shifting was employed to estimate forces in the specimen at failure. This approach removes the requirement for quasi-static stress equilibrium, allowing much higher strain rates to be achieved. However, the approach requires corrections for dispersion and the assumption of one-dimensional wave propagation through the bar and specimen. The failure location was determined post-mortem with the strength estimated using the maximum computed stress seen by that position. Some failed specimens exhibited substantial residual strength after a crack had initiated. Failure surfaces showed signs of fibre bridging, which suggests that the interlaminar failure is not purely brittle [66]. The results from this study could not be used to assess the effect of strain rate as only one strain rate was considered and no quasi-static values were reported for comparison. Quasi-static testing was unsuccessful due to consistent failure within the grips. Instead, the authors compare strength to the manufacturer's quoted resin strength. While the spall test arrangement appears promising for higher strain rate characterisation, more information must be collected during the test in order to remove the limiting assumptions of the SHPB that remain.

The scatter in reported strengths have been attributed to a number of issues associated with tensile testing. Machining defects prevented Lifshitz and Leber [71] from obtaining reliable strength measurements on their carbon/epoxy specimens. For tensile testing in the through-thickness direction, machining defects are particularly problematic as cracks can easily propagate between plies. Specimen geometry was shown to have a significant influence on the dynamic response. Using full-field measurements, Gilat *et al.* [52] showed that less than half of the gauge region on a waisted specimen was subjected to uniform stress. This results in overestimation of strain and strain rate using SHPB theory. Lifshitz and Leber [71] also had issues obtaining consistent bonds between specimen halves (machined in two pieces). This is also expected to have an effect on those studies where the specimens are directly bonded to the input bar [66, 71, 74]. Others have chosen to introduce the load by bonding the specimen onto threaded inserts [47, 48, 72, 73]. Slight misalignments between the specimen and loading axis will introduce bending stresses in the specimen, resulting in considerable scatter in measured strength values. Similar issues have been reported for high strain rate tensile testing of epoxy resins [12, 54]. Variability in the technique used to introduce the load contributes to scatter and is a result of the lack of test standards for high strain rates.

In summary, scatter across the literature is too large to conclude that there is any influence of strain rate on tensile strength.

Ultimate tensile strain

Similar to tensile strength, it is difficult to obtain reliable strain measurements with existing techniques. In studies performed by Gerlach *et al.*, the gauge region dimensions [51], or customised loading fixtures [47] prevented measurements of strain to be made. Some studies report values of ultimate strain at high strain rates, but do not supply quasi-static values for comparison [71, 74]. In other studies, the focus was on obtaining measurements of strength and stiffness, and ultimate strains were not reported [62, 66, 75]. Strain gauges have been used to measure strain directly from the specimen [71, 72]. Medina and Harding [72] measured a 22% and 65% increase in failure strain at $9.5{\times}10^2$ s^{-1} for carbon/epoxy pre-preg and woven composites, respectively. This study highlights two challenges with using strain gauges. In their study, it was difficult to place the strain gauge appropriately so that it was positioned on the failure plane. A similar challenge was reported by Liftshitz and Leber [71]. An additional

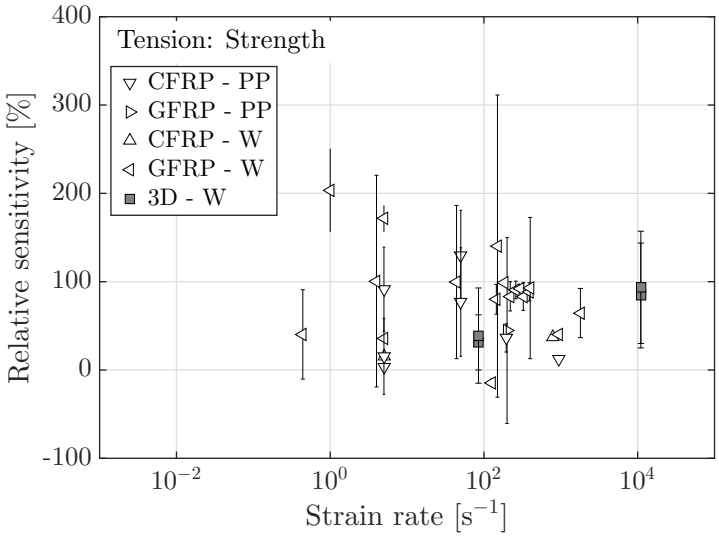

Figure 2.9: Summary of relative strain rate sensitivity for tensile strength from the literature. 'PP' and 'W' denote pre-preg and plain weave reinforcement, respectively. Error bars denote the range of reported sensitivity and not standard deviation. Data taken from [11, 47, 48, 51, 66, 71–75]. For reference [66] (shaded symbols) values are reported relative to the matrix properties

issue experienced by Medina and Harding [72] was premature failure of the strain gauges. The ultimate strains measured by Medina and Harding [72] at such high strain rates (9.5×10^3 s^{-1}) are likely to be contaminated by inertia effects. Therefore, the trends reported by Medina and Harding [72] are unlikely to be reliable representations of the true effect of strain rate on ultimate strain.

There are a few studies that report failure strains based on SHPB theory [11, 48, 73], but the reported trends are inconclusive. A summary of the failure strains presented in the literature is shown in Fig. 2.10. Nakai and Yokoyama performed two studies on carbon/epoxy pre-preg composites [11, 48]. They reported a general increase in failure strain for strain rates up to approximately 10^2 s^{-1}. The reported magnitude is unreliable due to the high scatter in their measurements (strain rate sensitivity ranges from -50% to + 90% within scatter). Hufenbach *et al.* [73] reported that failure strain has little sensitivity to strain rate between quasi-static and strain rates up to 4×10^2 s^{-1}.

In summary, obtaining reliable strain measurements at high strain rates has proven to be a challenge. As a result, very few studies report ultimate strains. From those that attempt to measure ultimate strains, the influence of strain rate cannot be determined with certainty.

The limited available literature suggests there is much outstanding work to be done to develop testing procedures for reliable measurement of interlaminar properties under tensile loading. Tensile tests are highly sensitive to gripping, alignment and stress concentrations. This does not facilitate reliable measurement of material properties using existing techniques, which rely on a number of assumptions about the material response. Further, not only is there significant scatter in the measured high strain rate properties, but there is high scatter in the quasi-static measurements to which they are compared. A potential alternative to strain gauges is optical full-field measurement techniques. Full-field measurements provide far more information about the specimen response, which is required to alleviate assumptions and advance high strain rate tensile characterisation.

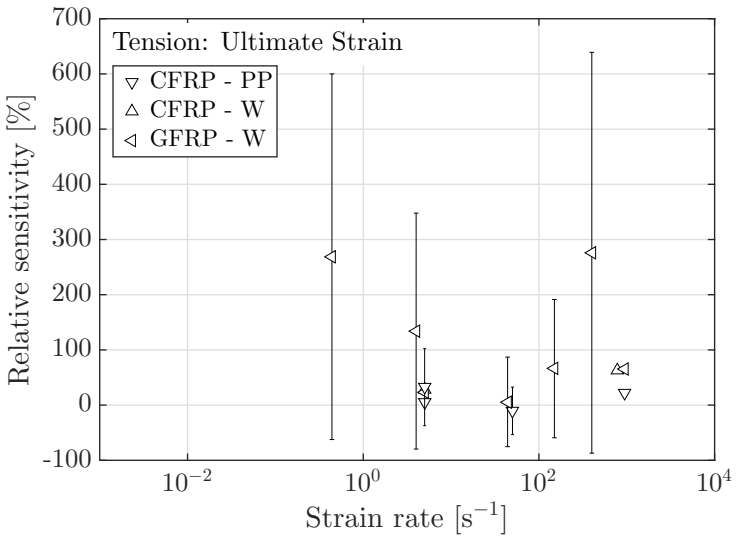

Figure 2.10: Summary of relative strain rate sensitivity for ultimate tensile strain from the literature. 'PP' and 'W' denote pre-preg and plain weave reinforcement, respectively. Error bars denote the range of reported sensitivity and not standard deviation. Data taken from [11, 48, 72, 73]

2.3.3 Strain rate effects on interlaminar shear properties

Shear modulus

The combined stress states induced in many existing shear tests complicates the matter of obtaining a true estimate for the shear modulus. Therefore, far fewer studies attempt to extract the interlaminar shear modulus, compared to the interlaminar shear strength (ILSS). A summary of relative strain rate sensitivity for shear modulus is presented in Fig. 2.11.

Bouette *et al.* [44] reported no appreciable variation in shear modulus measured using double and single lap joints. The modulus was estimated using failure stress and strain assuming linear elastic behaviour to failure. However, strain gauge measurements by Bouette *et al.* [44] reveal a non-linear behaviour near failure, and would act to reduce the 'apparent modulus'. Hallett *et al.* [45] also used single lap specimens and reported an average decrease in stiffness with increasing strain rate. The magnitude of sensitivity is difficult to determine as their measurements had significant variance. The authors suggested that normal stresses at the notches were responsible for the scatter. Using thin-walled tubular specimens, Naik *et al.* [10] reported a net increase in apparent shear modulus (+33% for glass/epoxy and +41% for carbon epoxy) up to $1{\times}10^{3}$ s^{-1}. Similar to the study by Bouette *et al.* [44], the shear response was found to be non-linear by Naik *et al.* [10]. This makes it difficult to obtain an estimate of the true shear modulus. Naik *et al.* [10] provided an estimate on the lower bound of shear modulus by fitting a line between the origin and a point on the curve near peak stress. Naik *et al.* [10] also claimed that the values obtained with the tubular specimens are more representative of the true behaviour since notch effects are eliminated. Interestingly, this did not seem to have a significant effect on the level of scatter in their measurements. Scatter in properties measured using tubular specimens may be attributed to micro cracks/damage induced from machining [10], specimen geometry (fillet radius, wall thickness) [10, 14], and layup orientation [14].

In summary, the effect of strain rate on shear modulus is not clearly understood. This is primarily due to mixed stress states in the specimen leading to biased estimates of shear modulus, as well as inherent limitations of the Hopkinson bar analysis as for the tensile modulus.

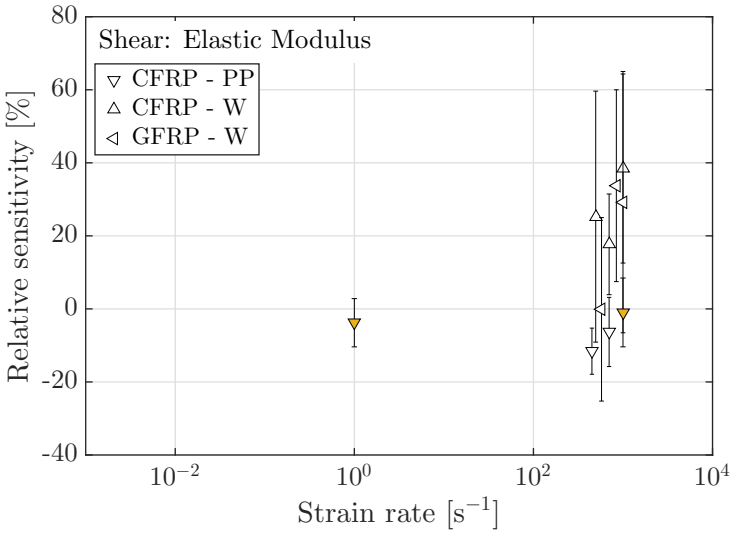

Figure 2.11: Summary of relative strain rate sensitivity for shear modulus from the literature. 'PP' and 'W' denote pre-preg and plain weave reinforcement, respectively. Orange and purple symbols denote testing in the 1-3 and 2-3 directions, respectively. White denotes that direction is not specified. Error bars denote the range of reported sensitivity and not standard deviation. Data taken from [10, 44, 45]

Shear strength

The through-thickness response of composites is particularly sensitive to combined states of tension and shear. When tensile stresses are present, the interlaminar shear strength has shown to decrease significantly [8, 76]. It is very difficult to achieve the desired state of uniform shear in quasi-static and HSR testing and therefore, most studies are limited to reporting 'apparent shear strength' [15, 19, 46]. The influence of strain rate on shear strength, based on studies from the literature, is illustrated in Fig. 2.12.

Single and double lap specimens were initially the most popular choices for high strain rate shear testing since they could be tested using a compressive SHPB. Bouette *et al.* [44], Harding and Li [77] and Harding and Dong [8] used double lap specimens to extract the ILSS. These studies found that lap joint specimens are unreliable since failure initiates near the ends of the overlap under a state of combined shear and normal stresses. The same was found for single-lap specimens [8, 44, 45]. The work with single lap specimens shows that the amplitude of stress concentration can be reduced if the overlap is kept small [44, 45]. While gauge region geometry can be altered to reduce the combined stress state, it cannot be eliminated. This is a likely contributor to the high levels of experimental scatter on reported shear modulus and failure stresses.

Other approaches to measuring the interlaminar shear properties include the use of the double V-notch shear test (Iosipescu) [78], the out-of-plane off-axis tests [46], the double notched shear test in dynamic compression [79], short beam shear tests [79], and thin-walled tubular specimens loaded using a torsional SHPB [10, 14]. Yokoyama and Nakai [79] found that strengths obtained with the double-notched shear specimens compared well with the short-beam shear tests. Further, measured ILSS values agree well with simulated stress levels in the centre of the specimens. This lead them to conclude that the influences of the stress concentrations from the notches were negligible. Further, the compressive normal stresses at the notches acted to suppress delamination. The result was much lower levels of scatter compared to previous studies using a single or double lap specimen. Hufenbach *et al.* [78] used a lightweight Iosipescu fixture for testing at intermediate strain rates up to approximately $6{\times}10^{1}$ s^{-1} [78]. This appeared to

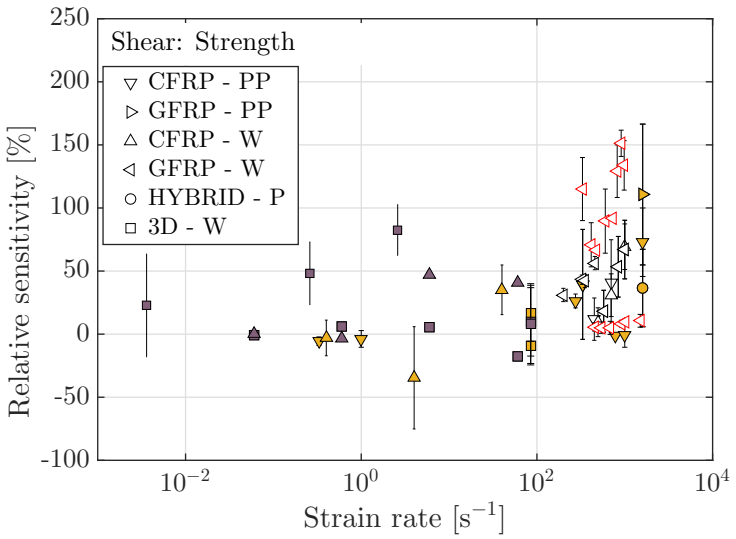

Figure 2.12: Summary of relative strain rate sensitivity for shear strength from the literature. 'PP' and 'W' denote pre-preg and plain weave reinforcement, respectively. Red symbol outline denotes that values are quoted with respect to strain at lowest strain rate considered (2.6×10^{2} s^{-1} for [46], 4×10^{-2} s^{-1} for [78] and 3×10^{2} s^{-1} for [14]). Orange and purple symbols denote testing in the 1-3 and 2-3 directions, respectively. White denotes that direction is not specified. Error bars denote the range of reported sensitivity and not standard deviation. Data taken from [8, 10, 14, 44–47, 73, 77–79]

work reasonably well for testing in the 2-3 plane, but yielded unacceptable levels of scatter in strength measurements for the 1-3 plane and thus, the strain rate sensitivity could not be determined. This was attributed to low stress and strain levels and measurement resolution of the load cell. Naik *et al.* [10] compared thin-walled tubular specimens, loaded with a torsional SHPB, to single-lap specimens loaded in dynamic compression using a SHPB. Tubular specimens were selected for detailed analysis as they created a purer state of shear stress. The level of scatter from single lap specimens was similar but produced slightly lower strength values. This is likely a result of the combined tension-shear stress state. The opposite was found by Gowtham *et al.* [14] who reported lower strengths measured using a torsional SHPB compared to a single lap shear joint. This was attributed to stress concentrations from the weave reinforcement in the failure plane of the tubular specimens. The weave reinforcement was shown to create variations in stiffness and stress along the radial and circumferential directions, acting as stress concentrations. This violates one of the primary assumptions that stress is uniform throughout the thickness.

A common characteristic to many of these studies is the high levels of scatter, which prohibits definitive claims from being made about the strain rate sensitivity [45, 47, 78]. Qualitative trends may still be useful, and there appears to be more of a general agreement between studies in these trends. Many studies report that the interlaminar shear strength increases moderately with increasing strain rate [8, 10, 14, 46, 79]. The level of strain rate sensitivity has yet to be determined reliably, with reports of strength increases ranging from 15% [14] to 200% [14]. There is also a collection of studies that report a constant strength over a range of strain rates [44, 73, 79].

In summary, there is some indication of a positive influence of strain rate on interlaminar shear strength. However, the presence of combined tension and shear stresses, and stress concentrations have prevented reliable characterisation of the high strain rate behaviour.

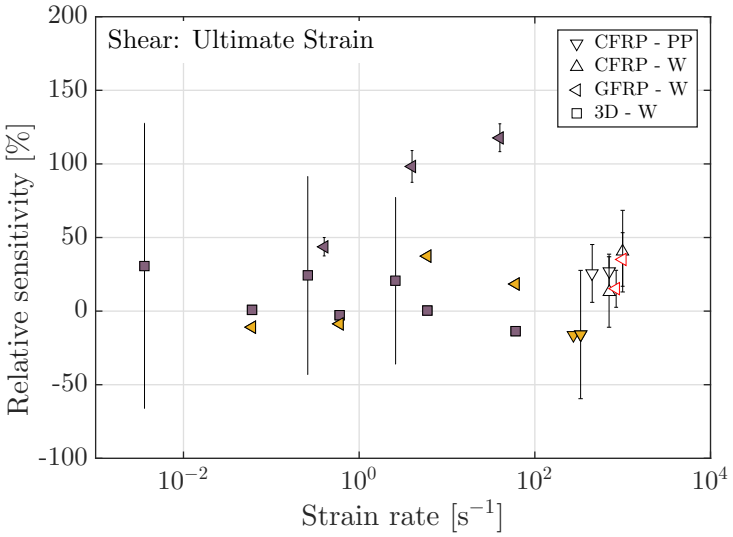

Figure 2.13: Summary of relative strain rate sensitivity for ultimate shear strain from the literature. 'PP' and 'W' denote pre-preg and plain weave reinforcement, respectively. Red symbol outline denotes that values are quoted with respect to strain at lowest strain rate considered (5×10^{2} s^{-1} and 6×10^{2} s^{-1} for [10], and 4×10^{-2} s^{-1} for [78]). Orange and purple symbols denote testing in the 1-3 and 2-3 directions, respectively. White denotes that direction is not specified. Error bars denote the range of reported sensitivity and not standard deviation. Data taken from [8, 10, 45, 73, 78]

Ultimate shear strain

In the majority of cases, it appears that strain was either not reliably measured [78], or the focus of the study was on shear strength and thus, strains at failure were not reported [14, 46, 79]. Some fixtures and specimen geometries make shear strain measurements challenging or impossible [47]. Of the remaining studies, there is very little agreement as to the effect of strain rate on failure strain. The variation in strain rate sensitivity across the literature is presented in Fig. 2.13. Two studies by Bouette *et al.* [44] and Hufenbach *et al.* [73] report that shear strain at failure is independent of strain rate, up to 1×10^{3} s^{-1} and 4×10^{2} s^{-1}, respectively. The lack of sensitivity to strain rate may be a shortcoming of lap specimens with failure being heavily influenced by normal stresses at the ends of the overlap, similar to Hallett *et al.* [45]. In contrast, Gillespie *et al.* [46] reported an increase in peak strain up to a strain rate of 582 s^{-1}, followed by a reduction at higher strain rates. These higher strain rates approach the upper limit for equilibrium, set by the 'R criterion', and are likely contaminated by inertia effects. Harding and Li [77] found a significant increase (approx. 250%) in failure strains with impact speed. Unfortunately, the strain rates at failure were not reported. Naik *et al.* [10] measured a 38% increase in failure strain between strain rates of 5.8×10^{2}- 1×10^{3} s^{-1}, but did not provide quasi-static reference values for comparison.

Much like the cases of shear modulus and shear strength, ultimate shear strains presented in the literature are heavily influenced by mixed stress states and stress concentrations. As a result the current literature cannot be used to determine the influence of strain rate on ultimate shear strain.

2.4 High-Speed Imaging Technologies

To measure dynamic events with small time scales, requires the capability to capture images with very small inter-frame times. To perform meaningful quantitative measurements further requires low noise and high quality images. High-quality, multi-mega-pixel cameras are used ubiquitously for quasi-static full-field measurements. However, the architecture of these cameras is designed such that image data is read during image capture using multiple parallel channels to the internal storage of the camera. Since recording length is determined by the amount of memory available, the record time can be extended with additional memory. Unfortunately, camera readout is limited with this sensor/memory readout structure, which limits the amount of data that can be transferred. Therefore, to increase framing rate, one must reduce the number of pixels being read (reduced field-of-view) [80]. This technology was first implemented by Etoh *et al.* [81] in a camera which could record at 4,500 fps - the fastest recording speed at the time [82]. This architecture then became the standard for the category of cameras now referred to as 'high-speed cameras' (1,000's to 100,000's of frames per second [83]).

Another category of cameras have emerged in the last few decades, which can produce framing rates upwards of 1 Mfps. These cameras are referred to as 'ultra-high-speed' cameras [83]. A summary of high-speed and UHS technology is shown in Fig. 2.14. In Fig. 2.14, each camera is represented by a rectangle, with the centre of the rectangle indicating the frame rate and record length, and the size of the rectangle representing the field of view. A variety of techniques have been explored in pursuit of faster framing rates, which will be described in the following sections.

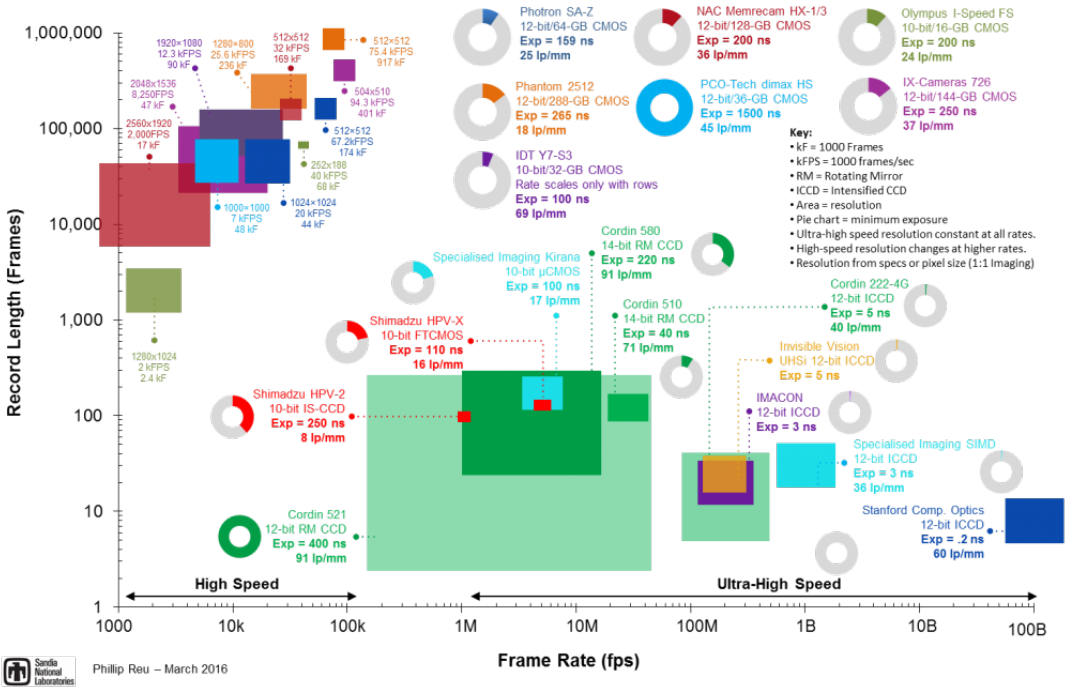

Figure 2.14: Summary of cameras available on the market as a function of framing rate, array size, and recording time. Courtesy of Dr. Phillip Reu from Sandia National Laboratories [84]

2.4.1 Rotating mirror cameras

These cameras, such as the Cordin 500 series cameras, use a rotating mirror to project images onto separate CCD sensors as shown in Fig. 2.15. The drum is rotated at high speeds, using an

electric or gas drive, and can achieve framing rates up to 25 Mfps [85]. The number of sensors on the drum can vary from 20 to 78 [85].

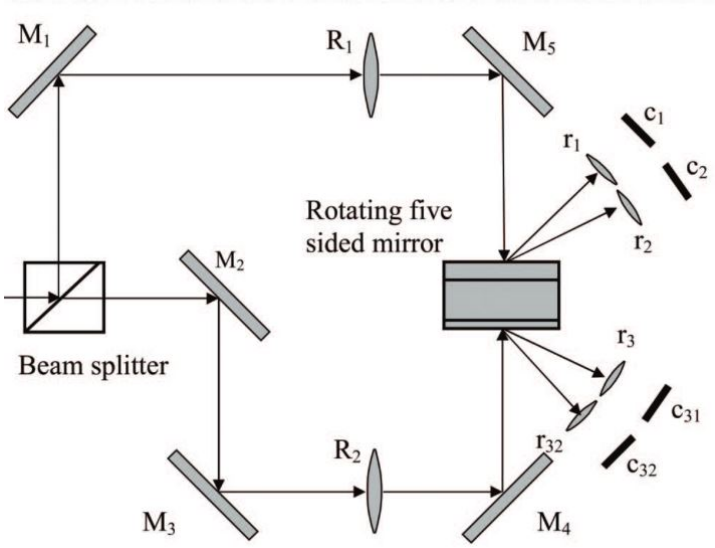

Figure 2.15: Schematic of Cordin 550 rotating mirror camera [86]

The advantage of using separate charged-coupled device (CCD) sensors is that much higher resolution images (up to 8 megapixel) can be acquired. However, these cameras tend to suffer from different geometrical distortions and misalignments between images. This is caused by the spatially different optical paths which the light travels through to reach each CCD sensor [80, 86]. The effects can be minimised using extensive calibration procedures, as outlined in [86], but cannot be completely eliminated. Kirugulige *et al.* [86] concluded that these misalignments precluded the possibility of performing image correlation between images collected on different sensors. Therefore, one set of images needs to be collected in a reference configuration, and a second set during the event, with image correlation performed between images collected on the same sensor [26, 86].

2.4.2 Beam splitting cameras

These cameras (such as the Imacon 220) rely on a beam splitter to project the images to a series of CCD sensors (see Fig. 2.16). Image acquisition is controlled by electronic shuttering, which offers very high framing rates (2.5 ns inter-frame time [87]). The split light is first directed to micro-channel plate image intensifiers before being projected onto the individual CCD sensors using fibre-optic bundles [87].

These cameras suffer from the same issues as the rotating mirror camera (*e.g.*: separate optical paths for each image, distortions, different field of view between images, *etc.*). Therefore, a series of static images, unique to each sensor, must be collected to perform image correlation [88]. Pierron *et al.* [88] showed that a major drawback to these cameras is photon leaking between neighbouring pixels. This is a result of the highly non-linear fibre-optic bundle and micro-channel plate combinations [87]. The result is spatially correlated blurring/noise patterns, which are very detrimental for image correlation.

The technologies discussed so far rely on splitting the light and recording on separate sensors. This inevitably creates image distortion and misalignments, which are highly undesirable for performing quantitative full-field measurements. Another category of UHS cameras has been

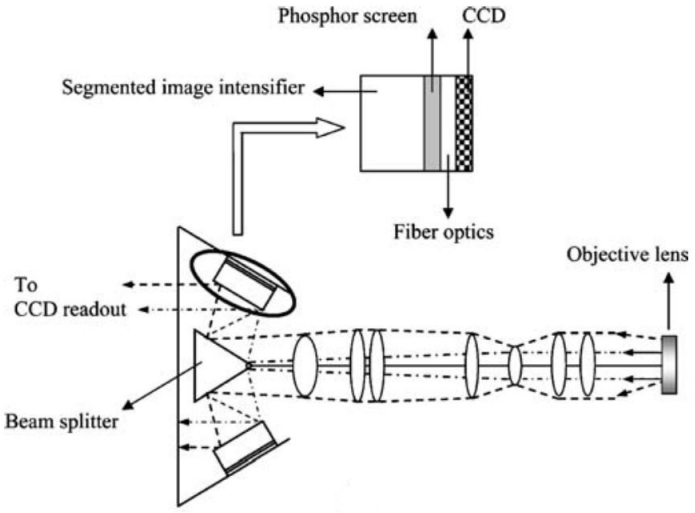

Figure 2.16: Schematic of Imacon 220 camera [87]

developed, which eliminates these issues through integrated memory on the image sensor. These technologies are described in the following sections.

2.4.3 In-situ image storage sensor charged-coupled device (ISIS-CCD) camera

In 1996 a new type of burst-sensor was developed by Kosonocky *et al.* [89], with integrated memory on the image sensor. This provided 30 images, with a 360 x 360 pixel array at frame rates up to 833,000 fps. The shortcomings of this sensor was that only burst-mode operation was possible, and the two-dimensional image signal transfer readout halved the framing rate (or halved the array size) [82, 90]. This was the first rendition of the now-called *in-situ* image storage charged-coupled device (ISIS-CCD) sensor. This design was improved by Etoh *et al.* [90], to enable continuous capturing, of 103 frames at framing rates of up to 1 Mfps for an array of 312 x 260 pixels. The basic architecture of the sensor is shown in Fig. 2.17. This technology was integrated into the Shimadzu HPV-1 and HPV-2 cameras.

Each pixel element is composed of a photodiode (shaded region in Fig. 2.17), an *in-situ* CCD storage channel, extending downward from the photodiode, and a memory drain at the end of the storage channel. In continuous capturing mode, frames are sequentially stored in the storage channel until the channel is full, at which point the earliest frames are drained. After image capturing is complete, the signals are stored within the channel and read out into a buffer at the bottom of the vertical CCD storage channels [82].

Since memory is stored on the sensor, the actual photo-sensitive area is quite small, which results in low fill-factors (13% in the horizontal direction for the Shimadzu HPV-1 [88]) compared to standard CMOS or CCD sensors (near 100%). The relatively high heat generation with ISIS-CCD sensors limits the achievable frame rates to about 1 Mfps [80]. Additionally, the exposure time of the ISIS-CCD sensor is dependent on the frame rate and cannot be adjusted. This can result in image blurring at low/intermediate frame rates [80].

This technology has since been advanced into the so-called 'backside illuminated' (BSI)-ISIS sensor, which can achieve frame rates up to 16 Mfps [91]. A schematic of the BSI-ISIS-CCD sensor is provided in Fig. 2.18. The BSI structure increases the sensitivity and fill-factor to near 100%. The noise is also independent of frame rate so a reasonable dynamic range is

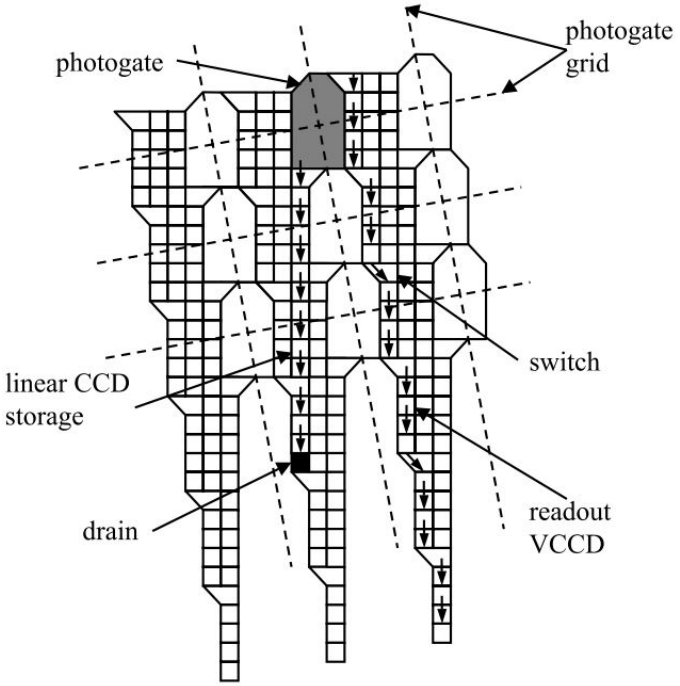

Figure 2.17: Schematic of an ISIS-CCD linear storage sensor [90]

guaranteed at all frame rates. A drawback to this architecture is that the sensor requires a more complex double-trigger, as described in [91], to reduce the time recording and avoid excessive heat generation. It also suffers from noise generation during the readout phase after overwriting recording [91].

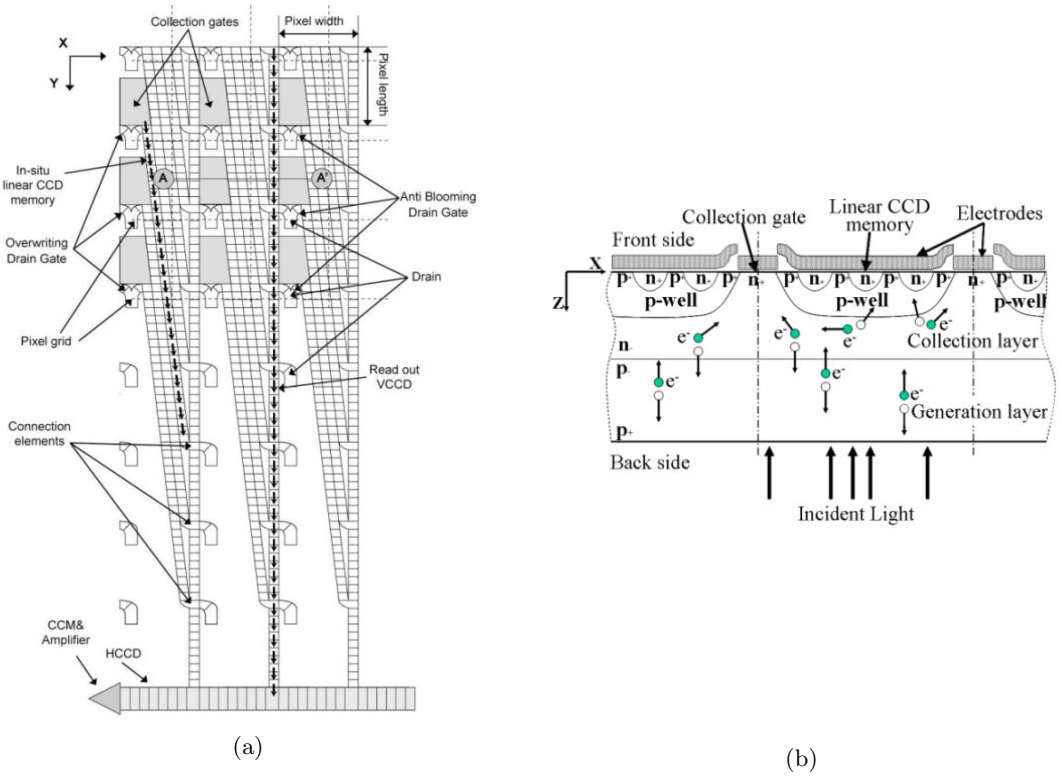

Figure 2.18: (a) Schematic of an ISIS-CCD linear storage sensor, and (b) cross-section 'A-A' in (a) [91]

2.4.4 Frame-transfer complimentary metal oxide semiconductor (FTCMOS) sensors

To reduce issues with heat generation at frame rates upwards of 1 Mfps for ISIS-CCD sensors, Shimadzu developed a burst-type image sensor based on the CMOS image sensor technology. This is referred to as an FTCMOS sensor, is and incorporated in the Shimadzu HPV-X camera. A schematic of the FTCMOS sensor structure is shown in Fig. 2.19.

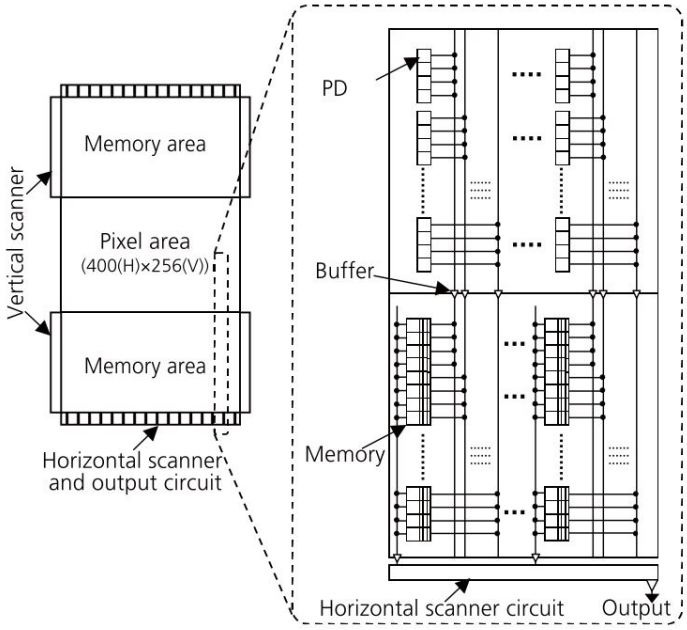

Figure 2.19: Schematic of the FTCMOS sensor used in the Shimadzu HPV-X camera [80]

Image signals are connected via metal wires to serial memory above and below the pixel area. This configuration enables concurrent recording at high speeds. Each wire connects 4 pixels to memory. With all pixels recorded, this enables 128 frames to be captured at a rate of 5 Mfps with an array of 400 x 250 pixels. The frame rate can be doubled if only half of the pixels are recorded. In this mode, pixels are recorded in a zig-zag pattern, with interpolation between them to recover the full 400 x 250 pixel array. As a result of the interpolation, this mode is not useful for performing full-field quantitative measurements. Full details about the sensor/memory readout structure can be found in [80]. In addition to reduced power consumption, the exposure time can be set independently of framing rate. Compared to the Shimadzu HPV-1 and HPV-2 (ISIS-CCD), the noise with the Shimadzu HPV-X is much improved, as demonstrated in [27, 29]. The main drawback with these types of cameras is the low spatial resolution, compared to rotating mirror or beam splitting cameras.

2.5 Full-Field Measurement Techniques

To perform quantitative measurements using the images collected with UHS cameras requires image processing algorithms. A number of image processing techniques are currently available, which can generally be categorised as interferometric, or non-interferometric. Interferometric techniques include speckle pattern interferometry (SPI) [92], moiré interferometry [93], and holography [94]. The most common non-interferometric techniques include digital image correlation (DIC) [95] and the grid method [96]. Interferometric techniques offer a much higher

spatial resolution (on the order of 1 pixel, or 10's of μm) compared to non-interferometric techniques (on the order of 10's of pixels, a few hundred μm). Interferometric techniques have seen extensive use in quasi-static testing, but have limited use in dynamic applications due to the time delay to perform phase shifting. The use in dynamics has been limited to measuring harmonic phenomena where time-averaging can be used [97, 98]. Additional drawbacks include high sensitivity to vibrations, and the need for lasers, mirrors, or beam splitters, making them less practical for industrial applications. On the contrary, non-interferometric techniques are based on post-processing of images, and so can be applied to measure both harmonic and time-dependent, dynamic events. These techniques have been used in several applications for dynamic full-field measurements [27, 27–30, 33]. Therefore, the non-interferometric techniques of DIC and the grid method will be focus of this section.

2.5.1 Digital image correlation

Digital image correlation (DIC) is a non-contact, white light, optical technique for measuring displacements and strains. Deformation is computed by correlating images of a random pattern before and after deformation. Correlation is performed over small regions, or subsets, such that the pattern within each subset is nominally unique. Displacements are parameterised using shape functions. The shape function coefficients are determined through the minimisation of a correlation matching criterion. Sub-pixel information is then retrieved using an interpolation function.

Digital image correlation (DIC) was first proposed in the 1980's by Sutton *et al.* [99], and has since seen widespread use in experimental mechanics. DIC can be performed using a single camera for in-plane measurements, or using stereo cameras to obtain three-dimensional displacements. A schematic of a typical 2D DIC measurement system is shown in Fig. 2.20. Because displacements are determined using subset-based correlation, the measurement resolution of DIC is generally much lower than other optical techniques (*e.g.* on the order of the subset size compared to 1 pixel resolution for interferometry). This causes problems in cases of small strains or highly heterogeneous deformations.

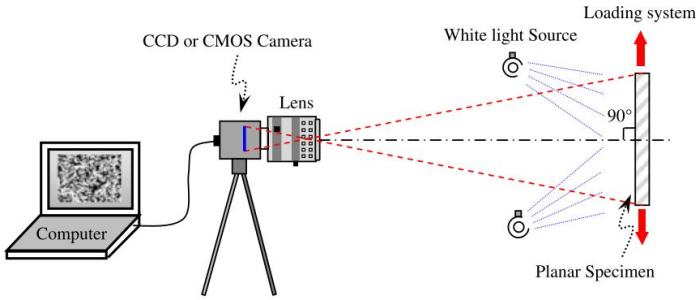

Figure 2.20: Schematic of the typical 2D DIC system [100]

Other extrinsic factors influence the measurement resolution, *e.g.* image contrast; lighting intensity and uniformity; speckle size and quality [101]; camera performance; and out-of-plane movements [102]. These factors affect all optical measurement techniques, and become critical for UHS measurements, where issues with lighting and camera performance become more pronounced. When full-field measurement techniques are used for materials characterisation, the effect of these experimental uncertainties must be understood. A useful tool for evaluating these factors independently is to use an experiment simulator [103, 104]. A representative finite element model is first developed to obtain displacement fields. These fields are then used to

deform a set of synthetically generated images. The effect of experimental uncertainties are introduced into the simulator to quantify the experimental error on identified material properties. This can then be used to optimise processing parameters and test geometry. Further details on the implementation of this procedure for quasi-static testing can be found in [103–105]).

Compared to quasi-static studies, DIC has seen limited application to high strain rate loading [51, 52, 65, 75, 88, 106]. As explained in previous sections, spatial resolution of traditional high-speed and UHS cameras are inadequate to perform meaningful full-field measurements. This is especially problematic when the fields to be measured are highly heterogeneous (*e.g.* inertial effects under high strain rate loading) [52, 65]. For such cases, a more favourable trade-off between measurement and spatial resolution is required. One possible alternative is the grid method, which will be the focus of the next section.

2.5.2 Grid method

The grid method is a technique based on processing images of regular grids to obtain in-plane displacement and strain. The grid method is most notably different from DIC in that image processing algorithms are used to extract phase distributions from the regular grids, rather than tracking individual points [96, 107]. Grid images are assumed to be aligned with the image sensor, and with light intensity, $s(x,y)$, varying in space according to quasi-periodic function (Eq. 2.2)[96, 108].

$$s(x,y) = \frac{A}{2}\left(2 + \gamma \cdot frng(2\pi fx + \phi_x(x,y)) + \gamma \cdot frng(2\pi fy + \phi_y(x,y))\right) + n(x,y) \tag{2.2}$$

where,

- A is the average field illumination;
- γ is the pattern contrast amplitude (between 0 and 1);
- $frng$ is a real 2π periodic function with an amplitude equal to 1, and average equal to 0;
- f is a spatial frequency of the pattern, or inverse of the grid pitch, p;
- $\phi_x(x,y)$ and $\phi_y(x,y)$ are the phase modulations (2π periodic) along the x- and y-axes, respectively;
- $n(x,y)$ is a noise term inherent to any digital imaging device.

When UHS cameras are used to capture grid images, low fill factors amplify the effects of aliasing in the presence of grids/patterns with high spatial frequency contrast. This creates parasitic fringe patterns in the strain fields [88]. The high frequency content of the grid is reduced by intentionally blurring the image, thus significantly mitigating the effects of the fill factor. Therefore, the quasi-periodic grid model is a good representation of experimental grid images captured with the ISIS-CCD or FTCMOS camera sensors. A comparison of a synthetic grid, generated using a sinusoidal function of grey level intensity, is compared to an experimental image in Fig. 2.21.

A slight movement of the grid is interpreted as a change in phase. Therefore, displacements are directly related to phase. Some approaches have been developed to obtain strain fields directly from phase maps [109]. This mitigates the amount of noise introduced into strain fields by skipping the spatial differentiation of displacement maps. However, in this work, the displacement maps are required to compute acceleration maps. To obtain the phase information,

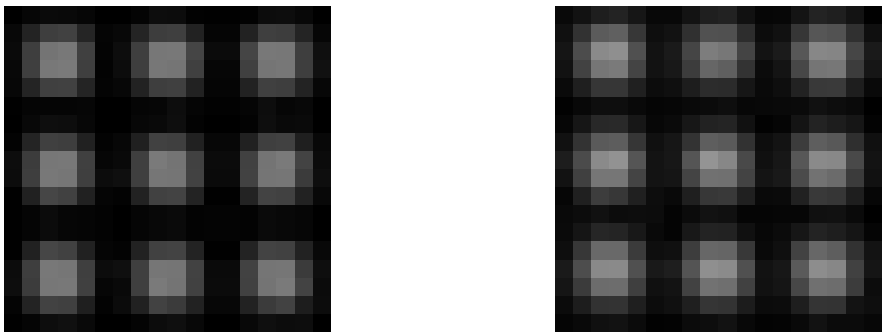

(a) (b)

Figure 2.21: Magnified views of grid images: (a) 0.3 mm synthetic grid (6 pixels/period), (b) 0.3 mm experimental grid (6 pixels/period)

a windowed Fourier transform (WFT) is used [110]. The WFT is a localised version of the Fourier transform (FT), in that the FT is calculated only over a small region surrounding each point. The phase distribution is retrieved by performing the WFT of the image, filtering the corresponding spectrum for the first harmonics, performing the inverse FT, and extracting the phase information. The choice of the windowing function will influence the metrological performance of the grid method, as investigated in [107, 108]. Based on these studies, a bi-triangular window should be used in cases with low noise, as it requires a smaller subset size compared to the Gaussian analysis window. From the phase fields, one can obtain the displacement fields using two approaches. One can estimate the displacement directly from the phase difference according to:

$$u_x(x,y) = -\frac{p}{2\pi}(\Delta\phi_x(x,y)) \tag{2.3}$$

$$u_y(x,y) = -\frac{p}{2\pi}(\Delta\phi_y(x,y)) \tag{2.4}$$

However, since this approach does not take into account the actual displacement at each point, differentiation of these fields to obtain strain becomes problematic when there are grid defects, such as slight irregularity in grid pitch, or missing grid. This assumption also tends to break down when displacements become larger. In these cases, it is more appropriate to use an iterative approach. This displacement for iteration $n+1$ is defined as:

$$u_x^{n+1}(x,y) = -\frac{p}{2\pi}(\phi_x^2(x+u_x^n(x,y),y) - \phi_x(x,y)) \tag{2.5}$$

$$u_y^{n+1}(x,y) = -\frac{p}{2\pi}(\phi_y^2(x,y+u_y^n(x,y)) - \phi_y(x,y)) \tag{2.6}$$

In this approach, the approximate calculation is used as the initial guess, and the calculation is performed iteratively until the change in displacements falls below a defined threshold. This approach is more robust in practice, since it is likely that the real deposited grids will contain some defects.

The grid method is a well-established technique with several studies devoted to reliable measurement of displacement and strain [96, 108, 111]. As mentioned previously, a key advantage of the grid method over subset-based DIC is the better compromise between spatial and measurement resolution [111]. For example, the grid method provides one independent measurement point for every grid pitch (typically 5-7 pixels), compared to 21 pixels as the recommended minimum subset size for DIC [112]. The metrological performance of the grid method is superior to DIC particularly in cases where strain levels are low and high gradients occur (*e.g.*: wave prop-

agation in the through-thickness direction of a composite material)[111]. If the measurement resolution is not sufficient, small deformations cannot be captured, which may introduce bias into the identifications of material properties. This is particularly important when using UHS cameras, such as the Shimadzu HPV-X, having a low spatial resolution. The grid method has been successfully implemented with UHS imaging in a number of studies to capture dynamic displacement fields during impact events [26–29, 32]. Therefore, the grid method is selected in this work to perform UHS, full-field measurements of displacement during impact tests.

2.6 Inverse Techniques for Constitutive Parameter Identification

In solid mechanics, many test methods aimed at measuring constitutive mechanical properties have been designed such that a desired state of stress is known within the specimen. When coupled with direct measurement of strain, these tests give direct access to the constitutive equation linking the two. Examples of these tests include: simple tension tests, compression tests, and three-point bend tests. The necessary assumptions required for this approach are rather restrictive and can be particularly challenging to achieve when testing anisotropic materials, where coupling terms arise in the constitutive equations. In the case of dynamic loading, the problem is complicated further due to inertial effects. Even if these conditions can be reached, full characterisation of such materials may be very costly and time consuming as a limited number of parameters can be obtained from a single test. Therefore, new experimental methods are required that do not rely on the assumption of a known simple stress state. Since the purpose of material characterisation tests is to predict the response under much more complex multi-axial loading conditions, such tests would give access to this information directly. In these cases, an experimental inverse approach is required [43, 113]. The advancement of full-field measurement techniques has created opportunities for experimentalists to develop new test methods suited to inverse identifications.

A number of computational and experimental approaches have been proposed to resolve these inverse problems. The most common strategies are model updating approaches, or the VFM. These techniques will be briefly reviewed in the rest of this section.

2.6.1 Model updating approaches

In model updating approaches, the objective is to construct a finite element model of the test with representative boundary conditions, geometry, and applied loads. The model is used to compute the response of the material to a given set of constitutive parameters. A cost function is then constructed using the difference between simulated and measured responses, with the identified parameters being those which minimise the cost function. A number of cost functions have been considered in the literature including the "displacement gap" [114], "constitutive equation gap"[115, 116], and the "equilibrium gap" [117].

These approaches offer flexibility in the identification procedure since it can be formulated using a range of measured quantities (displacements, strains, forces, *etc.*), which do not need to be measured as a field, but rather as any set of over-determined data. This approach has been applied in many cases to identify linear-elastic parameters for laminated panels [118, 119], and elastic and visco-elastic parameters for isotropic plates [114], and wood-based panels [120]. Some applications of the finite element model updating (FEMU) approach for high strain rate

loading can be found in [121, 122]. Both studies focused on the identification of elasto-plastic material properties for metals at strain rates of approximately 10^3 s^{-1} [121] and 10^4-10^5 s^{-1} [122]. In the case of Piers *et al.* [121], full-field strains obtained with DIC and high speed imaging are used in the identification procedure, whereas identifications are performed using only force in [122].

In some studies, only a few measurement points are considered for the identification [116, 121–123]. Fewer measurement points reduces the computational time, however, including the whole field increases the redundancy and thus, increases the robustness of the identification procedure [113]. Care must also be taken when comparing experimental fields to simulated fields, as measured quantities are subjected to an 'experimental' filter caused by the optical setup (*e.g.*: noise, lighting, spatial resolution, *etc.*). The updating approach is also sensitive to the accuracy of modelling assumptions, specifically in modelling the boundary conditions, and may suffer from convergence issues. Interpolation errors can also arise when attempting to compare data between the imaged field of view and the FE mesh. Some studies have proposed alternative methods for obtaining displacements from images based on a finite-element decomposition, where displacements are obtained at the mesh nodal locations [119, 124]. This has shown to improve robustness and reduce computational time, however, the intrinsic properties of the simulations (*e.g.:* boundary conditions, mesh size, time increment, damping, *etc.*) will inevitably influence the identifications.

The robustness of model updating approaches is also dependent on the cost function selected. A study by Avril & Pierron [113] showed that when the displacement gap cost function is used, the identifications are similar to that obtained with the virtual fields method, but with non-optimal virtual fields. Therefore, in cases where fewer data points are available, the model updating approaches are better suited for identifications. However, when full-field measurements are available, the virtual fields method is more robust, as will be discussed in the next section.

2.6.2 Virtual fields method (VFM)

The VFM is based on the principle of virtual work and is applicable to cases where experimental strain fields are available. In the absence of body forces, the principle of virtual work has the form of Eq. (2.7).

$$-\int_V \boldsymbol{\sigma} : \boldsymbol{\epsilon}^* dV + \int_{\delta S} \boldsymbol{T} \cdot \boldsymbol{u}^* dS = \int_V \rho \boldsymbol{a} \cdot \boldsymbol{u}^* dV \tag{2.7}$$

In Eq. (2.7), where V denotes the volume of the region of interest, $\boldsymbol{T}$ is the Cauchy stress vector, which is applied to the in-plane boundaries denoted by δS, ρ is the material density, $\boldsymbol{a}$ the acceleration field, $\boldsymbol{\sigma}$ is the Cauchy stress tensor, $\boldsymbol{u}^*$ is the virtual displacement field, and $\boldsymbol{\epsilon}^*$ the virtual strain field deriving from the virtual displacement fields through $\epsilon^*_{ij} = 1/2(u^*_{i,j} + u^*_{j,i})$. Note that : and $\cdot$ denote the dot product in matrix and vector forms, respectively. The first term and second terms on the left hand side of Eq. (2.7) represent the internal and external virtual work, respectively and the right hand side represents the virtual work due to inertial forces.

The VFM exploits Eq. (2.7) with strategic selection of virtual fields for a given identification problem. For the case of linear elasticity, the unknown constitutive parameters can be identified by selecting as many independent virtual fields as there are unknown constitutive parameters. These parameters are then obtained by solving the system of linear equations generated by evaluating Eq. (2.7) with each set of virtual fields [125, 126]. The principle of virtual work

is satisfied by any virtual displacement fields that respect the physical force and displacement boundary conditions (known as 'kinematically admissible'). The virtual fields can be tailored such that the virtual work only involves resultant forces, or completely removes the contributions from external forces. In the absence of virtual work from external forces, only ratios of stiffness parameters can be extracted [125, 126]. For simplicity, virtual fields are commonly defined as polynomial functions [126], but can also be formulated as piece-wise functions to accommodate complex geometries or boundary conditions. If the data are corrupted by noise, as is inevitable with experimental measurements, the choice of virtual fields will have an influence on the results. To address this, automated procedures have been developed for selection of *special* optimal virtual fields with minimal sensitivity to strain noise [127]. This procedure selects a set of virtual fields, which act like filters for direct identification of each unknown constitutive properties from heterogeneous strain fields.

A number of examples can be found in the literature for identification of linear-elastic and elasto-plastic constitutive parameters under quasi-static loading. More recently, a number of studies have shown that the VFM can be applied for dynamic loading thanks to the advancement of UHS imaging technology [26, 28–30, 32, 33, 128]

Detailed comparisons of the approaches mentioned above can be found in [113, 129]. In [113], it was found that the FEMU technique provides similar identifications to the VFM in linear-elasticity, but with non-optimal virtual fields. Further, the VFM is much faster, and avoids issues with finite element modelling such as accurately representing the boundary conditions. Therefore, the VFM is selected to perform identifications of high strain rate constitutive properties in this work.

2.7 Advanced Testing Approaches Using High-Speed, Full-Field Measurements

A review of the literature highlights several key limitations with existing test methods that hinder the advancement of material characterisation for composites in the through-thickness direction. The assumptions required for a SHPB test are particularly restrictive to the maximum strain rate that can be obtained. In compression, strain rates are limited generally to less than 1.5×10^3 s^{-1}, and to an even greater extent in tension (typically less than 10^2 s^{-1}). This is due to the assumption that the specimen is subjected to a state of uniform stress. This is not the case, especially in early stages of a test where inertia effects create heterogeneous deformation [52, 65]. For example, Pankow *et al.* [65] used high speed imaging in an attempt to resolve full-field strain profiles on a specimen subjected to compression with a SHPB. Despite poor quality measurements and lack of temporal resolution, they found that the strain field was highly non-uniform. This was also found by Gilat *et al.* [52] and it was noted SHPB theory overestimates strain for waisted specimens due to heterogeneous deformation [48, 52]. Strain gauge measurements also become highly sensitive to gauge position and are generally unreliable for obtaining measurements of ultimate strain [71, 72].

Govender *et al.* [66] configured a Hopkinson bar into a spall test in an attempt to remove some of the restrictive assumptions of the SHPB and measure tensile strength. The spall test, commonly used for concrete [53], is used sparingly in the literature for through-thickness testing. The spall test approach was also used by Gerlach *et al.* [12] for high strain rate tensile testing of epoxy resins. The approach of Govender *et al.* [66] utilised phase shifting of the waves measured on the bar to infer the stress in the material at failure. High speed cameras were required to

record the approximate time and location of the failure. The major shortcoming of the spall test approach used by Govender *et al.* [66] is that the input stress is inferred from measurements on the incident bar. Tensile strength is also inferred based on measurements of the global response (reflected pulse measured in the input bar), which is affected by dispersion.

In the studies by Govender *et al.* [66], Pankow *et al.* [65] and Gilat *et al.* [52], the temporal resolution is insufficient to properly resolve the initial response of the material. In these cases, common high speed cameras were used, which can achieve frame rates on the order of a 1-5×10^5 fps. The advantage of these cameras is that they offer relatively long record times, at the expense of frame rates (see Fig. 2.14[83]). Moreover, as frame rate increases, the spatial resolution decreases due to memory read out limitations. Therefore, to achieve the necessary frame rates for quantitative imaging at high strain rates, UHS cameras are required. These cameras use different strategies to overcome memory read out issues. An example of this is the ISIS-CCD camera, in which the memory for each pixel is located on the sensor [130]. These cameras offer significant opportunity for dynamic material characterisation as they are simple to operate and trigger, can be used for stereo imaging, and offer framing rates up to 5 Mfps.

An issue with testing brittle materials (*i.e.*: through-thickness tension for a composite) is that they exhibit small strains to failure. This requires high spatial/temporal resolution and low noise. With the development of UHS cameras and full-field measurement techniques, such as DIC [95] or the grid method [96], some of the fundamental assumptions attached to current test methods may be alleviated. This offers great potential to improve current test methods or develop new techniques with kinematic fields that are not necessarily uniform, or are intentionally non-uniform, as also proposed in [52]. With the ability to resolve the temporal evolution in surface displacement, and hence acceleration, the specimen's acceleration field may be used as an embedded load cell (see Chapter 3). These full-field maps may be processed using an inverse identification technique, such as the VFM [27, 28, 125] to reconstruct stress and extract material properties without need for measurement of the external force. This removes the requirement for stress equilibrium and uniform uniaxial strain states attached to SHPB testing. In fact, the presence of a heterogeneous strain field during impact may be beneficial as multiple constitutive properties could be extracted from a single test using the VFM. This may be used to overcome some of the limitations of current test methods for shear characterisation as the combined stress state could be characterised and potentially used for robust and accurate stiffness and strength identification.

Very encouraging results have been obtained recently, demonstrating the potential of this approach for identifying the in-plane strength and stiffness of composite laminates at very high strain rates (> 2×10^3 s^{-1}) [26, 29]. Moulart *et al.* [26] used the SHPB to generate a pulse with full-field maps processed using the VFM to identify Young's modulus and Poisson's ratio for a quasi-isotropic laminate. Zhu [29], Pierron *et al.* [28], and Pierron and Forquin [27] have demonstrated that this approach can be extended to spall test configurations to extract the stiffness and strength of brittle materials. This approach opens up a wide design space for innovative test configurations to accurately determine the mechanical response of materials at strain rates not achievable with any current technique. In particular, it offers a very promising alternative for high-strain-rate testing in the interlaminar planes for polymer matrix fibre composites as it removes the need to grip the material, and issues with inertia are avoided by using the acceleration as a load cell.

2.8 Motivation

From Section 2.3 it is clear that the methods for measuring high-strain-rate material properties in the interlaminar planes of polymer-matrix composites are limited to strain rates on the order of 10^2 s^{-1}. For the most widely used technique, the SHPB, the inertial effects from loading at high strain rates violate a key assumption that the material is in a state of quasi-static equilibrium. Under these conditions, the strain gauges on the input and output bars cannot be used to reliably determine stress and strain in the sample and thus, the stiffness or failure stress. Inertial effects are thought to be the largest contributor to scatter in reported values of stiffness and failure stress.

In this work, a new IBII test method is proposed to address these limitations and in turn improve the accuracy of stiffness and failure stress measurements for the interlaminar material planes at high strain rates (on the order of 10^3 s^{-1}). This method was developed according the the objectives presented in Chapter 1. A general design framework, that can be applied to any IBII test, was presented and experimentally validated with two configurations for the measuring the interlaminar elastic and shear moduli, as described in Chapters 4-6. This work represents an important first step in developing the IBII test method so that it can be extended for more detailed interlaminar characterisation of composites at high strain rates.

Chapter 3

Theory

3.1 Overview

This chapter starts with a description of the material model assumed in this work (Section 3.2, followed by the general formulation of the principle of virtual work in Section 3.3. The following sections then outlines how the principle of virtual work can be used to identify constitutive mechanical properties by exploiting the inertial effects that occur during high strain rate loading. The relevant theory for the interlaminar IBII tension/compression test is first presented in Section 3.4. The IBII tension/compression theory is sub-divided to consider first the case where the test is assumed to be two-dimensional, followed by the extension to three dimensions to account for through-thickness effects using thin plate theory and back-to-back measurements. Section 3.5 then presents relevant theory for the interlaminar IBII shear test.

3.2 Material and constitutive model

The material used in this work is a unidirectional carbon/epoxy pre-preg laminate (MTM45-1/AS4-145). This composite system is modelled using a linear-elastic, transversely orthotropic material with the constitutive model in Eq. (3.1):

$$\begin{bmatrix} \sigma_{11} \\ \sigma_{22} \\ \sigma_{33} \\ \sigma_{12} \\ \sigma_{23} \\ \sigma_{13} \end{bmatrix} = \begin{bmatrix} Q_{11} & Q_{12} & Q_{13} & 0 & 0 & 0 \\ Q_{12} & Q_{22} & Q_{23} & 0 & 0 & 0 \\ Q_{13} & Q_{23} & Q_{33} & 0 & 0 & 0 \\ 0 & 0 & 0 & G_{12} & 0 & 0 \\ 0 & 0 & 0 & 0 & G_{23} & 0 \\ 0 & 0 & 0 & 0 & 0 & G_{13} \end{bmatrix} \cdot \begin{bmatrix} \epsilon_{11} \\ \epsilon_{22} \\ \epsilon_{33} \\ \gamma_{12} \\ \gamma_{23} \\ \gamma_{13} \end{bmatrix} \tag{3.1}$$

Note that the standard convention for material coordinates is adopted with '1' being the fibre direction, '2' the transverse direction and '3' being the through-thickness direction. In the IBII interlaminar tests, the '3' direction is aligned with the x axis, and the fibres are either oriented parallel to the y axis (1-3), or to the z axis (2-3 plane) as shown in Fig. 3.1. Both cases are considered in the following sections.

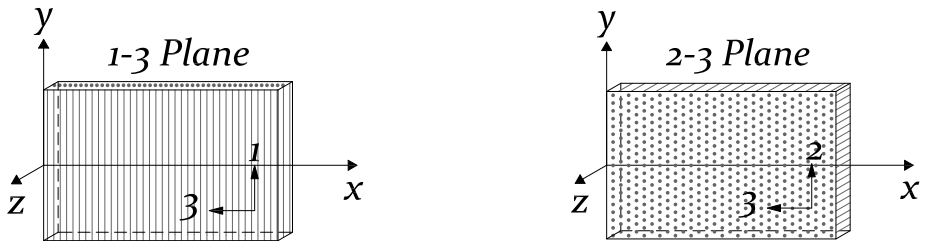

Figure 3.1: Typical material orientation for testing in the interlaminar planes. Fibres are either (a) parallel to the y axis (1-3 interlaminar plane) or (b) parallel to the z axis (2-3 interlaminar plane)

3.2.1 1-3 interlaminar plane

For the 1-3 interlaminar plane (Fig. 3.1a), Eq. (3.1) can be re-written as:

$$\begin{bmatrix} \sigma_{xx} \\ \sigma_{yy} \\ \sigma_{xy} \end{bmatrix} = \begin{bmatrix} Q_{33} & Q_{13} & 0 \\ Q_{13} & Q_{11} & 0 \\ 0 & 0 & G_{13} \end{bmatrix} \cdot \begin{bmatrix} \epsilon_{xx} \\ \epsilon_{yy} \\ \gamma_{xy} \end{bmatrix} \tag{3.2}$$

Further, it is assumed that shear strains generated in the tension/compression test are comparatively small (< 1%) and non-linear effects have been neglected. Even if shear is introduced by the loading (*i.e.:* misalignment of the projectile), the shear behaviour is decoupled from the in-plane behaviour. To obtain the interlaminar elastic modulus, E_{33} the stress component of most interest is σ_{xx}, which has the following stress-strain relationship:

$$\sigma_{xx} = Q_{33}\epsilon_{xx} + Q_{13}\epsilon_{yy} \tag{3.3}$$

where Q_{33} is the plane stress, interlaminar normal stiffness, and Q_{13} is the plane stress stiffness associated with Poisson's effect ($Q_{13} = \nu_{13}Q_{33}$). Substituting this into Eq. (3.9) results in:

$$\sigma_{xx} = Q_{33}\epsilon_{xx}(1 + \nu_{13}\epsilon_{yy}) \tag{3.4}$$

Since the loading is predominantly axial, it is reasonable to neglect σ_{yy} stresses and in this case, Eq. (3.4) is approximated by:

$$\sigma_{xx} = E_{33}\epsilon_{xx} \tag{3.5}$$

For the case of interlaminar shear, where the measurements are made in the material coordinates ($x - y$ aligned with $1 - 3$ plane), Eq. (3.2) shows that the shear component is de-coupled from the in-plane stiffness components and shear stress is obtained directly from measurements of shear strain (assuming linear-elasticity) as:

$$\sigma_{xy} = G_{13}\gamma_{xy} \tag{3.6}$$

In reality, following some initial linear-elastic behaviour, there will be some non-linearity in shear, but this is not considered here as attempts are made only to measure the shear modulus where Eq. (3.6) holds. Characterisation of the non-linear behaviour is a topic for future investigation as discussed in Chapter 7.

3.2.2 2-3 interlaminar plane

For the 2-3 interlaminar plane (Fig. 3.1b), Eq. (3.1) can be re-written as:

$$\begin{bmatrix} \sigma_{xx} \\ \sigma_{yy} \\ \sigma_{xy} \end{bmatrix} = \begin{bmatrix} Q_{33} & Q_{23} & 0 \\ Q_{23} & Q_{22} & 0 \\ 0 & 0 & G_{23} \end{bmatrix} \cdot \begin{bmatrix} \epsilon_{xx} \\ \epsilon_{yy} \\ \gamma_{xy} \end{bmatrix} \tag{3.7}$$

It is worth noting that in this plane the material is essentially orthotropic and thus, Q_{33} is approximately equal to Q_{22}. Here, the ϵ_{yy} strains cannot be neglected and the stress-strain relationship for σ_{xx} is expressed as:

$$\sigma_{xx} = Q_{33}\epsilon_{xx} + Q_{23}\epsilon_{yy} \tag{3.8}$$

3.3 Principle of Virtual Work

In this work, the VFM [125] is used to relate full-field displacement measurements, to material properties through the principle of virtual work. The following general assumptions are made in the interlaminar IBII tests: 1) constant density and thickness in space; and 2) plane stress loading, and 3) body forces are negligible. With single sided-measurements it is also assumed that the kinematic fields are uniform through-the-thickness; however, with back-to-back measurements this assumption is not necessary. Under these assumptions the three-dimensional form of the principle of virtual work is expressed as:

$$-\int_V \boldsymbol{\sigma} : \boldsymbol{\epsilon}^\star dS + \int_{\delta S} \boldsymbol{T} \cdot \boldsymbol{u}^\star dS = \rho \int_V \boldsymbol{a} \cdot \boldsymbol{u}^\star dS \tag{3.9}$$

where V denotes the volume of the region of interest, $\boldsymbol{T}$ is the Cauchy stress vector, which is applied to the boundaries denoted by δS, ρ is the material density, $\boldsymbol{a}$ is the acceleration field, $\boldsymbol{\sigma}$ is the Cauchy stress tensor, $\boldsymbol{u}^\star$ is the virtual displacement field, and $\boldsymbol{\epsilon}^\star$ is the virtual strain field deriving from the virtual displacement field through $\epsilon^*_{ij} = 1/2(\partial u^*_i/\partial j + \partial u^*_j/\partial i)$. Note that : and $\cdot$ denote the dot product in matrix and vector forms, respectively. It should also be noted that all mechanical fields are a function of time and space but this is omitted for clarity. For simplicity, the time and space function notation is omitted. The first term and second terms on the left hand side of Eq. (3.9) represent the internal and external virtual work, respectively. The term on the right hand side of the equation represents the virtual work due to inertial forces.

The following sections present a number of different ways in which virtual fields can be used to evaluate Eq. (3.9) for stiffness identification and failure stress estimation. The relevant theory is divided into cases where it is assumed that the test is 2D (*i.e.*: measurements made on the surface are representative of the through-thickness behaviour), followed by the case where through-thickness effects are considered. Two approaches for 2D stiffness and failure stress estimation are presented: 1) from stress-strain curves reconstructed from full-field maps of acceleration, and 2) direct identification of stiffness parameters from full-field maps of acceleration and strain.

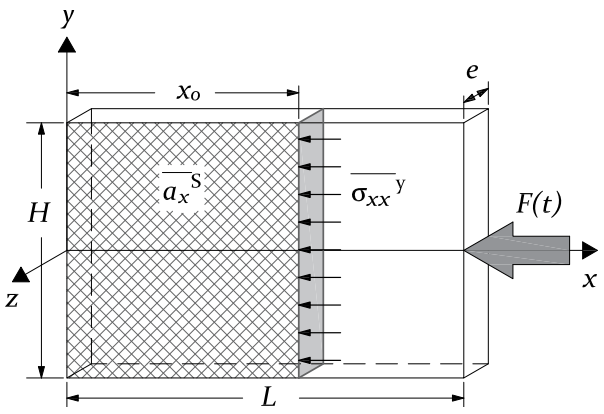

Figure 3.2: Schematic of the interlaminar tension IBII specimen subjected to an arbitrary, time-varying end load, $F(t)$

3.4 Interlaminar IBII tension/compression test

3.4.1 Stress reconstruction for stiffness identification and estimating failure stress

Average axial (membrane) stress fields

Consider the schematic of a typical interlaminar IBII specimen, having length L, height H, and a constant thickness e, subjected to a time-varying end load $F(t)$ (shown in Fig. 3.2). When the external virtual work is sufficiently activated by inertia, virtual fields can be strategically selected to remove internal virtual work. This is achieved by having zero virtual strains, and using the external virtual work of the inertia as a load cell.

When the test is assumed to be 2D (*i.e.*: measurements made on the surface are representative of the through-thickness behaviour) the thickness can be factored out of the integrals in Eq. (3.9) and the principle of virtual work becomes:

$$-\int_S \boldsymbol{\sigma} : \boldsymbol{\epsilon}^* dS + \int_{\delta l} \boldsymbol{T} \cdot \boldsymbol{u}^* dl = \rho \int_S \boldsymbol{a} \cdot \boldsymbol{u}^* dS \tag{3.10}$$

where S denotes the surface of the region of interest, and $\boldsymbol{T}$ is applied to the line boundaries denoted by δl. Consider the simplest case of a rigid-body virtual field in the coordinate system shown in Fig. 3.2:

$$\begin{cases} u_x^* = 1 \\ u_y^* = 0 \end{cases} \qquad \begin{cases} \epsilon_{xx}^* = 0 \\ \epsilon_{yy}^* = 0 \\ \epsilon_{xy}^* = 0 \end{cases} \tag{3.11}$$

Substituting this into Eq. 3.10 provides a direct relationship between the external virtual work and tractions along any axial section within the specimen:

$$\int_{\delta l} \boldsymbol{T} \cdot \boldsymbol{u}^* dl = \rho \int_S \boldsymbol{a} \cdot \boldsymbol{u}^* dS \tag{3.12}$$

The traction vector is related to stress by $\boldsymbol{T} = \boldsymbol{\sigma} \cdot \boldsymbol{n}$. Therefore, $\boldsymbol{T} \cdot \boldsymbol{u}^*$ in Eq. (3.12) is written

as:

$$\boldsymbol{T} \cdot \boldsymbol{u}^* = \begin{pmatrix} \sigma_{xx} \\ 0 \\ 0 \end{pmatrix} \tag{3.13}$$

Substituting Eq. (3.13) and Eq. (3.11) into Eq. (3.12) provides a direct relationship between the axial stress along a vertical slice in the sample at position x_o:

$$\int_{-H/2}^{H/2} \sigma_{xx} dy = \rho \int_0^{x_0} \int_{-H/2}^{H/2} a_x u_x^* dy dx \tag{3.14}$$

If full-field displacements are measured with sufficient spatial resolution, the integral quantities can be estimated using discrete sums. For example, the right hand side of Eq. (3.14) is approximated as,

$$\rho \int_0^{x_0} \int_{-H/2}^{H/2} a_x dS \approx \rho x_o H \overline{a_x}^S \tag{3.15}$$

where the superscript S coupled with an overline denotes the surface average between the free edge and x_o (Fig. 3.2). The line integral on the left hand side of Eq. (3.14) represents the average stress along the cross-section (denoted by overline with a superscript y), and Eq. (3.14) becomes:

$$\overline{\sigma_{xx}}^y = \rho x_o \overline{a_x}^S \tag{3.16}$$

which is referred to here as the 'stress-gauge' equation. The advantage of this approach is that stress averages can be reconstructed at any location along the length of the specimen. When combined with measured average strains, stress-strain curves can be constructed to identify stiffness so long as the material remains linear-elastic. For 1-3 plane specimens, using a linear regression fit to the compression loading response of $\overline{\sigma_{xx}}^y$ plotted against $\overline{\epsilon_{xx}}^y$ provides a spatial identification of E_{33} (see Eq. (3.5)). For the 2-3 material plane, the slope of $\overline{\sigma_{xx}}^y$ plotted against $\overline{\epsilon_{xx} + \nu_{23}\epsilon_{yy}}^y$ yields Q_{33}. To compute axial strain, the identified value of ν_{23} from the special optimised virtual fields routine is used (presented in Sec. 3.4.2). Very recently, an extension to the stress-strain curve approach for stiffness identification has been proposed in [131] that does not require one to neglect Poisson's effects. It has not been implemented here as most of the work has concentrated on the 1-3 interlaminar plane where this assumption is reasonable.

Note that spatial smoothing effects influence the measurements within one kernel at the impact and free edges (as shown in Chapter 4). Therefore, the stiffness value for the test is generally taken as the average spatial identification over the middle 50% of the sample. Equation (3.16) can also be used for failure stress estimation if σ_{xx} does not depend on y.

Linear approximation for axial stress field

The stress-gauge equation will only provide a good approximation of the failure stress in cases where the stress distribution is relatively uniform through the width. Misalignments at impact can create a linear distribution of stress through the width as well as wave dispersion following reflection off the free edge. In these cases, it is possible to consider additional rigid body virtual fields to resolve a linear distribution of axial stress along the height, which has the form:

$$\sigma_{xx} = \sigma_{xx}^0 + \frac{y}{H} \sigma_{xx}^1 \tag{3.17}$$

The same rigid-body virtual field describing a translation in the x direction (Eq. (3.11)) is used

to derive the constant coefficient in the linear stress-gauge formulation (Eq. (3.17)):

$$\sigma^0_{xx} = \rho x_o \overline{a_x}^S \tag{3.18}$$

Consider a second virtual field, describing a rigid-body rotation about the origin:

$$\begin{cases} u^*_x = y \\ u^*_y = -x \end{cases} \qquad \begin{cases} \epsilon^*_{xx} = 0 \\ \epsilon^*_{yy} = 0 \\ \epsilon^*_{xy} = 0 \end{cases} \tag{3.19}$$

Substituting into Eq. (3.10) results in:

$$\int_{-H/2}^{H/2} (\sigma^0_{xx} + \frac{y}{H}\sigma^1_{xx}) y dy - \int_{-H/2}^{H/2} (\sigma^0_{xy}) x dy = \rho \int_0^{x_0} \int_{-H/2}^{H/2} (a_x y - a_y x) dy dx \tag{3.20}$$

Simplifying Eq. (3.20) by approximating integrals with discrete sums results in:

$$\sigma^1_{xx} \frac{H}{12} - \overline{\sigma^0_{xy}}^y x_o = \rho x_o (\overline{a_x y}^S - \overline{a_y x}^S) \tag{3.21}$$

A third rigid-body virtual field, describing a virtual translation in the y direction is used to relate $\overline{\sigma^0_{xy}}^y$, in Eq. (3.21) to surface accelerations.

$$\begin{cases} u^*_x = 0 \\ u^*_y = 1 \end{cases} \qquad \begin{cases} \epsilon^*_{xx} = 0 \\ \epsilon^*_{yy} = 0 \\ \epsilon^*_{xy} = 0 \end{cases} \tag{3.22}$$

Substituting into Eq. (3.10) and simplifying the integrals, as was done previously, one obtains:

$$\overline{\sigma^0_{xy}}^y = \rho x_o \overline{a_y}^S \tag{3.23}$$

This provides an estimate for the average shear stress at any axial position. Substituting Eq. (3.23) into Eq. (3.21) and rearranging results in:

$$\sigma^1_{xx} = \frac{12\rho x_o}{H} (\overline{a_x y}^S - \overline{a_y x}^S + x_o \overline{a_y}^S) \tag{3.24}$$

By combining Eq. (3.18) and Eq. (3.24), one obtains the final expression for the linear distribution of axial stress at any axial location. This is referred to as the 'linear stress-gauge' equation.

$$\sigma_{xx}(LSG) = \rho x_o \overline{a_x}^S + \frac{12\rho x_o y}{H^2} (\overline{a_x y}^S - \overline{a_y x}^S + x_o \overline{a_y}^S) \tag{3.25}$$

It is important to highlight that the stress-gauge equations are valid regardless of the constitutive behaviour. It can also be combined with local strains to approximate the stress-strain response at any position on the sample. Note that the linear stress-gauge approach provides a linear approximation of axial stress along y, and does not fully resolve σ_{xx} across the width of the specimen. Also note that when stress does not depend on y, the linear stress-gauge equation reduces to Eq. (3.16). In this work, the linear stress-gauge equation is used for estimating interlaminar tensile failure stress using the maximum reconstructed stress at the crack initiation location.

Strain-based stress fields

An additional, *post-hoc* way to reconstruct stress is to use the identified stiffness parameters to convert strain maps to stress maps using the constitutive model presented in Sec. 3.2. Comparing the strain-based and acceleration-based reconstructions is useful for identifying cases when the constitutive model or measurement assumptions break down (*i.e.:* at the onset of plasticity, damage, failure, *etc.*). This can also be used to validate the constant and linear approximations for the stress field as reconstructed with the stress-gauge equations. In this work, stress calculated from strain is not used to directly estimate the interlaminar tensile failure stress due to uncertainties as to when strains become non-physical during crack formation.

3.4.2 Direct stiffness identification from full-field measurements

The principle of virtual work is satisfied by any virtual displacement fields that are continuous and piecewise differentiable. In the case of the 1-3 interlaminar plane, the orthotropic constitutive model from Sec. 3.2 reduces Eq. (3.10) to:

$$-E_{33}\int_S \epsilon^*_{xx}\epsilon_{xx}dS + \int_{\delta l} \boldsymbol{T}\cdot\boldsymbol{u}^* dl = \rho\int_S \boldsymbol{a}\cdot\boldsymbol{u}^* dS \tag{3.26}$$

The larger value of Poisson's ratio in the 2-3 material plane ($\nu_{23} \approx 0.25$) suggests to use the full isotropic version of the VFM, without the need to assume predominantly axial stresses and Eq. (3.10) becomes:

$$\begin{aligned} -Q_{33}\int_S(\epsilon_{xx}\epsilon^*_{xx} + \epsilon_{yy}\epsilon^*_{yy} + \frac{1}{2}\gamma_{xy}\epsilon^*_{xy})dS - \ldots \\ \ldots - Q_{23}\int_S(\epsilon_{xx}\epsilon^*_{yy} + \epsilon_{yy}\epsilon^*_{xx} - \frac{1}{2}\gamma_{xy}\epsilon^*_{xy})dS + \ldots \\ \ldots \int_{\delta l}\boldsymbol{T}\cdot\boldsymbol{u}^* dl = \rho\int_S \boldsymbol{a}\cdot\boldsymbol{u}^* dS \end{aligned} \tag{3.27}$$

The identification of E_{33} requires one virtual field, whereas the isotropic formulation requires two virtual fields to identify Q_{33} and Q_{23}. There are an infinite number of admissible virtual fields that can be selected to evaluate Eq. (3.26) and Eq. (3.27). When fields are corrupted by noise the identification of constitutive parameters becomes dependent on the selected virtual fields. If chosen intuitively, it is not possible to verify that the chosen virtual fields result in the most stable identification [125, 127]. In this work, special optimised virtual fields are adopted, as developed in reference [127]. This procedure automates the selection of virtual fields for direct identification of the stiffness parameters such that the sensitivity to strain noise is minimised.

Special optimised virtual fields

In this procedure, a system of equations is developed from the principle of virtual work using 'speciality conditions'. The speciality conditions uniquely constrain the virtual displacement fields such that each field results in the direct identification of a constitutive parameter [127]. The resulting virtual fields can be thought of as 'optimal' spatial filters for the strain maps with higher weighting given to regions on the sample where the material response is more strongly activated (high signal-to-noise ratio) and lower weighting to regions that are not.

The IBII tension/compression test is designed such that the mechanical response of the material

is heavily dependent on the modulus E_{33}. For the 1-3 material plane, a reduced formulation is adopted, which constrains the fields to uni-axial virtual displacement (*i.e.*: $u_y^* = 0$), which results in the direct identification of E_{33} from Eq. (3.26). Since the material response is activated by a propagating stress wave the 'optimal' virtual fields will be unique for each time step. The development of these virtual fields was first implemented by the author as a contribution to the paper in [32] for the direct identification of the transverse in-plane elastic modulus using an IBII test. For the 2-3 plane, lateral strains become more significant and the more general special optimised virtual field formulation, which includes u_x^* and u_y^* degrees of freedom is used to directly identify Q_{33} and Q_{23}. An overview of the procedure is provided here, but the reader is referred to [127] and [125] for full details.

Reduced special optimised virtual fields: For the 1-3 interlaminar plane the virtual mesh is formulated with only u_x degrees of freedom (virtual uni-axial deformation). If the number of nodes along the x and y axes are denoted by 'n' and 'm', respectively, then this gives a total of mn conditions.

$$u_x^*(x = x^i, y^{i+1}) = u_x^*(x = x^i, y^i) \tag{3.28}$$

To eliminate the external virtual work from the unknown impact forces (second term on the left-hand side of Eq. (3.26)), a null virtual displacement boundary condition at the impact edge is defined as: $u_x^* = 0$ for $x = L$. This results in an additional $n + 1$ conditions. The resulting virtual fields have the general form shown in Fig. 3.3.

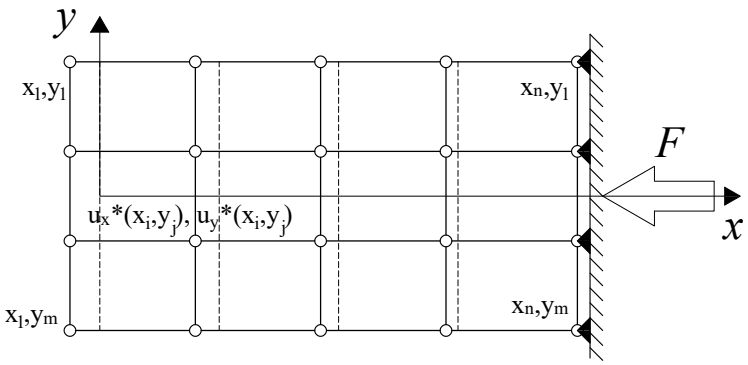

Figure 3.3: Uniaxial special optimised virtual fields for the identification of E_{33}. Un-deformed virtual mesh shown in dashed lines

The speciality condition is given by $\int_S \epsilon_{xx}\epsilon_{xx}^* dS = 1$, imposing another constraint on the virtual fields. Since this depends indirectly on the actual strain fields the resulting virtual fields will tend to follow regions of high strain in the measured fields. This maximises the virtual work contribution associated with the parameter to be identified and minimises the others. Note that an identification is performed on each image, and therefore, the optimal virtual fields will vary with each time step. With this condition, Eq. (3.26) becomes:

$$E_{33}^{app} = -\int_S \rho a_x u_x^* dS \tag{3.29}$$

E_{33}^{app} is used to account for the fact that the measured fields are contaminated by noise. For exact data $E_{33} = E_{33}^{app}$. If noise is present with a Gaussian distribution Π_x of amplitude γ,

then Eq. (3.26) becomes:

$$E_{33} = \gamma\Big[E_{33}\int_S \Pi_x \epsilon^*_{xx} dS\Big] - \int_S \rho a_x u^*_x dS \tag{3.30}$$

The inclusion of noise into the virtual work creates a recursive set of equations since the virtual work contribution depends on the actual constitutive parameters. It is assumed here that the noise amplitude is much smaller than the magnitude of the measured strains, allowing one to substitute the actual stiffness parameters by their approximate counterparts. This is to keep the process analytical. Therefore, Eq. (3.30) can be rewritten as follows:

$$E_{33} \simeq \gamma E^{app}_{33}\int_S \Pi_x \epsilon^{*(1)}_{xx} dS + E^{app}_{33} \tag{3.31}$$

The noise minimisation is based on the variance of the constitutive parameters under the influence of random strain noise as detailed in the work by Avril *et. al* [127]. Again, it is assumed that integral quantities can be approximated by discrete sums. The variance (V) associated with E_{33} is therefore approximated as:

$$V(E_{33}) \simeq \gamma^2\left(\frac{S}{N}\right)^2\left[(E^{app}_{33})^2\sum_{i=1}^{N}\left(\epsilon^*_{xx}(M_i)\right)^2\right] = \left(\frac{S}{N}\right)^2 E^{app}_{33}\boldsymbol{G}E^{app}_{33} \tag{3.32}$$

where S denotes the area of the field of view in consideration (given by $L \times H$), M_i the ith measurement point, and N the total number of measurement points. Since only one parameter is identified, the matrix $\boldsymbol{G}$ in Eq. (3.32) [127] is a simple scalar here:

$$\boldsymbol{G} = \sum_{i=1}^{N}\left(\epsilon^{*(i)}_{xx}(M_i)\right)^2 \tag{3.33}$$

Solving the minimisation problem using the Lagrangian multipliers method [127] produces a single set of optimal virtual field coefficients, which are used to obtain E_{33}.

$$E_{33} = -\rho\frac{S}{N}\left[\sum_{i=1}^{N} a^i_x \cdot \boldsymbol{Y}^*\right] \tag{3.34}$$

In Eq. (3.36) the vector denoted $\boldsymbol{Y^*} = \left[\tilde{u}^{*(i)}_1 \dots \tilde{u}^{*(N)}_1\right]$ contains the unknown virtual degrees of freedom $\tilde{u}^{*(i)}_x$, which are expanded to the measurement locations using linear shape functions.

Isotropic special optimised virtual fields: For 2-3 plane specimens, which are modelled using a 2D isotropic linear elastic model, the principle of virtual work can be written as in Eq. (3.27). In this case, two virtual fields ($u^{*(1)}_x$, $u^{*(1)}_y$), ($u^{*(2)}_x$, $u^{*(2)}_y$) are required to identify the two stiffness parameters. For the isotropic case the nodes of the virtual mesh have both u_x and u_y degrees of freedom. Again, the virtual work due to the unknown force distribution at the impact edge is removed by setting all $u^*_x = 0$ and $u^*_y = 0$ at $x = L$. The speciality condition for Q_{33} is written as:

$$\begin{cases}\int_S(\epsilon_{xx}\epsilon^{*(1)}_{xx} + \epsilon_{yy}\epsilon^{*(1)}_{yy} + \frac{1}{2}\gamma_{xy}\epsilon^{*(1)}_{xy})dS = 1\\ \int_S(\epsilon_{xx}\epsilon^{*(1)}_{yy} + \epsilon_{yy}\epsilon^{*(1)}_{xx} - \frac{1}{2}\gamma_{xy}\epsilon^{*(1)}_{xy})dS = 0.\end{cases} \tag{3.35}$$

Similar equations can be readily derived for the direct identification of Q_{23} as shown in [28]. Using the same noise minimisation procedure described above and in [127], two sets of optimised

virtual fields coefficients are identified, which are used to obtain Q_{33} and Q_{23}. Full details of this derivation are provided in [125].

$$Q_{33} = -\rho \frac{S}{N} \left[\sum_{i=1}^{N} \left(a_x^i \tilde{u}_x^{*(i,1)} + a_y^i \tilde{u}_y^{*(i,1)} \right) \right] \tag{3.36}$$

$$Q_{23} = -\rho \frac{S}{N} \left[\sum_{i=1}^{N} \left(a_x^i \tilde{u}_x^{*(i,2)} + a_y^i \tilde{u}_y^{*(i,2)} \right) \right] \tag{3.37}$$

For the case of 2-3 plane specimens, ν_{23} can be calculated from Q_{33} and Q_{23}. This is used to determine axial strain to identify Q_{33} from stress-strain curves as described in Sec. 3.4.1.

3.4.3 Through-thickness effects (bending & membrane stress)

The theory presented in the previous sections are valid only if the stresses and strains are uniform through-the-thickness. If this is not the case, it is possible to combine the VFM with thin-plate theory to reconstruct a linear approximation of stress through-the-thickness under the assumption of plane stress loading. Here we denote the z axis as the mid-plane of the sample. The displacement (u_x,u_y), acceleration (a_x,a_y), strain (ϵ_{xx}, ϵ_{yy}, ϵ_{xy}) and stress fields (σ_{xx}, σ_{yy}, σ_{xy}) are written as a function of their membrane, $\boldsymbol{x}^o$ and flexural $\boldsymbol{x}^f$ components in the following general form:

$$\boldsymbol{x}(x, y, t) = \boldsymbol{x}^o + \frac{2x}{e} \boldsymbol{x}^f \tag{3.38}$$

and the out-of-plane component for u_z, and a_z are written as:

$$\begin{cases} u_z = u_z^o \\ a_z = a_z^o \end{cases} \tag{3.39}$$

The membrane and flexural components of displacement (u_x, u_y) can be derived from front and back face measurements according to:

$$\begin{cases} \boldsymbol{u}^o = \frac{1}{2}(\boldsymbol{u}^F + \boldsymbol{u}^B) \\ \boldsymbol{u}^f = \boldsymbol{u}^F - \boldsymbol{u}^o \end{cases} \tag{3.40}$$

where superscripts 'F' and 'B' denote the front face ($z = +e/2$) and back face ($z = -e/2$). These quantities are spatially differentiated to obtain in-plane strain components ($\boldsymbol{\epsilon}$: $\epsilon_{xx}, \epsilon_{yy}, \epsilon_{xy}$):

$$\boldsymbol{\epsilon} = \boldsymbol{\epsilon}^o + \frac{2z}{e} \boldsymbol{\epsilon}^f \tag{3.41}$$

and twice differentiated temporally to obtain in-plane acceleration components ($\boldsymbol{a}$: a_x, a_y):

$$\boldsymbol{a} = \boldsymbol{a}^o + \frac{2z}{e} \boldsymbol{a}^f \tag{3.42}$$

As a first step, this formulation for the field quantities will be used to recover Eq. (3.16) from the full 3D version of the principle of virtual work. Substituting the same rigid-body virtual field ($u_x^* = 1$, $u_y^* = u_z^* = 0$) in Eq. (3.9) results in:

$$\int_{-H/2}^{H/2} \int_{-e/2}^{e/2} \sigma_{xx} dz dy = \rho \int_0^{x_0} \int_{-H/2}^{H/2} \int_{-e/2}^{e/2} a_x dz dy dx \tag{3.43}$$

Replacing a_x and σ_{xx} by the linear combination of the membrane and flexural components results in:

$$\int_{-H/2}^{H/2}\int_{-e/2}^{e/2}\left(\sigma_{xx}^{o}+\frac{2z}{e}\sigma_{xx}^{f}\right)dzdy=\rho\int_{0}^{x_0}\int_{-H/2}^{H/2}\int_{-e/2}^{e/2}\left(a_x^{o}+\frac{2z}{e}a_x^{f}\right)dzdydx \tag{3.44}$$

This expression simplifies to Eq. (3.45), which represents an equivalent form of the stress-gauge equation for width-averaged membrane stress as a function of membrane acceleration:

$$\overline{\sigma_{xx}^{o}}^{y}=\rho x_0\overline{a_x^{o}}^{S} \tag{3.45}$$

Therefore, if a_x^F and a_x^B are measured, then $a_x^o = 1/2(a_x^F + a_x^B)$ and $\overline{\sigma_{xx}^o}^y$ can be calculated without bias. Moreover, this can then be plotted against the membrane component of strain ($\epsilon_{xx}^o = 1/2(\epsilon_{xx}^F + \epsilon_{xx}^B)$) to obtain the stress-strain response, from which stiffness can be identified without bias. However, even if σ_{xx} does not depend on y, it may depend on z and therefore, $\overline{\sigma_{xx}^o}^y$ will not be a good approximation for failure stress. Therefore, the question becomes: "is it possible to identify σ_{xx}^f from back-to-back acceleration measurements?" To do this, a rigid-body rotation virtual field about the y axis is introduced ($u_x^* = z$, $u_y^* = u_z^* = -x$). In this case:

$$\boldsymbol{T}\cdot\boldsymbol{u}^{*}=\begin{pmatrix}z\sigma_{xx}\\0\\-x\sigma_{xz}\end{pmatrix} \tag{3.46}$$

Substituting Eq. (3.46) into Eq. (3.9), assuming σ_{xz} can be neglected results in:

$$\int_{-H/2}^{H/2}\int_{-e/2}^{e/2}\left(\sigma_{xx}^{o}z+\frac{2z^2}{e}\sigma_{xx}^{f}\right)dzdy=\rho\int_{0}^{x_0}\int_{-H/2}^{H/2}\int_{-e/2}^{e/2}\left(a_x^{o}z+\frac{2z^2}{e}a_x^{f}-a_z^{o}x\right)dzdydx \tag{3.47}$$

This simplifies to give the width-averaged flexural stress component as a function of acceleration (Eq. (3.48)).

$$\overline{\sigma_{xx}^{f}}^{y}=\rho x_0\left(\overline{a_x^{f}}^{S}-\frac{6}{e}\overline{a_z^{o}x}^{S}\right) \tag{3.48}$$

Clearly, the flexural component of stress (Eq. (3.48)) is dependent on out-of-plane acceleration, a_z^o, which cannot be resolved from in-plane measurements. Therefore, in the presence of out-of-plane bending, the true stress will be underestimated by stress reconstructed from surface measurements of acceleration. In this work, full-field measurements made with synchronised ultra-high-speed cameras will be used to quantify the bias caused by out-of-plane loading on the reconstruction of stress-strain curves, and the identification of stiffness and failure stress for the IBII test. This is the focus of Chapter 5.

3.5 Interlaminar IBII shear test

3.5.1 Shear moduli identification

For the case of interlaminar shear, where the measurements are made in the material coordinates ($x - y$ aligned with 1 – 3, or with the 2 – 3 material coordinates), the shear component is decoupled from the in-plane stiffness components, as in Eq. (3.2) giving $\sigma_{xy} = G_{13}\gamma_{xy}$. The theory presented here is used for characterising the 1-3 interlaminar shear behaviour, but applies in

the same way to the 2-3 interlaminar plane. For the 1-3 plane, the 2D form of the principle of virtual work reduces (Eq. 3.10) to:

$$-G_{13}\int_S \epsilon^*_{xy}\gamma_{xy}dS + \int_{\delta l}\boldsymbol{T}\cdot\boldsymbol{u^*}dl = \rho\int_S \boldsymbol{a}\cdot\boldsymbol{u^*}dS \tag{3.49}$$

Shear stress reconstruction for stiffness identification

Similar to the case of the interlaminar tension/compression sample, measured surface accelerations can be used to reconstruct average shear stress, and shear stress-strain curves. Consider an interlaminar specimen subjected to shear loading along one edge, with the free body diagram shown in Fig. 3.4. A simple rigid-body virtual field ($u^*_x = 1$, $u^*_y = 0$) can be used to derive a shear stress-gauge (SG) equation as was done for the average axial stress (Eq. (3.16)). This provides a direct relationship between acceleration and average shear stress along any horizontal cross-section positioned at y_0:

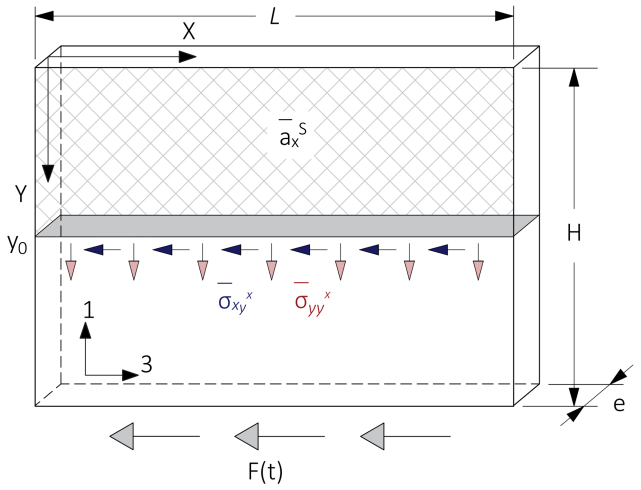

Figure 3.4: Schematic of impacted interlaminar shear sample

$$\overline{\sigma_{xy}}^x = \rho y_o \overline{a_x}^S \tag{3.50}$$

where superscript 'S' denotes the surface between the top free edge and the cross-section of interest, and superscript 'x' denotes the line average along the horizontal cross-section at y_0. The shear stress-gauge equation is used to reconstruct $\overline{\sigma_{xy}}^x$ at every cross-section for every frame, which is combined with average shear strain ($\overline{\gamma_{xy}}^x$) to generate shear stress-strain curves. Fitting the stress-strain curves with a linear regression model provides a measure of the shear modulus. Compiling all stiffness identifications at each cross-section provides a spatial distribution of the shear modulus along the height of the sample.

Manually selected virtual fields

Additional virtual fields can also be considered for interlaminar shear modulus identification, such as:

$$\begin{cases} u^*_x = y - H \\ u^*_y = 0 \end{cases} \qquad \begin{cases} \epsilon^*_{xx} = 0 \\ \epsilon^*_{yy} = 0 \\ \epsilon^*_{xy} = 1 \end{cases} \tag{3.51}$$

This field was selected so that $u_x^* = u_y^* = 0$ at $y = H$ to remove the contribution of virtual work from the unknown impact load at the bottom of the overhanging region. Substituting this into Eq. (3.49) results in:

$$-\int_0^H \int_0^L G_{13} \cdot \gamma_{xy} dx dy = \rho \int_0^H \int_0^L a_x (y - H) dx dy \tag{3.52}$$

Approximating integrals with discrete sums provides a direct relationship between the interlaminar modulus and acceleration, as in Eq. (3.53), defined only when the denominator is different from zero:

$$G_{13} = -\frac{\overline{\rho a_x (y - H)}^{S_o}}{\overline{\gamma_{xy}}^{S_o}} \tag{3.53}$$

Here, the overline superscripted with 'S_o' denotes averaging over the whole field of view. Therefore, the interlaminar shear modulus, G_{13}, can be determined from Eq. (3.53) at every frame of the dynamic test. Since these virtual fields were selected manually based on intuition, Eq. (3.53) is henceforth referred to as the 'manual VFM' approach.

Special optimised virtual fields

Similar to that presented for the IBII tension/compression test, the selection of virtual fields can also be automated such that the identification of the shear modulus has minimal sensitivity to measurement noise. The virtual fields are expanded using a piecewise virtual mesh that is formulated with only u_x^* degrees of freedom. The u_x^* degree of freedom is constant along x but allowed to vary along y (*i.e.:* only virtual shear permitted) as:

$$\begin{cases} u_x^*(x^i, y^j) = u_x^*(x^{i+1}, y^j) \\ u_x^*(x^i, y^j) \neq u_x^*(x^i, y^{j+1}) \end{cases} \tag{3.54}$$

where i and j denote the column and row number of the virtual mesh. In addition, the virtual displacements are set to null at the bottom of the region of interest ($y = H$) to remove the virtual work contribution of the unknown loading as was done with the manual VFM approach. The general form of the resulting virtual displacement fields is shown schematically in Fig. 3.5.

Starting from Eq. (3.52) the noise minimisation procedure was carried out in the same way as presented in Section 3.4.2 assuming that the noise amplitude is much smaller than the magnitude of the measured strains, and integral quantities can be approximated by discrete sums. This generates a single set of optimal virtual field coefficients ($\boldsymbol{Y}^* = \left[\tilde{u}_1^{(i)*} \dots \tilde{u}_1^{(N)*}\right]$) at each time step, which are used to find G_{13} using the following expression:

$$G_{13} = -\rho \frac{S}{N} \left[\sum_{i=1}^{N} a_x^i \boldsymbol{Y}^* \right] \tag{3.55}$$

where S denotes the surface area of the region of interest (given by $L \times H$) and N denotes the number of measurement points. Using Eq. (3.55) it is possible to identify the shear modulus directly from full-field maps of a_x acceleration at each time step. Since this virtual field provides the optimal identification, at least optimal in the sense of minimal sensitivity to measurement noise under the scheme of assumptions, Eq. (3.55) is henceforth referred to as the 'optimised VFM approach'.

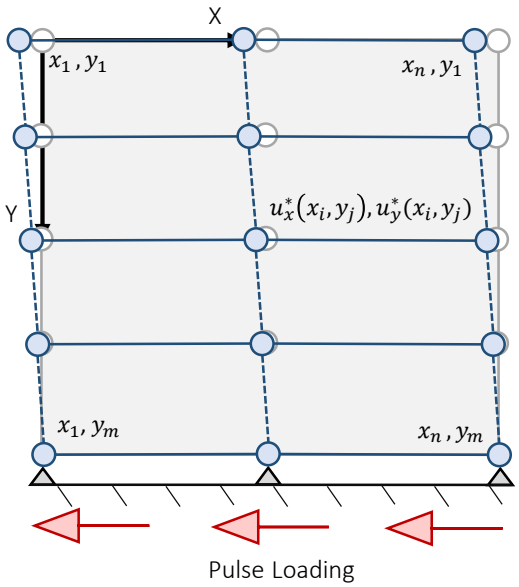

Figure 3.5: Virtual mesh for interlaminar shear modulus identification. Un-deformed virtual mesh shown in grey

The next chapter presents the design and experimental validation of the interlaminar IBII tension/compression test. The theory presented in Section 3.4 is implemented to identify the interlaminar elastic modulus and tensile failure stress.

Chapter 4

IBII Test for Interlaminar Elastic Modulus and Tensile Failure Stress

4.1 Overview

This chapter describes the design and experimental validation for a new interlaminar IBII test for measuring the elastic modulus and failure stress under tension/compression loading. The principle and generic configuration of the test is first described in Section 4.2. Following this, Section 4.3 describes the implementation of the numerical simulations and parametric design sweeps to select the test parameters (*e.g.*: projectile length and impact velocity). The materials and experimental setup are presented in Section 4.4. The image deformation framework used to rigorously quantify experimental errors introduced by the imaging system and post-processing is the focus of Section 4.5. The image deformation simulations are also used to select smoothing parameters which minimise the error for stiffness identification routines. Experimental results are presented and discussed in Section 4.6. Finally, a summary of key outcomes from the first phase of this project is provided in Section 4.7. Note that All data supporting this chapter are openly available from the University of Southampton repository at: https://doi.org/10.5258/SOTON/D0561.

4.2 Test Principle

In an IBII test the specimen is loaded with a dynamic pulse generated from an impact with a projectile. The general arrangement for an interlaminar IBII tension/compression test is shown in Fig. 4.1. The impact induces a compressive wave, which travels through the specimen towards the free edge. When the wave reaches the free edge, it reflects back towards the impact edge as a tensile pulse. The idea is to tailor the experimental parameters to ensure that the reflected tensile pulse is sufficient to cause specimen failure. Ultra-high-speed imaging is combined with the grid method to capture dynamic full-field displacements. The underlying constitutive properties are encoded in these maps, and are extracted using the VFM. The initial compressive loading is used to identify the elastic modulus, and the 'linear stress-gauge' equation [37] is used to estimate the tensile strength of the specimen.

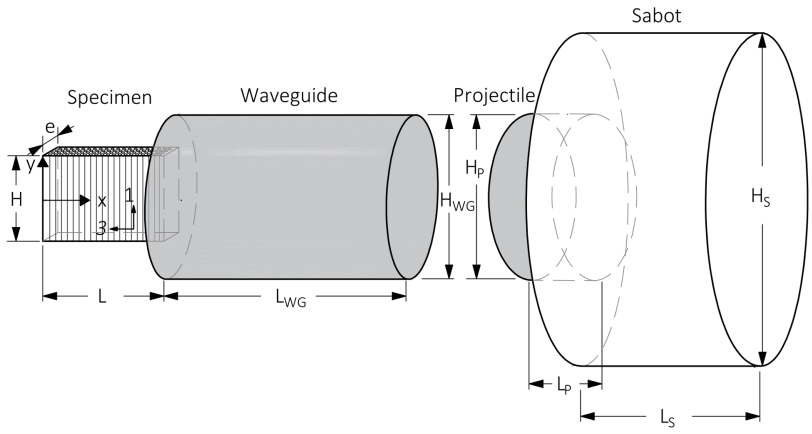

Figure 4.1: Schematic of the interlaminar IBII tension/compression test

The challenge here is to relate full-field displacement measurements, to material properties. This can be achieved with the virtual fields method. The specific application of the VFM to the interlaminar IBII tension/compression test was outlined in Section 3.3 and is thus omitted here for conciseness.

4.3 Numerical Design and Optimisation

4.3.1 Model configuration and parametric design sweep

In the generic IBII tension/compression test configuration shown in Fig. 4.1 fibres are either parallel to the y-axis (1-3 plane) (as shown in Fig. 4.1), or parallel to the z-axis (2-3 plane)(recall Fig. 3.1b), respectively. It is desirable to tailor the experimental parameters such that the reflected tensile stress is sufficiently high to cause failure. It is also desirable to maximise the ratio of reflected tensile stress to input compressive stress. This reduces the risk of damage during compressive loading. Numerical simulations are used to establish a design envelope such that both requirements are satisfied.

There are some important differences between the test design for interlaminar and in-plane properties. For direct imaging of the specimen, the geometry of an interlaminar test specimen is dependent on the thickness of the laminate. In this work, a thicker laminate (18 mm) is considered for practical reasons. Specifically, this enables plate-like specimen to be machined and accurate grids to be deposited for full-field measurement purposes. To maximise measurement spatial resolution, a smaller grid pitch is required (on the order of 0.3 mm compared to 0.9 mm in [37]). With a smaller length compared to the transverse tension specimens, the wave transit time is also shortened. This requires a higher framing rate to ensure sufficient temporal resolution of the kinematic fields (the Shimadzu HPV-X camera allows for frame rates up to 5 Mfps at full resolution).

Separate design sweeps were performed for each interlaminar plane. The length of specimens from both material planes was fixed at the nominal plate thickness of 18 mm. A height of 12 mm was selected to maximise the spatial resolution of the camera (Shimadzu HPV-X, 400 x 250 pixels), including approximately 2 mm at the free edge of the specimen to account for rigid body motion. The material used in this study is a unidirectional carbon/epoxy composite, AS4-145/MTM45-1. The properties of this material were characterised by the National Center for Advanced Material Performance (NCAMP) as summarised in [132]. Unfortunately, only quasi-

Table 4.1: Summary of simulated values used in parametric sweep for test design

Parameter	Min	Max	Increment
Projectile length, L_P [mm]	2.5	20	2.5 ($L_P \leq 5$) 5 ($L_P > 5$)
Impact speed, V_P [m·s^{-1}]	20	50	10

static interlaminar tensile strength was measured in that campaign ($\sigma_T^{ult} = 50.4$ MPa). Therefore, for test design it was assumed that reported values for the in-plane transverse Young's modulus, shear modulus, and Poisson's ratio were representative of that for the interlaminar planes. The quasi-static, in-plane transverse compressive strength ($\sigma_C^{ult} \approx 290$ MPa) was assumed as a conservative limit for allowable compressive stress. To the authors' knowledge, the HSR properties for this material have not been measured. Therefore, it was also assumed that the material strength will exhibit a similar strain rate sensitivity to that reported in [37] measured using the same IBII test (+57% increase in strength at strain rates on the order of $2{\times}10^3$ s^{-1}). Even though reference [37] focussed on the in-plane transverse properties, the reported strain rate sensitivity was expected to be reasonably representative of the interlaminar behaviour as a matrix dominated property. Therefore, the interlaminar tensile strength at high strain rates is estimated to be 80 MPa. For the IBII interlaminar test the design space is defined by the tensile and compressive strengths as: -290 MPa $< \overline{\sigma_{xx}}^{y} <$ 80 MPa.

The design sweep in [37] showed that the experimental parameters that primarily influence the stress state in the material are projectile length and impact velocity. Therefore, these are the only parameters considered in the design sweep of the IBII test here. In the design sweep the height of the waveguide, H_{WG}, and projectile, H_P, were fixed at 25 mm. Having a larger projectile and waveguide improves contact alignment and stability of the sample on the test stand. This also prevents the sabot from striking the alignment stand. A separate simulation study showed that the impactor height has little influence on the test provided that it does not exceed three times the specimen width. The height of the sabot is also fixed at the barrel diameter of the purpose-built gas gun (50 mm). The projectile length and projectile speed were selected using a parametric design sweep. The range of simulated values for these variables are listed in Table 4.1.

The sabot length was variable such that the total length of projectile-sabot assembly was a constant 50 mm. A maximum projectile length of 20 mm was set to avoid creating an input pulse length that exceeds the specimen length. This would result in a superposition of the input and reflected waves, reducing the maximum tensile stress in the specimen. Since the waveguide and projectile are made of the same material, the waveguide length must be at least twice the length of the projectile to avoid clipping the pulse. Therefore, the waveguide length, L_{WG}, is fixed at 50 mm.

4.3.2 Finite element implementation

All simulations were performed in ABAQUS/Explicit. Plane stress CPS4R elements (2D, 4 node, reduced integration) were used in all simulations. The mesh size, and stiffness-proportional damping coefficient, β, were first selected using a separate parametric sweep. Some numerical damping is required to control the artificial high frequency oscillations that occur in the explicit dynamic simulations. The criterion for selection was minimisation of the error between the reconstructed stress averages, using the stress-gauge equation (Eq. (3.16)), and simulated stress averages, over an entire wave reflection. This sweep resulted in a mesh

Table 4.2: Simulation parameters and material properties for the interlaminar IBII tension/compression test

Specimen (AS4-145/MTM45-1)	
E_{11} [GPa]	129^{a*}
E_{22} [GPa]	7.9^{a*}
E_{33} [GPa]	7.9^{a*}
G_{13} [GPa]	3.65^{a**}
G_{23} [GPa]	3.65^{a**}
ν_{13} [–]	0.015^{a}
ν_{23} [–]	0.225^{a}
Specimen length [mm]	18
Specimen height [mm]	12
ρ [kg·m^{-3}]	$1{,}605^{b}$
Mesh size [mm]	0.1
Waveguide & Projectile (Aluminium 6061-T6)	
E [GPa]	70
ν [–]	0.3
ρ [kg·m^{-3}]	2,700
Waveguide length [mm]	50
Waveguide height [mm]	25
Projectile height [mm]	25
Mesh size [mm]	0.2
Sabot (Nylon 6-6)	
E [GPa]	3.45
ν [–]	0.4
ρ [kg·m^{-3}]	1,140
Sabot length [mm]	50
Sabot height [mm]	25
Mesh size [mm]	0.2

^{a}: from [132]
^{b}: measured using a micro balance and water immersion
*: average transverse modulus
**: average in-plane shear modulus

size of 0.1 mm and β coefficient of 7x10^{-7} ms. For the remaining components in the simulation a mesh size of 0.2 mm was used to maintain a similar mesh density. The time step incrementation was not fixed, however, the data output step was set to match that of the camera used for the experiments (0.2 μs inter-frame time). Isotropic linear elasticity was assumed for the projectile, waveguide, sabot and 2-3 plane interlaminar specimens. For 1-3 plane specimens a transverse isotropic, linear elastic material model was used. The simulated geometries and material properties for the interlaminar IBII test are listed in Table 4.2.

4.3.3 Parametric sweep results

The results from the parametric sweep for 1-3 and 2-3 plane specimens are shown in Fig. 4.2a and Fig. 4.2b, respectively. Based on the design space defined in Section 4.3.1, it is possible to select a range of experimental parameters that satisfy the design requirements. For both specimens, the design envelope that satisfies the requirements is given by: projectile length [10 mm < L_P < 20 mm] and impact velocity [V_P > 40 m·s^{-1}]. From this, the test configuration selected for both experiments is as follows: L_{WG} = 50 mm, L_P = 10 mm, and V_P = 50 m·s^{-1}. Based on simulated stress fields, the design strength of 80 MPa is expected to be reached at approximately x = 10 mm from the free edge.

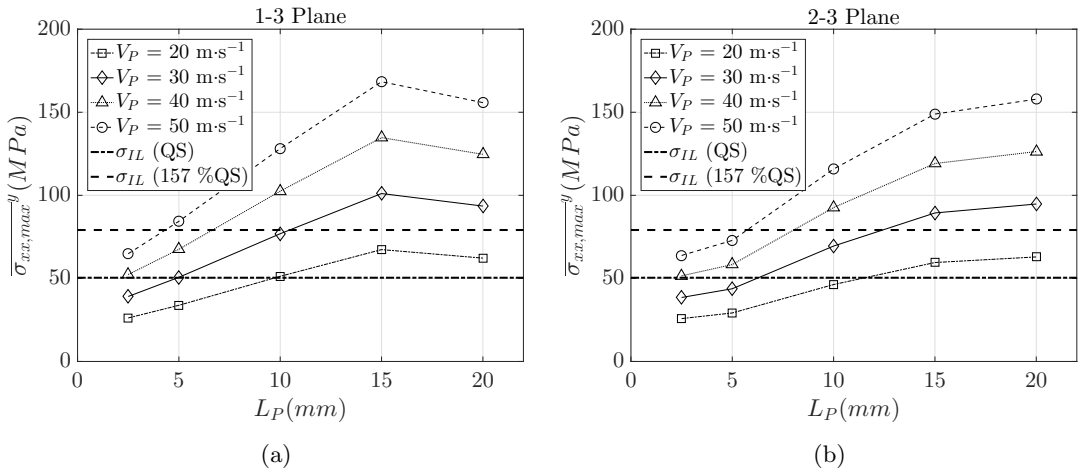

(a) (b)

Figure 4.2: Maximum reflected tensile stress, $\overline{\hat{\sigma_{xx}}}^{y}$ for interlaminar IBII specimens as a function of projectile length and velocity: (a) 1-3 plane specimens, (b) 2-3 plane specimens

4.4 Material and Experimental Setup

4.4.1 Specimen manufacturing

Material properties of AS4-145/MTM45-1 are provided in Table 4.2. The density of the plate was measured using a micro balance and water immersion to be 1,605 ± 20 kg·m^{-3}. The plate had an average measured cured thickness of 17.9 mm (est. 128 layers, 0.14 mm cured ply thickness [132]). Twenty interlaminar specimens were cut (10 x 1-3 material plane and 10 x 2-3 material plane). The specimens were first rough cut from the plate using a large tile saw with a diamond cutting wheel. The specimen faces were then cut using a Streurs E0D15 diamond saw. The automated stage was set to a low feed rate of 0.1 mm·s^{-1} to reduce the likelihood of inducing machining defects. For the 1-3 plane, specimen dimensions (L x H x e) were measured to be 17.9 mm x 12.1 mm x 2.6 mm (std. dev.: ±0.2 mm, ±0.2 mm, ±0.6 mm). Similarly, 2-3 plane specimen dimensions were measured to be 18.2 mm x 12.0 mm x 2.6 mm (std. dev.: ±0.1 mm, ±0.3 mm, ±0.4 mm). Note that reported thickness measurements include the grid deposited on the surface.

4.4.2 Grid deposition techniques

Grids with a pitch p of 0.3 mm were bonded to ten specimens (5 for each interlaminar plane), using the process outlined in [133]. The epoxy layer had a typical thickness of approximately 225 μm. While this deposition procedure worked quite well in [37] for in-plane specimens, the smaller specimens in this study were more susceptible to grid defects from air bubbles in the underlying resin layer. Since grid defects are detrimental to the inverse identification procedures, a second grid deposition process was explored for the remaining ten specimens (5 for each interlaminar plane). A thin coat of white rubber paint (Rust-Oleum Peel Coat) was first applied to the specimen. The paint layer had a typical thickness of approximately 20 μm. A series of black squares were then printed onto the painted surface with a Canon Océ Arizona 1260 XT flat bed printer. This formed a white grid with an average pitch of 0.337 mm. Trial prints of uniform grids were found to contain periodic defects every 80 mm in the horizontal direction. This was used to define the true print resolution and adjust the grid pitch when printing on specimens. As grids were defined according to a constant 'points-per-pitch' ratio (6:7 (x:y) closely matches that of the true resolution), the actual pitch in the vertical and

Table 4.3: Imaging system and full-field measurement parameters for the IBII tension/compression test

Optical Setup	
Camera	Shimadzu HPV-X
Pixel array size	400 x 250
Sensor	FTCMOS
Inter-frame time	0.2 μs
Integration (shutter) time	110 ns
Number of images	128
Lens	Sigma 105 mm
Flash	Bowens Gemini 1000 Pro
Grid Method	
Grid pitch (mm)	0.3, 0.337
Sampling (pixels/period)	6, 7
Field of view (mm)	20 x 12.5, 19.25 x 12.04
Displacement computation	Iterative [96]

horizontal directions is 0.338 mm and 0.336 mm, respectively. More information is available online [134, 135]. This required processing of the grid images using the iterative procedure described in [96]. The limited printer resolution reduces the spatial resolution compared to the bonded grids. However, this was a manageable compromise given the simplicity of the deposition process and significant reduction in grid defects.

4.4.3 Specimen naming convention

Specimens will be referred here by specimen number followed by a dash and a letter specifying the grid type; 'P' denotes a printed grid (p = 0.337 mm), and 'B' denotes a bonded grid (p = 0.3 mm), respectively. The interlaminar plane is specified in square brackets. For example, specimen #1 from the 1-3 plane with a 0.337 mm printed grid pitch is referred to as: '#1-P[1-3]'.

4.4.4 Experimental setup

All tests were performed using the compressed air impact rig described in [136]. The gas gun reservoir pressure was set for a nominal impact velocity between 50 and 55 m·s^{-1}. Each specimen was bonded to the back of a 6061-T6 aluminium waveguide (50 mm length, 25 mm diameter) using a thin layer of cyanoacrylate glue. A copper contact trigger on the front of the waveguide was used to trigger the camera. A 10 μs delay was programmed between the trigger event and image capture to account for the traverse time of the wave through the waveguide. All images were captured using the Shimadzu HPV-X camera (frame rate = 5 Mfps) with a Sigma 105 macro lens. The optical setup and a mounted specimen are shown in Figs. 4.3a and 4.3b, respectively. Further details about the optical measurement system are provided in Table 4.3. The low fill factor of the Shimadzu HPV-X required intentional blurring of the images to avoid aliasing of the grid and parasitic fringes in the strain maps [88]. An out-of-plane movement test (2 mm) was performed prior to each test to minimise the strain fringes (below the noise threshold) and thus, ensure that the images were sufficiently blurred. The camera stand-off distance was adjusted according to the grid being imaged. To maximise the spatial resolution of the Shimadzu HPV-X camera, the 0.3 mm grids were sampled at 6 pixels per pitch, whereas the 0.337 mm grids were sampled at 7 pixels per pitch.

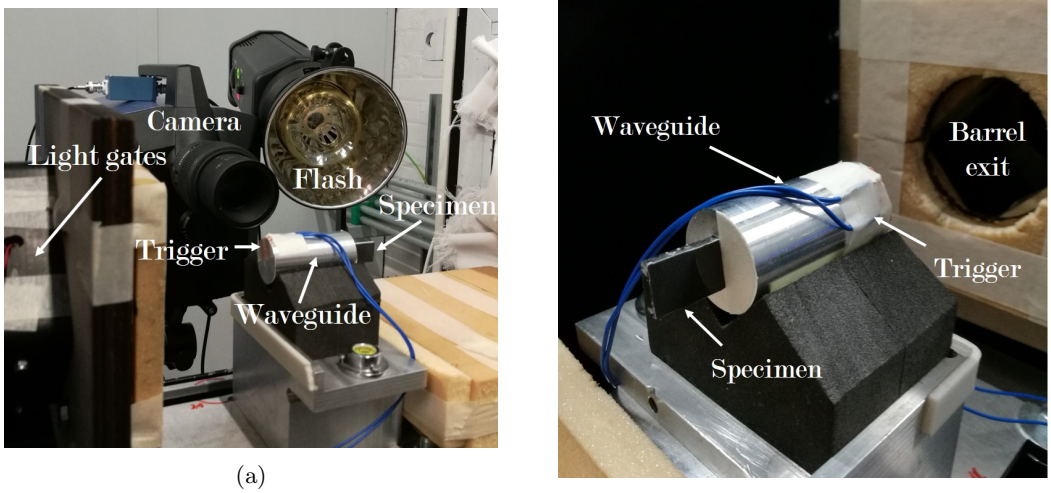

(a) (b)

Figure 4.3: Experimental setup used for all interlaminar IBII tests: (a) camera and flash arrangement around the test chamber, and (b) a mounted specimen supported on a test stand in the test chamber

4.4.5 Image processing and identification of material properties

The full image processing procedure is described in the following sections to explain how material properties can be extracted from deformed images of a specimen with a grid on its surface. The key steps are summarised in a flow chart shown in Fig. 4.4.

Obtaining displacement fields from deformed grid images

The Shimadzu HPV-X camera is used to collect a set of deformed grid images. These grid images are processed using the grid method to obtain phase maps, using a windowed discrete Fourier transform. For the bonded grids only, the phase maps were corrected for air bubble defects using a three-step procedure. 1) Each ϕ_x phase map was fitted with a mesh of linear finite elements (8x5 elements (x,y)) to capture gradients in the phase fields. The phase values at the nodal positions were determined using a least-squares regression fit and linear shape functions were used to interpolate the phase within each element. The regression plane fit was then subtracted from the raw phase field to obtain a map of residuals. Grid defects were first characterised by regions with phases values exceeding a 2σ threshold on the residual. 2) A second linear regression plane fitting was performed to the phase maps, with the defects identified in 1) removed. The full extent of the defect was characterised by again using a 2σ threshold. These defect maps were then used to remove defects in the ϕ_y maps. 3) A sliding square window of seven pitches in length was used to linearly interpolate the phase information over the defective regions identified in 2). The displacement fields were then computed from the 'corrected' phase maps using the iterative approach described in [96]. The iterative approach accounts for initial phase modulations in the grid (*e.g.*: remaining small grid defects, slight grid spacing irregularities). The phase maps contain discontinuous jumps when the grid displaces more than one pitch. These jumps were corrected using spatial and temporal unwrapping. Spatial unwrapping was performed using the procedure described in [137]. Temporal unwrapping was performed using an in-house MATLAB routine. In this procedure, the spatial mean of the unwrapped phase is plotted against time and the 2π mean phase jumps in time are corrected to obtain a monotonic increase of the longitudinal displacement representative of the rigid body translation in the impact direction.

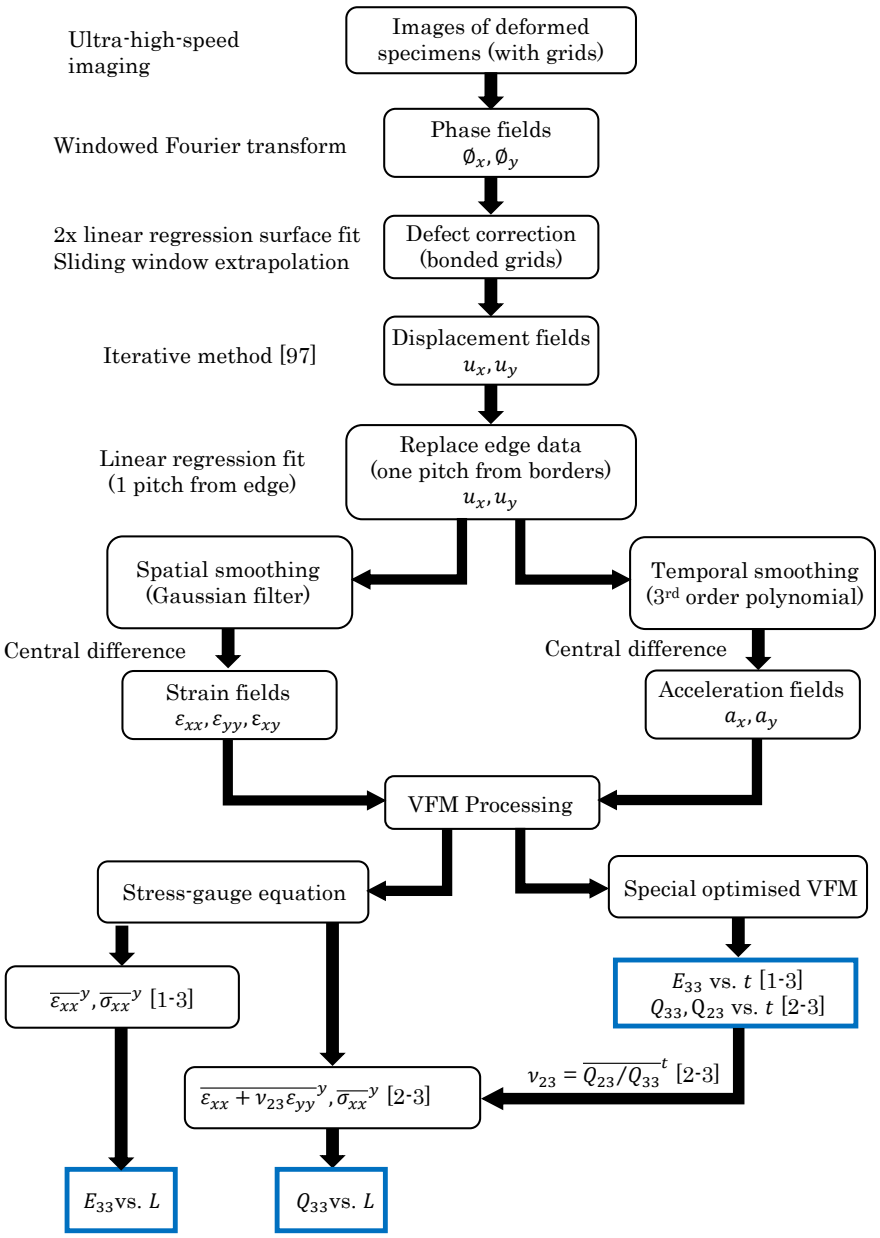

Figure 4.4: Flow chart of processing procedure to identify material stiffness parameters from deformed grid images. Note that the exact same procedure is used for processing the experimental data and the image deformation simulations

Obtaining strain and acceleration fields

One pitch of information is corrupted on the border of the phase maps due to edge effects from the windowed Fourier transform. Rather than discarding this data, previous studies have shown that identifications using the virtual fields method were drastically improved when this data was recovered using some sort of extrapolation [104, 138]. In this work, the corrupted displacement data was replaced using a linear regression fitting based on the data over one pitch (6 pixels (0.3 mm grids) or 7 pixels (0.337 mm grids)) inwards from the corrupted region. The extrapolation was performed independently for each row of pixels (u_x fields), or column of pixels (u_y fields). This approach was found to be better at rejecting noise compared to the approach in [37], where data was recovered using a linear extrapolation based on two points inward from the corrupted region. The displacement maps were then processed in two ways to obtain acceleration and strain fields (Fig. 4.4). Displacement maps were smoothed temporally using a third order Savitsky-Golay filter, and then differentiated twice in time to obtain acceleration maps. Displacement fields were padded in time by one half of the kernel size (in frames) to minimise edge effects from the filter. Raw displacement maps were also smoothed spatially, using a Gaussian filter, before differentiating to obtain strain maps. Both temporal and spatial differentiations were computed using a central difference. Strain rate maps were computed from the smoothed strain maps using a central difference, except for computing strain rate at fracture, which was performed using a backward difference based on the raw strain maps to avoid temporal leakage from unrealistic strains computed after crack initiation. To reduce edge effects from spatial smoothing, the displacement fields were first padded out by 3 smoothing kernels using a linear extrapolation. The fields were smoothed and then cropped back to the original size.

Identifying material properties from kinematic fields

The special optimised virtual fields methods presented in Sec. 3.4.2 were used to process acceleration and strain fields to identify stiffness parameters. Material properties were identified from acceleration and strain maps using two VFM approaches: 1) using special optimised virtual fields, and 2) using reconstructed stress averages to compute stress-strain curves at each position along the specimen length.

Special optimised virtual fields: The special optimised virtual fields approach provides an identification of each stiffness parameter for each time step. For 1-3 plane specimens, the reduced approach was used to process a_x and ϵ_{xx} fields to directly identify E_{33}. For 2-3 plane specimens, the a_y, ϵ_{yy} and ϵ_{xy} fields were also included in the general isotropic formulation of the special optimised virtual fields approach. In this case, Q_{33} and Q_{23} were identified, from which E_{33} and ν_{23} were determined. The value of each identified stiffness parameter for the test was taken as the average over all time steps where the identification is stable. The identification is generally poor during the first few frames of the test due to low strains as the wave enters the specimen. Stability is also challenged as the wave reflects from the free-edge, as the incoming and reflected waves superimpose, resulting in temporary low strain and acceleration signal. When the material cracks in tension, non-physical strains corrupt the identification. Therefore, optimal conditions for identification (high strain and acceleration signal) generally occurs during the first compressive loading after the stress wave has entered the specimen, but before it reflects at the free edge. The optimized virtual fields were expanded using a basis of piecewise functions (finite elements), as proposed initially in [139]. A virtual mesh refinement study was performed on the image deformation data (described in Sec. 4.5) and the results showed that

the identification converged at a virtual mesh of 5x1 elements (x,y) and 5x4 elements (x,y) for the reduced and isotropic special optimised routines, respectively. Data is discarded within one pitch plus one spatial smoothing kernel at the impact edge to reduce smoothing filter edge effects on the identification.

Reconstructed stress-strain curves: Here, the stress-gauge equation (Eq. (3.16)) was used to calculate stress averages ($\overline{\sigma_{xx}}^{y}$) from a_x fields for all specimens. Using these stress averages, combined with axial strain ($\overline{\epsilon_{xx}}^{y}$ for 1-3 plane specimens, and $\overline{\epsilon_{xx}+\nu_{23}\epsilon_{yy}}^{y}$ for 2-3 plane specimens), stress-strain curves were generated along the length of the specimen. For the case of 2-3 plane specimens, the identified value of ν_{23} from the special optimised virtual fields procedure was used. The interlaminar stiffness (E_{33} for 1-3 plane specimens, and Q_{33} for 2-3 plane specimens) was identified using a linear regression fit to the stress-strain curve up to the maximum compressive stress. This is henceforth referred to as the 'stress-strain curve' approach. E_{33} was calculated for 2-3 plane specimens using the identified value of ν_{23} from the special optimised virtual fields approach. The identification of E_{33} tends to be poor near the free and impact edges due to extrapolated data at the edges of the specimen, and edge effects from spatial smoothing. Therefore, the value of E_{33} for the test was taken as the average of identified values over the middle 50% of the specimen. The stress-average reconstructed at the first crack location using linear-stress gauge equation was used to estimate the interlaminar tensile strength.

Clearly, the selection of spatial and temporal smoothing parameters will influence the identification procedures. The smoothing parameters were selected using an image deformation simulation procedure similar to [39, 104, 140], as described in the following section.

4.5 Smoothing Parameter Selection and Error Quantification

4.5.1 Generating synthetic images

The purpose of this section is to select optimal smoothing parameters to be used for the experiments and estimate the experimental error using an image deformation procedure. The general concepts are described here, but the reader is referred to [39, 104, 140] for further details. A sequence of 'static' synthetic images were generated for both types of grids used in the experiments using an analytical function to describe the light intensity, $s(x,y)$. For the white-on-black grids, with a 0.3 mm pitch, the intensity at any position was described as:

$$s(x,y) = A + \gamma \cdot \left(1 + \frac{1}{2}\big(1+\cos(2\pi x/p)\big)\cdot\big(1+\cos(2\pi y/p)\big)\right) \tag{4.1}$$

while the intensity at any position for the black-on-white grids, with a 0.337 mm pitch, was defined as:

$$s(x,y) = A + \gamma \cdot \left(1 - \frac{1}{2}\big(1+\cos(2\pi x/p)\big)\cdot\big(1+\cos(2\pi y/p)\big)\right) \tag{4.2}$$

where A is the average grey level illumination, γ is the pattern contrast amplitude (between 0 and 1), and p is the grid pitch. Displacement fields from finite element simulations were used to create a set of deformed images using super-sampling interpolation. Up-sampled images were generated, and then sub-sampled by pixel averaging to simulate the resolution of the Shimadzu HPV-X camera (400 x 250 pixels). Specifically, synthetic images were generated for the bonded, 0.3 mm, white-on-black grids, and the printed, 0.337 mm, black-on-white grids, using contrast

Table 4.4: Summary of parameters used to generate synthetic images for processing parameter optimisation

Image Parameter	Printed Grids	Bonded Grids
Grid pitch (mm)	0.3	0.337
Mean grey level (% dyn. range)	50	40
Grid contrast amp. (% dyn. range)	20	25
Noise amplitude (% dyn. range)	0.4	0.25
Pixel sampling (pixels/period)	7	6

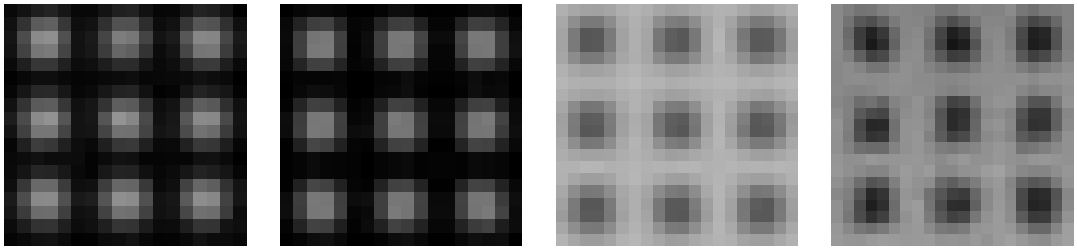

(a) (b) (c) (d)

Figure 4.5: Magnified views of grid images: (a) 0.3 mm synthetic grid (6 pixels/period), (b) 0.3 mm experimental grid (6 pixels/period), (c) 0.337 mm synthetic grid (7 pixels/period), and (d) 0.337 mm synthetic grid (7 pixels/period)

values measured from experimental static images. The parameters used to generate each set of synthetic images are listed in Table 4.4. Magnified views of the synthetic grid images are compared with experimental grids in Fig. 4.5. The lighting gradient along the specimen length is more pronounced on the black-on-white grids. Therefore, the synthetic image is based on average intensity and contrast of the experimental grids over the length of the specimen. This explains the slight differences in contrast between synthetic and experimental 0.337 mm pitch grids.

The deformed synthetic images were then processed using the same procedure as the experimental images (Sec. 4.4.5). Different combinations of spatial and temporal smoothing were used to quantify the effect of processing parameters on the identification of stiffness parameters.

4.5.2 Identification sensitivity to smoothing parameters

Each combination of smoothing kernels was used to process synthetic images with 30 copies of noise. Gaussian white noise with a uniform standard deviation was used to approximate experimental noise. In reality, noise is dependent on grey level intensity, which could be accounted for in the future. The standard deviation was set to that measured from a series of static grid images captured with the Shimadzu HPV-X camera (Table 4.4). The sensitivity to smoothing parameters was assessed using the maximum total error (e_T) between the reference stiffness value and the value identified from the processed synthetic images. The total error was defined as the absolute value of the systematic error e_S, plus or minus two times the random error, e_R ($e_T = |e_S \pm 2e_R|$). The systematic error (e_S) was considered as the difference between the mean identified stiffness parameter and the reference stiffness, normalised by the reference stiffness as,

$$e_{S,ij} = \frac{1}{Q_{FE,ij}}\left(\frac{1}{N}\sum_{k=1}^{N} Q^k_{ID,ij} - Q_{FE,ij}\right) \quad \text{for} \quad i = 2,3, j = 3 \tag{4.3}$$

where $Q^k_{ID,ij}$ is the identified stiffness parameter from the image deformation simulations for

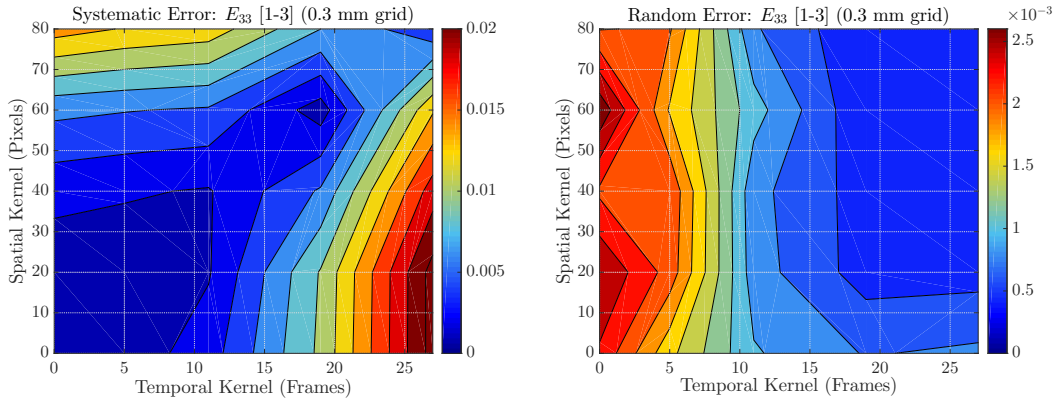

(a) (b)

Figure 4.6: Simulated identification error for E_{33} as a function of spatial and temporal smoothing kernel size using the reduced special optimised virtual field (1-3 plane specimen, 0.3 mm grid, 6 pixels per period sampling): (a) normalised systematic error, and (b) normalised random error

noise iteration k, N is the number of noise copies ($N = 30$), and $Q_{FE,ij}$ is the reference stiffness value used to generate the simulated displacement fields and deformed images. Random error (e_R) was defined as the standard deviation of the identified stiffness over the 30 copies of noise normalised by the reference stiffness as,

$$e_{R,ij} = \frac{1}{Q_{FE,ij}} \sqrt{\frac{\sum_{k=1}^{N} (Q_{ID,ij}^{k} - \overline{Q_{ID,ij}})^2}{N}} \quad \text{for} \quad i = 2,3; j = 3 \tag{4.4}$$

where $\overline{Q_{ID,ij}}$ is the mean identified stiffness parameter from the image deformation simulations over all copies of noise. The reader is encouraged to recall Section 4.4.5 for a description of the identification procedures.

For each combination of smoothing kernels, the systematic, random and total error were calculated. Examples of systematic and random error maps for the identification of E_{33} [1-3] with 0.3 mm grid, using the reduced special optimised virtual fields approach are shown in Fig. 4.6a and 4.6b, respectively. The error maps were very similar for identifications using the stress-gauge approach and therefore, only maps for the optimised VFM will be presented. The systematic and random errors follow similar trends as shown in previous works for quasi-static tests [39], with minimum systematic error and high random error when no smoothing is applied. The band of low systematic error represents a consistent trade-off between bias from smoothing acceleration fields (temporal smoothing), and strain fields (spatial smoothing), such that the reference stiffness is most accurately identified. The magnitude of random error is low since the identification is derived from the average over several temporal frames. The random error is more strongly influenced by temporal smoothing (noise in acceleration signal) since the optimised virtual field routine are optimised to minimise strain noise, and not acceleration noise, and there is a double differentiation in time compared to a single differentiation in space.

For the 1-3 interlaminar plane specimen, the total error maps are shown in Figs. 4.7a (0.3 mm grid, 6 pixels/period) and 4.7b (0.337 mm, 7 pixels/period). The total error maps for 6 and 7 pixels/period are very similar in shape and magnitude. This implies that grid sampling has only a small influence on the identification in the present case. These maps suggest that optimal levels of smoothing correspond to a spatial kernel of 41 pixels, and a temporal kernel of 11 frames. For these parameters the estimated error on E_{33} is approximately 0.5%.

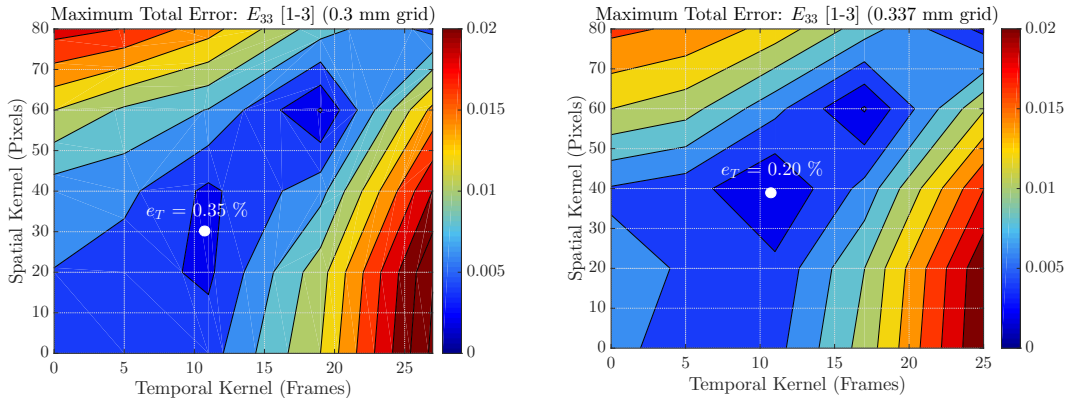

(a) (b)

Figure 4.7: Maximum, simulated identification error for E_{33} as a function of spatial and temporal smoothing kernel size using the reduced special optimised virtual field (1-3 plane specimen): (a) normalised total error for 0.3 mm grid (6 pixels/period sampling), and (b) normalised total error for 0.337 mm grid (7 pixels/period sampling). Minimum error indicated by white circle

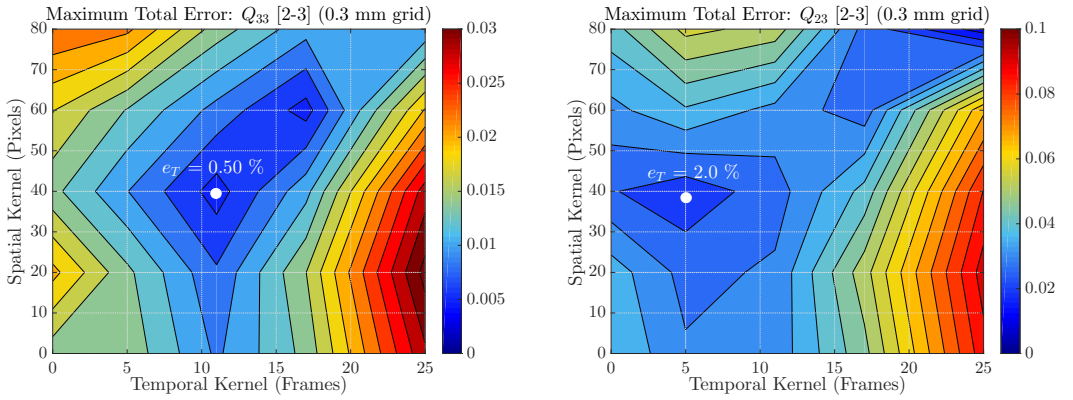

(a) (b)

Figure 4.8: Maximum, simulated identification error for Q_{33} and Q_{23} as a function of spatial and temporal smoothing kernel size using special optimised virtual fields (2-3 plane specimen, 0.3 mm grid, 6 pixels/period sampling): (a) normalised total error for Q_{33}, and (b) normalised total error for Q_{23}. Minimum error indicated by white circle

The total error maps for Q_{33} and Q_{23}, for 2-3 plane specimens with 0.3 mm (6 pixels/period) and 0.337 mm (7 pixels/period) grids are shown in Figs. 4.8 and 4.9, respectively. The higher total error at low smoothing indicates a higher sensitivity to random error. This is to be expected as ϵ_{yy} and a_y have a lower signal-to-noise ratio. The inclusion of these fields into the identification increases the sensitivity to noise of both Q_{33} and Q_{23}, which are identified simultaneously. Nevertheless, the minimum total error is not significantly increased compared to the 1-3 plane identification, with the minimum occurring around a 41 pixels spatial smoothing kernel, and 11 frames for the temporal smoothing kernel. These parameters have an associated error on the identification of Q_{33} and Q_{23} of approximately 0.5% and 2-3%, respectively.

The total error maps are extremely useful for selecting the optimal smoothing parameters in a rational way and provide an estimate of the total error associated with the experimental identifications. The optimal smoothing parameters selected for processing experimental images are listed in Table 4.5. Also included are the corresponding error estimates and measurement resolution (standard deviation of field) from static experimental images processed with the selected smoothing parameters. Image deformation simulations indicate that the predicted errors are very low, despite having limited spatial resolution. Simulations also suggest that this

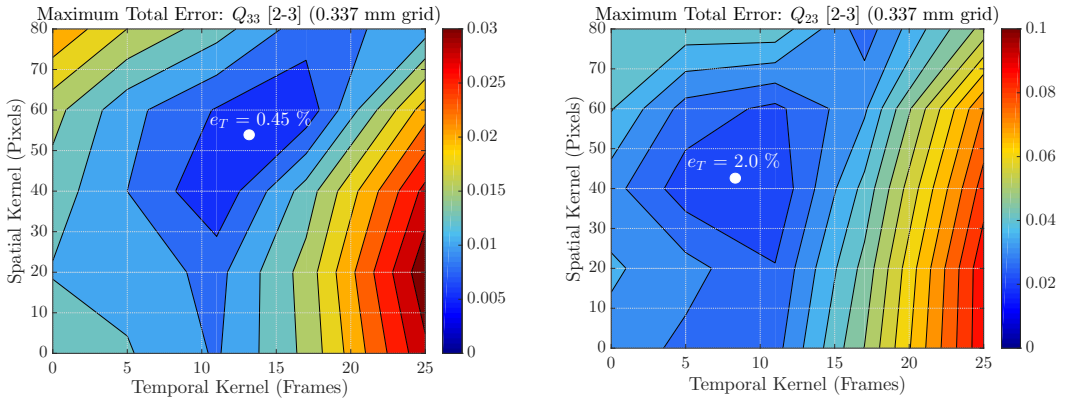

(a) (b)

Figure 4.9: Maximum, simulated identification error for Q_{33} and Q_{23} as a function of spatial and temporal smoothing kernel size using the special optimised virtual fields (2-3 plane specimen, 0.337 mm grid, 7 pixels/period sampling): (a) normalised total error for Q_{33}, and (b) normalised total error for Q_{23}. Minimum error indicated by white circle

Table 4.5: Selected smoothing parameters for processing experimental images and corresponding measurement performance

	1-3 Plane		**2-3 Plane**	
	Grid Pitch (mm)			
Parameter	0.3	0.337	0.3	0.337
Spatial Kernel (Pixels)	31	41	41	41
Temporal Kernel (Frames)	11	11	11	11
Error Q_{xx} (%)	0.4	0.2	0.5	0.5
Error Q_{xy} (%)	–	–	2.8	2.1
Measurement Resolution				
Displacement (μm)	0.3	0.4	0.3	0.4
(pixel)	0.006	0.008	0.006	0.008
(pitch)	p/1,000	p/850	p/1,000	p/850
Strain (μm·m^{-1})	46	56	46	56
Acceleration ($\times 10^5$ $m \cdot s^{-2}$)	8.4	5.1	8.4	5.1

configuration is highly robust to spatial and temporal smoothing, so long as the user does not select extreme smoothing parameters. This is a key advantage of this IBII test configuration. The user can quickly establish reasonable limits on the bounds of smoothing for a given grid pitch assuming a rough knowledge of the material in question. For example, looking at the contour maps, the temporal smoothing is the parameter that mostly influences the error. The total error sharply rises when the temporal smoothing kernel approaches the time for the wave pulse to traverse across the specimen. Therefore, so long as the user can estimate the wave speed in the material with reasonable accuracy, an upper bound on temporal smoothing can be quickly established. Likewise, simulations suggest that spatial smoothing does not significantly effect the identification so long as the total kernel is less than 10 grid pitches.

4.6 Experimental Results and Discussion

4.6.1 Full-field measurement results

In this section typical experimental kinematic fields are presented for two time steps for a 1-3 plane and 2-3 plane interlaminar specimen. Full-field maps of u_x and u_y are shown for specimen #2-P[1-3] in Fig. 4.10 for two time steps; the first time step corresponds to a state where the

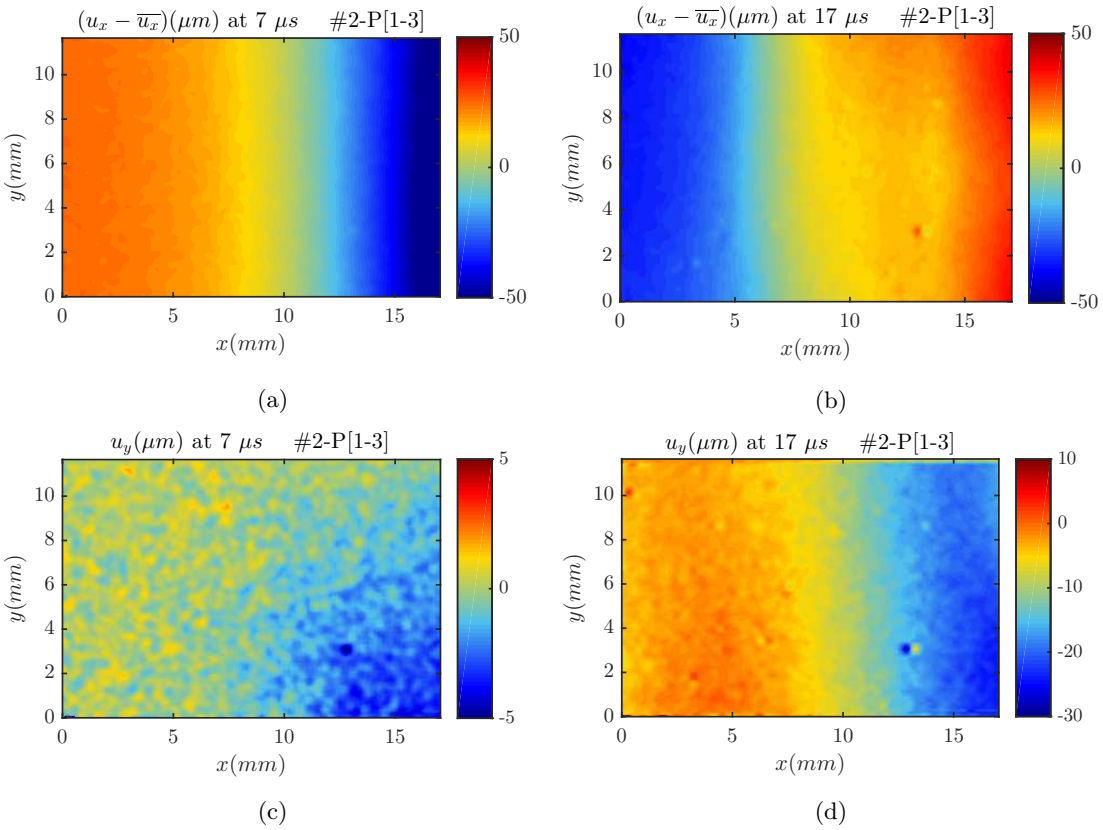

Figure 4.10: Experimental displacement fields; (a),(b) u_x (μm), and (c),(d) u_y (μm), for specimen #2-P[1-3] at 7 μs and 17 μs. Note that the mean u_x displacement has been subtracted to remove the rigid-body displacement

initial compressive pulse is well within the specimen (t = 7 μs), and the second corresponds to a time after the pulse has reflected but before tensile failure (t = 17 μs). Similar maps for specimen #6-B[2-3] are provided in Fig. 4.11. Note that the mean u_x displacement has been subtracted to remove the rigid-body displacement and show the deformation. Due to the high lateral stiffness from the fibre reinforcement for specimen #2-P[1-3], the magnitude of u_y is much smaller and the signal to noise ratio is much poorer compared to u_x. In the case of specimen #6-B[2-3], u_y is approximately one order of magnitude larger. The corresponding acceleration fields for the two specimens are shown in Figs. 4.12 and 4.13. The edges of the pulse are most clearly identified in a_x maps, which show that local accelerations are on the order of $10^7 \mathrm{m{\cdot}s^{-2}}$. This corresponds to average axial forces on the order of 4 kN, or axial stress on the order of 100 MPa (Fig. 4.14). Defects are difficult to remove from acceleration fields since no temporal information is considered in the correction procedure. While this provides a reasonable reconstruction in the majority of cases, the defective region is still identifiable in some frames, as shown in Fig. 4.13d. While defects cannot be completely removed, providing some compensation for defects is beneficial as it acts as an outlier removal. This is particularly beneficial for identifications from stress-strain curves, which rely on local strain values.

The ϵ_{xx}, ϵ_{yy} and ϵ_{xy} strain maps for the two specimens, at the same two time steps, are shown in Figs. 4.15 and 4.16. The experimental strain maps for the 1-3 interlaminar specimen confirm that the ϵ_{yy} strains are much lower than for the ϵ_{xx} strains. Significant ϵ_{yy} strains are measured in the case of the 2-3 plane interlaminar specimen, however, the signal-to-noise ratio remains less favourable than the ϵ_{xx} strains. As a result, the edge data extrapolation procedure does not perform as well, creating some localised regions of high artificial strain. As mentioned

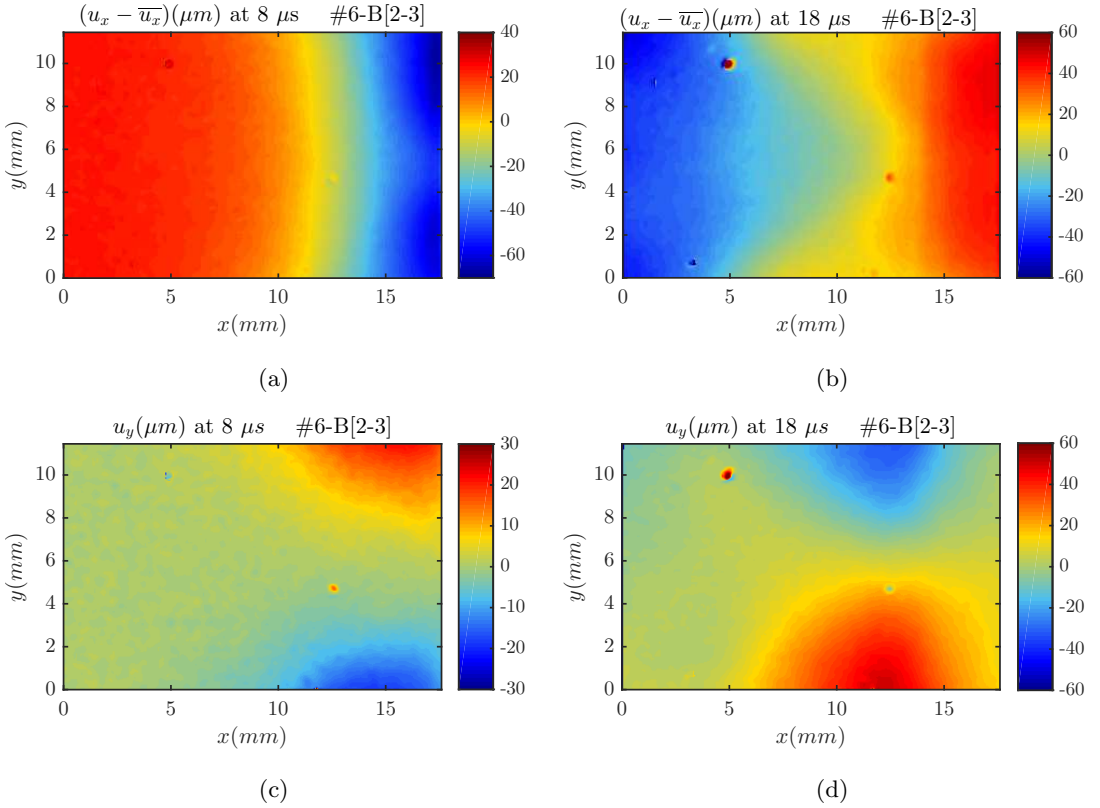

Figure 4.11: Experimental displacement fields; (a),(b) u_x (μm), and (c),(d) u_y (μm), for specimen #6-B[2-3] at 8 μs and 18 μs. Note that the mean u_x displacement has been subtracted to remove the rigid-body displacement

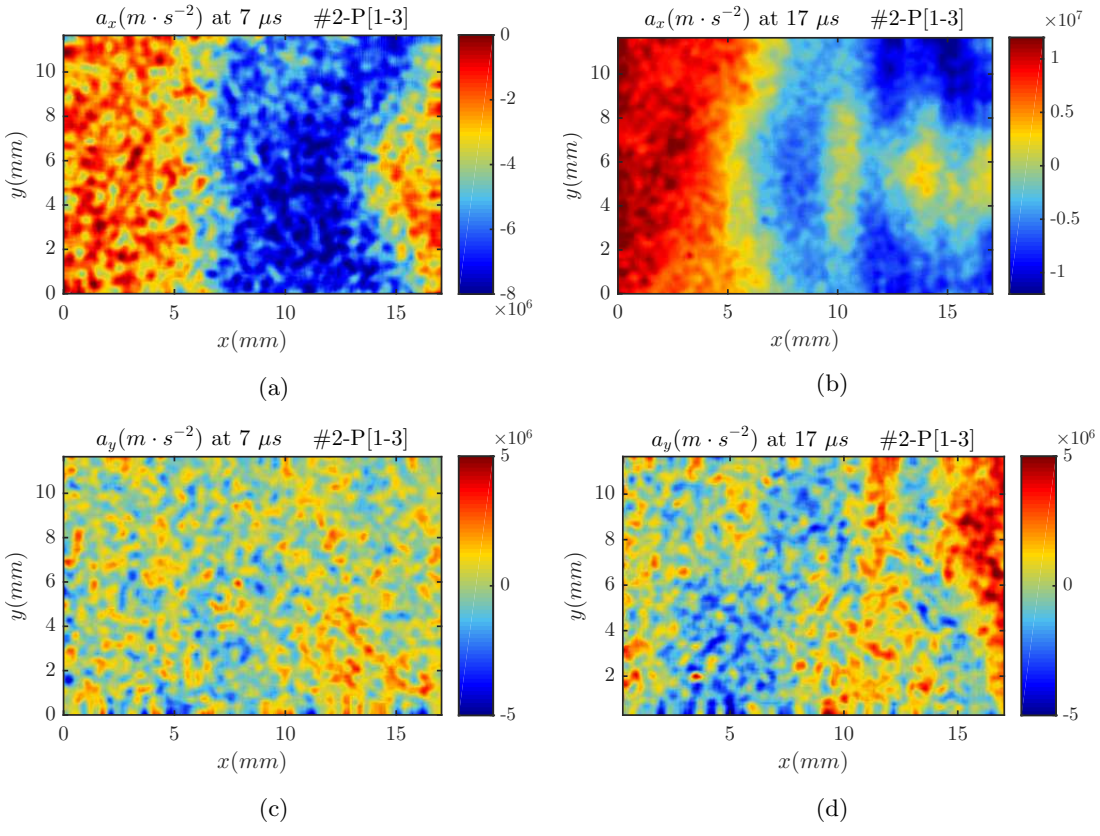

Figure 4.12: Experimental acceleration fields; (a),(b) a_x (m·s^{-2}), and (c),(d) a_y (m·s^{-2}), for specimen #2-P[1-3] at 7 μs and 17 μs

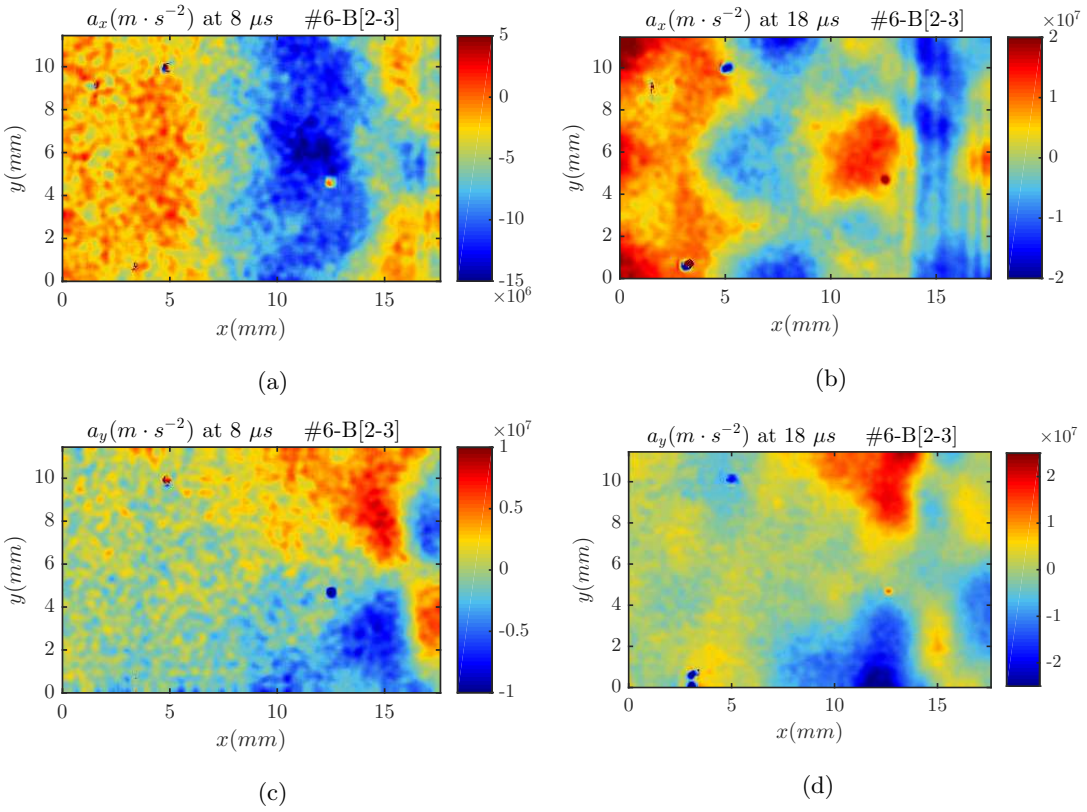

Figure 4.13: Experimental acceleration fields; (a),(b) a_x (m·s^{-2}), and (c),(d) a_y (m·s^{-2}), for specimen #6-B[2-3] at 8 μs and 18 μs

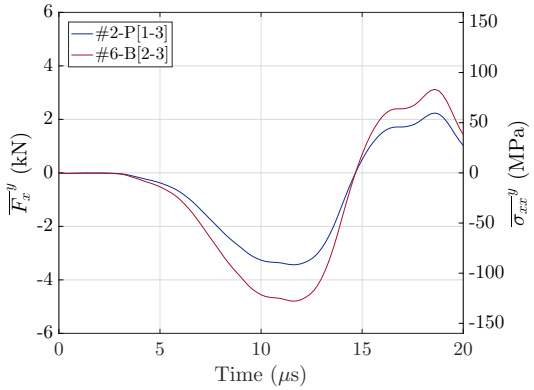

Figure 4.14: Average axial force and average axial stress profiles for specimens #2-P[1-3] and #6-B[2-3]

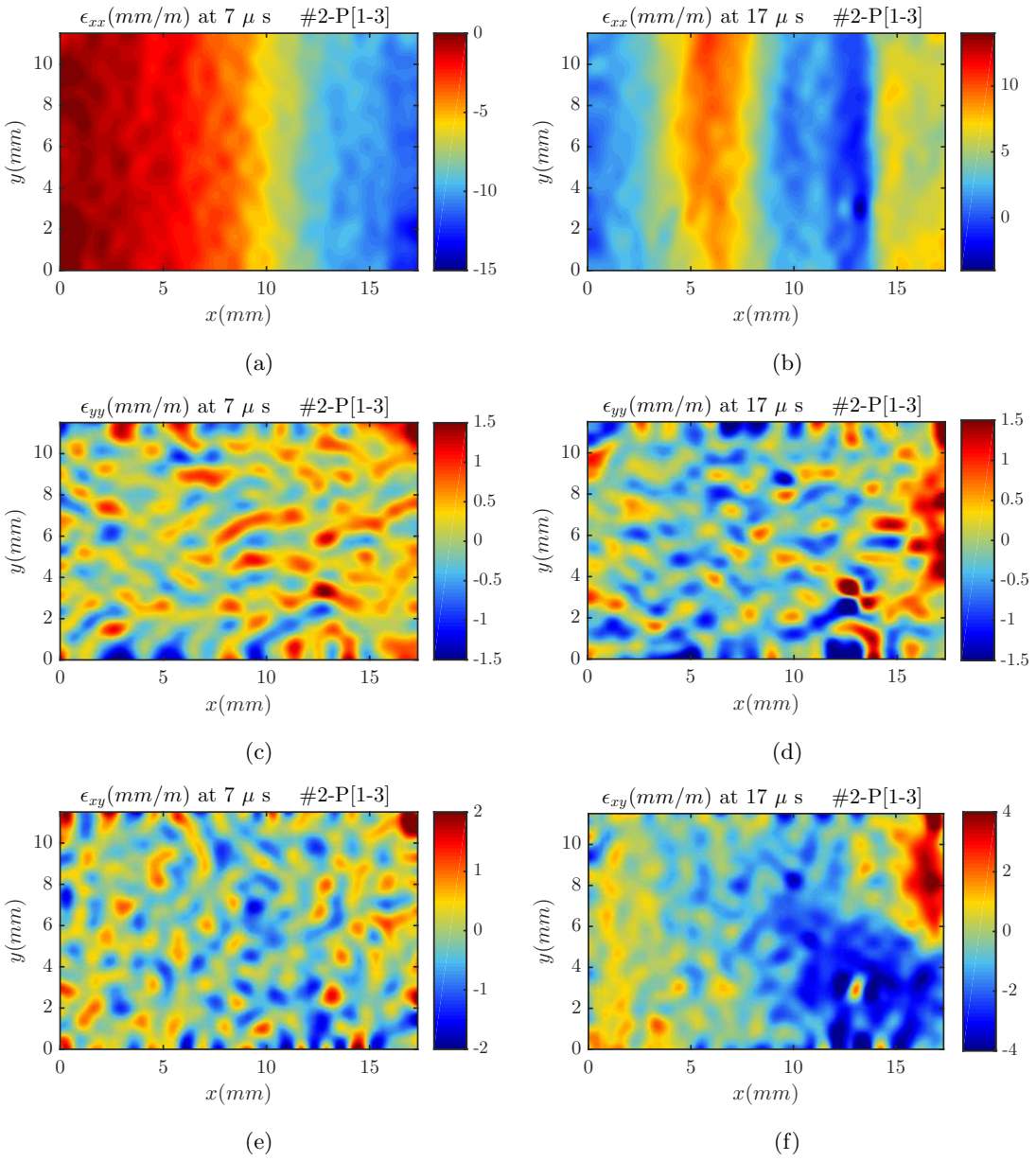

Figure 4.15: Experimental strain fields; (a),(b) ϵ_{xx} (mm·m^{-1}); (c),(d) ϵ_{yy} (mm·m^{-1}), and (e),(f) ϵ_{xy} (mm·m^{-1}) for specimen #2-P[1-3] at 7 μs and 17 μs

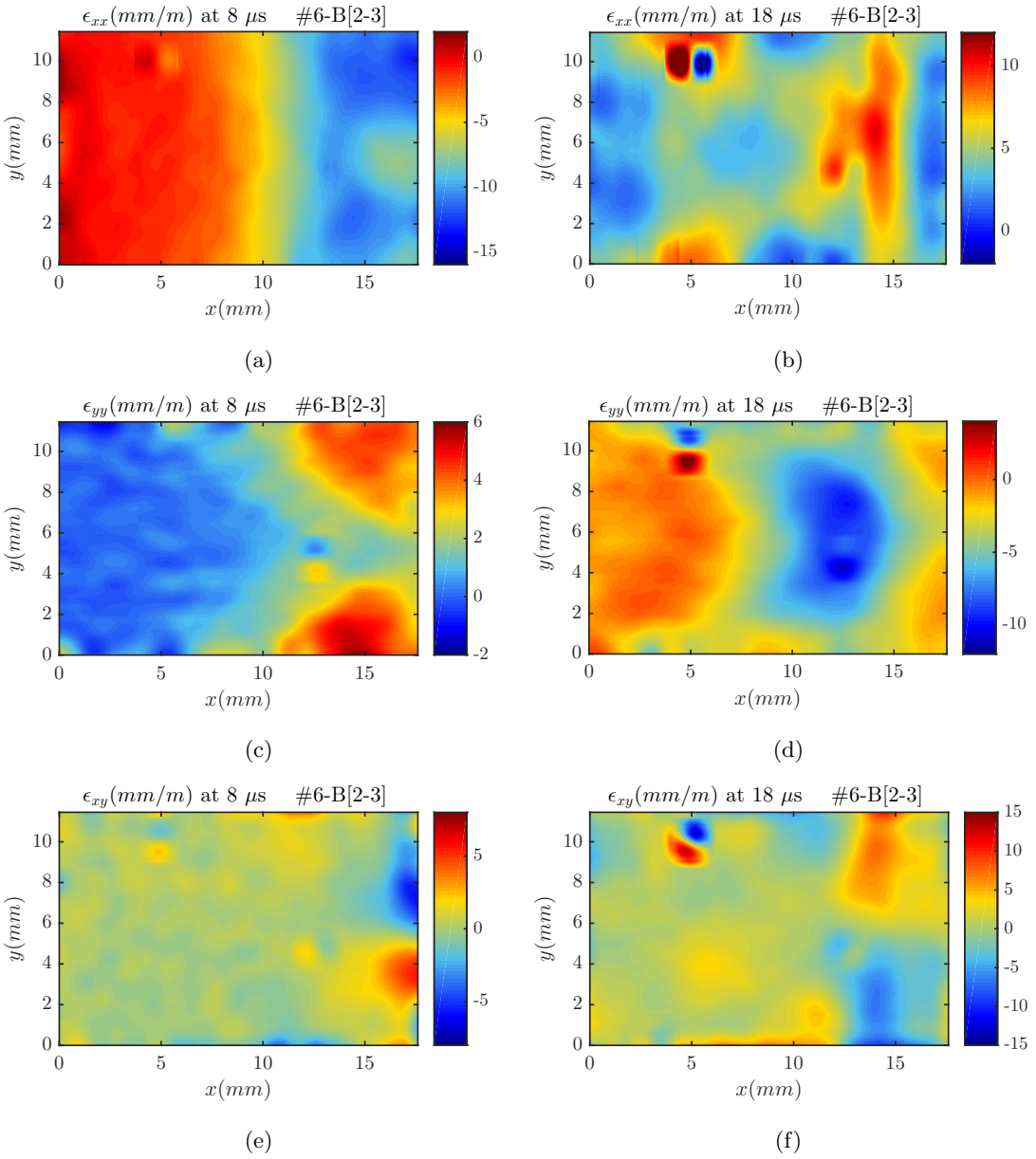

Figure 4.16: Experimental strain fields; (a),(b) ϵ_{xx} (mm·m^{-1}); (c),(d) ϵ_{yy} (mm·m^{-1}), and (e),(f) ϵ_{xy} (mm·m^{-1}) for specimen #6-B[2-3] at 8 μs and 18 μs

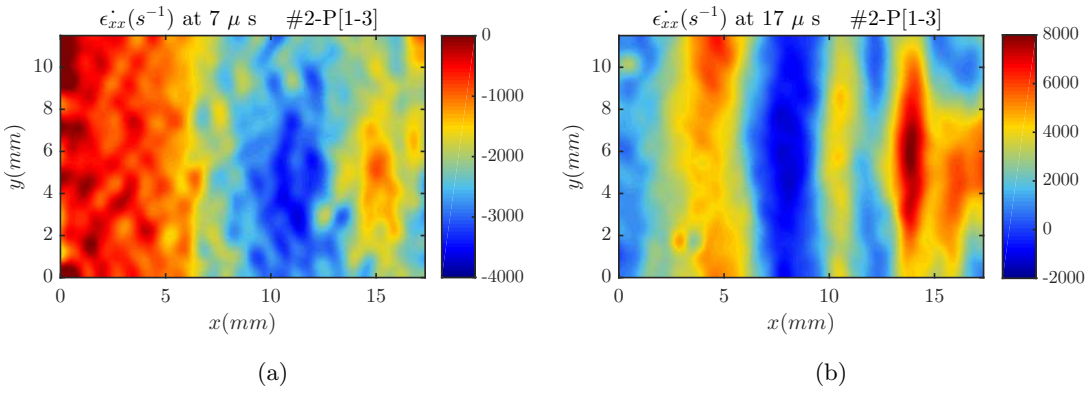

Figure 4.17: Experimental strain rate fields; (a),(b) $\dot{\epsilon_{xx}}$ (s^{-1}) for specimen #2-P[1-3] at 7 μs and 17 μs

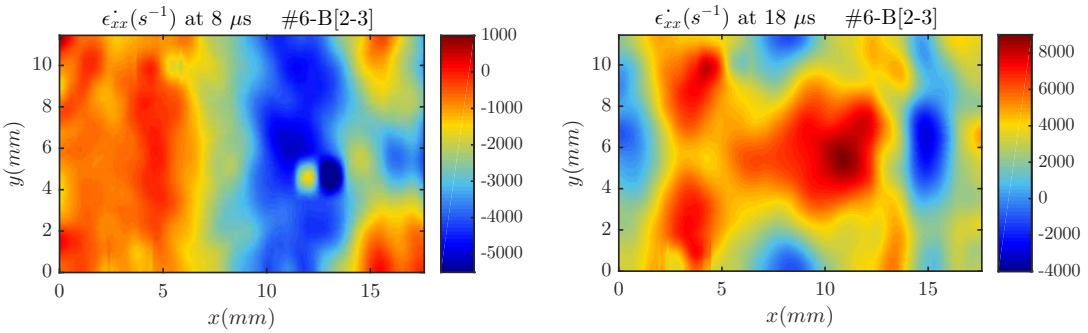

(a) (b)

Figure 4.18: Experimental strain rate fields; (a),(b) $\dot{\epsilon}_{xx}$ (s^{-1}) for specimen #6-B[2-3] at 8 μs and 18 μs

previously, despite having high signal in the ϵ_{xx} fields, the lower signal in the ϵ_{yy} and ϵ_{xy} fields will act to reduce the identification stability since these strains are used to simultaneously identify Q_{33} and Q_{23}. Strain rate maps ($\dot{\epsilon}_{xx}$) are shown in Fig. 4.17 and Fig. 4.18 for specimen #2-P[1-3] and specimen #6-B[2-3], respectively. Local $\dot{\epsilon}_{xx}$ strain rates are on the order of 4-7×10^3 s^{-1}. For specimen #6-B[2-3], $\dot{\epsilon}_{yy}$ were measured on the order of 3×10^3 s^{-1}. Strain rates in the experiments are slightly lower than that predicted from processed synthetic images based on simulated fields (peak compressive strain rates on the order of 1.4×10^4 s−1 and peak tensile strain rates on the order of 10^4 s^{-1}). As previously explained, this is expected since the simulation assumes perfect, hard contact at waveguide interfaces between the projectile and specimen. Some 'pulse-shaping' is expected in the experiments from the thin layer of tape on the front face of the waveguide for the camera trigger, and the thin layer of glue between the waveguide and specimen.

Interlaminar properties were identified from the acceleration and strain fields using the methods presented in Sec. 3.4 and Sec. 4.4.5. The identification of interlaminar stiffness parameters are presented in Sec. 4.6.2 and the identification of interlaminar tensile failure stress are presented in Sec. 4.6.3.

4.6.2 Stiffness identification

Experimental measurements of interlaminar stiffness parameters are presented separately for each of the identification techniques. The identifications using the special optimised virtual fields methods are presented first followed by the stiffness identifications with the stress-strain curve approach.

Special optimised virtual fields approach

Identifications of E_{33} with the reduced optimised virtual fields method for all specimens are shown in Fig. 4.19. Similarly, identifications of Q_{33} and Q_{23} are shown in Figs. 4.20 and 4.21, respectively. From identifications of Q_{33} and Q_{23}, ν_{23} and E_{33} can be determined (not shown). The identified value for all parameters was taken as the average over the time frames that Q_{33} was stable. Note that identifications are stopped just prior to the wave reflection from the free edge (approx. $t = 10$ μs). The identifications do not recover beyond this due to data reconstruction errors at the free edge, low strains as the wave reflects, and the formation of macro cracks shortly after. A summary of identified interlaminar stiffness parameters for 1-3

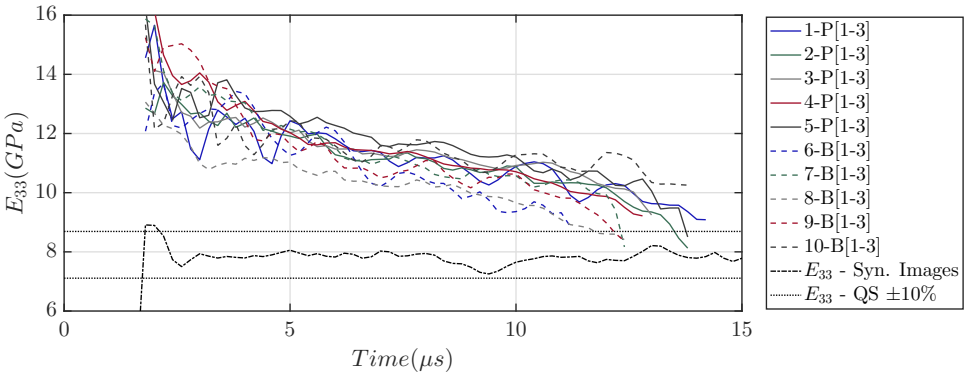

Figure 4.19: Interlaminar Young's modulus, E_{33}, identified for all 1-3 plane specimens using the reduced special optimised virtual field. Identification from image deformation simulation processed with the same smoothing parameters is provided for comparison

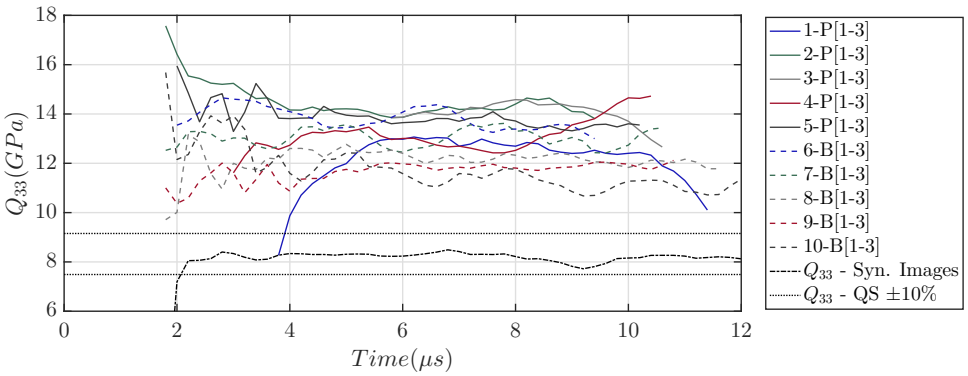

Figure 4.20: Interlaminar Q_{33} stiffness identified for all 2-3 plane specimens using the isotropic, special optimised virtual fields. Identification from image deformation simulation processed with the same smoothing parameters is provided for comparison

plane specimens and 2-3 plane specimens is provided in Tables 4.6 and 4.7, respectively. In the case of specimens #6-B[1-3], #7-B[1-3], #3-P[2-3], #5-P[2-3] and #10-B[2-3], the trigger delay was too long and a true static reference was not captured, as the wave had partially propagated into the specimen in the first image. To determine how far the pulse had propagated into the specimen when image capture began, a reference image taken before the test was correlated with the first image captured during the test. The region where ϵ_{xx} exceeded the noise floor was used to locate the pulse front. Images were then reprocessed with this region excluded (these specimens marked with a superscript 'r' in Table 4.6 and Table 4.7). Note that this does not affect interlaminar strength measurements as the test was designed so that failure occurs in the middle of the specimen, where a reference grid was maintained.

The random error associated with identifications for 2-3 plane specimens is higher compared to the 1-3 plane. A possible explanation for this is the inclusion of a_y, ϵ_{yy} and ϵ_{xy} fields in the identification procedure, which have a lower-to-noise ratio. The optimised virtual fields method is formulated such that each set of virtual fields results in the direct identification of each stiffness parameter. Since these parameters are identified simultaneously, the identification of a weakly activated material parameter will influence the identification of the other parameters.

The minimisation based on strain noise also makes the identifications sensitive to defects, which have a high signal-to-noise ratio, particularly in the case where the activated strain fields have low signal-to noise-ratio. This is particularly problematic when defects occur around the edges of the specimen and interact with the edge extrapolation procedures. This will inevitably

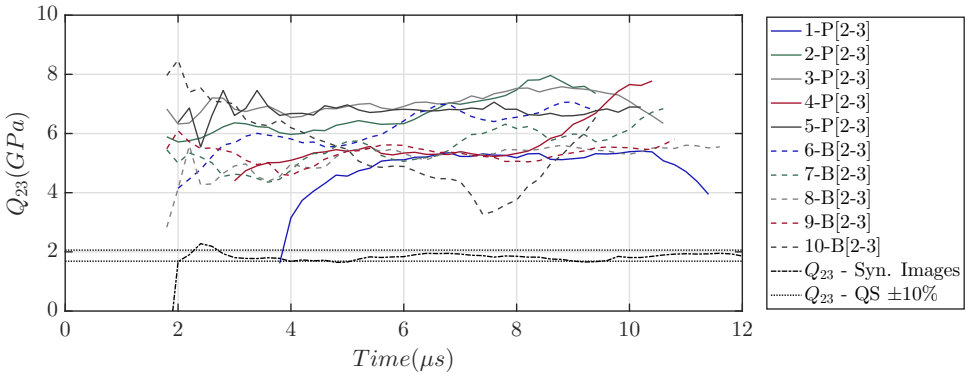

Figure 4.21: Interlaminar Q_{23} stiffness identified for all 2-3 plane specimens using the isotropic, special optimised virtual fields. Identification from image deformation simulation processed with the same smoothing parameters is provided for comparison

Table 4.6: Measured high-strain-rate interlaminar elastic modulus for AS4-145/MTM45-1 (1-3 plane specimens)

Specimen	**1-3 Plane** E_{33} (SS) [GPa]	E_{33} (VFM) [GPa]
1-P	10.3	11.0
2-P	10.3	10.8
3-P	10.5	11.7
4-P	10.5	11.0
5-P	10.8	11.1
6-B^r	10.3	10.3
7-B^r	10.3	10.7
8-B	9.8	10.3
9-B	9.9	10.9
10-B	10.9	11.3
Mean	10.4	10.9
SD	0.34	0.35
COV (%)	3.3	3.5
Diff. to Q-S (%)	+31	+38

VFM: Special optimised virtual fields approach
SS: Stress-strain curve approach
^{r}: Identification performed over reduced field of view

influence the identification routines and may account for the higher inter-specimen scatter in identified values for 2-3 plane specimens. To some extent, grid defects and their interaction with low signal to noise ϵ_{yy} strains will also influence the identification of Q_{33} using stress-strain curves (presented in the next Section). However, this is thought to be minimal since strains generated from the Poisson effect are small compared to the axial strains. The interaction of the virtual fields with defects may also explain the low-frequency oscillations in the identification of E_{33} from some 1-3 plane specimens (*e.g.:* #1-P[1-3]), however further investigation is required to confirm this.

The average value for E_{33}[1-3] was 10.9 GPa with a coefficient of variation (COV) of 3.5 %. This level of scatter is quite low and comparable to that for quasi-static testing of this material (COV = 3.6 %) [132]. E_{33} [2-3] is identified from Q_{33} and ν_{23} with an average value of 10.4 GPa, and a COV of 6.1%. The slightly higher scatter in E_{33} [2-3] is likely caused by the inclusion of fields with low signal-to-noise ratios into the identification routine as described previously. Therefore, the stiffness measured on the 1-3 plane specimens is thought to be more reliable. The measured interlaminar modulus of 10.9 GPa represents an increase of 38% compared to quasi-static values [132].

Table 4.7: Measured high-strain-rate interlaminar stiffness for AS4-145/MTM45-1 (2-3 plane specimens)

Specimen	**2-3 Plane**				
	Q_{33} (SS) [GPa]	Q_{33} (VFM) [GPa]	ν_{23} (VFM)	E_{33} (SS) [GPa]	E_{33} (VFM) [GPa]
1-P	12.6	12.5	0.41	10.4	10.5
2-P^r	14.1	14.1	0.45	11.3	11.3
3-P^r	13.1	13.9	0.50	9.9	10.4
4-P	13.1	13.1	0.43	10.7	10.7
5-5^r	13.7	13.7	0.49	10.4	10.4
6-B	12.1	13.9	0.44	9.8	11.2
7-B	13.0	13.1	0.43	10.7	10.7
8-B	11.7	12.2	0.44	9.4	9.9
9-B	13.3	11.9	0.46	10.5	9.4
10-B^r	11.8	12.15	0.44	9.4	9.5
Mean	12.8	13.0	0.45	10.2	10.4
SD	0.83	0.87	0.03	0.61	0.64
COV (%)	6.5	6.7	6.4	6.0	6.1
Diff. to Q-S (%)	–	–	–	+30	+32

VFM: Special optimised virtual fields approach
SS: Stress-strain curve approach
^{r}: Identification performed over reduced field of view

Table 4.8: Peak compressive width-average strain rate ($\overline{\dot{\epsilon}_{xx}}^y$)

Specimen	**1-3 Plane** $\overline{\dot{\epsilon}_{xx}}^y[s^{-1}]$ ($\times 10^3$)	**2-3 Plane** $\overline{\dot{\epsilon}_{xx}}^y[s^{-1}]$ ($\times 10^3$)
1-P	-3.0	-2.2
2-P	-3.1	-4.4
3-P	-3.7	-3.8
4-P	-3.2	-2.8
5-P	-3.7	-1.7
6-B	-4.8	-4.5
7-B	-3.9	-5.1
8-B	-3.3	-2.9
9-B	-3.3	-5.4
10-B	-2.0	-3.0

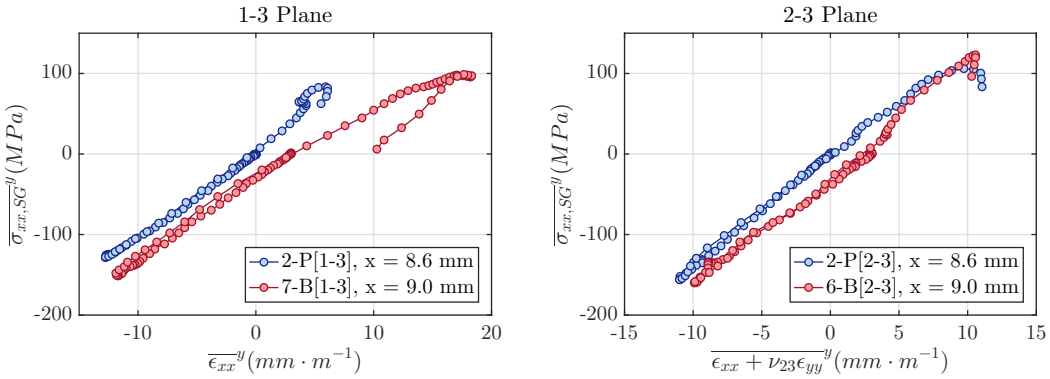

Figure 4.22: Stress-strain curves generated near the middle of the sample using the stress-gauge equation for: a) specimens #2-P[1-3] and #7-B[1-3] and (b) specimens #2-P[2-3] and #6-B[2-3]. Note that all stress-strain curves begin near the origin but have been offset by 3 mm·m^{-1} for clarity

Overall, the measurements are quite promising considering this is the first implementation of the IBII test to obtain interlaminar properties at such high strain rates. Regarding strain rate, it is difficult to assign a single strain rate value to the measurements due to the heterogeneity of the fields. However, when axial strain is high, so too is strain rate (see Figs. 4.15, 4.16, 4.17 and 4.18). Therefore, the peak, width-average strain rate ($\overline{\dot{\epsilon}_{xx}}^{y}$) achieved during the compressive loading sequence can be considered as the limiting case for an 'effective' strain rate for these measurements (Table 4.8). It is part of future work to derive an effective strain rate using the virtual fields and the virtual strain rate fields to be able to quote a well-defined value. However, the strain rate sensitivity of this material is low enough so that this is not a critical issue and a mean or peak value is a good estimate. For most specimens, the peak compressive strain rate is on the order of $3.5{\times}10^{3}$ s^{-1}. Obtaining stiffness measurements at such strain rates with the SHPB test is challenging and generally unreliable. Identifications using reconstructed stress-strain curves are presented next.

Stress-strain curve approach

The stress-gauge equation is used to reconstruct $\overline{\sigma_{xx}}^{y}$ at each cross-section. This can be drawn as a function of $\overline{\epsilon_{xx}}^{y}$ (1-3 plane) or $\overline{\epsilon_{xx}+\nu_{23}\epsilon_{yy}}^{y}$ (2-3 plane) to generate stress-strain curves at each cross-section. Examples of stress-strain curves generated at a cross-section near the middle of the sample are shown for specimens #2-P[1-3], #7-B[1-3], #2-P[2-3], and #6-B[2-3] in Fig. 4.22. The linearity of the stress-strain responses is quite remarkable considering the high strain rates at which these measurements are made. A linear regression fitting to the compressive loading region of the curve was used to identify the interlaminar stiffness at each cross-section.

The spatial identification of E_{33} is presented for all 1-3 plane specimens in Fig. 4.23, and for all 2-3 plane specimens in Fig. 4.24. Note that in the case of 2-3 plane specimens, the identified value of ν_{23} from the special optimised virtual fields procedure is used for determining Q_{33}. Note that one pitch, plus one smoothing kernel is excluded from the free edge and impact edge. The identification is unreliable in these regions due to smoothing edge effects and low spatial averaging near the free edge.

In general, the identifications from reconstructed stress-strain curves are quite consistent and stable over the middle portion of the specimen. A slightly lower stiffness is measured near the

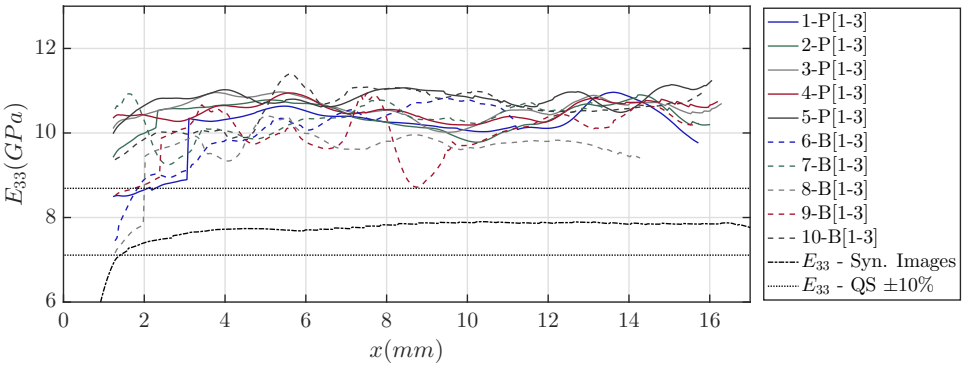

Figure 4.23: Interlaminar Young's modulus, E_{33}, for all 1-3 plane specimens identified from stress-strain curves reconstructed with the stress-gauge equation and average axial strain up to maximum compressive load. Identification from image deformation simulation processed with the same smoothing parameters is provided for comparison. Note that the extrapolated data at the edges of the specimen has been removed

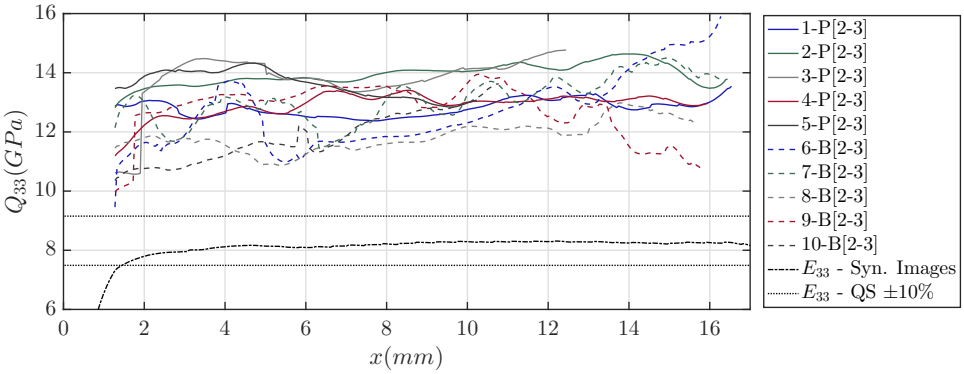

Figure 4.24: Interlaminar stiffness, Q_{33}, for all 2-3 plane specimens identified from stress-strain curves reconstructed with the stress-gauge equation and average axial strain up to maximum compressive load. Identification from image deformation simulation processed with the same smoothing parameters is provided for comparison. Note that the extrapolated data at the edges of the specimen has been removed

free edge on some samples with bonded 0.3 mm grids, particularly specimens #6-B[1-3], #8-B[1-3], and #9-B[1-3]. Since this is not observed on specimens with printed, 0.337 mm grids, this is thought to be a result of a slight rotation of the grid with respect to the specimen. This could also be a result of some missing data at the edge from trimming the overflow epoxy during the grid de-bonding process. Both have the effect of increasing the amount of missing data at the free edge, and thus the error on reconstructed stress. This highlights another key advantage of using printed grids, as alignment is easily and consistently controlled, and no additional steps are required to clean up the edges of the specimen following grid application. The identification of E_{33} [1-3] and E_{33} [2-3] was measured to have an average value of 10.4 GPa, and 10.2 GPa, respectively. The coefficient of variation for both types of specimens is low ranging between 3% and 6%. Between 1-3 and 2-3 plane specimens, this represents a 30% increase in stiffness compared to quasi-static transverse stiffness measurements ($E_{33} = 7.9$ GPa) [132].

Figure 4.23 and Fig. 4.24 show that the identifications of E_{33} and Q_{33} fluctuate periodically along the length of the specimen by approximately 0.5 GPa from the mean. This pattern was also observed in the identifications from synthetic images, although with a lower magnitude (0.2 GPa). Image deformation simulations suggest that this oscillation is primarily attributed to fluctuating error on reconstructed acceleration and strain as the pulse moves through the extrapolation region at the free edge (one pitch). Extrapolation errors are highest as the high signal information within the pulse travels through the extrapolated region. It is thought that the experimental images are more sensitive to this since the pulse is smoother compared to the simulated pulse (*i.e.:* extrapolation errors affect high signal information for a longer period of time). The effect is more pronounced on the 0.337 mm grids due to lower measurement resolution and a larger extrapolation region at the free edge.

To the authors' knowledge, no interlaminar HSR data are available for AS4-145/ MTM45-1. Furthermore, existing studies are limited to reporting an 'apparent' modulus, and scatter is so large that strain rate effects cannot be reliably extracted [13]. Therefore, it is difficult to make direct comparisons with other studies. This preliminary study shows that a consistent measurement of E_{33} can be obtained by processing measured strain and acceleration fields in two different ways. Both approaches are suitable for identifying a global stiffness value in this study since material properties do not vary in space or time. Therefore, a comparison of the two methods provides a kind of validation of the measured values. The use of image deformation also shows that both routines can identify the reference E_{33} within 1% when smoothing parameters are chosen appropriately. However, when material properties vary in space and time preference might be given to a single identification method depending on the information desired. For example, the stress-strain curve method might be preferred in cases where a spatial variation in stiffness is of interest, since it provides a stiffness measurement for each transverse slice along the length of the specimen. Alternatively, the special optimised virtual fields might be more useful if one was interested in resolving time-dependent behaviours, as it gives a single stiffness value for each point in time. This level of information and versatility is not available with existing test methods and highlights the potential of image-based test methods for HSR testing.

4.6.3 Failure stress identification

The linear stress-gauge equation (Eq. (3.25)) is used to estimate the tensile failure stress of the material, as described in Sec. 3.4.1. A comparison of the stress fields reconstructed using the identified constitutive model and the linear stress-gauge equation are shown at a frame before fracture ($t = 15.0$ μs) in Fig. 4.25a and 4.25b, respectively. The agreement is excellent apart

Table 4.9: Measured high-strain-rate interlaminar tensile strength for AS4-145/ MTM45-1 and peak tensile strain rate ($\overline{\dot{\epsilon}_{xx}}^{VG}$) within virtual gauge at fracture location

Specimen	**1-3 Plane** $\overline{\sigma_{xx}}^{VG}$ (SG) [MPa]	$\overline{\sigma_{xx}}^{VG}$ (LSG) [MPa]	$\overline{\dot{\epsilon}_{xx}}^{VG}$ [s^{-1}] ($\times 10^3$)	**2-3 Plane** $\overline{\sigma_{xx}}^{VG}$ (SG) [MPa]	$\overline{\sigma_{xx}}^{VG}$ (LSG) [MPa]	$\overline{\dot{\epsilon}_{xx}}^{VG}$ [s^{-1}] ($\times 10^3$)
1-P	94.3	95.0	3.1	72.6^x	83.9^x	4.3^+
2-P	83.2	95.7	4.6	107.2	109.7	4.6
3-P	90.3	94.9	5.3	112.0	115.6	4.1
4-P	86.1	121.3	3.5	74.5	81.5	6.3
5-P	107.7	135.6	4.9	54.4^x	71.5^x	6.8^+
6-B	130.5	157.6	5.3	116.4	122.9	3.9
7-B	91.1	106.6	6.2	136.9	143.5	4.9
8-B	92.1^x	98.8^x	6.0^+	77.4	79.9	4.7
9-B	82.4^x	83.7^x	6.0^+	126.7	130.8	5.8
10-B	44.6^x	50.7^x	4.0^+	88.1^x	134.1^x	5.3^+
Mean	97.6	115.2	4.7	107.3	112.0	4.9
SD	16.5	24.2	1.1	23.6	24.0	0.9
COV (%)	16.9	21.0	22.8	22.0	21.4	17.6
Diff. to Q-S (%)	+96	+135	–	+113	+122	–

SG: stress-gauge approach
LSG: linear stress-gauge approach
^{x}: Not included in average strength calculation
$^+$: Peak value over test

from the region close to the impact, demonstrating that for such a test, the linear representation in Eq. 6 provides a reasonable actual approximation of the stress field. Fracture initiation is identified using the raw, un-smoothed maps of ϵ_{xx}. A crack becomes clearly visible in the ϵ_{xx} field as a concentrated region of high (artificial) strain, as shown in Fig. 4.25c. The temporal variations of local stress, computed with the linear stress-gauge equation, was extracted from a 2 pitch x 4 pitch ($2p$ x $4p$) virtual gauge region centred on the identified crack initiation site (as shown in Fig. 4.25c). The corresponding stress maps, and stress-strain curve over the virtual gauge region are shown in sub figures (d), (e) and (f). While not clearly shown in the strain map in Fig. 4.25c a second crack had started to form at $x = 9.5$ mm, but did not crack the paint. The crack clearly appears three frames later. At the fracture frame shown, the acceleration fields are strongly influenced by these two cracks, explaining the discrepancy between the stress field in Fig. 4.25d and the reconstructed field using the linear stress-gauge shown in Fig. 4.25e.

The interlaminar tensile failure stress is taken as the maximum stress over time within the gauge region. A summary of measured tensile strength using the stress-gauge and linear stress-gauge is provided in Table 4.9. The tensile average strain rates from within the virtual gauge region ($\overline{\dot{\epsilon}_{xx}}^{VG}$) just prior to failure are also provided in Table 4.9. Some specimens fractured but the initiation of a crack was not clearly identifiable within the kinematic maps. This suggests that either a crack initiated on the back face, or the specimen fractured from impact with the back of the test chamber. For these cases, the peak stress average is reported in Table 4.9 for comparison, but is excluded from the calculation of strength statistics (identified by a superscript 'x' in Table 4.9). Note that strain rate maps were computed using a backward differentiation scheme to avoid temporal leakage from non-physical forward strains caused by the crack. Strain rate at fracture was estimated by extrapolating from a regression fitting to $\overline{\dot{\epsilon}_{xx}}^{VG}$ over five frames prior to fracture. For specimens where a macro crack was not visible, the peak value of $\overline{\dot{\epsilon}_{xx}}^{VG}$ is listed (identified by a superscript '+' in Table 4.9).

The results in Table 4.9 suggest that strain rate has a significant influence on the interlaminar tensile failure stress. The interlaminar failure stress with the linear stress-gauge equation was

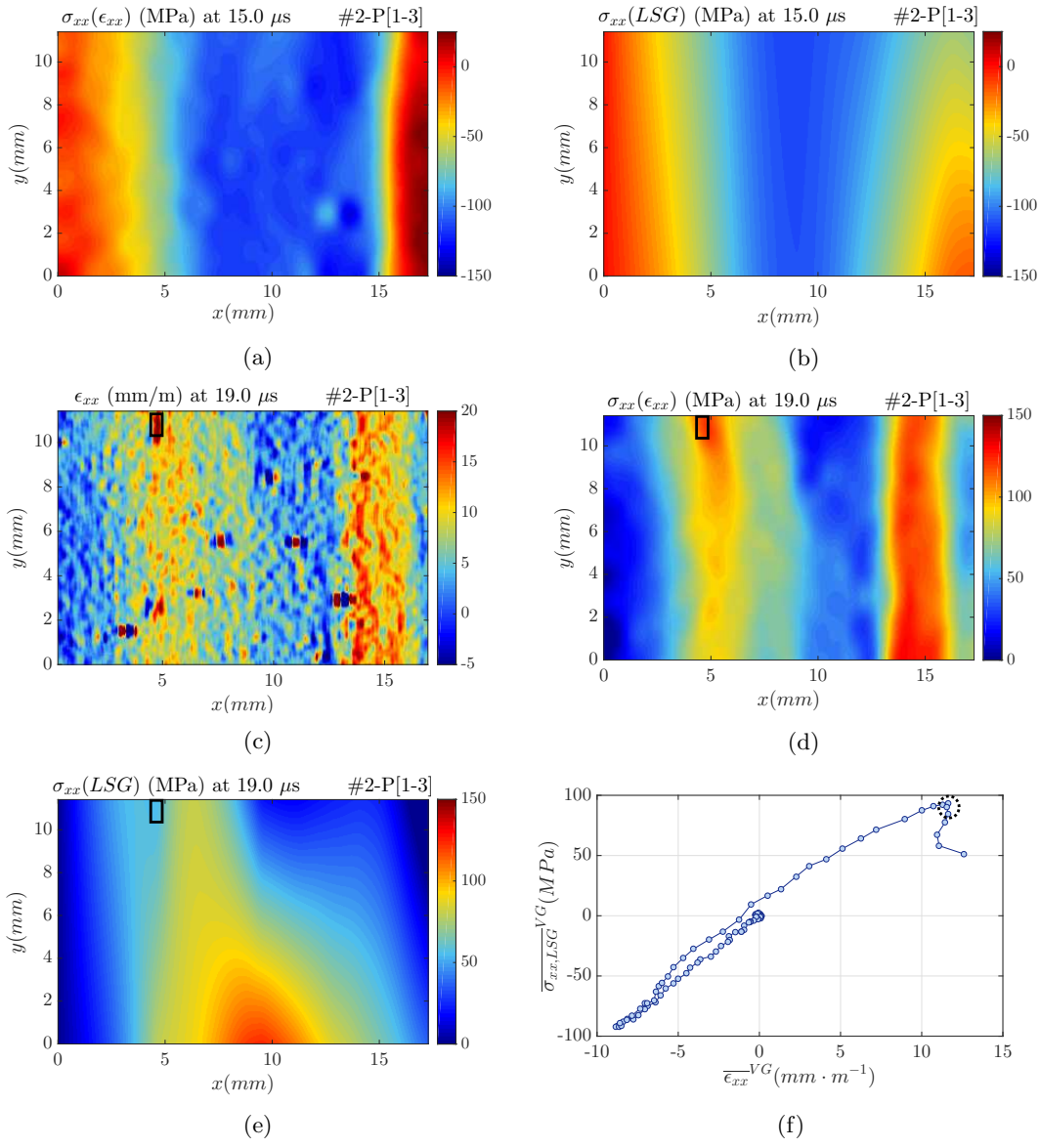

Figure 4.25: Failure stress identification diagnostics for specimen #2-P[1-3]. Diagnostic figures before fracture ($t = 15.0$ μs): (a) stress field (MPa) constructed from ϵ_{xx} using identified E_{33} ($\sigma_{xx}(\epsilon_{xx})$), and (b) stress field (MPa) constructed using the linear stress-gauge equation ($\sigma_{xx}(LSG)$). Diagnostic figures for a time just after the identified fracture time ($t = 19.0$ μs): (c) raw, un-smoothed ϵ_{xx} strain field (mm·m^{-1}), (d) $\sigma_{xx}(\epsilon_{xx})$ (MPa), (e) $\sigma_{xx}(LSG)$ (MPa), and (f) stress-strain curve generated using average $\sigma_{xx}(LSG)$ and ϵ_{xx} within the virtual gauge region. In (c), (d) and (e) the virtual gauge is shown as the black rectangle. In (f) the dashed circle indicates the point of fracture and extracted failure stress estimate using the linear stress-gauge equation

measured to be 115 MPa (COV = 21%) for the [1-3] specimens and 112 MPa (COV = 21%) for the [2-3] specimens. Combining the two interlaminar planes results in an average strength of 114 MPa, with a COV = 20 %. This represents an increase in failure stress of 125% compared to the quasi-static value of 50.4 MPa (COV = 13%) in [132]. Since the strain rate is generally high when the strain is high, the peak width-averaged strain rate at the plane of fracture offers an 'effective' strain rate for the measurements. This is generally on the order of $5{\times}10^3$ s^{-1}. It is worth noting that comparisons to quasi-static values need to be interpreted with some caution because quasi-static interlaminar tensile tests are quite sensitive to experimental factors such as misalignment, gripping and volume effect. Typical scatter in the literature for quasi-static strength measurements ranges from 10% to 50% [11, 48, 51, 75]. Therefore, the reported coefficient of variation for quasi-static interlaminar strength of this material is comparatively low. The level of scatter in the current measurements at high strain rates is promising, with scatter comparable to well controlled quasi-static tests.

The time histories of stress averages at the fracture location are shown in Fig. 4.26 for four specimens (2 from each interlaminar plane). Also shown for comparison is the average stress in the gauge region as reconstructed using the stress-gauge equation (Eq. (3.16)) and the constitutive model. In the latter, the interlaminar stiffness is taken as the average values identified from stress-strain curves and the special optimised virtual fields routine. However, this strain-based stress is not used as a measure of failure stress due to the uncertainty in determining when strains become non-physical and contamination from grid defects as explained later. Figure 4.26 shows the initial compressive loading, where all three stress measures agree well. Two of the presented specimens (Fig. 4.26a and 4.26b) show good agreement during the unloading, until a marked drop in average stress (stress-gauge and linear stress-gauge equations) is observed between t = 15.5 - 19 μs. Specimen #2-P[1-3] shows a small offset and low-amplitude oscillation in stress averages at the start of the unloading phase. It is suspected that some through-thickness wave dispersion may have occurred as the wave reflects due to a non-square free edge cut. This effect is observed over a very short duration, and is unlikely to influence strength measurements.

In some cases an offset in stress arises between the stress reconstructed from acceleration and stress computed using the constitutive model (#3-P[1-3]; 2-P[2-3], 3-P[2-3], #6-B[2-3], 7-B[2-3], 8-B[2-3] and 9-B[2-3]), as exemplified in Fig. 4.26c and 4.26d. This is a result of fracture occurring near a grid defect (within one smoothing kernel). Artificial strains caused by the defect biases the strain at the fracture location. The offset increases during the unloading phase when the wave reflects from the free edge. This suggests that the quality of grid defect corrections diminish as the test progresses and the kinematic fields become more complex. This is more problematic for specimens with bonded grids, which suffer from high numbers of defects caused by missing grid or bubbles in the resin layer as discussed in Section 4.4.2. The number of defects are significantly reduced when grids are printed, making it the preferred grid deposition technique. This also supports the use of the stress-gauge equations for estimating tensile failure stress. The stress-gauge equations provide a much more robust estimate of failure stress since acceleration fields are not smoothed spatially, and because of the spatial averaging procedure used to reconstruct stress.

As previously mentioned, no HSR studies have been reported on AS4-145/ MTM45-1, thus, no direct comparisons can be made. However, indirect comparisons can be made with studies on the HSR through-thickness properties of other composite systems. Comparison of the current measurements to those in other studies shows the robustness of the IBII test for measuring interlaminar strength. For example, a similar strain rate sensitivity was measured by Nakai &

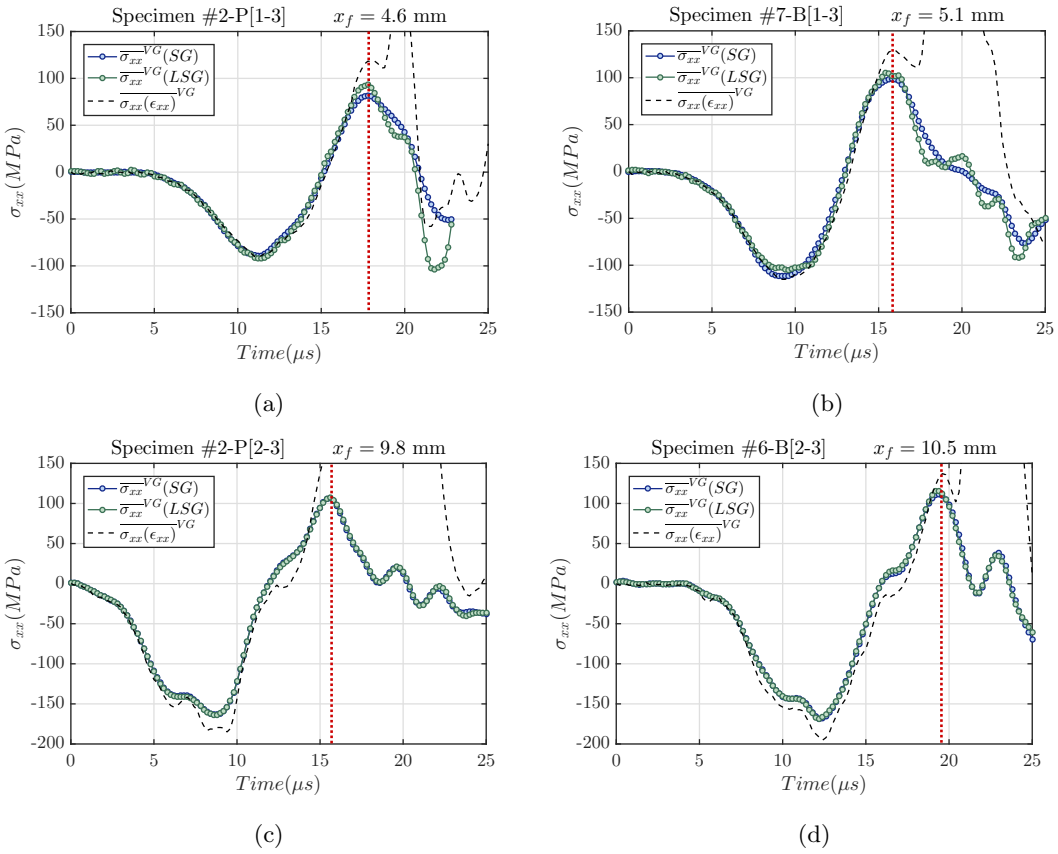

Figure 4.26: Comparison of the temporal variations in average stress within the virtual gauge area at the location of fracture as reconstructed using the stress-gauge equation ($\overline{\sigma_{xx}}^{VG}$(SG)), linear stress-gauge ($\overline{\sigma_{xx}}^{VG}$(LSG)) and strain ($\overline{\sigma_{xx}(\epsilon)}^{VG}$) for (a) specimen #2-P[1-3], (b) specimen #7-B[1-3], (c) specimen #2-P[2-3], and (d) specimen #6-B[2-3]. Note that the location of failure is included in the header of each sub figure and the red dashed line indicates the time at which a macro-crack is clearly visible in the un-smoothed strain maps

Yokoyama (+77%) [11, 48]. However, the scatter on measured failure stress was significantly higher (39% COV), and measurements were made at much lower strain rates (50 s^{-1}). This amount of scatter is typical of most studies reporting HSR tensile failure stress measurements using a SHPB [47, 73, 74]. Govender *et al.* [66] used pulse time-shifting to avoid the assumption of quasi-static equilibrium, and produced strength measurements of similar consistency to the current study. However, their approach relied on predicted stresses based on 1-D wave theory and no quasi-static values were provided to quantify the strain rate sensitivity. By using UHS imaging and full-field measurements, many of the assumptions tied to existing techniques are removed. The measurements reported here exemplify the potential for such techniques to be applied to obtain remarkably consistent failure stress measurements.

4.7 Summary

This chapter presented the design and experimental validation of the IBII test to measure interlaminar tensile properties at high strain rates. By combining ultra-high-speed imaging with the grid method, full-field maps of displacement, strain and acceleration were obtained. The virtual fields method was used to identify interlaminar stiffness and tensile failure stress from the measured kinematic fields. The key results from this chapter are summarised as follows:

- Despite limited spatial resolution, the results presented here demonstrate that measurement quality of current UHS cameras is sufficient to identify interlaminar stiffness and tensile failure stress from the same test.
- Stiffness and failure stress were found to exhibit a substantial sensitivity to strain rate. An average interlaminar elastic modulus of 10.3 GPa was identified across all 1-3 plane specimens using reconstructed stress-strain curves. For the same specimens, the reduced special optimised virtual fields approach identified an average modulus of 10.7 GPa. Stiffness measurements were made at peak average strain rates on the order $3.5{\times}10^3$ s^{-1}. This represents an increase between 30-35% compared to quasi-static values.
- Tensile failure stress was found to have a higher strain rate sensitivity than stiffness. The average tensile failure stress over all specimens was measured to be 114 MPa at peak average strain rates on the order $4.5{\times}10^3$ s^{-1}. This corresponds to an increase of approximately 125%, compared to quasi-static values.
- Image deformation simulations are a powerful diagnostic tool for characterising the errors arising from measurement resolution and noise. This enables one to robustly select optimal smoothing parameters. It is also a useful diagnostic tool for studying the effect of post-processing operations (*e.g.*: effect of data extrapolation at the edges) and experimental factors (*e.g.*: grid size, specimen geometry, grid contrast) on the identification of stiffness parameters.
- The use of printed grids was proven to be effective for significantly reducing the number of grid defects. Therefore, this approach is recommended for interlaminar testing where higher magnification is required. However, the current technology is limited to grid periods on the order of 0.3 mm, which will not be enough either for higher spatial resolution cameras or for higher magnification (smaller specimens). Other deposition routes like the one recently proposed by Brodnik *et al.* [141] could be pursued.

As part of continued development of the IBII test methodology, it is important to understand

how well the underlying assumptions are satisfied, and identify scenarios where they may break down. A key assumption is that the test is two-dimensional so that surface measurements can be used to identify stiffness and failure stress. The relevance of this assumption is explored in the next chapter using synchronised back-to-back cameras.

Chapter 5

Effect of Out-Of-Plane Loading on Stiffness and Failure Stress Identification

5.1 Overview

This chapter describes the experimental studies conducted to evaluate the importance of the assumption that the test is two-dimensional and the bias introduced on stiffness and failure stress identifications when this assumption does not hold. Section 5.2 describes the experimental implementation of the back-to-back ultra-high-speed camera setup used to measure the dynamic kinematic fields on the front and back face of samples in the tension/compression IBII test. Section 5.3 presents the results from the back-to-back camera experiments including full-field maps, reconstructed stress-strain curves, stiffness identifications and failure stress estimates from each side of the sample, and using back-to-back averaging. The same results from a follow-up set of experiments with improved alignment are presented in Section 5.4. Finally, a summary of key findings from these experimental studies are presented in Section 5.5. Note that all data supporting this study are openly available from the University of Southampton repository at: https://doi.org/10.5258/SOTON/D1093.

5.2 Materials and Experimental Setup

The material used in this study was the same unidirectional carbon/epoxy composite (AS4-145/MTM45-1) as was used in Chapter 4 and [38]. Seven samples were cut from the 1-3 interlaminar plane with dimensions (length x height x thickness) of 18.3 mm x 11.58 mm x 2.56 mm (standard deviations: ±0.03 mm, ±0.17 mm, ±0.4 mm). Specimens were painted white and black grids, with an average pitch of 0.337 mm, were printed onto both sides of the sample according to [136]. Specimens were mounted onto the waveguides with cyanoacrylate glue using a set square for alignment during bonding. The waveguide, projectile and sabot were the same as in Chapter 4 [38].

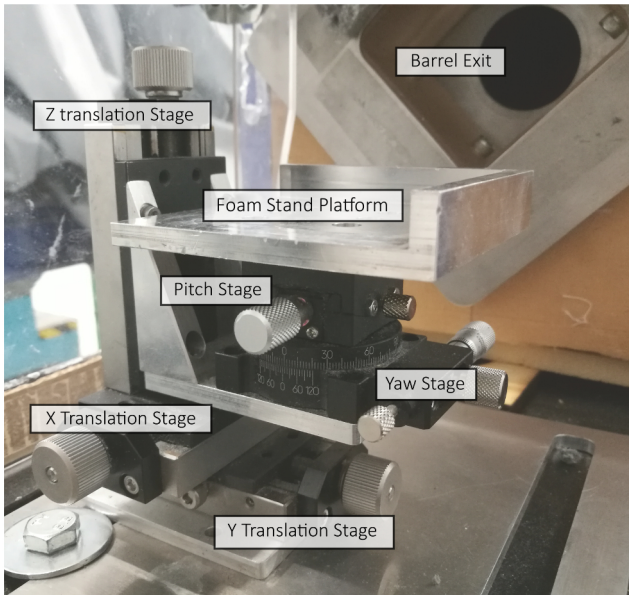

Figure 5.1: New 5-axis waveguide alignment stand (translational degrees of freedom in x, y and z, and rotational degrees of freedom in pitch and yaw)

5.2.1 Impact rig and waveguide alignment

All impact experiments were performed using the compressed air impact rig described in [37, 136]. Since the study presented in Chapter 4, a new 5-axis platform was commissioned that enables more control over the waveguide alignment. The stand consists of several mechanical stages (Fig. 5.1) to adjust the yaw, pitch and 3D translations of the platform on which the foam stand and waveguide sit.

A machined alignment rod was first used to set the approximate position of the stand. The diameter of one end of the rod was machined to fit in the bore of the barrel, and the other end was machined to the same diameter as the waveguide. The stand was adjusted such that the impact face of the waveguide was flush (within visual inspection and touch) to the end of the alignment rod once inserted in the barrel. To correct for the movement of the projectile in free flight, test shots were then performed with the Shimadzu HPV-X camera to visualise the impact between the projectile and the waveguide from the side-on perspective (x-y plane as defined in Fig. 3.2). Images just prior to impact were processed to extract the coordinates of the top and bottom of the waveguide and projectile faces. From these coordinates, it was possible to quantify the vertical and angular misalignment of the impact faces. The stage was adjusted accordingly, and test shots repeated, until the translation and angular misalignments were below 1-pixel (uncertainty of coordinate selection), which corresponds to 0.1 mm and 0.2° for position and pitch angle, respectively.

5.2.2 Synchronised ultra-high-speed imaging

Two Shimadzu ultra-high speed cameras were used to image the front face (HPV-X model) and back face (HPV-X2 model) of the sample through transparent windows in the side walls of the capture chamber. A schematic of the camera arrangement is shown in Fig. 5.2. Both cameras used a Sigma 105mm lens and illumination was provided by a pair of Bowens Gemini 1000pro flashes. To synchronise the flash lights and cameras, the trigger from the light gates was split and sent to each flash, and the copper contact trigger on the waveguide was sent directly to the Shimadzu HPV-X camera. The cameras were run in a master-slave configuration to

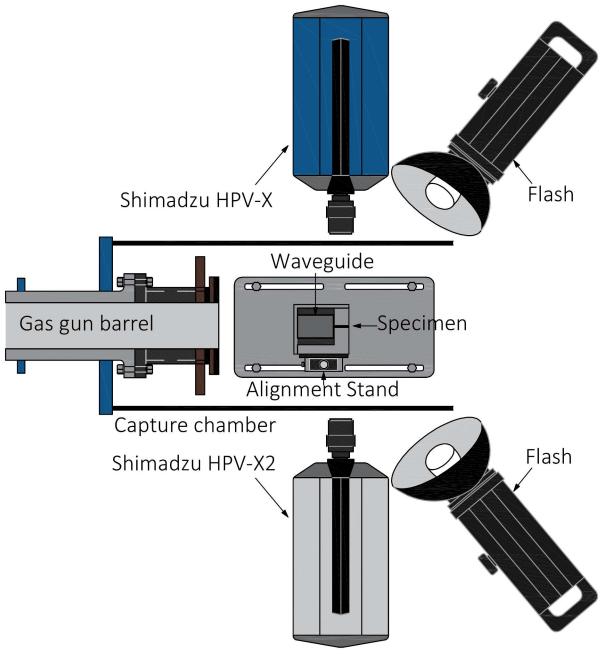

Figure 5.2: Schematic of the experimental multi-camera configuration

synchronise the internal clocks, with the HPV-X camera used to trigger the HPV-X2. The stand-off distance of each camera was adjusted iteratively using a series of static images so that the grids were sampled by exactly 7 pixels/pitch (pitch size = 0.337 mm). This resulted in a stand-off distance of approximately 310 mm. For consistent depth-of-field, both camera apertures were set to f/11 with illumination adjusted accordingly for each camera. Less light was required for the Shimadzu HPV-X2 camera, which had a higher sensor sensitivity. To minimise fill factor effects, the images were intentionally blurred as in [32, 37, 38]. The amount of blurring was checked using a 2 mm out-of-plane movement test to ensure that no parasitic fringe patterns from the fill-factor effect were visible in the static strain images.

This back-to-back camera and flash arrangement (Fig. 5.2) has the drawback that the flash from one side of the capture chamber is pointed towards the camera on the other side, leading to saturation. To control the grid lighting on each side, a disposable light shield was installed around the sample, as shown in Fig. 5.3. A slot just larger than the specimen size was cut from the edge of a thin piece of board. The screen was then slotted over the specimen and fixed to the bottom of the capture chamber.

5.2.3 Image processing

Images from both cameras were processed using the same procedure as described in the flow chart in Fig. 4.4. Spatial and temporal smoothing parameters for each camera were selected using an image deformation sweep, as performed in [38]. The reader is also referred to [39, 140] for additional details on the image deformation procedure. In this process, synthetic images were generated that were representative of those collected with each camera (see Table B.1 in the appendix for a summary of parameters used to generate the images). These images were deformed using displacement fields from a finite element model [38] and processed with a range of spatial and temporal kernel sizes to assess the effect of smoothing on the identification of stiffness. Optimal parameters were selected as those which minimised the total error between the identified stiffness from the synthetic images and the reference value in the finite element model. The Shimadzu HPV-X2 sensor had approximately twice as much grey-level noise as the

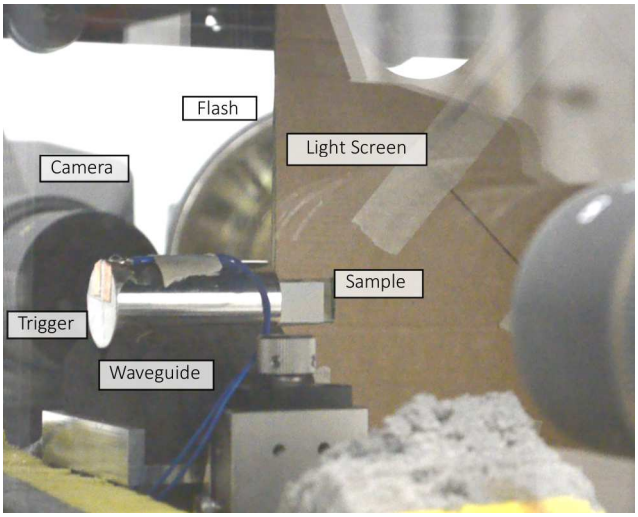

Figure 5.3: Light screen installed in the test chamber to allow for independent control of light intensity and uniformity on each side of the sample

HPV-X and therefore, optimal parameters were different for each camera. Selected smoothing parameters for processing experimental images, along with typical measurement performance for each camera are listed in Table B.2.

5.2.4 Coordinate transformation to common reference coordinates

A coordinate system transformation, outlined in the flow chart shown in Fig. 5.4, was developed to enable fields measured on the front and back faces to be directly compared. The approach was to transform the fields measured in the back face coordinate system (X^B,Y^B) to the front face coordinate system (X^F,Y^F). In each field of view the coordinates of the top corner on the free edge (x^F_{FE}, y^F_{FE} and x^B_{FE}, y^B_{FE}) was used as a common reference point. The difference between these coordinates defined the translation required ($\Delta x^B, \Delta y^B$) from the original back face coordinates to the equivalent position in the front face coordinates ($X^{B'}$,$Y^{B'}$). The displacement fields in the transformed coordinates were then interpolated to the same measurement locations on the front face over the common field of view. Acceleration and strain fields were then computed in the same way for both sides of the sample using the parameters defined in Table B.2. Note that no rotational mapping was performed as variations in grid orientation between the front and back of the sample were small (<1°).

5.3 Results

5.3.1 Full-Field Measurements

Comparing full-field maps of strain and acceleration provides a quick way to assess the uniformity of loading through-the-thickness. Tests on different samples showed varying levels of differences in the kinematic fields. Specimen #1 is presented here as a case where the response was substantially different on each face to provide a clearer understanding of the evolution of through-thickness heterogeneity. In the case of the 1-3 interlaminar plane, only the x-fields are strongly activated due to high lateral stiffness of the fibres [38]. Therefore, only the axial strain and acceleration maps are presented here. Full-field maps of a_x and ϵ_{xx} are shown at three time steps for both cameras in Fig. 5.5 and 5.6, respectively. The differences between the two

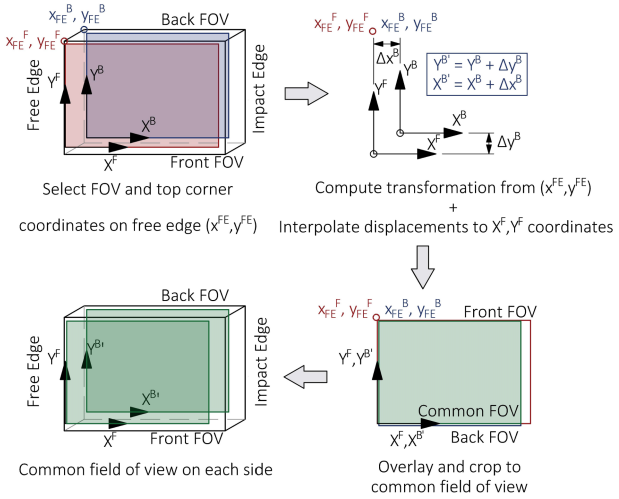

Figure 5.4: Procedure for transforming back face displacement fields to front face coordinates

sides are also included for each time step. Note that the fields have been transformed to the same coordinate system using the procedure described in Section 5.2.4.

The fields at 8 μs represent the time just before the front of input pulse reached the free edge. Up until this point, only regions near the impact edge showed measurable differences (up to 2 mm·m^{-1} in width-averaged strain). As the test progressed ($t = 13\ \mu s$) differences between the front and back response increased up to 10 mm·m^{-1} near the impact edge. At this point, subtle differences in the fields were also measured further into the sample (up to $x = 5$ mm). The through-thickness effects continue to propagate into the sample, and at 17 μs a clear 'wave-like' pattern was revealed in the difference maps for acceleration and strain (Fig.5.5-5.6).

For specimen #1 it is clear that the assumption of through-thickness uniformity is not well satisfied near the impact edge but may hold near the free edge. The effect of this varying non-uniformity along the length of the sample on the reconstruction of stress-strain curves, and identifications of stiffness and failure stress is investigated in the following sections for all tested samples.

5.3.2 Stress-strain curves and stiffness identification

Stress-strain curves were reconstructed along the length of each sample by combining the stress-gauge equation (Eq. (3.16)) with the average axial strain (ϵ_{xx}), neglecting Poisson's effects. This was performed separately for each face, and using back-to-back averaged fields as a linear approximation to the through-the-thickness distribution. Stress-strain curves from three specimens are presented at four locations in Fig. 5.7. These three samples were chosen to demonstrate the variability measured across the seven tests. Specimen #3 represents a case where comparatively minimal differences were observed between the front and back face measurements (Fig. 5.7a-5.7d). The remaining samples showed more significant differences between the front and back faces similar to specimen #1 (Fig. 5.7e-5.7h) and specimen #5 (Fig. 5.7i-5.7l).

Generally, the stress-strain curves reconstructed on each face show a reasonable agreement during the initial compressive loading, but a dramatically different unloading response. As indicated by the full-field maps (Fig. 5.5-5.6), the largest differences in loading and unloading response were measured over half of the sample closest to the impact edge ($x/L > 0.50$). In the case of specimens #1 and #5 differences are observed later in the unloading up to x/L

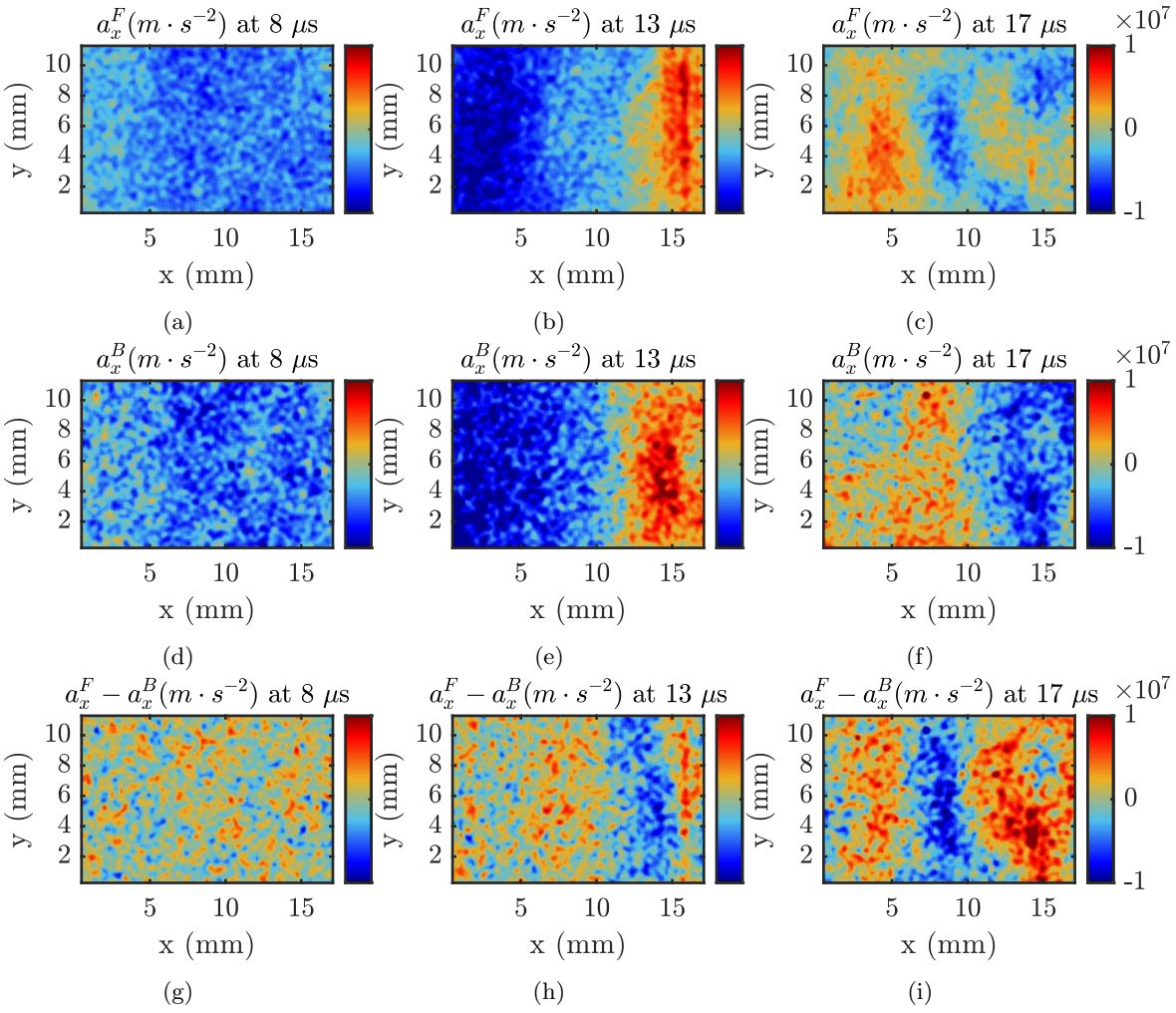

Figure 5.5: Acceleration fields (a_x, m·s^{-2}) for specimen #1 measured on the front and back faces of the sample at three time steps and the difference between the two fields at each time step

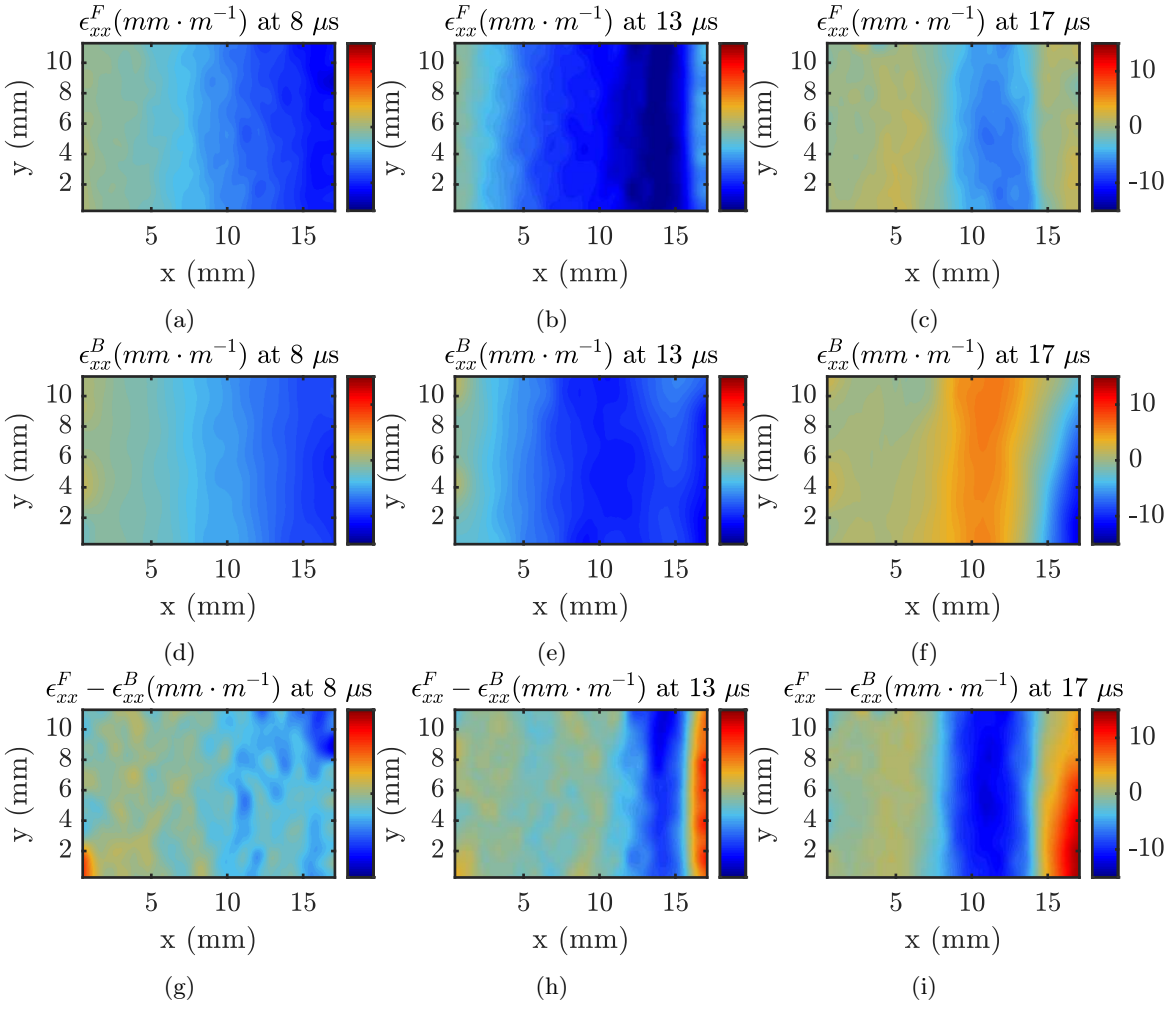

Figure 5.6: Strain fields (ϵ_{xx}, mm·m^{-1}) for specimen #1 measured on the front and back faces of the sample at three time steps and the difference between the two fields at each time step

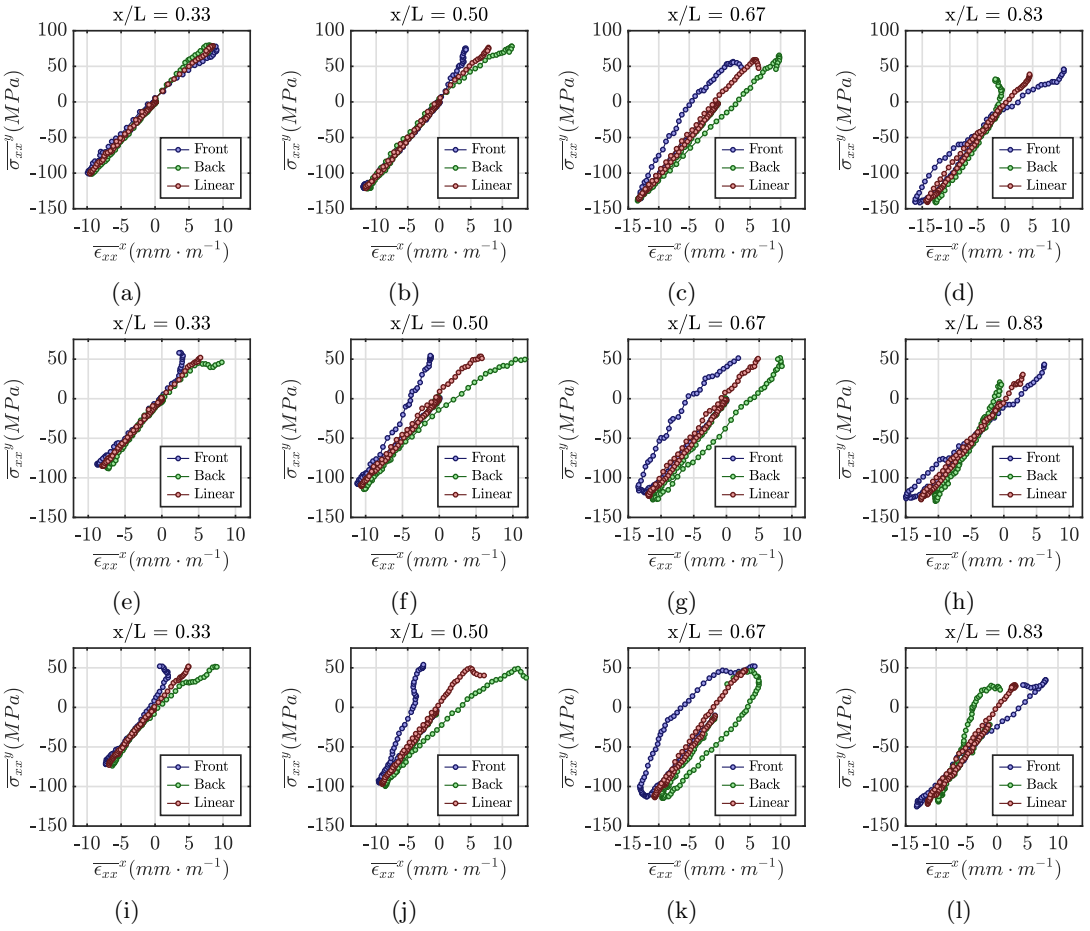

Figure 5.7: Stress-strain curves for specimen #3 ((a)-(d)), #1 ((e)-(h)) and #5 ((i)-(l)) as reconstructed with the stress-gauge equation using fields measured on the front and back faces independently, as well as assuming a linear through-thickness distribution between the two surface measurements (back-to-back averaging)

= 0.33. The variability in non-uniform through-thickness loading along the length, and in the load-unload response, will influence stiffness and failure stress identifications differently. The rest of this section focuses on the effect on stiffness, and the failure failure stress identification will be discussed in the following section.

Figure 5.8 shows the spatial variation in the interlaminar stiffness for the three representative samples. Smoothing edge effects corrupt the measurements within one spatial smoothing kernel at the impact and free edges, which are omitted in Fig. 5.8. Identified stiffness values are reported in Table 1, obtained as the average over the middle 50% of each sample. It is worth noting that the three-dimensional effects caused a parasitic, non-linear stress-strain response towards peak compressive load and therefore, stiffness was calculated using a strain threshold of 8 mm·m^{-1}, for which such effects are negligible.

The stiffness identifications from fields measured on both sides of specimen #3 closely agree (within 2%) up until $x/L = 0.5$. The identifications begin to diverge closer to the impact edge where three-dimensional effects are more significant. Specimen #1 and #5, show stronger three-dimensional effects which create an offset between the identifications from the front and back faces at all locations. The stiffness from each face differs between 10% ($x/L = 0.33$) and 20% ($x/L = 0.67$). Conversely, identifications using back-to-back averaged fields remains stable over the entire sample with an average value of 10.5 GPa.

When the accelerations and strains are averaged through-the-thickness the stress-strain response becomes linear, as reported by others in [41, 142]. Moreover, the spatial variation and intra-test scatter were reduced on the identifications from back-to-back averaged fields (coefficient of variation (COV) = 2% over all samples). Back-to-back averaging for specimen #1 and #5, where 3D effects are greater, gives a very similar identification to specimen #3, with measured values of 10.6 GPa and 10.5 GPa, respectively. This shows that the linear through-thickness approximation from back-to-back averaging is a good representation of the actual distribution. This is because averaging through-the-thickness is the same as resolving the membrane component of stress and strain, which are unbiased by the three-dimensional loading as discussed in Sec. 3.4.3. For applications where three-dimensional loading is of concern, back-to-back cameras are recommended to reduce scatter and bias of stiffness measurements, and can be used to determine the limits of stiffness variability in single-sided measurements.

In the case that only single-sided measurements are available, the consequences of three-dimensional loading on stiffness measurements are not severe when averaged over several tests. While stiffness identifications can vary significantly for an individual test, the process of averaging over the middle 50% of the sample regularises the scatter significantly. In the case of specimens #1 and #5, the averaging process reduces the local variations (of up to 20%) down to 5-9% compared to the value identified with back-to-back averages. Further regularisation occurs with averaging over multiple samples. The difference between the average for all samples on each face, and the average identified from back-to-back averages, reduces to 3% over all seven samples. However, the user must be cognisant of the fact that the measurements may have a systematic error, as these tests show a systematically higher stiffness identification from the back face (11.0 GPa) than from the front face (10.5 GPa). The scatter on the single-sided measurements was less than 5% (COV) at strain rates on the order of $3{\times}10^3$ s^{-1}, which is still exceptional given the measurement inconsistencies reported with existing test methods at similar strain rates (see summary figures in [13]).

These tests also suggest that the bias from 3D effects on single-sided measurements may be reduced further by more strategic selection of the region over the sample used for averaging. The normalised root-mean-square (RMS) variation ($v_{RMS} = \mathrm{RMS}(E_{33}(x) - \overline{E_{33}})/\overline{E_{33}}$ in Table 5.1) of

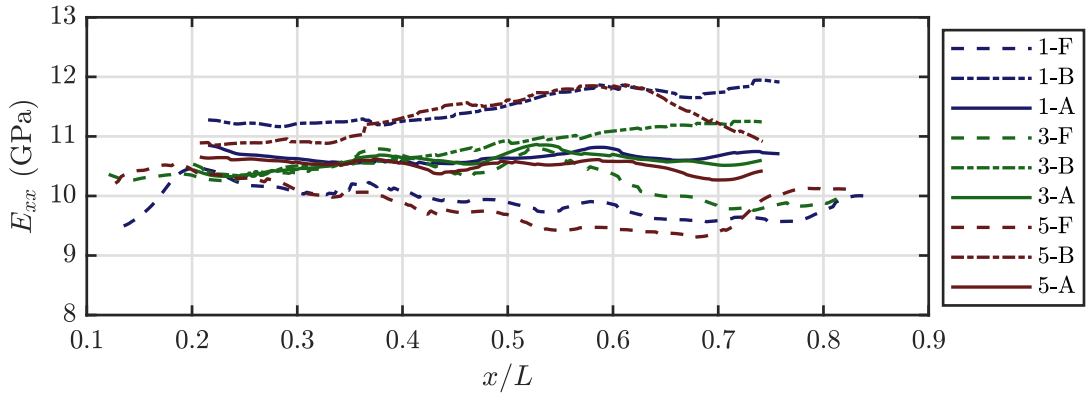

Figure 5.8: Interlaminar Young's modulus, E_{33}, identified from stress-strain curves reconstructed with the stress-gauge equation and average axial strain up to 8 mm·m^{-1} for specimens #1, 3 and 5. Note that 'F', 'B' 'A' denote the front and back faces, and back-to-back averaging, respectively

the spatial identification, relative to the average over the middle 50% of the sample, is proposed here as an indicator of when this may be required. This is included in Table 5.1 for all samples. The RMS variation of the identifications from the front and back faces where three-dimensional effects were substantial ranged between 3-7%. In comparison, the majority of identifications made from back-to-back averages had a lower RMS variation in the range of 0.7-1.5%. In cases with high RMS variation (≥3%) the identifications were generally stable between x/L = 0.25-0.5, where three-dimensional effects were smaller. The average identification could be weighted towards this region to reduce measurement bias. As an example, for specimen #1 this procedure reduces the back-to-back difference in stiffness from 1.6 GPa, to 1.2 GPa. Therefore, in tests where three-dimensional effects are of concern, it is recommended that the spatial average of the identified stiffness be weighted towards the free edge, (*e.g.:* 25-50% from the free edge).

5.3.3 Failure stress identification

The failure stress diagnostics from [38] are presented for specimen #1, which showed substantial differences in the stress-strain curves as the material unloaded (Fig. 5.7a-5.7d). Stress was reconstructed with the linear stress-gauge, $\sigma_{xx}(LSG)$ (Eq. (3.25), and from strains (Eq. (3.5)) ($\sigma_{xx}(\epsilon_{xx})$) separately on each face. The failure stress reported in Table 5.1 represents the peak tensile stress within a virtual gauge at the fracture location, as reconstructed from fields on both sides of the sample and back-to-back averaged fields using the linear stress-gauge equation. The strain-based and acceleration-based stress fields were also reconstructed using back-to-back averaged fields. Each of these stress reconstructions, as well as the difference between the two are shown in Fig. 5.9 at the time when a crack is first observed (occurs on the back face first). Fig. 5.10a shows the temporal evolution of average stress reconstructed within the virtual gauge located on the crack initiation site for each face, and using back-to-back averages. Fig. 5.10b shows the corresponding stress-strain curves using the linear stress-gauge equation and local strains. From these fields, three estimates of tensile failure stress ($\sigma_{xx}(LSG)$) were obtained (front, back and back-to-back average), as summarised for all tests in Table 5.1.

Fig. 5.9a and 5.9d show clear differences between the stress calculated from strain $\sigma_{xx}(\epsilon_{xx})$ on each face and large differences compared to the acceleration-based stress fields $\sigma_{xx}(\epsilon_{xx})$ (Fig. 5.9c and 5.9f). When stress is calculated from back-to-back averaged fields the two reconstruction are in much better agreement (Fig. 5.9g - 5.9i). If we consider the evolution of

Table 5.1: High-strain-rate interlaminar elastic modulus and tensile failure stress for AS4-145/MTM45-1 (1-3 plane) from front and back face measurements individually, and using back-to-back averaging

Specimen	E_{33} [GPa]^a (v_{RMS}(%)) Front	Back	Avg.†	$\overline{\dot{\epsilon}_{xx}}$ [s^{-1}] (x10^3)^b Front	Back	Avg.†	$\overline{\sigma_{xx}}^{VG}$ [MPa]^c Front	Back	Avg.†	$\overline{\dot{\epsilon}_{xx}}$ [s^{-1}] (x10^3)^d Front	Back	Avg.†
1	9.9 (3.1)	11.5 (3.3)	10.6 (0.9)	-2.3	-2.0	-2.0	82.3*	67.6	65.0	2.4	5.3	3.6
2	10.2 (5.4)	10.8 (3.0)	10.5 (1.8)	-1.8	-1.5	-1.5	57.7*	49.5	44.5	1.4	3.8	2.6
3	10.5 (3.6)	10.6 (3.6)	10.5 (1.5)	-2.5	-2.3	-2.3	90.7*	84.1	81.4	3.6	6.8	5.2
4	10.9 (7.5)	10.3 (3.6)	10.6 (2.3)	-3.8	-4.7	-3.9	86.3	107.3*	95.6	8.9	8.1	8.5
5	9.9 (4.0)	11.5 (4.4)	10.5 (1.1)	-1.7	-1.6	-1.6	53.7*	63.3	53.6	2.3	4.2	3.3
6	11.0 (4.1)	10.9 (4.0)	11.0 (0.7)	-2.9	-2.6	-2.7	73.6*	65.4	66.5	5.1	6.6	5.8
7	11.0 (2.7)	10.9 (3.3)	11.0 (0.8)	-4.1	-3.7	-3.7	95.3*,**	71.8	72.3^x	6.9	8.7	7.7^x
Mean	10.5	10.9	10.7	-2.7	-2.6	-2.5	77.1	72.7	71.2	4.4	6.2	5.2
SD	0.50	0.38	0.21	1.0	1.1	1.0	16.1	18.4	19.2	2.8	2.2	1.9
COV (%)	4.7	3.5	2.0	63.3	44.8	43.3	20.9	25.3	27.0	25.6	29.9	43.8
Diff. to Q-S (%)	+33	+37	+35	–	–	–	+53	+44	+41	–	–	–

a: Stiffness identified from stress-strain curves
b: Strain rates reported as maximum width-averaged strain rate in compressive loading
c: Failure stress identified using linear-stress gauge equation, as detailed in Sec. 3.4.1
d: Strain rates reported as maximum averaged strain rate in virtual gauge up to frame before fracture
†: Back-to-back average of fields measured on the front and back faces (Sec. 3.4.3)
*: Crack appears first on other side of sample
**: Crack appears at different location to where crack appears first on other side of the sample
x: At crack location on back face

stress within the virtual gauge area where the sample fractures, it can be seen that the differences between the faces develops progressively starting near peak compressive load (approx. $t = 11$ μs) as shown in Fig. 5.10a. At this point the stress-strain response between the two faces also diverged (Fig. 5.10b). We can associate the divergence of $\sigma_{xx}(LSG)$ and $\sigma_{xx}(\epsilon_{xx})$ with a break down of the measurement assumptions, and not the constitutive model, since the stress-measures on each face agreed throughout much of the compressive loading sequence with the back-to-back averaged response. The observation that the strain on one surface of the sample is compressive while the other face is tensile suggests there is an out-of-plane bending load superimposed on the main axial loading. Interestingly, differences between the front face, back face, and back-to-back averages does not appear to be as significant when considering the stress field calculated using the linear stress-gauge equation, see Fig. 5.9e, 5.9e and 5.9h. This suggests that the of a_z component of acceleration and through-thickness shear stress introduced by the out-of-plane loading affect single-sided measurements in a similar way. As discussed in Sec. 3.4.3, since these components cannot be resolved from measurements made by a single camera on each face, the stress reconstructed from in-plane acceleration will underestimate the true stress. The effect of these unresolved components on fracture stress estimates is investigated in later sections with additional tests where three-dimensional effects are reduced.

Despite the agreement between the two stress reconstructions at the frame where fracture first occurs (Fig. 5.10b), the failure stress identified from each face in Table 5.1 was not the same when measurements were processed individually. This is because tensile load continues to build up during the time required for the crack to propagate through-the-thickness and be detected on the other face. However, at the instant a crack forms on one face, the stress reconstruction on the opposite face becomes biased since the assumption of two-dimensional loading and uniform

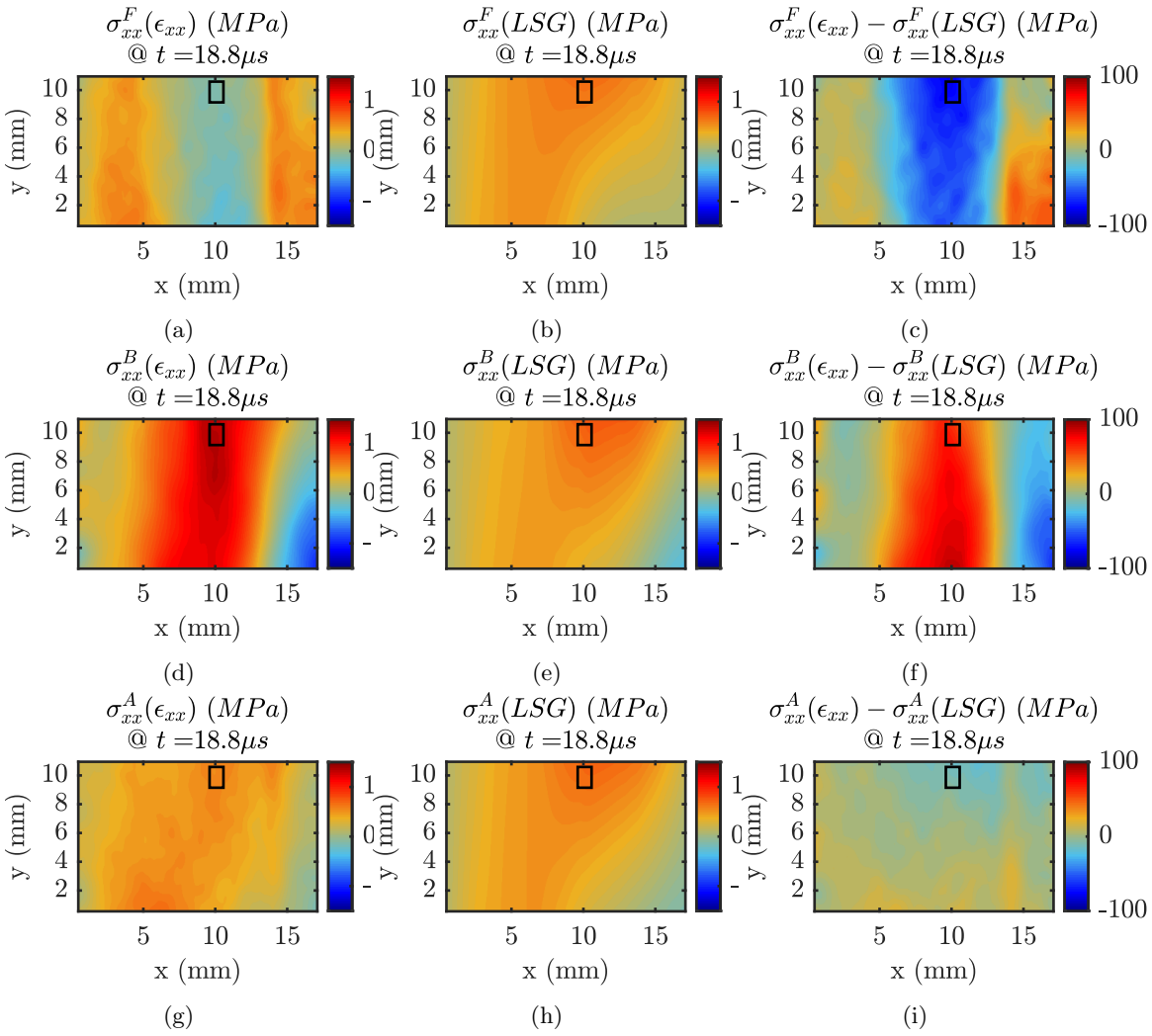

Figure 5.9: Failure stress identification diagnostics for specimen #1 at $t = 18.8$ μs corresponding to the frame of maximum tensile stress on the back face when the crack first appears: (a) strain-based stress field (MPa) constructed from ϵ_{xx}, using identified E_{33} from the front face ($\sigma^F_{xx}(\epsilon_{xx})$), (b) acceleration-based stress field (MPa) reconstructed using the linear stress-gauge equation on the front face ($\sigma^F_{xx}(LSG)$), (c) difference between strain-based and acceleration-based stress fields on the front face, (d) strain-based stress field (MPa) from the back face ($\sigma^B_{xx}(\epsilon_{xx})$), (e) acceleration-based stress field (MPa) on the back face ($\sigma^B_{xx}(LSG)$), (f) difference between strain-based and acceleration-based stress fields on the back face, (g) strain-based stress field (MPa) from back-to-back averaged fields ($\sigma^A_{xx}(\epsilon_{xx})$), (h) acceleration-based stress field (MPa) from back-to-back averaged fields ($\sigma^A_{xx}(LSG)$), (i) difference between strain-based and acceleration-based stress fields using back-to-back averages. Note that the virtual gauge is shown as a black rectangle

thickness no longer hold. There may be some indication of this in the stress-strain response from the front face by the change in loading rate towards peak tensile stress (front face in Fig. 5.10b), but this would not be immediately obvious if only single-sided measurements were available. Interestingly, every test except specimen #4 failed on the back side of the sample first, and tensile failure stress from the front surface measurements were systematically higher in those cases.

The tensile failure stress measurements made from each face individually (Table 5.1) had relatively high scatter (COV = 20-25%) compared to stiffness. While this may be expected for failure stress measurements, the scatter is likely amplified by the varying level of three-dimensional loading in each test, which will be explored further in later sections. On average, the failure stress identified from back-to-back averaged fields of the acceleration was similar to

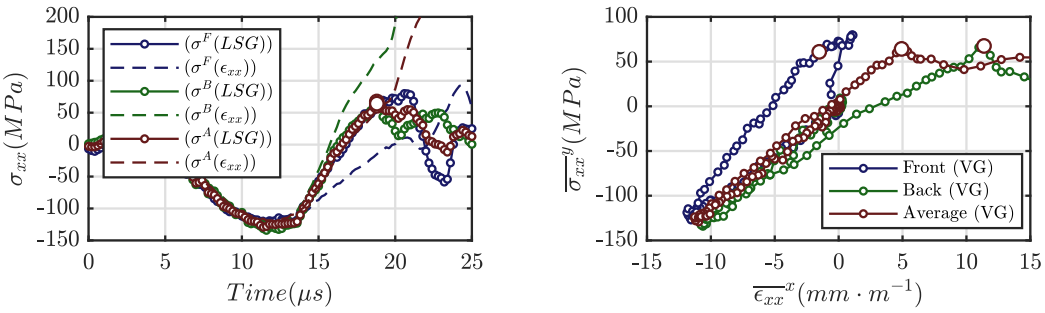

(a) (b)

Figure 5.10: Failure stress diagnostics for specimen #1 showing: (a) comparisons of stress over time within the virtual gauge, (b) comparisons of stress-strain curves reconstructed using average stress (linear stress-gauge) and strain within the virtual gauge. Note that 'F', 'B' 'A' in (a) denote the front and back faces, and back-to-back averaging, respectively

each face individually and with comparable scatter. Therefore, back-to-back measurements do not offer any improvement for tensile failure stress, and the diagnostics have highlighted the importance of two-dimensional loading for unbiased estimates of failure stress.

5.3.4 Back-to-back measurement summary

The back-to-back imaging experiments have resulted in the following key conclusions:

1. There was a back-to-back difference between the kinematic fields that builds over time, which propagated from the impact edge into the sample.

2. The unloading response observed on the stress-strain curves produced with the stress-gauge equation was substantially different on each side of the sample. The differences were generally largest over the half of the sample closest to the impact edge.

3. Three-dimensional effects can have a significant influence on the identification of stiffness from a single side of a sample (up to 20% difference). However, the scatter is regularised by taking the average stiffness over the middle 50% of the sample. Over all tests, the modulus identified from single-sided measurements only differed by 3% compared to identifications made with the back-to-back averaged fields (see results in Table 5.1).

4. Three-dimensional effects were smallest near the free edge and therefore, scatter in stiffness measurements may be improved by refining the region on the sample used for spatial averaging. A large RMS variation (≥3%) of the spatial identification relative to the average over the middle 50% of the sample provides an indicator of when this refinement may be required.

5. Average failure stress measured from each side of the sample were similar (see Table 5.1), but with relatively high scatter (COV = 20-27%). It is suspected that this was a result varying levels of three-dimensional loading in each test.

6. Failure stress diagnostics provide evidence that most samples failed under combined in-plane tension and out-of-plane bending. While large differences in strain are measured between the two faces, the difference between in-plane accelerations are lower, and thus, the linear stress-gauge reconstructions are similar on each face. This suggests that the out-of-plane component of acceleration and through-thickness shear stress generated under this out-of-plane loading affect single-sided measurements in a similar way. Moreover,

since these components are required to fully resolve axial stress (Sec. 3.4.3), stress reconstructions based on in-plane acceleration will underestimate the true failure stress. This is confirmed in later sections, when compared to tests where the effects of out-of-plane bending are reduced.

Overall, in the presence of three-dimensional loading, back-to-back measurements provide more stable and consistent stiffness identification, but do not offer any improvement for failure stress. The remainder of this chapter will focus on three things: 1) identifying the source of this three-dimensional loading, 2) developing a method to correct it, and 3) performing a final series of experiments with significantly reduced through-thickness heterogeneity to quantify the effects on stiffness and failure stress measurements.

5.3.5 Identifying the physical mechanisms behind the out-of-plane loading

The consistency of three-dimensional loading across all samples indicates that it was introduced systematically through the experimental setup. The most likely cause was a misalignment in the impact chain. This was investigated with experiments where a mirror system was installed in the test chamber to visualise the out-of-plane impact alignment (Fig. 5.11).

Several test shots revealed that the waveguide was systematically misaligned to the projectile by 0.8°-1.2°. It is hypothesized that this misalignment arises from slight deviations in the barrel bore, which affects the flight of the short sabot (45 mm), but not the machined rod that sits deeper in the barrel when the alignment is performed. Images taken with the mirror system revealed that angular misalignment induces a bending wave in the waveguide leading to appreciable lateral displacement and rotation of the free end. This is apparent when comparing images taken before and after impact; two of which are overlaid in Fig. 4.12. When a sample was bonded to the back of the waveguide it was observed that the lateral motion introduces out-of-plane bending in the sample near the waveguide. Videos of these tests are included in the data repository listed in Section 5.1.

This indicates that the pulse was applied non-uniformly through-the-thickness. As observed in the back-to-back imaging experiments (Sec. 5.3.2 & 5.3.3), the effect on the compressive loading decreases with increasing distance from the impact edge. This is believed to be a result of the Saint-Venant effect in dynamics, as reported by others [143, 144], which acts to even out the wave as it propagates away from the impact edge. The reason the three-dimensional effects amplify as the material unloads is a result of structural dynamics of the sample. Before the wave reaches the free edge, the specimen behaves like it is infinite in length. As the wave reflects from the free edge, the loading excites a bending mode in the sample, which propagates from the impact edge. The pulse length is also slightly longer than the length of the sample, and therefore, a type of 'forced' vibration is introduced until the specimen de-bonds from the waveguide. The effect of this bending wave is superimposed on the in-plane loading.

Plotting the membrane components of stress and strain reveal the underlying linear-elastic response of the material (shown at four location in Fig. 5.13), which can be used to identify the unbiased estimate of the interlaminar elastic modulus (Sec. 3.4.3). However, back-to-back measurements are unable to fully resolve stress for the purposes of estimating failure stress in the presence of out-of-plane loading (see Eq. (3.48)). The large flexural strains (up to 7 $\text{mm}\cdot\text{m}^{-1}$) suggest the out-of-plane effects are significant for this specimen, and flexural stress is clearly not well captured when the second term on the right hand side of Eq. (3.48) are neglected (see Fig. 5.13e-5.13f). Moreover, it can be said that the first term in Eq. (3.48) contributes little to

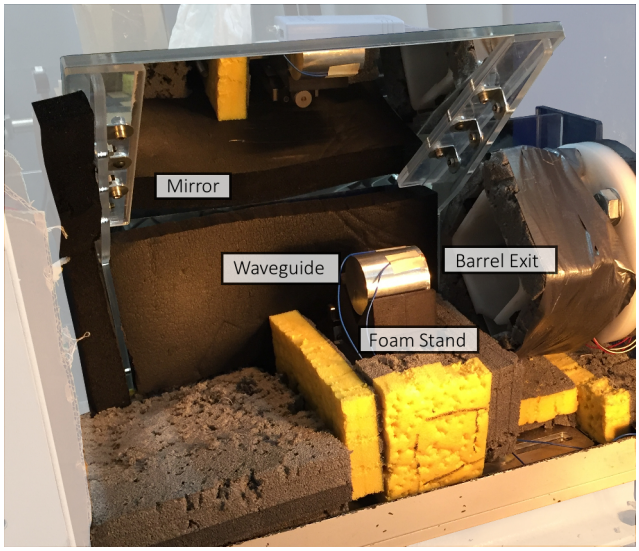

(a)

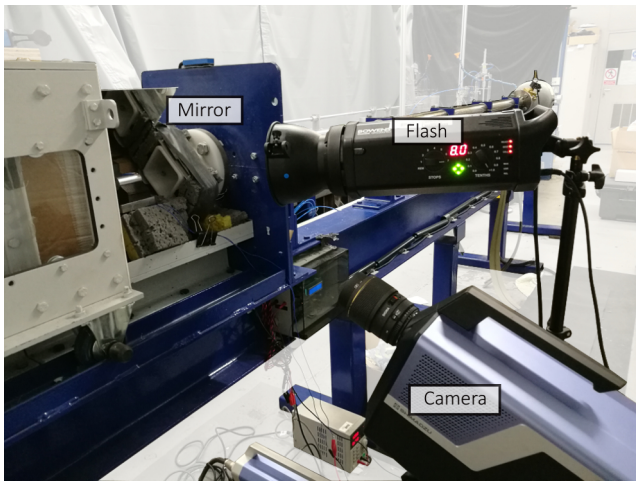

(b)

Figure 5.11: Mirror system installed in the capture chamber to enable visualisation of the impact in the 'top-down' perspective. a) mirror installed in the chamber, b) camera setup to visualise mirror through side windows of the test chamber

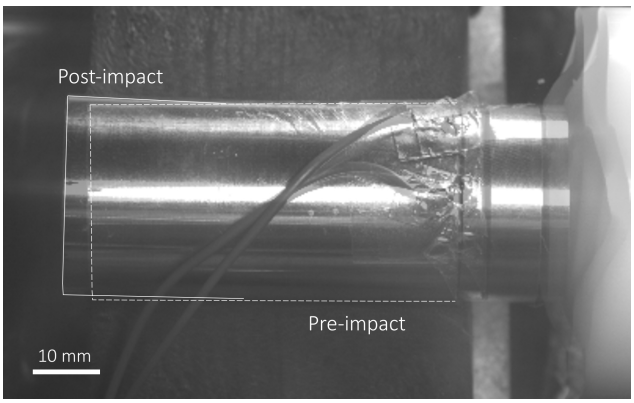

Figure 5.12: Overlaid images before and after a misaligned impact showing the effect on the out-of-plane waveguide dynamics

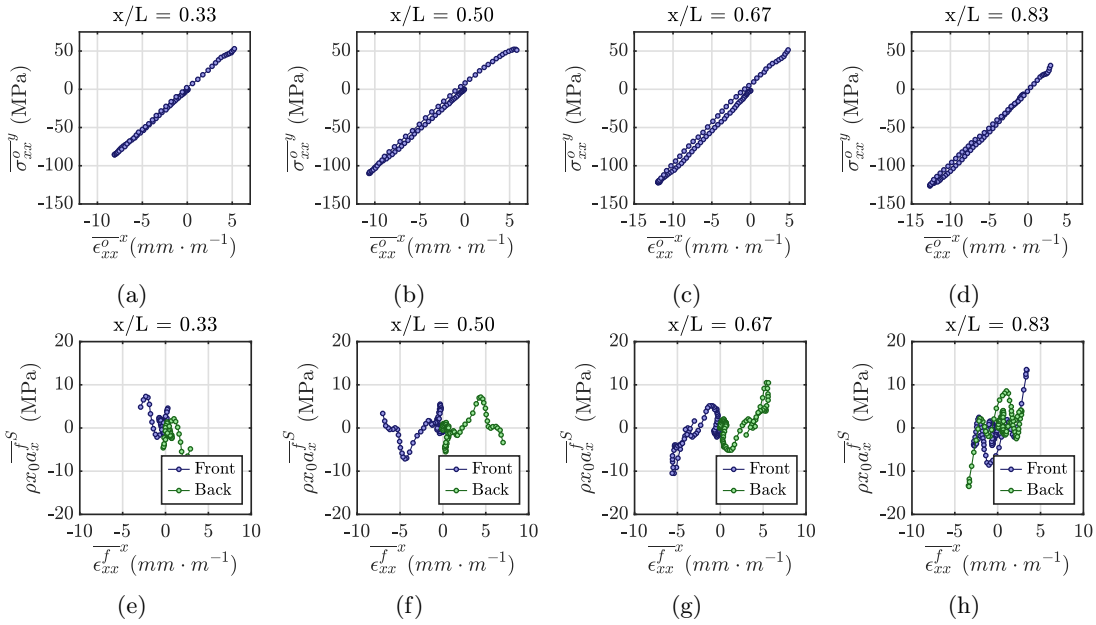

Figure 5.13: Stress-strain curves for specimen #1 reconstructed from decoupled membrane ((a)-(d)) and flexural ((e)-(h)) components of in-plane strain and acceleration

the calculation of $\overline{\sigma_{xx}^{f}}^{y}$, since the stress-strain response diverges significantly from the back-to-back average response as otherwise, the responses would be linear for each face. This confirms that the true failure stress is underestimated using the linear stress-gauge reconstructions from each face when three-dimensional effects are present.

These experimental studies provide compelling evidence for a need to improve the alignment procedure for further testing. The mirror system used for diagnostics (Fig. 5.11a) was used to implement a new alignment procedure which reduced the misalignment error to $\approx 0.2°$. The impact tests were then repeated with improved alignment to quantify the bias introduced by the three-dimensional loading on stiffness and failure stress measurements, as described in the following section.

5.4 Follow-up experiments with improved alignment

The alignment procedure in Sec 5.2.1 was extended to include additional test shots in the out-of-plane perspective to correct for yaw misalignment from the projectile trajectory. Using an image-based alignment process results in an angular and positional accuracy of 0.2° and 0.2 mm, respectively. Full details on the procedure can be found in [136]. To quantify the effect of the improved alignment, eight impact tests with a single Shimadzu HPV-X camera were performed at impact speeds ranging from 25 m·s^{-1} to 54 m·s^{-1}. The objective was to characterise: 1) the relative effect of improving the alignment on stiffness and failure stress measurements, and 2) the response of the material under varied impact speeds where the specimen fails and does not fail. When combined with the back-to-back imaging experiments, the intention was also to establish a set of diagnostics for detecting three-dimensional effects from single-sided measurements. This has considerable practical benefit as most users will only have access to one camera.

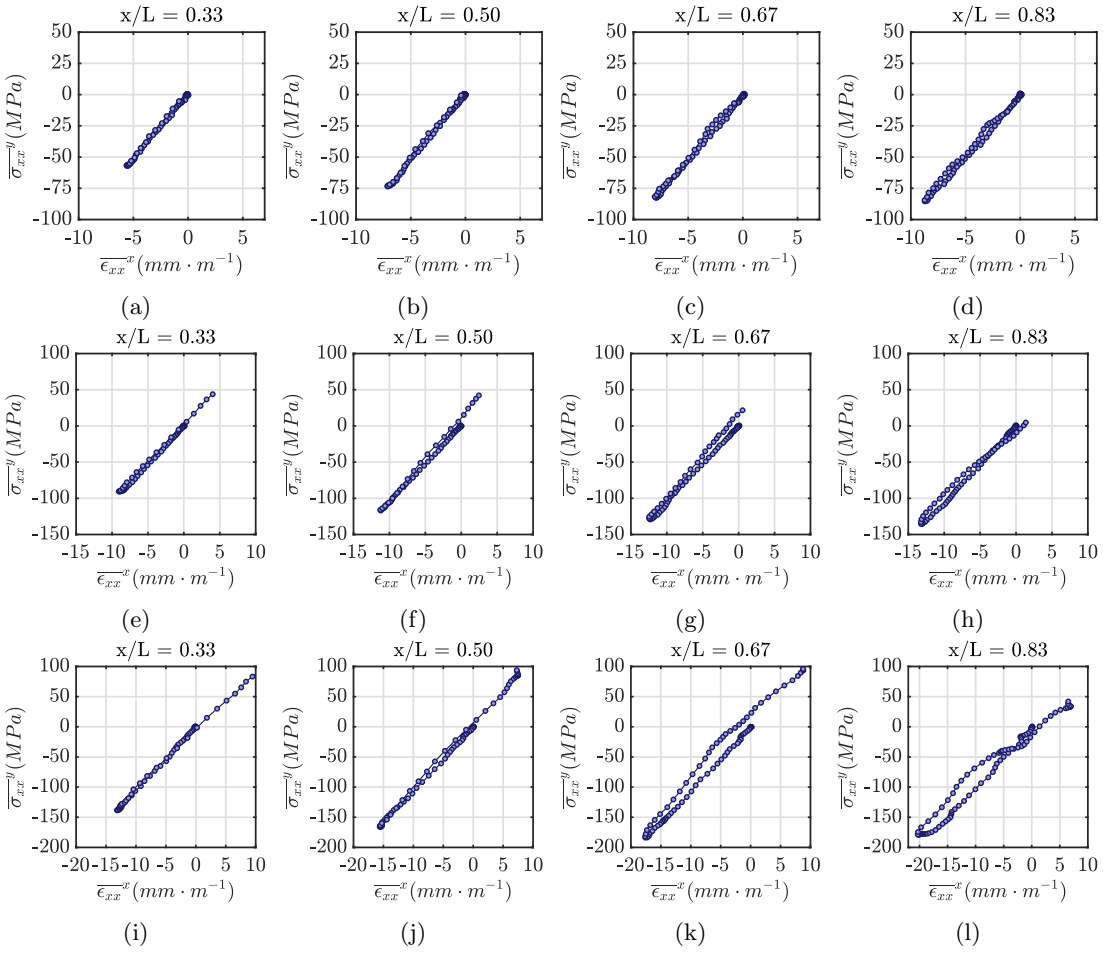

Figure 5.14: Stress-strain curves for specimens tested with improved alignment as reconstructed with the stress-gauge equation: (a)-(d) R7 (25 m·s^{-1}), (e)-(h) R6 (35 m·s^{-1}), and (i)-(l) R4 (50 m·s^{-1})

5.4.1 Reconstructed stress-strain response and stiffness identification

The stress-strain curves at four locations for a sample impacted at 25 m·s^{-1} (R7), 35 m·s^{-1} (R6) and 50 m·s^{-1} (R4) are shown in Fig. 5.14. The stiffness and failure stress measured for each sample are included in Table 5.2. The spatial identifications of E_{33} for all samples are shown in Fig. 5.15. Note that the identification of E_{33} in Table 5.2 was determined by fitting the compressive stress-strain response up to 8 mm·m^{-1}, for consistency with the previous tests. Specimens tested with the revised alignment procedure are denoted by 'R' preceding the specimen number.

An impact speed of 25 m·s^{-1} (specimen R7) was selected to quantify the effect of improving the alignment on the stress-strain response under conditions where material damage can be ruled out. The stress-strain curves for this sample are shown in sub figures (a)-(d) in Fig. 5.14. These measurements verify the expected linear-elastic behaviour of the material, with negligible spatial variation in the unloading behaviour, unlike that measured in the first set of tests (recall Fig. 5.7). As the impact speed is increased to 35 m·s^{-1}, the unloading portion of the stress-strain curves at $x/L = 0.67$ (Fig. 5.14g) and 0.83 (Fig. 5.14h) differ from the loading behaviour and some parasitic non-linearity is measured near peak compressive load. This unloading divergence becomes more pronounced as impact speed increases (Fig. 5.14k-5.14l). It is speculated that this is a result of weakly activated bending modes caused by residual misalignment of the waveguide, or of the sample. The non-linearity observed in the curves is not a material behaviour, since

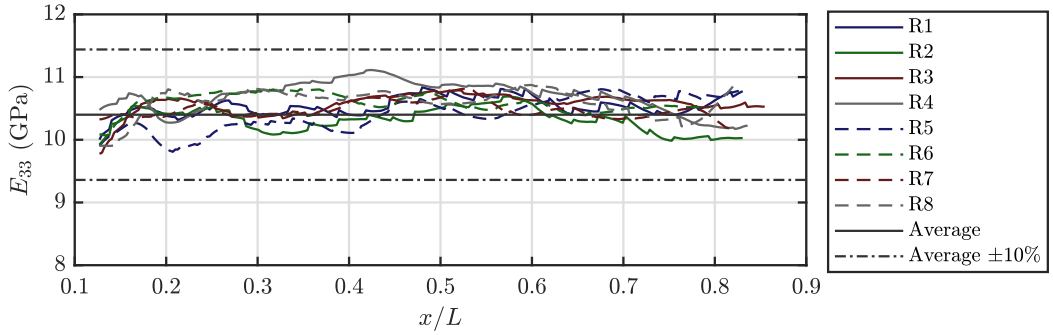

Figure 5.15: Spatial identifications for all specimens tested with the new alignment procedure. Note that E_{33} is determined with a linear fitting to the initial compressive loading behaviour up to 8 mm·m^{-1}

Table 5.2: High-strain-rate interlaminar elastic modulus and tensile failure stress for AS4-145/MTM45-1 (1-3 plane) with the revised alignment procedure

Specimen	V_{Impact} [m·s^{-1}]	E_{33} [GPa] (e_{RMS}(%))	$\overline{\dot{\epsilon}_{xx}}$ [s^{-1}] (×10^3)	$\overline{\sigma_{xx}}^{VG}$ [MPa]	$\overline{\dot{\epsilon}_{xx}}^{VG}$ [s^{-1}] (×10^3)
R1	54	10.5 (1.6)	-6.0	108.1	10.8
R2	51	10.3 (1.9)	-6.5	111.8	9.8
R3	51	10.5 (1.9)	-5.4	103.4	9.7
R4	50	10.9 (3.0)	-5.4	95.3	9.2
R5	37	10.3 (3.0)	-4.0	91.5	7.3
R6	35	10.7 (2.2)	-3.9	128.1	5.7
R7[a]	25	10.5 (1.4)	-1.7	– *	3.3
R8	50	10.7 (2.5)	-5.8	99.3	9.2
Mean	–	10.4	-5.3	103.6	8.8
SD	–	0.23	1.0	6.6	1.7
COV (%)	–	2.0	18.3	6.4	19.6

[a]: Intentional low impact speed, excl. from statistics
*: No fracture

its onset is dependent on spatial location and not stress. For example, non-linear behaviour is observed below 150 MPa near the impact edge at 35 m·s^{-1} (Fig. 5.14h), but is not observed near the free edge at 50 m·s^{-1} where stresses exceed 150 MPa (Fig. 5.14j).

The effect of improved alignment is apparent in the stiffness measurements, where spatial identifications were much more stable (Fig. 5.15) over all tests (Table 5.2). Despite some lingering three-dimensional effects in the stress-strain curves, the RMS variation of all spatial identifications was reduced (all tests lower than 3%, and most lower than 2%). This provides additional confidence that the identifications were unbiased by 3D effects over most of the sample up to 8 mm·m^{-1} of strain.

The stiffness measurements from improved alignment tests can now be compared to the back-to-back imaging results to evaluate bias induced by the three dimensional loading. Individual stiffness identifications from each face may be biased by as much as 9%, but on average only by as much as 4%. The average stiffness measured using back-to-back averaging was within one standard deviation of that identified under improved alignment conditions. This shows that back-to-back surface measurements can provide an unbiased estimate for interlaminar stiffness even under the effects of three-dimensional loading.

5.4.2 Failure stress identification

Here we will consider specimen R7 (25 m·s^{-1}) and specimen R4 (50 m·s^{-1}), to investigate how impact speed and residual misalignment influence stress reconstructions. It is worth noting that sample R7 did not fracture so $\sigma_{xx}(LSG)$ and $\sigma_{xx}(\epsilon_{xx})$ should agree throughout the whole test. The failure stress diagnostics from Section 5.3.3 are presented for specimen R7 and R4 in Fig. 5.16 and Fig. 5.17, respectively. In Fig. 5.17, two virtual gauge regions are considered to compare the response at the location of fracture, and at $x/L = 0.67$ where the average stress-strain curve shows a dissimilar unloading behaviour.

The failure stress diagnostics for specimen R7 (Fig. 5.16) show a good agreement between the stress reconstructed from strain, and from the linear stress-gauge equation. Average stresses within a virtual gauge in the centre of the sample agree well over the entire test (Fig. 5.16c) and the material response is linear elastic during loading and unloading (Fig. 5.16d). This validates the assumed constitutive model and implies that the loading remains two-dimensional throughout the entire test in this region of the sample.

For sample R4 impacted at 50 m·s^{-1}, the two stress maps, and temporal evolution of stress within the virtual gauge at the point of fracture are also in good qualitative agreement until the crack forms. At this point, the strains become non-physical and the strain-based stress diverges (Fig. 5.17c). Similar to sample R7, tested at 25 m·s^{-1}, the stress-strain curve at the crack location (Fig. 5.17d) is linear up to fracture, with no sign of three-dimensional effects on the unloading response.

The effects of misalignment are detected in sample R4 closer to the impact edge, as demonstrated using the stress and strain reconstructed with a virtual gauge at $x/L = 0.67$. In the centre of the sample the linear stress-gauge reduces to the average stress-gauge equation (Eq. 2.2), but is used here to show how the stress-strain response in Fig. 5.14k directly compares to stress reconstructed from strain. In a similar manner to the back-to-back imaging tests, the two stress reconstructions start to diverge near peak compressive load (Fig. 5.17e). At this time in the test it is believed that structural bending has propagated to this location. As discussed previously, it is most likely that the offset occurs because of a bending wave, which

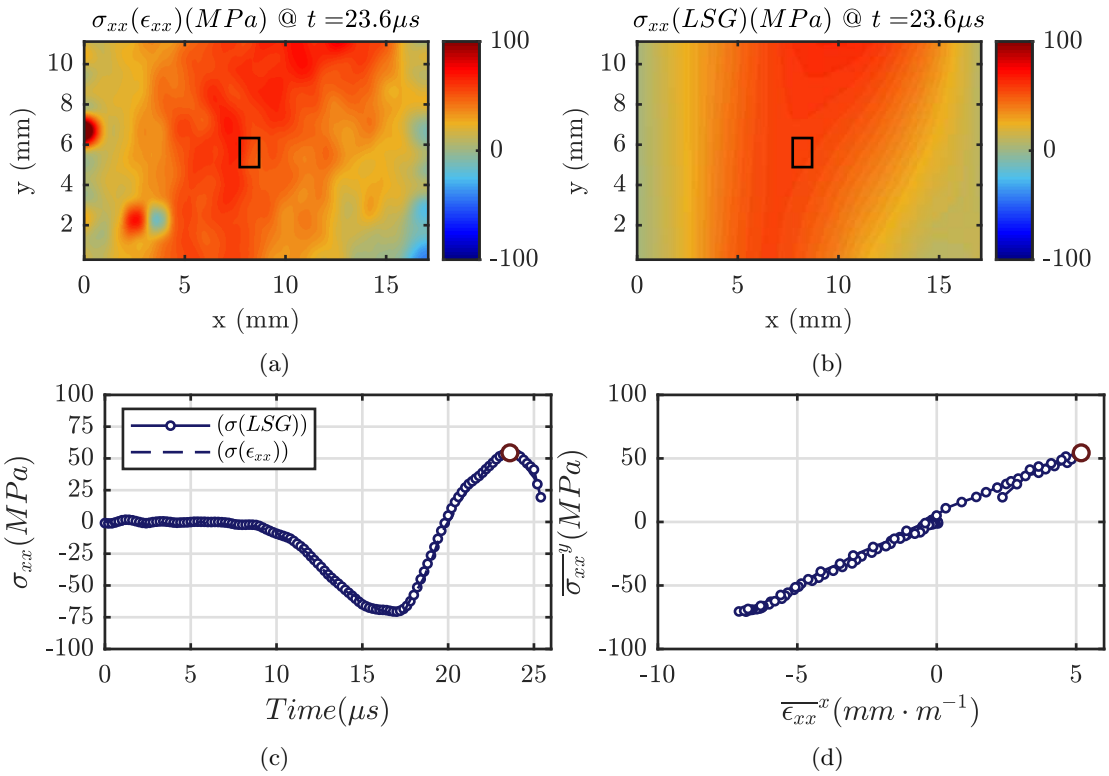

Figure 5.16: Failure stress identification diagnostics for sample #R7 at t = 23.6 μs corresponding to the frame of maximum tensile stress in the centre of the sample: (a) stress field (MPa) constructed from ϵ_{xx}, using identified E_{33} ($\sigma_{xx}(\epsilon_{xx})$), (b) stress field (MPa) reconstructed using the linear stress-gauge equation ($\sigma_{xx}(LSG)$), (c) comparison of stress over time within the virtual gauge, (d) stress-strain curves reconstructed using average stress (linear stress-gauge) and strain within the virtual gauge. The virtual gauge is shown as the black rectangle in (a)-(b)

primarily influences the in-plane strain measurements, but out-of-plane bending contributes little to the in-plane accelerations used to reconstruct stress. However, in this case, the offset is much smaller than in previous tests (see Fig. 5.10), and the region over which three-dimensional effects are witnessed does not reach the fracture location. The agreement between the stress measures shown in Fig. 5.17d gives confidence in the identified failure stress for this sample of 95 MPa. This represents a nearly 30% increase compared to measurements made under the effect of three-dimensional loading (recall results in Table 5.1).

Comparing these revised alignment tests to the previous back-to-back experiments shows that the three-dimensional effects cause failure stress to be underestimated by at least 30%. Under improved alignment conditions, the average failure stress was 104 MPa and measurement consistency was dramatically improved (COV < 7%) as listed in Table 5.2. This level of consistency is remarkable given that the strain rates are on the order of 5×10^3-1×10^4 s^{-1}. This is significantly lower than the reported scatter in the previous study by the authors (COV = 21% [38]) and the quasi-static characterisation (COV = 13% [132]). These results highlight the importance of test alignment for failure stress measurements.

5.5 Summary

As part of ongoing development of the image-based inertial impact (IBII) tests, it was important to understand the limitations of the experimental setup and validity of the two-dimensional assumption required to use full-filed measurements for material characterisation. Using two

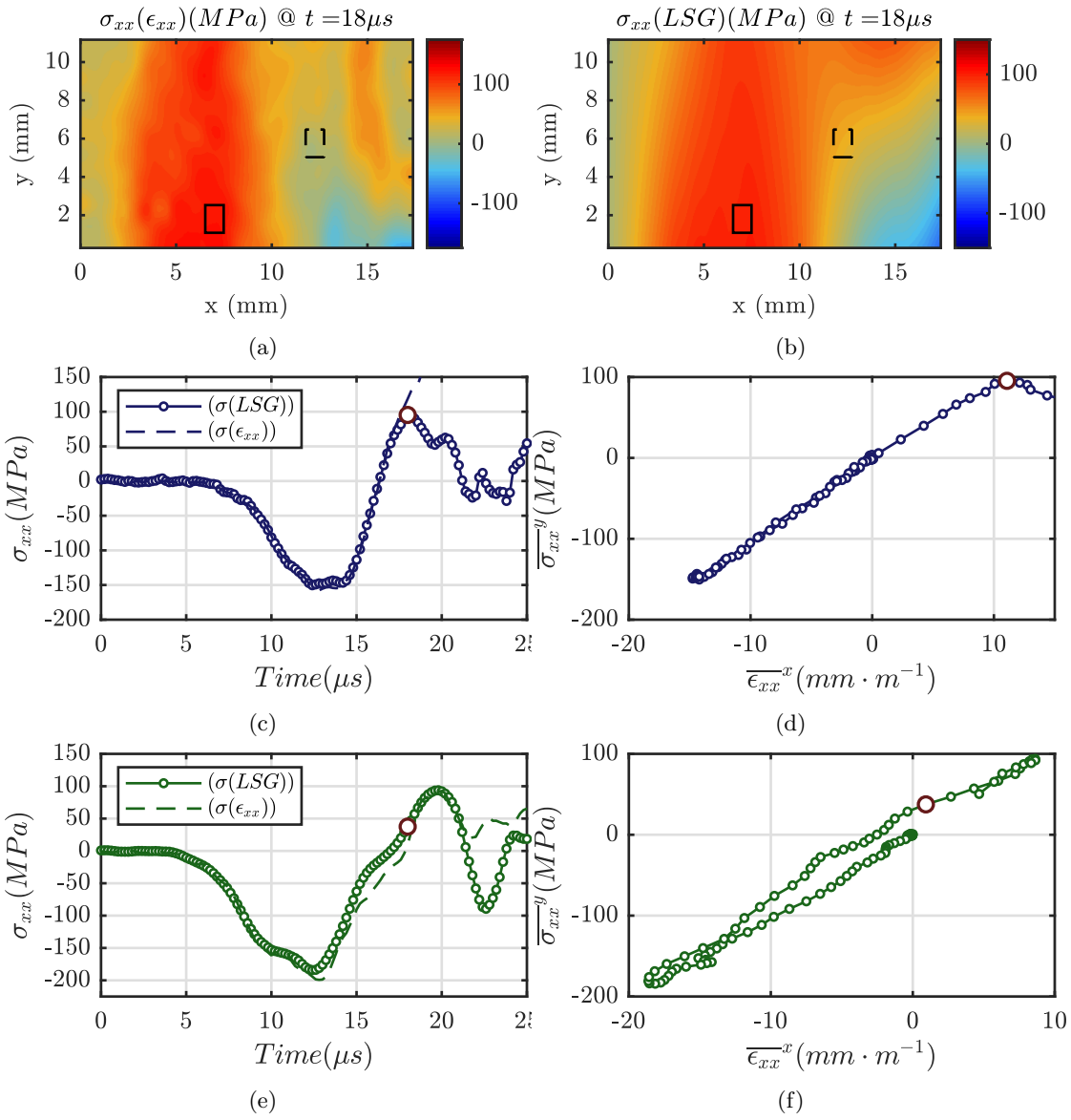

Figure 5.17: Failure stress identification diagnostics for sample #R4 t = 18 μs corresponding to the frame of maximum tensile stress at the location of fracture: (a) stress field (MPa) constructed from ϵ_{xx}, using identified E_{33} ($\sigma_{xx}(\epsilon_{xx})$), (b) stress field (MPa) reconstructed using the linear stress-gauge equation ($\sigma_{xx}(LSG)$), (c) comparison of stress over time within the virtual gauge at the fracture location, (d) stress-strain curves reconstructed using average stress (linear stress-gauge) and strain within the virtual gauge at the fracture location, (e) comparison of stress over time within the virtual gauge at $x/L = 0.67$, (f) stress-strain curves reconstructed using average stress (linear stress-gauge) and strain within the virtual gauge at $x/L = 0.67$. The black rectangles in solid and dashed lines in (a)-(b) respectively represent the virtual gauge at the location of fracture, and in the region where the unloading and loading responses differed and non-linearity was measured at peak compression load

synchronised, ultra-high-speed cameras combined with full-field measurements from both sides of the sample, it was possible to identify cases where the assumption of uniform through-thickness behaviour was not satisfied. To the authors' knowledge, this is the first time such a study has been performed in dynamics. Some recommendations for future test design can be drawn from these results, which are briefly discussed along with the key findings from this chapter in the points below.

- Results show that when the waveguide and projectile were misaligned between 0.8-1.2°, a bending wave was introduced into the sample after the wave reached the free edge.

This non-uniform loading through-the-thickness was shown to have a substantial effect on stiffness identified from individual tests (difference between faces up to 20%), but a lesser effect over several samples (difference between average identifications was at most 4%, with COV = 3-4%).

- A mirror system in the capture chamber was used to extend the alignment procedure to account for out-of-plane misalignments to within 0.2°.
- Follow-up experiments with a single camera showed a significant improvement in consistency for measurements of the interlaminar stiffness and failure stress at strain rates on the order of $3{\times}10^3$ s^{-1}. Scatter on interlaminar failure stress measurements (6.6%) were much improved compared to the previous study by the authors (21%, respectively) [38], which highlights the importance of two-dimensional loading for accurate failure stress measurements.
- Comparison of these experiments to tests with back-to-back measurements allowed us to estimate the bias introduced by the three-dimensional loading on stiffness and failure stress measurements. The identification of stiffness under three-dimensional loading was biased by 4% at most on average. The effect on failure stress was much larger as the bending stress was not captured by the linear stress-gauge reconstructions on each face, causing failure stress to be underestimated by 30% on average.
- The two sets of experiments under different amounts of misalignment were useful in establishing diagnostics for detecting issues with three-dimensional loading from single-sided measurements. This included analysis of the unloading behaviour of the stress-strain curves along the sample, and a divergence of stress reconstructed from strain and acceleration in the failure stress diagnostics.
- Single-sided failure stress diagnostics provide an excellent indication of when the loading becomes three-dimensional. In the current tests this appeared as a divergence between stress and strain after the wave reflects. If this is observed in measurements at the fracture location, the failure stress needs to be interpreted with caution as it could be underestimated by at least 30%.
- If one has the flexibility to machine longer samples (*e.g.*: for in-plane testing), the Saint-Venant effect can be better exploited by measuring the behaviour only over the region of the sample where three-dimensional effects are minimal. In the case of the interlaminar tests where the length is limited, it is important to design the test such that fracture occurs nearer to the free-edge, and that alignment is as good as possible to enable more of the sample to be used for stiffness identification. With the new alignment procedure it was possible to make unbiased measurements over approximately half of the sample ($x < 10$ mm).

Having quantified the effect of out-of-plane loading and developed an improved alignment procedure to mitigate these effects. The next objective was to extend the IBII test principle to measure the interlaminar shear moduli, as presented in Chapter 6.

Chapter 6

IBII Test for Interlaminar Shear Moduli

6.1 Overview

This chapter describes the design and experimental validation for a new interlaminar IBII test for measuring the HSR shear moduli. Section 4.2 describes the implementation of the numerical simulations to design the test configuration. The materials and experimental setup are presented in Section 4.3. The image deformation framework used for quantifying experimental errors introduced by the imaging system, grid rotation and smoothing is the focus of Section 4.4. The image deformation simulations are also used to select smoothing parameters which minimise the error for stiffness identification. Experimental results are presented and discussed in Section 4.5, and Section 4.6 summarises the key outcomes from the third phase of this project. Note that All data supporting this chapter are openly available from the University of Southampton repository at: https://doi.org/10.5258/SOTON/D1092.

6.2 Test Principle

Here, a simple rectangular geometry can be used to exploit the compressive pulse loading, and specimen inertia to generate shear in the region of the sample overhanging the waveguide (see Fig. 6.1). As the material adjacent to the waveguide is loaded by the pulse, the overhanging region will remain stationary until the shear wave has reached the top of the sample allowing shear to build up in the region near the waveguide. As in the IBII tension/compression test, a grid is deposited onto the sample and the overhanging region is imaged with an UHS camera to measure the dynamic, kinematic behaviour of the material. Displacement fields are used to compute strain and acceleration maps, which encode information about the constitutive behaviour in shear.

The relevant theory for implementing the VFM for identification of the interlaminar shear modulus directly from the fields was described in Sec. 3.5 and is, therefore, omitted here for conciseness. The following section describes the use of simulated experiments to select optimal experimental parameters for the test.

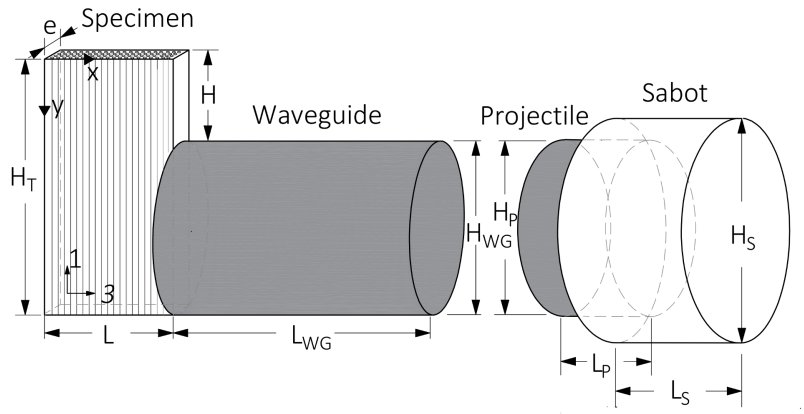

Figure 6.1: Generic configuration of proposed shear test using an overhanging impact specimen

6.3 Numerical Test Design

6.3.1 Design objectives

The objective was to design a test to characterise the HSR interlaminar shear modulus using a configuration that requires minimal preparation/machining while still enabling full-field measurements. To be consistent with the interlaminar IBII tension/compression test (Chapter 4), the same 18 mm thick carbon/epoxy unidirectional pre-preg laminate (MTM45/AS4-1) was used. For orthotropic materials the shear response in the material coordinates is de-coupled from the other in-plane stiffness parameters (Sec. 3.2). Therefore, the shear modulus should be identifiable from any configuration where significant shear is generated.

Following from the basic impact configuration in previous interlaminar IBII tests, the most intuitive configurations is to use a rectangular sample where part of the sample overhangs the waveguide in a type of 'short-beam shear' configuration. The configuration most suitable to the given camera spatial resolution (400x250 pixels), and minimum printable grid pitch (0.337 mm) are those having an overhang geometry of 18 mm x 12 mm (for 7 pixels/period grid sampling). The design was simplified by replacing the projectile, waveguide and sabot with a uniform pulse loading over part of the specimen as shown in Fig. 6.2 to better represent the experimentally-observed temporal evolution of the pulse. Using available waveguides and projectiles, the design space consisted of the two geometries listed in Table 6.1, and two pulse lengths, giving four total configurations.

Table 6.1: Specimen configurations considered in the design of an interlaminar IBII shear test

Config.	H_{WG} (mm)	H_T (mm)	H (mm)	L (mm)
1	25	37	12	18
2	45	57	12	18

6.3.2 Numerical simulation

Each configuration was simulated in three-dimensions using ABAQUS/Explicit v.6.14-3. Eight-node brick elements with reduced integration (C3D8R) were used in all simulations. The time step was allowed to vary automatically, with outputs generated every 0.2 μs to represent imaging at 5 MHz with the Shimadzu HPV-X camera. A small amount of numerical damping (β) is required to control numerical, high frequency oscillations in explicit simulations. The mesh size

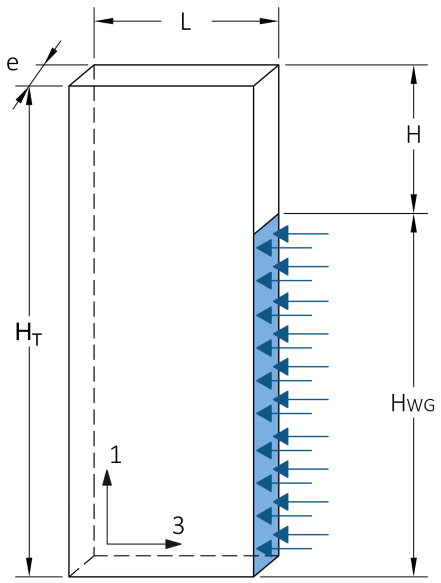

Figure 6.2: Simplified test configuration of proposed shear test with an applied pressure pulse used in design studies

and β damping coefficient were selected through separate convergence studies. The optimal values were chosen based on convergence of the computed average shear stresses and the stress averages reconstructed using the stress-gauge equation (Eq. (3.50)). These studies resulted in a mesh size of 0.2 mm and β damping of 10^{-8} s. The material properties and relevant simulation parameters are listed in Table 6.2.

A 25 μs pulse, with an amplitude of 125 MPa was used to represent the loading pulse from a 25 mm projectile travelling at 35 m/s from [37]. The rise time is assumed to be half of the pulse period based on experimentally observed pulses. Similarly, the simulated pulse for a 10 mm long projectile is based on the experimental pulse measured in [38]. Both pulse profiles are shown in Fig. 6.3. The effect of sample geometry and pulse duration on the amount of shear generated in the sample are investigated in the following section.

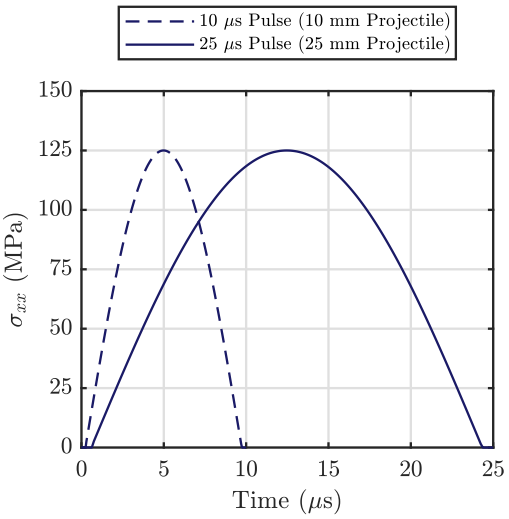

Figure 6.3: Simulated pulses applied uniformly on the face of the sample in contact with the waveguide

Table 6.2: Material properties and simulation parameters for the interlaminar IBII shear test

Material: AS4-145/MTM45-1	
E_{11} (GPa)	129[a]
E_{22} (GPa), assumed equal to E_{33}	10
E_{33} (GPa)	10[b]
G_{13} (GPa)	4.9[c]
G_{23} (GPa), assumed equal to G_{13}	4.9
ν_{13} (–)	0.015[a]
ν_{23} (–)	0.225[a]
Specimen height, H_T (mm)	37, 57
Specimen length, L (mm)	18
Specimen thickness, e (mm)	3
Density, ρ (kg·m^{-3})	1,605[d]
Simulation parameters	
Element type	C3D8R
Mesh size (mm)	0.2
Beta damping (s)	10^{-8}
Bulk viscosity damping, b_1, b_2	0, 0
Output time step (μs)	0.2
Time increment	Automatic
Pulse durations (μs)	10, 25
Pulse amplitude (MPa)	125

[a]: from [132]
[b]: interlaminar measurements using IBII test [38]
[c]: measured using IOSIPESCU tests (Sec. 6.6.1)
[d]: measured using a micro balance and water immersion
*: average in-plane shear modulus

6.3.3 Effect of geometry

The stress-strain space populated by each configuration (Fig. 6.4) was used as an initial metric to evaluate shear activation as a function of geometry and pulse duration. In general, Fig. 6.4 shows that the peak shear stress increases with increasing waveguide diameter and pulse duration. Configuration 1 with a 10 μs pulse is the only configuration which creates a full load-unload cycle, which explains why a larger region of the stress-strain space is populated. This occurs because the specimen length and pulse are short enough that the shear wave reflected from the top and bottom edges causing the material to fully unload and re-load in shear. This is not observed in configuration 2 (Table 6.1) since the shear wave must travel further before it reflects from the bottom edge, thus limiting the amount of unloading that occurs within the simulated time frame.

Increasing the specimen length provides some advantage for increased shear loading, but its effect is smaller than pulse duration. This is illustrated in Fig. 6.5 for configuration 2, which shows the temporal evolution of axial and shear stress in the sample near the bottom of the overhang ($x = L/2$, $y = 0.95H$) for both pulses. For the 10 μs pulse, σ_{xy} monotonically increases up to a maximum at approximately 8 μs, which corresponds to peak compressive σ_{xx}. The maximum shear stress is limited by the local σ_{xx} becoming tensile as the reflected wave superimposes with the release wave on the back edge of the pulse. This is expected since the 10 mm projectile was designed to load the sample to failure in tension [38]. When the pulse is longer, the superposition of the reflected wave from the free edge and the incoming compressive pulse prevents full unloading and enables shear stress to continue to build up in the sample. In this case, peak shear stress increases by 40% by increasing the pulse length from 10 μs to 25 μs. However, the extension of this is limited as simulations with a longer input pulse (40 μs) show little benefit for increasing peak shear stress. This is because unloading in shear occurs when the axial stress switches from compression to tensile, which is a function of axial wave speed and specimen length. For pulse durations exceeding 25 μs the reflected waves superimpose at

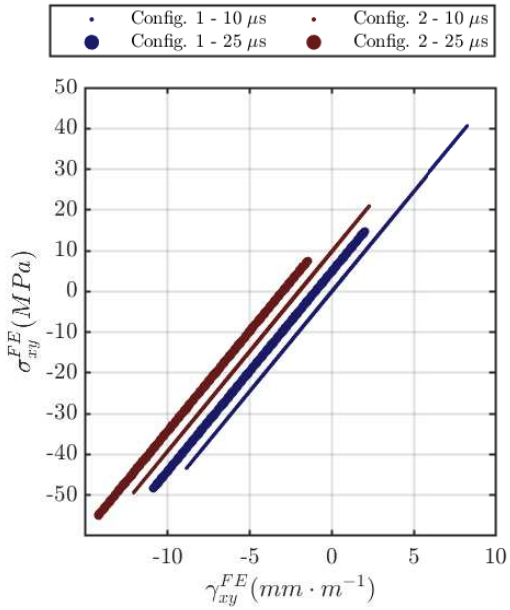

Figure 6.4: Full stress-strain space populated from all elements in the overhanging region of the sample for each configuration. Note that the stress-strain data are offset by 2 mm·m^{-1} for clarity and data within 1 mm × 1 mm of the lower right corner of the sample are omitted to exclude the stress concentration. Note that configuration 2 with the 25 μs pulse gives the highest peak shear stress

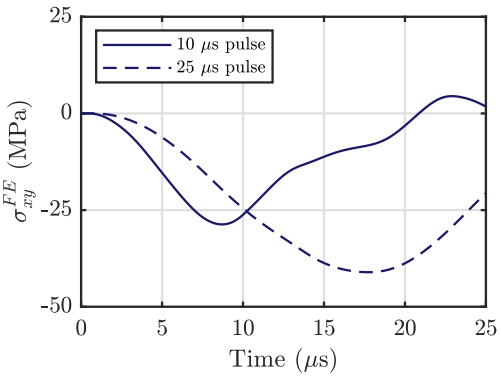

Figure 6.5: The effect of pulse duration on σ_{xy} for configuration 2 at the bottom of the overhanging region ($x = L/2$, $y = 0.95H$) for 10 μs and 25 μs pulses (pulse amplitude = 125 MPa)

a similar time to form a tensile pulse with a greater amplitude than the input pulse, causing a decrease in shear loading.

The results from the first two studies show that a larger waveguide and longer sample offer some advantage for increasing the maximum shear stress generated in the sample, but the effect is relatively small compared to increasing the pulse duration from 10 μs to 25 μs. Therefore, configuration 2 with a 25 μs will be carried forward for experimental validation. Aside from slight improvements in shear activation, a larger waveguide offers a number of other practical benefits for implementation including: 1) easier to align the specimen on the waveguide, 2) better imaging resolution in alignment shots used to set the position of the support stand (see [136]), and 3) reduced impact speed to generate the same stress pulse. The complete experimental configuration is listed in Table 6.3. The target impact speed of 35 m·s^{-1} is based on previous tests with this waveguide-projectile configuration [37], which produced a compressive pulse amplitude of approximately 125 MPa. The following section focuses on the

Table 6.3: Selected experimental parameters for the interlaminar IBII shear test

Parameter	Value
H_T (mm)	57
L (mm)	18
H (mm)	12
L_P (mm)	25
H_{WG} (mm)	45
L_{WG} (mm)	50
Impact speed ($\mathrm{m{\cdot}s^{-1}}$)	35

Recall Fig. 2.1 for symbol definition

validation of the stiffness identification routines presented in Sec. 3.5 using simulated fields for the selected configuration.

6.4 Numerical validation of stiffness identification routines

Here, the stiffness identification routines described in Sec. 3.5 are validated using the kinematic fields extracted from the finite element model described in the previous section. The same simulation parameters from Table 6.2 were used with the specimen geometry listed in Table 6.3. Displacement, strain and acceleration fields were extracted at 0.2 μs time steps from the model, mimicking a sampling at a frame rate of 5 MHz consistent with current experimental capabilities. A sample of these fields is shown at the time corresponding to peak shear stress in Fig. 6.6.

The acceleration fields (a_x) were processed using Eq. (3.50) to reconstruct average shear stress at each horizontal cross-section along the overhanging region of the sample. Combining average shear stress with average shear strain at each slice provides the shear stress-shear strain response. An example is shown at $y = 0.95H$ in Fig. 6.7a. Using a linear regression to fit the stress-strain response, the spatial distribution of the shear modulus was extracted along the overhanging region as shown in Fig. 6.7b.

The identification with the manual virtual fields and special optimised virtual fields are shown in Fig. 6.8a and Fig. 6.8b, respectively. A virtual mesh convergence study showed that the shear modulus could be identified with a virtual mesh as coarse as 1×2 elements, but the best temporal stability was obtained with a 1×5 mesh. Further refinement provided no benefit at the expense of increased processing time. At the start of the test both identifications are poor when the wave first enters the sample. The stability of the identification is also challenged past 17 μs due to low signal as the specimen unloads in shear. This has a larger effect on the manual virtual fields where both terms in Eq. (2.5) approach zero. This is because the manual virtual fields provide a static filter on the fields, whereas the special optimised virtual fields adjust in time according to the locations where strain signal is highest.

The results shown in Fig. 6.7 and 6.8 demonstrate that all stiffness identification methods are able to identify the reference modulus well within 1%. The simulation data serves as a perfect reference for validating the stiffness identification procedures. However, it does not account for experimental errors such as: spatial/temporal resolution of the camera, rigid-body rotation of the grid, and measurement noise. The effect of these parameters on each stiffness identification routine will be studied using synthetic image deformation as described in the following section.

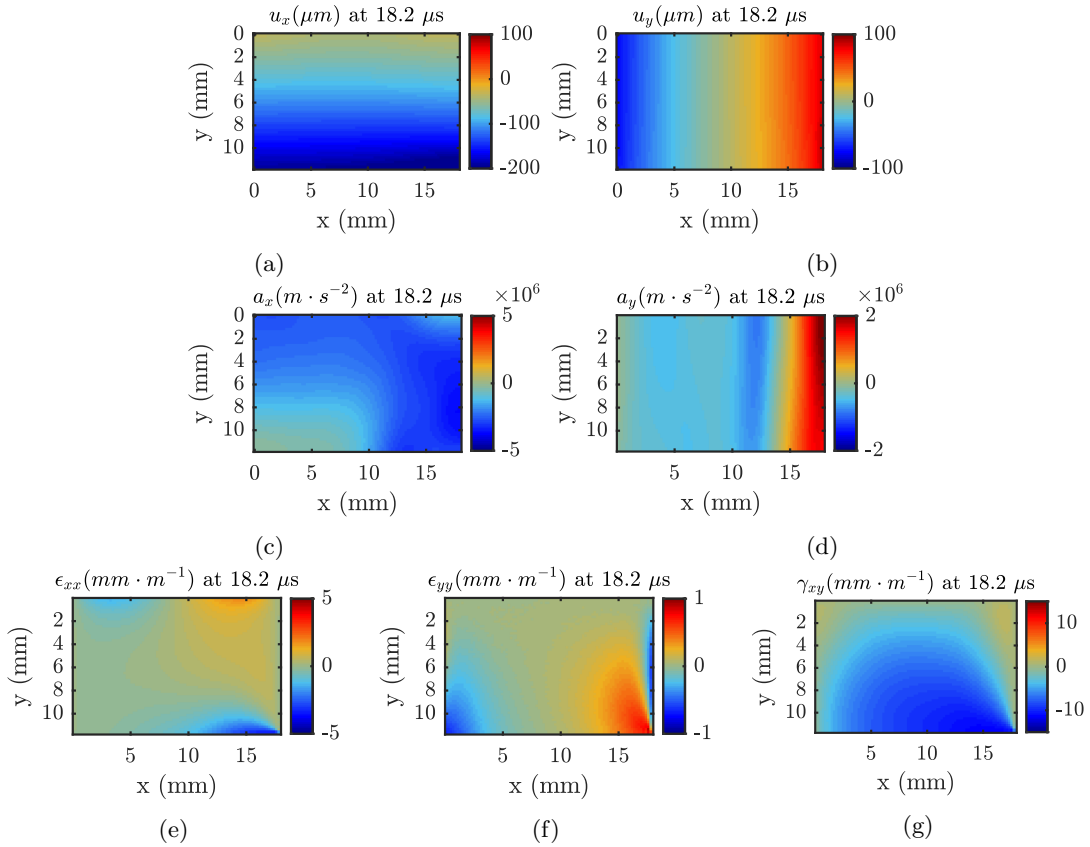

Figure 6.6: Simulated fields for the IBII shear specimen at the time step when peak shear stress is reached at the bottom of the overhang region ($x = L/2$, $y = 0.95H$): (a): u_x (μm), (b): u_y (μm), (c): a_x (m·s^{-2}), (d): a_y (m·s^{-2}), (e): ϵ_{xx} (mm·m^{-1}), (f): ϵ_{yy} (mm·m^{-1}), and (g) γ_{xy} (mm·m^{-1})

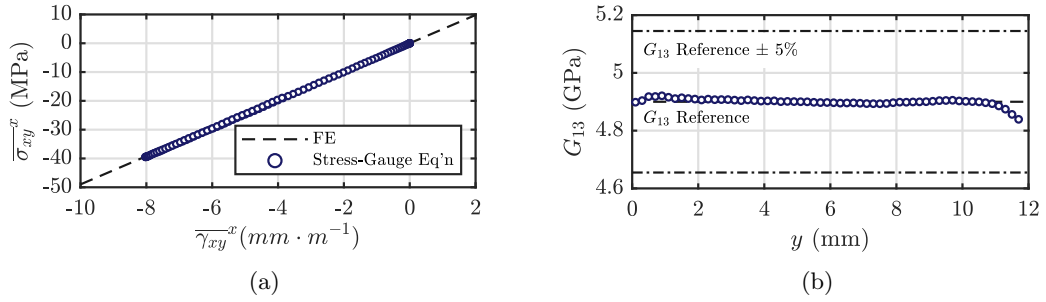

Figure 6.7: (a) Reconstructed shear stress-shear strain curve at $y = 0.95H$, and (b) spatial identification of the shear modulus, G_{13}, by fitting the stress-strain curves with a linear regression model

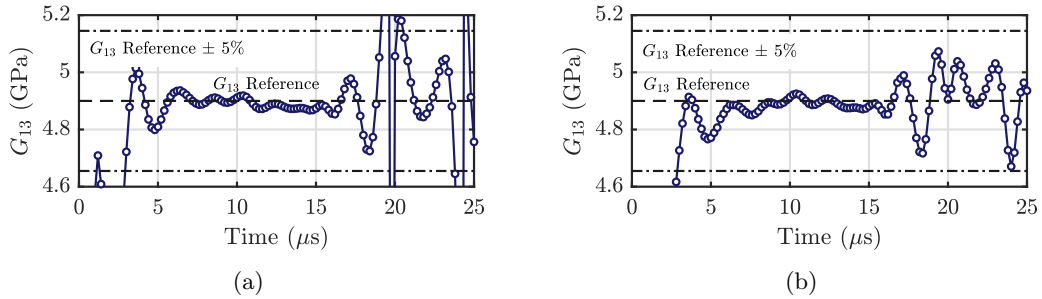

Figure 6.8: Identification of the interlaminar shear modulus, G_{13} from simulated strain and acceleration fields using: (a) manual virtual fields (Eq. (3.53)), and (b) special optimised virtual fields (Eq. (3.55))

6.5 Error quantification using image deformation

In this section image deformation simulations are used to explore the effect of experimental errors on the measured kinematic fields and identification of the shear modulus with the various VFM routines (Sec. 3.5). This section begins by investigating the two main sources of systematic error (apart from the camera itself) including edge data reconstruction and rigid body rotation of the grid. After this, the following section investigates the effects of camera resolution/noise as well as selection of optimal smoothing parameters. The general concepts of the image deformation procedure are described below, but a full description of the process has been well documented [39, 104, 140]. The specific application of the image deformation procedure to the IBII test can be found in [32, 38, 136].

6.5.1 Image deformation procedure

The idea is to generate a set of synthetic black-on-white grid images that are representative of the experimental grids. Here we use an analytical function for the grey level intensity, and a super-sampling interpolation routine described in [38] to create the images. The simulated displacement fields from the FE model in Sec. 6.4 were encoded in these images based on an inter-frame time of 0.2 μs (frame rate of 5 MHz). All parameters required to generate the grid images are provided in Table C.1. Thirty combinations of grey-level noise were added to the images according to typical experimental setup. Each set of images were processed using a range of spatial and temporal smoothing parameters. The systematic error (e_S) represent the difference between the mean identified stiffness parameter from the 30 cases of noise, and the reference stiffness in the FE model. Random error was defined as the standard deviation of the identification over the 30 cases of noise. The optimal parameters were chosen as those which minimised the total error defined as the absolute value of the systematic error plus or minus two times the random error ($e_T = |e_S \pm 2e_R|$). The errors were normalised by the reference shear modulus as was done in Chapter 4 and in [38].

6.5.2 Shear strain reconstruction at field edges

Grey level images were processed using the same procedure as described in the flow chart in Fig. 4.4 with exception to the way shear strain maps are treated. Full-field displacements from the grid method are unreliable within one pitch of the edge of the grid. This data was replaced by using a linear extrapolation of the data within one pitch of the edge as discussed in Sec. 4.4.5. This approach works well for reconstructing a_x, a_y, ϵ_{xx} and ϵ_{yy} fields from u_x and u_y, but is less effective for accurately reconstructing shear strains in this region since this is done independently for each row (u_x, a_x) or column (u_y, a_y). Moreover, the edge effects from the spatial smoothing filter also contaminate the data near the edge. If the shear strains near the edge are left uncorrected, a bias is introduced into the identification routines. Fortunately, it is possible to use the free-edge boundary conditions to reconstruct the shear strain fields along the top and vertical edges of the sample. Here we correct γ_{xy} over one pitch plus half of the smoothing window width by linearly extrapolating to zero strain at the free edges, based on the shear strains within one pitch of the corrupted data. The corrected strain fields are then used for stiffness identification.

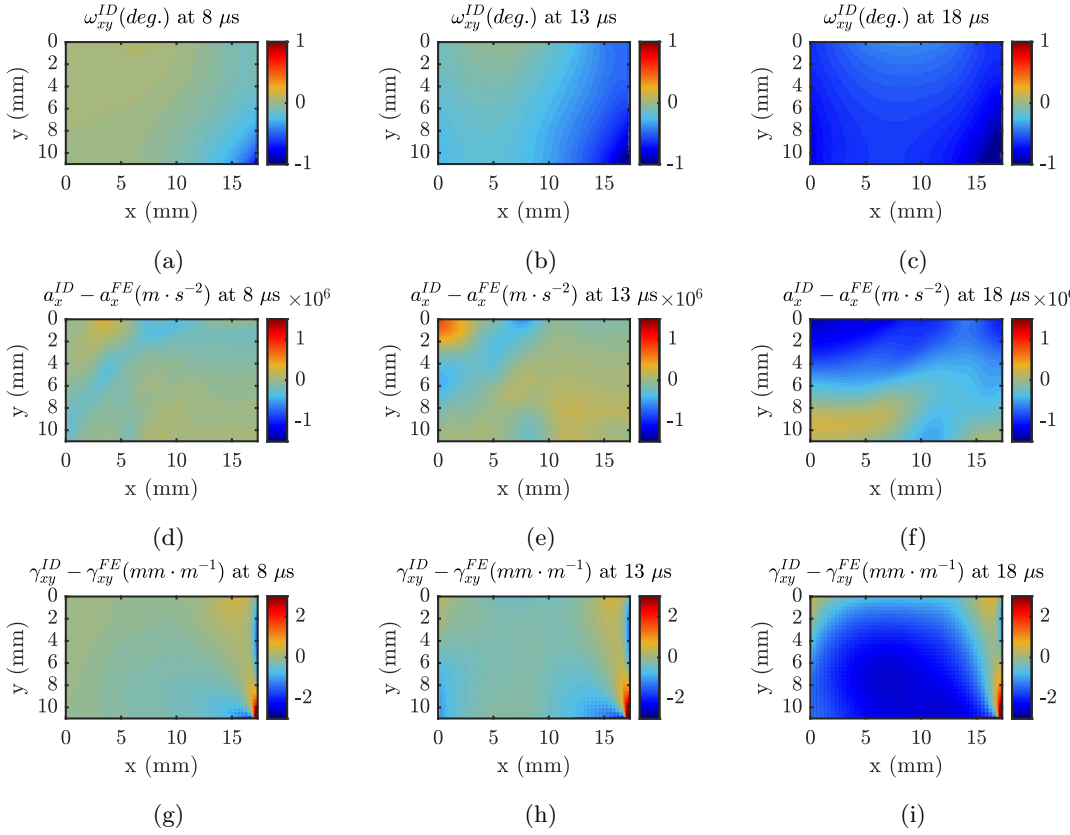

Figure 6.9: Comparison of grid rotation with acceleration and strain fields at three time steps: (a)-(c) rotation calculated from grid method, (d)-(f) differences between acceleration from synthetic images and simulation, and (g)-(i) difference between shear strain from synthetic images and simulation

6.5.3 Effect of grid rotation

Unlike previous tests where the grid remained aligned throughout the entire test, the loading in this case introduces rotation. This grid rotation creates a bias due to the fact that the phase in the x and y directions are computed in the camera coordinates, which remains fixed while the grid rotates [109]. Badulescu *et al.* [109] demonstrated that local grid rotations of 1° tend to be problematic for accurate strain measurements. In this test grid rotation will occur locally as a result of shear deformation, and also globally when rigid-body rotation of the sample begins. Image deformation simulations are used here as a tool to investigate the temporal evolution of rotation over the field of view, and quantify this effect on the measurement of the kinematic fields and stiffness identification routines.

Using displacement fields derived from phase maps, a map of local grid rotation can be obtained (ω_{xy}). This is shown at three time steps in Fig. 6.9. The simulated shear wave takes 8 μs to reach the top edge of the sample ($c_s = \sqrt{(G_{13}/\rho)} \approx 1{,}750$ m·s^{-1} plus 1 μs delay before the load was applied). During this time, the rotation map at 8 μs (Fig. 6.9a) shows that grid rotation is contained to the region closest to where the loading is applied. As the test progresses rigid-body rotation increases gradually from the impact edge (Fig. 6.9b), and eventually over the entire field of view. At $t = 18$ μs (Fig. 6.9c) the majority of the field has rotated by nearly 0.7°, and near the impact edge up to 1°. This level of rotation is significant enough to bias full-field maps, as shown in [109]. Grid rotation in this case requires careful consideration due to the potential compounding effect on strain and acceleration, from which stress is derived.

In order to visually quantify the bias induced by grid rotation on the underlying kinematics the

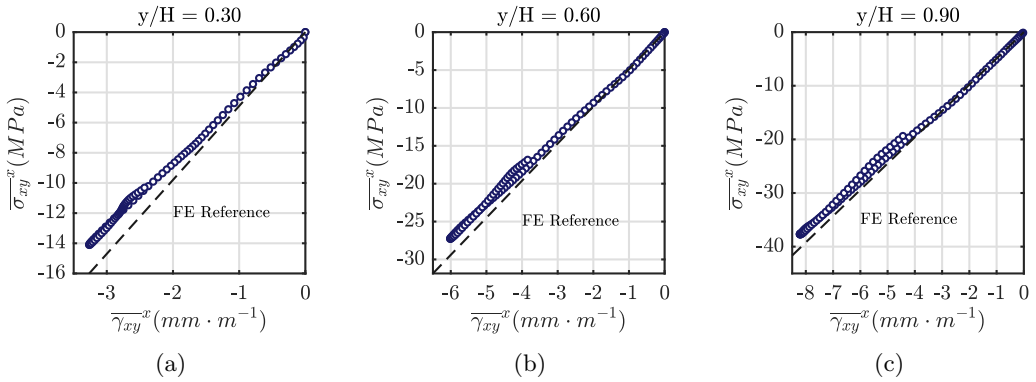

Figure 6.10: Shear stress-strain curves from noise-free image deformation simulations showing the bias caused by grid rotation at three cross-sections along the height of the sample. Note how the bias is introduced at lower strains further from the impact

fields taken directly from FE have been compared to those obtained by grid image deformation. It should be noted that these images also encode the systematic errors arising from the camera temporal/spatial resolution. Acceleration and strain fields derived from grid method displacements are compared to the simulated fields which are interpolated to the camera coordinates in Fig. 6.9d-6.9f and Fig. 6.9g-6.9i, respectively. From Fig. 6.9d-6.9i it is clear that there is minimal bias in the calculation of strain and acceleration prior to the onset of rigid-body rotation (t = 8 μs). For a period of time after the onset of rotation at the impact edge the difference between the fields from simulation and synthetic grid images is contained near the impact edge where shear loading is highest (up to $t = 13\ \mu s$). However, as rigid-body rotation ramps up, large differences are observed in shear strain fields and acceleration fields near the top edge at $t = 18\ \mu s$.

While it would appear that grid rotation does not become problematic until late in the test, reconstructed shear stress-strain curves at different cross-sections indicate that the effects are measurable early on and that the effect varies with position as shown in Fig. 6.10. For $y/H = 0.90$, the reconstructed behaviour first diverges from the simulated response at approximately 13 MPa, whereas at $y/H = 0.3$ this occurs almost immediately. It was found that the divergence of the stress-strain response roughly correlated with a width-averaged rotation of 0.10°. When width-averaged rotation reached this value, local grid rotations near the impact edge approached 0.7-1°, at which point the bias becomes measurable in stress strain curves. This agrees with the local grid rotation threshold of 1° cited by [109]. A width-averaged rotations of 0.10° was used to threshold the stress-strain data at each section in the sample to mitigate the effect of grid rotation on the stiffness identification. Width-averaged rotation is used rather than a local rotation threshold since strain and acceleration, from which stress is derived, are also averaged across the width.

The identification of the shear modulus along the height of the sample using a rotation threshold of 0.10° is shown in Fig. 6.11. Also shown is the identification from the full stress-strain response at each section to illustrate the reduction in bias by implementing a rotation threshold. The small oscillations in the identifications have a spatial frequency equal to that of the grid pitch and are believed to be caused by parasitic fringes in the strain maps arising from grid rotation as discussed in [109]. Even with the rotation threshold, it is very difficult to identify stiffness from areas near the top edge of the sample, but it can be identified reliably over roughly half of the sample closest to the top of the waveguide. With no rotation threshold the reference modulus is never identified successfully. Since rigid-body rotation begins once the shear wave reaches the top edge, the stress-strain response measured near to this edge becomes quickly

biased by rigid-body rotation. The signal-to-noise ratio in this region is also poorer than near the bottom of the sample, and therefore, the measurements are more sensitive to grid rotation. To reduce the systematic error on the identified shear modulus the spatial average is based on data from the lower half of the region of interest (y/H = 0.5-0.85). When no correction is applied the shear modulus is identified as 4.39 GPa (10% error), whereas the rotation threshold over a limited field of view results in an identified shear modulus of 4.8 GPa and a systematic error of 2%.

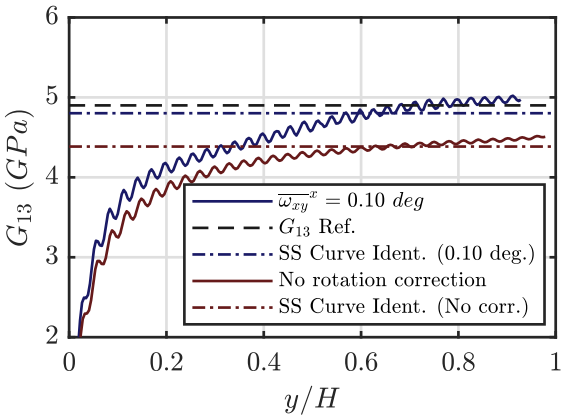

Figure 6.11: Spatial identification of shear modulus from synthetic images with no noise and no smoothing using the full stress-strain response, and with a width-averaged rotation threshold of 0.10°

Grid rotation influences the identifications with the manual and special optimised virtual fields in a similar way as shown in Fig. 6.12. The two virtual fields are able to roughly identify the reference modulus over a very limited window from t = 3-7 μs, but the identifications rapidly decrease between t = 7-9 μs as the rigid-body rotation of the gauge region begins. Following this, the identifications stabilise over a longer time frame (t = 10-20 μs). As will be shown later, the narrow range of time where the reference modulus can be approximately resolved (t = 3-7 μs) is much less evident in identifications from experimental images contaminated with noise. Therefore, when selecting optimal smoothing parameters, as discussed in the following section, the results are based on the time frame of t = 10-20 μs where the identifications are more robust. For perfect images, the manual and special optimised virtual fields identify the shear modulus to be 4.45 GPa and 4.52 GPa, representing a bias of 9% and 8%, respectively.

In the following section, the effects of grey level noise and spatial and temporal smoothing are added to the synthetic images to quantify their effect on the identification of the shear modulus with each of the VFM routines. This provides a robust way to select optimal spatial and temporal smoothing parameters, and obtain estimates of uncertainty associated with identifications from experimental images.

6.5.4 Selection of optimal smoothing parameters

The optimal parameters were determined as those which minimised the total error on the identification of G_{13} relative to reference value in the finite element model. The spatial smoothing windows considered here range from 0 to 69 pixels (standard deviation ranging from 0 to 17 pixels), and the temporal windows ranged from 0 to 21 frames. Note that spatial smoothing is applied to the displacement fields prior to spatially differentiating to calculate strain and temporal smoothing is applied separately to the raw displacement fields prior to temporally

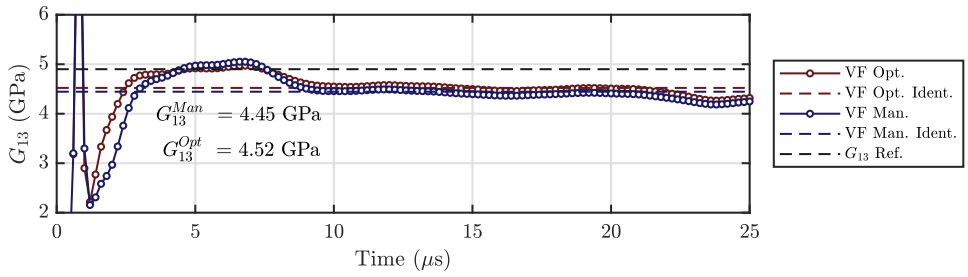

Figure 6.12: Temporal identifications of the interlaminar shear modulus using the manual and special optimised virtual fields approaches

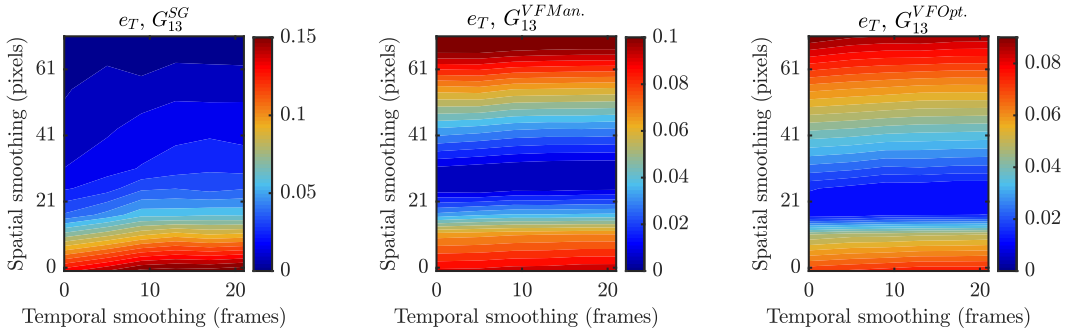

Figure 6.13: Image deformation sweep for selection of optimal smoothing parameters for processing experimental images - total error maps for the various identification approaches: (a) stress-strain curves, (b) manual virtual fields, and (c) optimised virtual fields

differentiating to obtain acceleration. Total error maps for each of the identification procedures as a function spatial and temporal smoothing windows are presented in Fig. 6.13.

Note that the total error on the identification of the shear modulus does not fall to zero when no smoothing is applied due to systematic errors from the camera (spatial and temporal resolution) as well as grid rotation as described in Sec. 6.5.3. Interestingly, the application of some spatial smoothing seems to compensate for the initial underestimation of the modulus from the special optimised virtual fields and stress-strain curve identifications. This same effect leads to a greater error on the manual virtual fields identification, which already overestimated the modulus when no smoothing was applied. The sensitivity to spatial smoothing is much larger than the sensitivity to temporal smoothing. In the case of identifications from stress-strain curves, this is likely due to low signal-to-noise in the strains used in the identification. The sensitivity to noise on acceleration is mitigated by the fact that the stress is calculated from a spatial average over the surface, whereas noise sensitivity will be higher for strain (*i.e.:* spatial smoothing) since strain is only averaged over a line. Moreover, as spatial smoothing increases a larger region is contaminated by filter edge effects near the edges of the sample. Based on the presented design study, the best compromise on total error for the special optimised virtual fields and stress-strain curve identifications is obtained by selecting a spatial smoothing window of 25 pixels and a temporal smoothing window of 5 frames. The estimated systematic error for identifications from special optimised virtual fields, manual virtual fields and stress-strain curves is 1.1%, 0.5% and 2.7% respectively. The typical measurement performance for experimental images processed with these smoothing parameters is listed in Table C.2.

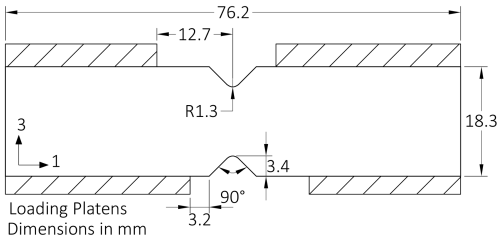

Figure 6.14: Schematic of Iosipescu specimens

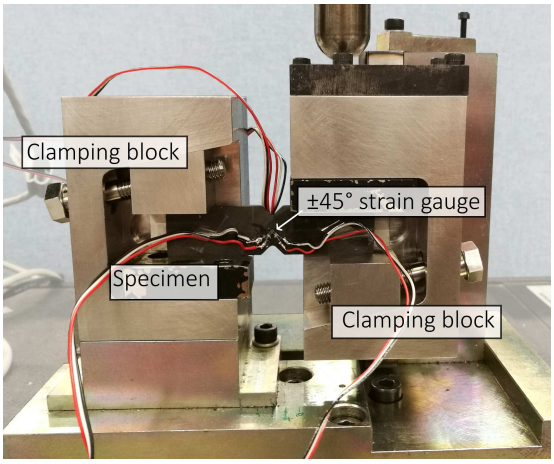

Figure 6.15: Rig used to perform Iosipescu shear tests with specimen installed

6.6 Materials and Experimental Setup

6.6.1 Quasi-static test setup

The MTM45-1/AS4-145 material selected for this study has been extensively characterised in [132] under quasi-static conditions. While the in-plane shear modulus is reported in [132] the interlaminar shear modulus is not. Therefore, to assess the strain rate sensitivity the quasi-static shear modulus was measured in-house using the quasi-static Iosipescu (or V-notch shear) test [145]. Five samples were cut from the 1-3 interlaminar plane using a diamond coated cutting wheel. The nominal dimensions were 76.2 mm × 18.3 mm (length × width) and the thickness of the samples ranged from 2.2 mm to 3.3 mm. The notches were waterjet cut according to the dimensions in Fig. 6.14.

All samples were instrumented on both sides with a Tokyo Measuring Instruments Lab (TML) FCA-1-23-120 0/90 strain rosette mounted at 45° in the centre of the notched region. The position and orientation of the gauge was checked by analysing images of the gauge taken with a microscope to ensure tolerances were within that used in [146]. The gauges were oriented within 45° ±0.6°, and within ±0.3 mm from the centre in the horizontal and vertical directions. The quasi-static stiffness was measured by loading the samples at a rate of 0.5 mm/min using the rig shown in Fig. 6.15.

Specimens were susceptible to through-thickness strain heterogeneity, as described in [142], since the loading was applied on the as-manufactured top and bottom surfaces of the laminate. Therefore, great care was taken when clamping the specimens in the fixture to mitigate this effect. Additionally, the specimens were loaded and unloaded several times to check the consistency of strain measurements. The specimen was taken out and re-installed when through-thickness effects were evident (opposite polarity of strain measurements on the front

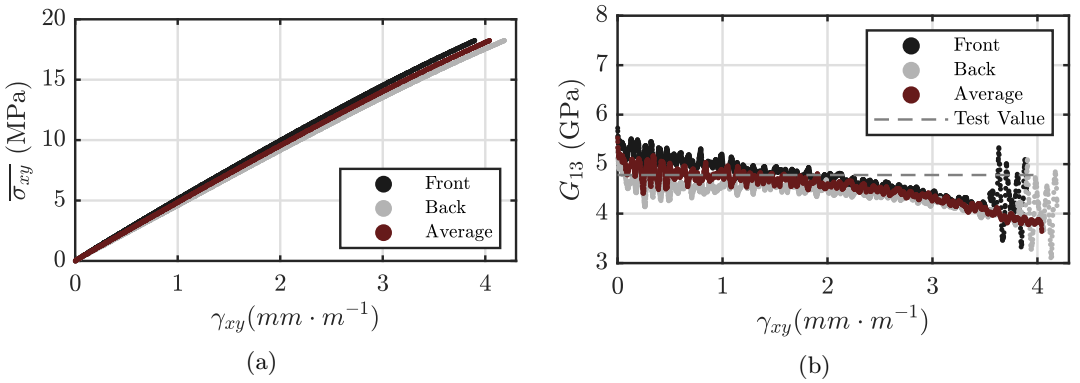

Figure 6.16: Results from Iosipescu shear tests for quasi-static characterisation of specimen #5: (a) stress-strain curves measured on front and back faces, and with back-to-back averaging, (b) evolution of tangent modulus with shear strain to determine shear modulus for the test. Note that a non-uniformity correction was applied to strains according to [146]

Table 6.4: Interlaminar shear modulus for MTM45-1/AS4-145 measured at quasi-static conditions

Specimen #	G_{13} (GPa)
1	4.91
2	5.05
3	5.17
4	4.77
5	4.78
Mean	4.93
Std. Dev.	0.17
COV (%)	3.5

and back face upon loading). This was repeated to eliminate slack in the fixture. Back-to-back strain measurements were used to account for the through-thickness heterogeneity, with the modulus taken from average stress-strain curves. A correction factor of 0.923 was applied to the measured modulus values according to [146] to account for strain non-uniformity over the gauge section. Representative examples of average shear stress ($\overline{\sigma_{xy}} = F/A_{notch}$) plotted against strain measured on each face and using back-to-back averaging are shown in Fig. 6.16a.

The strain threshold for identification of the shear modulus was determined by calculating the tangent modulus over a sliding strain window of 0.02% strain. At the onset of non-linearity a notable decrease in tangent modulus was observed as shown in Fig. 6.16b. The shear modulus for the test was taken as the average value up to strains where the tangent modulus decreased by more than 5% (between 0.1-0.2% strain for specimen #5 in Fig. 6.16). Table 6.4 summarises the measured shear modulus from all samples.

6.6.2 High strain rate test setup

All experiments were performed using the purpose-built gas gun and general experimental procedure described in [136]. The reservoir pressure was set for a nominal impact speed of 35 m·s^{-1}. The waveguide support stand was aligned to within 0.20 mm and 0.20° for position and angular alignments, respectively using the procedure outlined in [136]. Samples were cut as thin strips (nominally 2.5 mm in thickness), 57 mm in length from the 1-3 interlaminar plane of an 18 mm thick MTM45-1/AS4-145 laminate. Cuts were made with a Streurs E0D15 diamond saw with the automated stage set to a low feed rate of 0.1 mm·s^{-1} to reduce the likelihood of inducing machining defects. A thin coat of white paint (typ. 20 μm thick) was

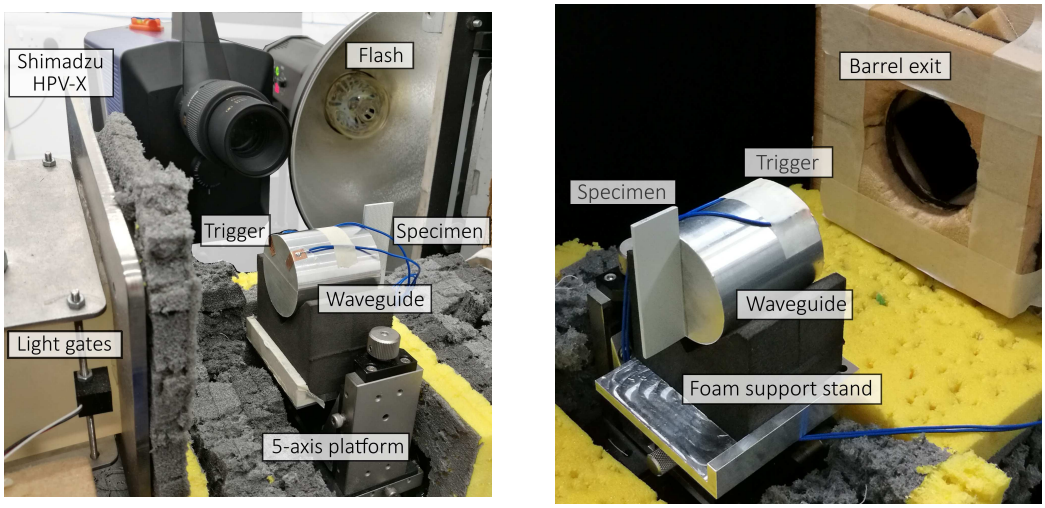

(a) (b)

Figure 6.17: Experimental setup used for all interlaminar tests: (a) camera and flash arrangement around the test chamber, and (b) mounted specimen supported on a test stand in the test chamber

first applied to the samples followed by black grids deposited onto the painted surface using a Canon Océ Arizona 1260 XT flat bed printer. The grids had an average pitch spacing of 0.337 mm. More information of the grid printing process can be found in [136]. Samples were bonded to a 45 mm diameter aluminium 7075-T6 waveguide using cyanoacrylate glue with a set square used for alignment during bonding. The bottom edge of the sample was aligned with the bottom of the waveguide.

A Shimadzu HPV-X camera with a Sigma 105 mm lens was used to image the region on the sample which extended above the top of the waveguide at a frame rate of 5 MHz. Lighting was provided by a Bowens Gemini 1000Pro flash triggered using the light gates as described in [136]. The camera stand-off was adjusted iteratively using a series of static images such that the grid (pitch = 0.337 mm) was sampled by exactly 7 pixels/period. To minimise the fill-factor effect the images were intentionally blurred as in [32, 37, 38]. Blurring was considered sufficient when no significant parasitic fringe patterns were visible in the strain fields calculated using a static image of the grid in the reference position, and an image with the camera displaced 1 mm out-of-plane. The optical setup and a specimen mounted on the support stand in the capture chamber are shown in Fig. 6.17.

6.7 Experimental Validation

6.7.1 Measured kinematic fields

This section presents full-field maps of acceleration and strain for a typical specimen at three time steps. The ϵ_{yy} fields are not included as the strains are below the noise floor due to the high lateral stiffness of the fibres. Raw images and maps of all displacement, strain and acceleration components are provided as supplementary material to this article.

Unlike the tension/compression configuration in Chapter 4, the pulse is not as distinguishable in the accelerations as the wave disperses into the part of the sample overhanging the waveguide. As the axial wave is applied to the material the shear loading is introduced beginning at the concentration at the top of the waveguide ($t = 8\ \mu s$). As the axial pulse reflects from

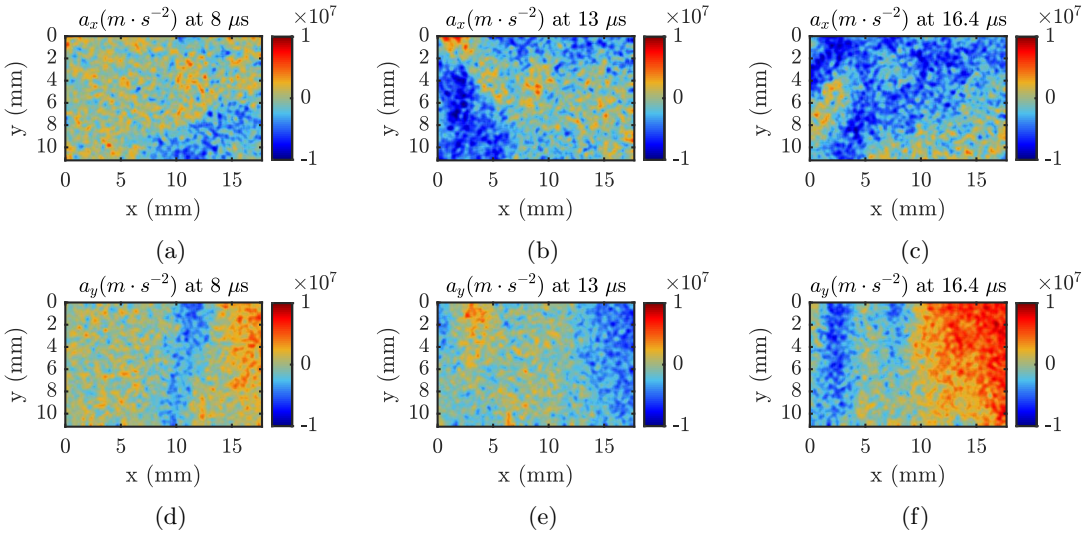

Figure 6.18: Acceleration fields (a_x, a_y) (m·s^{-2}) for specimen #1 measured at three time steps

the free-edge, the shear loading begins to increase and the acceleration fields become highly heterogeneous ($t = 13$ μs). The shear pulse lags behind the axial pulse due to the lower shear wave speed, resulting in a gradual build up of shear strain. The axial pulse traverses the specimen width approximately twice prior to reaching maximum shear strain, which is shown in the fields at 16.4 μs.

The rotation maps ($\omega_{xy} = 1/2(\partial u_x/\partial y - \partial u_y/\partial x)$) for specimen #1 are shown in Fig. 6.20 for the same three time steps. The map at 8 μs (Fig. 6.20a) shows a very similar behaviour to that predicted with the image deformation simulations, with grid rotation contained to the region closest to the loading prior to the shear wave reaching the top edge of the sample. The rotation gradually increases from the impact edge (Fig. 6.20b) towards the centre of the sample, and before rigid-body rotation becomes significant and rotation increases over the entire field of view. At $t = 18$ μs (Fig. 6.20c) the rotation reaches up to 1° at the loading edge. While it is difficult to directly compare the image deformation to the experimental maps the simulations appear to be a good representation of the physical behaviour.

The acceleration maps (Fig. 6.18) highlight the inertial effects present in the test, with values reaching almost 10^7 m·s^2. While such inertial effects would be problematic with existing test methods, the use of full-field measurements and the VFM allows us to identify the shear modulus directly from heterogeneous fields, as demonstrated in the following section.

6.7.2 Reconstructed stress-strain curves

Shear stress-strain curves reconstructed using the stress-gauge equation (Eq. (3.50)) and width-averaged shear strains ($\overline{\gamma_{xy}}^x$) are shown at four cross-sections for specimen #1 and #4 in Fig. 6.21. From impact speed of approximately 35 m·s^{-1} it was possible to consistently generate up to 60 MPa of width-average shear stress in the sample. The effect of grid rotation in the stress-strain response is most notable at $y/H = 0.72$ and 0.90, where the response artificially softens beyond 3-4 mm·m^{-1}. While it is not possible to reliably characterise the full material behaviour (because of spurious grid rotation), the measured stress-strain response does provide some indication that onset of non-linear material behaviour is delayed at high strain rates. For example, a linear behaviour is measured up to 4 mm·m^{-1} at $y/H = 0.90$ for specimen #1 (Fig. 6.21d), whereas non-linearity was measured in the quasi-static tests beyond 2 mm·m^{-1}

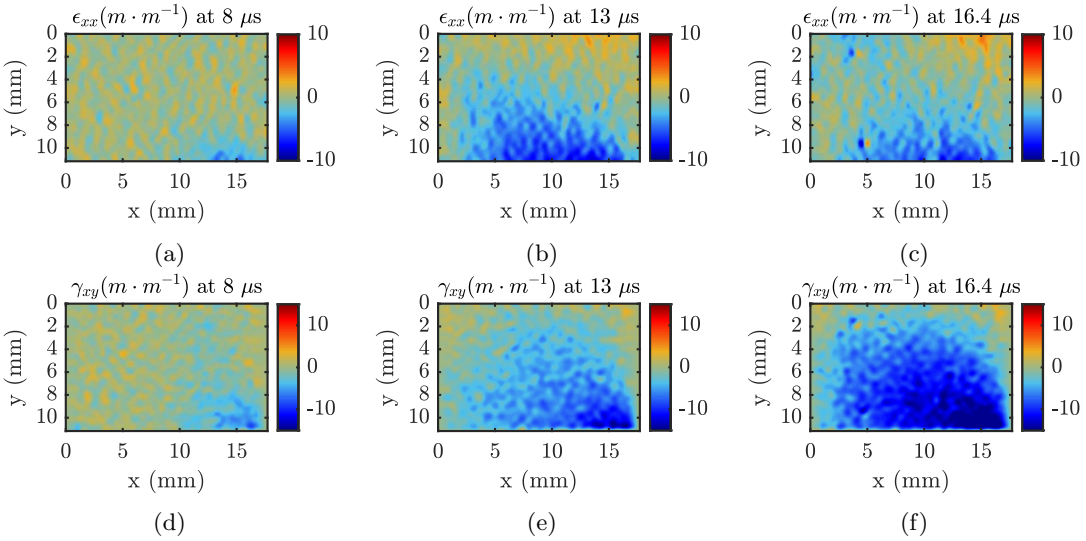

Figure 6.19: Strain fields (ϵ_{xx}, γ_{xy}) (mm·m^{-1}) for specimen #1 measured at three time steps

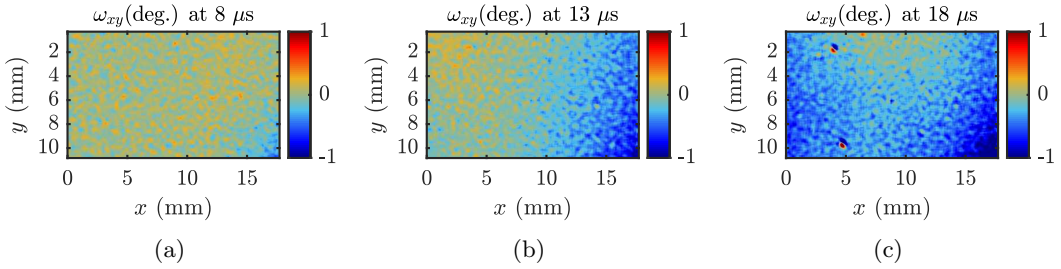

Figure 6.20: Rotation fields (ω_{xy}) (deg.) for specimen #1 measured at three time steps

(Fig. 6.16). Using a grid rotation threshold described in Sec. 6.5.3, it is possible to characterise the initial linear elastic behaviour of the material from the stress-strain curves as described in the following section. Identification of the shear modulus with the manual and special optimised virtual fields are also presented.

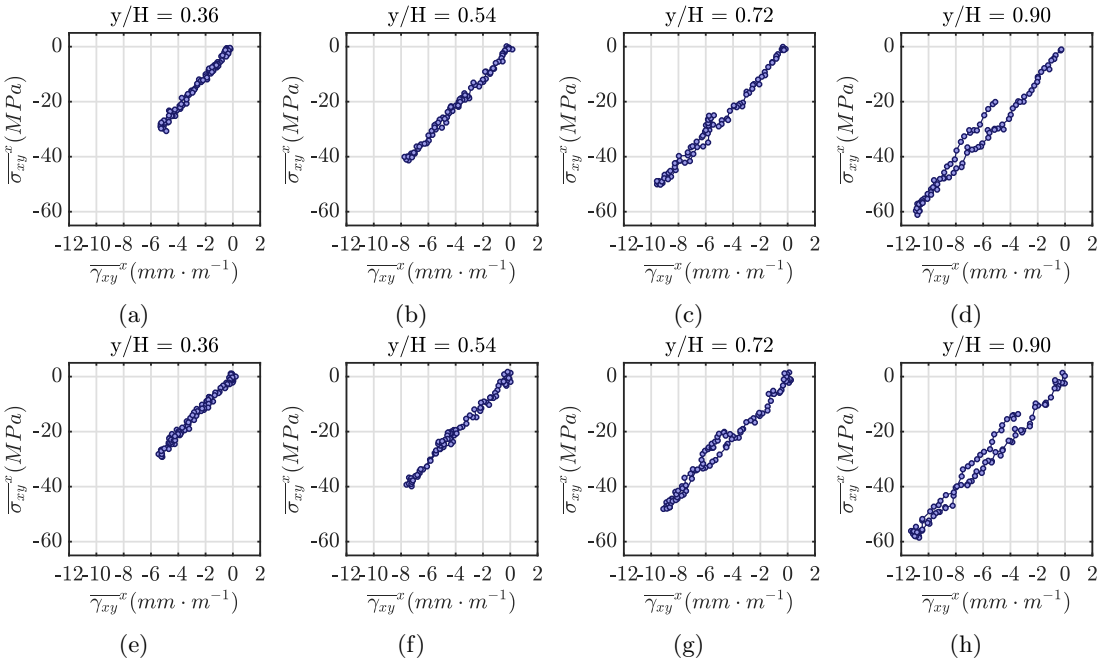

Figure 6.21: Stress-strain curves for specimen #1 ((a)-(d)) and #4 ((e)-(h)) reconstructed from measured strain and acceleration fields at different positions along the length of the sample

6.7.3 Stiffness identification

The shear modulus is identified from the stress-strain response measured at each cross-section using the slope of a linear regression fit up to 0.10° of width-averaged grid rotation. The spatial distribution of the shear modulus along the length of each sample is shown in Fig. 6.22a. Note that data is excluded within one spatial smoothing kernel at the free edge and impact edge. The spatial identification of the shear modulus is remarkably consistent across all five samples. The identification monotonically increases towards $y/H = 1$, as shown by the image deformation simulations in Fig. 6.11. To mitigate the bias on the identification, the average value over y/H = 0.50-0.85 is taken as the value for the test. Over all samples an average value of 5.69 GPa was measured with remarkable consistency (coefficient of variation (COV) = 3.7%) compared to reported measurements in the literature at similar strain rates. For example, in [10, 44, 45] the range of values reported varied by up to approximately 10-30% relative to the mean shear modulus over all tests.

The shear modulus was also identified from the manual and special optimised virtual fields. Note that both methods were used to identify the shear modulus using spatial smoothing of 25 pixels and temporal smoothing of 5 frames. The temporal identifications from each of these approaches are shown in Fig. 6.22b and 6.22c. Note that data at the start of the test is excluded where the signal-to-noise ratio is low. Similar to the stress-strain curves identifications, the temporal evolution of the shear modulus with each set of virtual fields are very consistent across all samples. As predicted by the image deformation simulations, the manual virtual fields over-predict the shear modulus compared to the special optimised virtual fields. The shear modulus value for each test was taken as the average temporal identification over t = 14-20 μs where the identification was most stable. This resulted in an average shear modulus over all samples of 5.82 GPa (COV = 3.1%) and 5.51 GPa (COV = 2.9%) from the manual and special optimised virtual fields, respectively. A summary of the measured shear modulus on all six samples is provided in Table 6.5.

The shear strain-strain rate space populated by the test is shown in Fig. 6.23 between t = 10-25 μs when the signal is highest. This test specimen primarily populates strain up to 5 mm·m^{-1} and strain rates up to 1.5×10^3 s^{-1}; however strains up to 12 mm·m^{-1} and strain rates up to 3.5×10^3 s^{-1} are measured. The range of strain rates seen by the material makes it challenging to assign a single strain rate value to the measurements of shear modulus. Therefore, two metrics are provided as effective strain rates for the measurements: 1) a shear-strain weighted strain rate ($|\overline{\dot{\gamma}_{xy}}^{W}|$, Eq. (6.1)) and and 2) the peak width-averaged shear strain rate ($\overline{\hat{\dot{\gamma}}_{xy}}^{x}$). The weighted average is believed to be a more representative measure of the effective strain rate since more emphasis is given to the areas with higher strain magnitude, which contribute most to the identification of the shear modulus. Both strain rate values reported in Table 6.5 represent the maximum of each metric over $t \leq 20$ μs (threshold for manual and optimised virtual fields identifications), excluding data from within one smoothing kernel of the edges of the field of view.

$$\overline{\dot{\gamma}_{xy}}^{W} = \frac{\sum^{S} \gamma_{xy} \cdot \dot{\gamma}_{xy}}{\sum^{S} \gamma_{xy}} \tag{6.1}$$

Since the spatial and temporal smoothing parameters were selected to minimise the error on the special optimised virtual fields identification, this value is used to comment on the effect of strain rate on the shear modulus. The measured averaged stiffness of 5.5 GPa at an average strain rate on the order of 1.6×10^3 s^{-1} represents a 12% increase compared to the quasi-static modulus

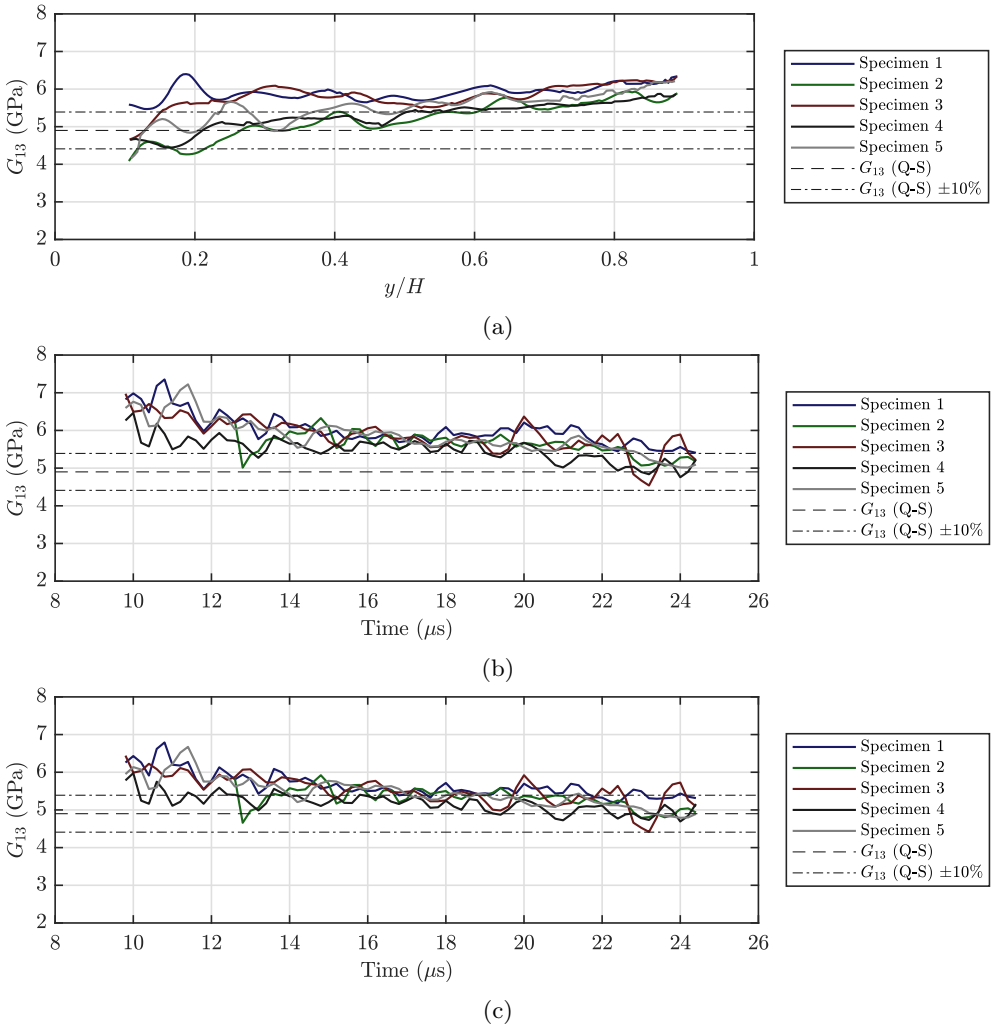

Figure 6.22: Identification of the interlaminar shear modulus, G_{13}: (a) fitting stress-strain curves using a width-average rotation threshold of 0.10°, (b) manual virtual fields (Eq. (3.53)), and (b) special optimised virtual fields (Eq. (3.55))

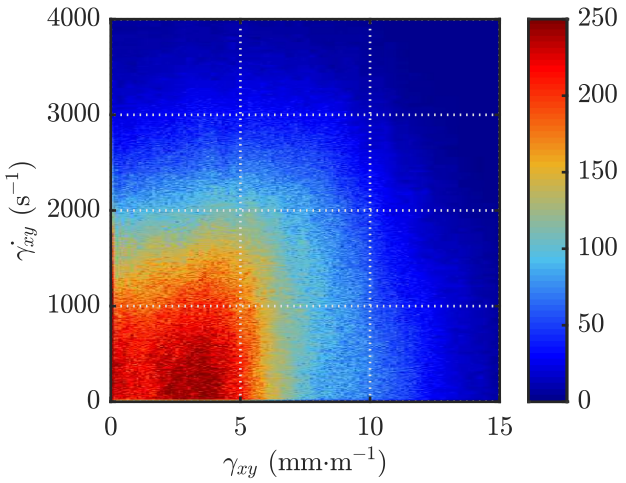

Figure 6.23: Shear strain-strain rate space populated by specimen #1, excluding one smoothing kernel plus one pitch from the edges, between t = 10-25 μs where the signal is highest. The colour map denotes number of occurrences. Note that strain rate on average over the field reaches 1×10^3 s^{-1} and locally up to 3.5×10^3 s^{-1}

Table 6.5: Measured high-strain-rate interlaminar shear modulus for MTM45-1/AS4-145

Specimen	G_{13}^{SS} (GPa)	G_{13}^{M} (GPa)	G_{13}^{O} (GPa)	$\lvert\overline{\dot{\gamma}_{xy}}^{W}\rvert$ (s^{-1}) ($\times 10^3$)	$\overline{\hat{\dot{\gamma}}_{xy}}^{x}$ (s^{-1}) ($\times 10^3$)
1	5.96	5.98	5.63	1.7	-2.1
2	5.55	5.85	5.58	1.3	-1.6
3	5.89	5.91	5.56	1.8	-2.4
4	5.54	5.57	5.23	1.6	-1.9
5	5.53	5.63	5.53	1.8	-2.4
Mean	5.69	5.82	5.51	1.6	-2.0
SD	0.21	0.18	0.16	0.22	0.37
COV (%)	3.7	3.1	2.9	13.3	18.1
Diff. to QS (%)	16	19	12	–	–

of 4.9 GPa (see Table 6.4). These experiments demonstrate the usefulness of the IBII test methodology, which can provide remarkably consistent measurements of the shear modulus from heterogeneous fields and at strain rates where existing test methods are unreliable due to inertial effects. The measured strain rate sensitivity is difficult to compare with the literature as, to the authors' knowledge, no interlaminar HSR data are available for AS4-145/MTM45-1. Moreover, the limited studies in the literature using the SHPB can only report an 'apparent modulus' since it is necessary to assume the loading is pure shear. The strain rate sensitivity measured here does fall within the range reported for unidirectional composites for in-plane [147] and interlaminar planes [13, 147]. However, the data is highly scattered in these studies (sensitivity between -14% and +33%) and does not offer a meaningful comparison. The measured values of G_{13} from the three VFM approaches fall within 5% of each other. This comparison can be considered as a type of self-validation of the measurements reported here, however, it would be interesting to test another composite system with the proposed IBII test for comparison.

6.8 Summary

This chapter has presented the design and experimental validation of an IBII test to measure the interlaminar shear modulus at strain rates on the order of 1.6×10^3 s^{-1}. This represents an important first step in establishing a new set of IBII tests aimed at stiffness identification at high strain rates. The key results from this study are summarised below:

- A simple short-beam shear configuration was used to activate the interlaminar shear behaviour and measure the shear modulus at high strain rates.

- Explicit dynamic simulations were used to perform a design study to identify the optimal test configuration based on available waveguide and projectiles.

- Pulse duration was found to have a large influence on the amount of shear introduced into the sample. A longer pulse delayed the onset of tensile axial loading, allowing more shear to build up in the sample.

- An image deformation framework was presented to quantify the effects of grid rotation, spatial resolution and smoothing on the identification of the shear modulus using three different virtual fields method routines.

- A new set of special optimised virtual fields was developed and successfully validated for the direct identification of the interlaminar shear modulus.

- The proposed test configuration was experimentally validated. An average shear modulus of 5.5-5.8 GPa (COV = 2.9-3.7%) across all three identification routines was measured at strain rates on the order of 1.6×10^3 s^{-1}, which represents an increase of 12% compared to the quasi-static modulus.

This study highlights the usefulness of image-based test methods for identifying the shear modulus from heterogeneous, dynamic kinematic fields. The proposed test configuration has shown that the shear modulus can be measured with remarkable consistency at strain rates that are well above what is possible with existing test methods. The next section presents some limitations of the IBII tests identified from this work, and discusses some of the exciting prospects for future development of the IBII test for more comprehensive characterisation of composites at high strain rates.

Chapter 7

Discussion and Conclusions

This project exemplifies the potential of test methods developed around full-field imaging to expand the range of strain rates where composite interlaminar properties can be reliably characterised. As part of the test development process, some limitations have been identified, which are discussed in this section. This is followed by a summary of possible future investigations to improve the test method and alternative test configurations for more comprehensive material characterisation. Concluding statements are then provided, along with a list of contributions resulting from this project.

7.1 Limitations

7.1.1 Limitations on strain rate

Since this test method relies on surface measurements it is necessary to assume that the test is two-dimensional. This work has shown that with careful control of the impact alignment, this assumption holds over much of the sample up to strain rates on the order of 3-5×10^3 s^{-1}. While the exact upper threshold on strain rate is unknown at this point, it is estimated to be on the order of 10^4-10^5 s^{-1} in the shock regime where the stress state becomes inherently three-dimensional. However, in the current setup the need for an insulating tape layer between the trigger and waveguide, and a glue layer between the sample and waveguide limits the upper bound of strain rate to approximately 5×10^3 s^{-1} for stiffness identification. To probe higher strain rates, it will be necessary to consider alternative triggering techniques that remove this low impedance layer from the front of the waveguide or perhaps stiffer materials for the waveguide/impactor. Some possible configurations include: strain measurement from a strain gauge on the waveguide, or photon Doppler velocimetry measurements on the back face of the waveguide. On the contrary, the reliance on surface accelerations to act as the dynamic load cell for stress reconstruction and stiffness identification with the VFM provides a lower bound on the strain rate that can be considered with this test. The design framework and image deformation simulations presented in Chapter 4 could easily be used to investigate this by reducing the simulated impact speed until stress can no longer be reliably reconstructed from the synthetic images. The limiting strain rate for failure stress will likely be higher due to the need for a strong pulse to induce enough stress to cause the material.

7.1.2 Grid defects

The presence of grid defects can introduce a bias on the identification of stiffness parameters using the optimised virtual fields routines, as was shown in the first major study presented in this thesis (see Chapter 4). Grid defects introduce a localised areas of artificially high signal in contrast to the lower signal associated with the underlying material response. The effect is amplified when defects occur near the edges of the specimen and interact with the data extrapolation procedures. Grid defects are also more of a concern with the interlaminar IBII test due to the higher magnification, where potentially more measurement points can become contaminated by the defect. Grid defects are thought to contribute to the larger temporal variation of the identifications of E_{33} and Q_{23} from experimental images compared to image deformation simulations, which do not take into account grid defects. However, there are a number of other factors that are not considered in the simulations and therefore, further work is required to isolate and quantify the effect of defects on the identification. Image deformation simulations serve as a useful tool for conducting such investigations. For example, systematic studies on defect position, size and density can be performed by corrupting grey-levels of synthetic images based on defect profiles from real grid images. The corrupted synthetic images may then be processed using the same procedure as experimental images to quantify the influence on identified stiffness parameters.

The first phase of this project showed that printed grids are the preferred alternative to bonded transfer grids for minimising the number of grid defects. However, the current technology is limited to grid periods on the order of 0.3 mm, which will not be enough either for higher spatial resolution cameras or for higher magnification (smaller specimens). Other deposition routes like the one recently proposed by Brodnik *et al.* [141] could be pursued.

7.1.3 Grid rotation

While grid rotation is not a significant issue for the standard edge on IBII configuration shown in Chapters 4 and 5, it becomes a significant problem when trying to induce shear deformation as described in Chapter 6. Grid rotation in the IBII shear test was too large for the grid method to reliably resolve shear strains above 4 mm·m^{-1}. It also introduced significant errors in the shear modulus identification from stress-strain curves. Reducing these effects will be critical for efforts to characterise the non-linear behaviour at high strain rates. One potential approach is to intentionally misalign the grid as was done by Sur *et al.* [108], or use a Gaussian window, rather than a bi-triangular window in the grid method. The disadvantage is that the Gaussian window requires the use of a larger subset of pixels to be used, which potentially enhances the missing edge data issue for such low resolution cameras. While these options may extend the upper limit of strain that can be reliably measured with this configuration, it is unlikely to eliminate the problem and alternative test configurations may need to be considered. For example, it may be possible to modify the specimen geometry or waveguide to introduce a more symmetric shear load to reduce rotation of the grid.

In this work, and previous studies using the IBII test [32], the grid method was chosen over digital image correlation (DIC) due to the better trade-off between spatial and measurement resolution. However, DIC does not suffer from issues with in-plane rotation and in this case, it may be worth-while to sacrifice spatial resolution in order to reliably measure the non-linear behaviour of the material.

Image deformation serves as a useful tool for evaluating new configurations and/or grid method

parameters. It will also be essential for quantitative studies of systematic and random error, particularly as DIC measurements involve many parameters (subset size, step, shape function, interpolation, matching criterion and image pre-smoothing) on top of spatial and temporal smoothing, so a full optimisation on the model of that presented in [105] will be necessary. This is especially relevant for the development of future tests where stress concentrations may be used to activate more heterogeneity and camera resolution becomes more critical.

7.1.4 Reconstructing heterogeneous stress fields

This work presented two ways to reconstruct stress from acceleration: 1) average stress along a cross-section using the stress-gauge equation, and 2) a linear approximation across the height of the sample using the linear stress-gauge equation. Combining average stress with average strain is appropriate for measuring the interlaminar elastic and shear moduli on resin systems which exhibit a significant linear-elastic response. However, this approximation of stress is less appropriate when the material undergoes localised non-linear deformation, or when the stress distribution varies across the height of the sample. In the case of the IBII tension test, the stress reconstructed with the linear stress gauge equation can be combined with local strains to approximate the local stress-strain behaviour and failure stress. However, the reliability of the stress reconstruction depends on the assumption that the stress field varies linearly across the sample, which is not the case in the IBII shear test. Therefore, more elaborate stress reconstruction methods must be considered to avoid 'smearing' the non-linear behaviour in the stress-strain response, and to obtain an improved estimate of stress at the failure location. This IBII shear test configuration has stress-free boundary conditions at the vertical edges, which can be combined with the average stress computed from the stress-gauge equation (Eq. (3.50)) to reconstruct a parabolic approximation of the shear distribution at every horizontal cross-section according to:

$$\sigma_{xy}^{PSG} = c_2 x^2 + c_1 x + c_0 \tag{7.1}$$

The stress-free boundary condition at $x = 0$ and $x = L$ yields $c_0 = 0$, and $c_1 = -c_2 L$. To solve for c_1 and c_2 the integral of the average shear stress over the width is equated to the integral of the reconstructed parabolic shear stress distribution as in Eq. (7.2). Recall that $\overline{\sigma_{xy}}^{x} = \rho y_0 \overline{a_x}^{S}$.

$$\overline{\sigma_{xy}}^{x} L = \int_0^L (c_2 x^2 + c_1 x) dx = \frac{1}{3} c_2 L^3 + \frac{1}{2} c_1 L^2 \tag{7.2}$$

Solving these equations as a system of linear equations for c_2 and c_1 gives the following reconstruction of a parabolic shear stress profile (σ_{xy}^{PSG}) across the width of the sample:

$$\sigma_{xy}^{PSG} = \frac{-6x}{L^2} \cdot \overline{\sigma_{xy}}^{x} \big(x - L\big) \tag{7.3}$$

The parabolic stress function can be evaluated at each position and time step to provide temporally resolved, but spatially approximated stress maps. This can be combined with local strains to populate a shear stress-shear strain space. Measurements from the presented shear test configuration show that the shear strain fields do not resemble a parabolic profile until later in the test ($t \geq 18\ \mu s$ in Fig. 6.19). Therefore, the parabolic stress-gauge equation is not appropriate for stiffness measurements, but may offer potential to better capture non-linear behaviour at later stages in the test. It will also provide a better estimate of failure stress compared to the average stress-gauge equation, and image deformation simulations can be used to establish the uncertainty on reconstructed values.

Another possible approach is to assume a model for the non-linear material behaviour and identify the parameters of the model using the VFM. This constitutive model can then be used to convert strain maps to stress maps. The benefit of the IBII test is that the appropriateness of constitutive models can be assess by comparison with stresses reconstructed directly from acceleration. Chapter 4 showed that stress reconstructions are very useful in detecting the onset of damage/fracture before it is obviously evident in strain fields. Seghir *et al.* [148] have also shown numerically that it is possible to reconstruct quasi 'full-field' stress maps from acceleration fields, though this has yet to be implemented on experimental data. Alternative 'data-driven' approaches are also underway, and have recently been applied to transient dynamics [149].

7.1.5 Reliance on laminate compressive strength for shear loading

The peak width-average shear stress in the IBII shear test reached approximately 60 MPa, which provided enough signal to identify the shear modulus, but not to cause fracture under the applied shear load. The easiest way to increase the shear load is to impact the material at a higher speed. However, a small set of trial shots showed that above 50 $\mathrm{m{\cdot}s^{-1}}$ the magnitude of the input compression stress exceeded the strength of the material. This resulted in local crushing near the waveguide interface and a significant reduction in shear stress.

Tabs were bonded to a few trial samples to try and reduce the axial loading in the material. To minimise the shear concentration created by the change in cross-section between the tabs and the specimen, the tabs were machined from the same material and from the same interlaminar plane so that the wave speed in the tabs matched that of the sample. It was shown experimentally that adding tabs enabled the impact speed to be increased further by almost 20 $\mathrm{m{\cdot}s^{-1}}$ before compression failure occurred. However, the average shear stress of 75 MPa was still insufficient to cause fracture. The combination of compression and shear will act to enhance the strength of the material and therefore, the constant cross-section design presented in this work may not be suitable for introducing fracture under shear without having premature failure near the loading point. Therefore, geometrical features may be required to concentrate the shear loading to fracture the material.

7.2 Future Work

This work shows that new test methods based on full-field measurements are very promising for measuring interlaminar properties at high strain rates. This enables data to be collected at strain rates where current techniques are unreliable. The capability of full-field measurements will only increase as ultra-high-speed camera technology improves. This will create additional opportunities for the development of advanced tests, and more complete characterisation of composite materials at high strain rates. This section attempts to highlight a few of the major opportunities for future development of the test method.

7.2.1 Identification of multiple interlaminar stiffness parameters from a single test

The main objective going forward is to design tests that provide the high-strain-rate interlaminar transverse and shear moduli from a single test. One potential configuration is an 'off-axis'

interlaminar specimen, similar to that used for high-strain-rate in-plane stiffness characterisation of composites [31]. Off-axis specimens provide a relatively straight-forward way to activate axial and shear loading, and may provide opportunity to identify the interlaminar transverse and shear moduli from a single test. This concept may also be combined with notches, holes, *etc.* to enhance the activation of multiple stiffness parameters. It may also be possible to use the interlaminar IBII tensile sample used in the first phase of this project with the impact load applied over half of the height, or an impact with a slight pitch misalignment to introduce combined axial and shear loading. The VFM (including stress-gauge based stress-strain curves) can then be used to identify the activated stiffness parameters from the heterogeneous deformation fields as in [31]. In both cases image deformation simulations would be required to evaluate the effect of limited spatial resolution on the measurement of heterogeneous deformation fields.

7.2.2 Effect of camera resolution and smoothing on failure stress identification

This work presented the use of image deformation simulations to assess the bias introduced on stiffness identification, but did not address the effect on failure stress estimates from the linear stress-gauge equation. The temporal differentiation required to obtain acceleration from displacement, as well as temporal smoothing will introduce a temporal bias on acceleration maps. This can be investigated using a similar image deformation routine to that presented in this work by generating a set of images based on a finite element model with a layer of cohesive elements with a defined strength. The bias is then calculated as the difference between the model cohesive strength, and failure stress obtained from the linear stress-gauge. Processing images with a range of smoothing windows also provides a way of selecting optimal parameters that minimise this bias. This will be important to quantify for future efforts to begin populating failure envelopes.

7.2.3 Identification of a strain rate sensitive constitutive law

Assigning a single strain rate to the measured properties is difficult with the IBII test due to the heterogeneous nature of the fields. This is unavoidable when testing at high strain rates when inertial effects are significant. While this is also problematic for existing techniques, full-field measurements create the potential to exploit the heterogeneity in strain rate fields. For example, the loading introduced with the IBII shear test was found to populate a vast range of strains and strain rates (strains up to 12 $mm{\cdot}m^{-1}$, strain rates up to $3.5{\times}10^3$ s^{-1} - see Fig. 6.23). For materials that exhibit a stronger strain rate sensitivity (*e.g:* composite systems with a thermoplastic matrix) the wealth of combinations of strain and strain rate seen by the material may provide enough information to identify a full strain rate sensitivity law using the VFM from a single test. One approach is to formulate the unknown stiffness parameters as a function of strain rate in the optimised virtual fields routine, or with the recently developed sensitivity based virtual fields [150, 151]. The potential of this approach can be explored using finite element modelling with a prescribed strain rate dependent material model, combined with synthetic image deformation routines to validate the identification of the model coefficients with the VFM.

7.2.4 Characterising non-linear material behaviour in shear

This test also provides opportunity to characterise the non-linear behaviour in shear at high strain rates. By assuming a model for the non-linear material behaviour, it should be possible to identify the parameters of the model using the VFM as in [152] for instance. Image deformation will be instrumental in selecting new test configurations which sufficiently activate the non-linear response for reliable identification with the VFM. It could then be used to quantify errors introduced by the camera and full-field measurement technique, and select spatial and temporal smoothing for optimal identification of the model parameters.

7.2.5 Extension to thinner specimens

A thick laminate was used to validate the IBII test concept for interlaminar characterisation to allow for direct imaging of the kinematic behaviour of the material. This significantly simplifies the test but properties identified from thicker laminates may not be representative of those from thinner laminates due to size effects. Therefore, it is of interest to try and extend the test method for characterising thinner laminates. The minimum thickness for direct imaging with the current experimental setup is limited by grid size and camera stand-off restrictions from the capture chamber walls. However, it may be possible to investigate the interlaminar stiffness of thinner laminates using a similar configuration to that adopted for high strain rate testing of adhesives [153]. In this configuration, aluminium tabs were bonded together with the adhesive, and full-field measurements of displacement on each tab near the bond line were used as a strain gauge for the adhesive strain (Fig. 7.1). A piecewise form of the stress-gauge equation was formulated to extract longitudinal stress within the bond line directly from measurements of acceleration made over the surface. A similar configuration may be used as a means of collecting preliminary stiffness measurements on thinner laminates, by substituting a thin laminate for the adhesive layer in the configuration shown in Fig. 7.1.

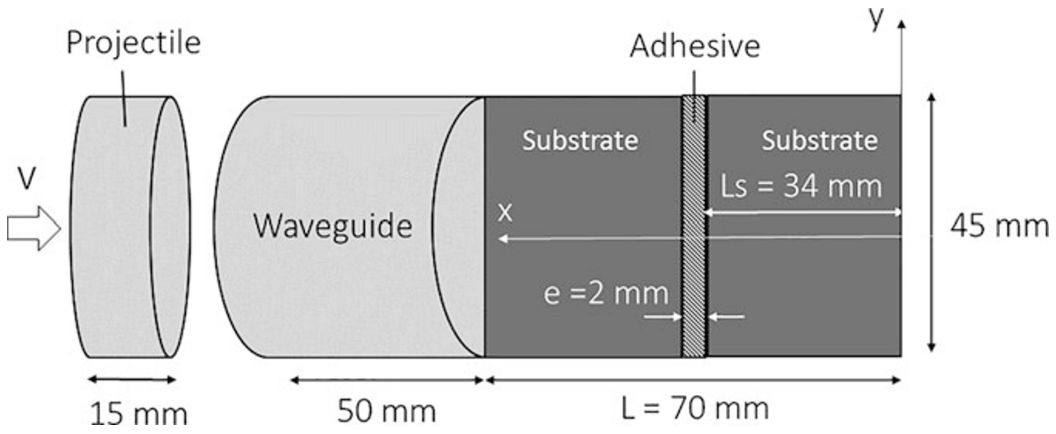

Figure 7.1: Schematic of test configuration used to measure elastic modulus and strength of adhesives, which could be implemented for preliminary stiffness and failure stress measurements for thinner laminates. Taken from [153]

7.2.6 Investigate the effect of secondary sources of misalignment in the impact chain

A key contribution of this work was the development of an alignment procedure that reduced the out-of-plane loading applied to the sample from misalignment of the waveguide and the

projectile. It may now be possible to investigate 'secondary effects' that may contribute to the residual three-dimensional loading measured very near to the impact edge (see Sec. 5.4.1). These include: specimen manufacturing quality (edge squareness) and alignment on the waveguide, the type of glue used to bond the specimen to the waveguide, and sample thickness. The most prominent secondary effect is the alignment of the sample on the waveguide, as this may interact with any residual projectile misalignment to amplify the three-dimensional loading. It is likely that this contributed to the scatter in severity of three-dimensional effects measured between samples with back-to-back cameras. The effect of this alignment could be studied by simulating the impact with a 3D model, and using experiments with intentional misalignment. More rigorous alignment procedures could be developed to reduce, and better control the waveguide misalignment. This would allow more of the sample to be used for stiffness and failure stress identification with the current interlaminar IBII tension configuration. Alternative impact arrangements may also be considered to expedite the alignment and reduce variability in the positioning of the waveguide on the support stand. It would be beneficial to increase the length of the waveguide to allow more time for the wave to even out before entering the sample. This could be combined with an arrangement where impact occurs nearer to the barrel exit to reduce variability in projectile flight.

7.2.7 Alternative test configurations for failure under multi-axial stress

Full failure envelopes at high strain rates are highly sought after for the design of composite structures. Based on the progress made in this work, the next logical point to target on the failure envelope is the shear strength. In the current interlaminar IBII shear test configuration, material non-linearity and strengthening under combined compression/shear makes it challenging to induce failure. Therefore, more sophisticated configurations may need to be considered to concentrate the shear loading over a smaller region of the sample. In the interlaminar planes the smaller specimens impose restrictions on the design space. In dynamics it is very difficult to obtain a state of pure shear stress and therefore, the idea would be to develop tests which provide fracture under combined compression/shear, and tension/shear to infer the shear strength of the material after fitting a failure model. With full-field measurements and the VFM it should be possible to quantify the combined stress at failure rather than assuming pure shear stress as is required with existing test methods (see ideas proposed in Sec. 7.2.1). The current shear test configuration is unable to produce sufficient shear loading to cause failure in the sample. The most obvious first step is to consider the combination of tabs and geometrical stress concentrators for the determination of failure stress. The incorporation of geometrical stress concentrators opens up a whole new design space, which can be explored using simulated experiments to optimise the number of notches, size, and placement and potentially probe different regions on the failure envelope. Again, the image deformation framework used in this work will be instrumental in evaluating new test configurations and taking into account the limited spatial resolution of current ultra-high speed cameras.

7.3 Conclusions

In this work, a new set of IBII tests were developed for characterising high-strain-rate constitutive properties of a carbon fibre-reinforced epoxy laminate in through-thickness tension/compression and shear. The idea was to use an impact from a projectile to introduce a dynamic load into the material. The impact creates a compressive pulse in the sample that travels towards the free

edge. At the free edge, it reflects as a tensile pulse, which unloads the material. For materials with greater strength in compression than in tension, this can be exploited to create a spall fracture in the sample using the reflected pulse. An ultra-high-speed camera was combined with the grid method to calculate full-field maps of displacement, from which strains and accelerations were derived. Various VFM identification routines were developed to identify stiffness and failure stress directly from the measured fields at strain rates on the order of several thousand s^{-1}.

In order to explore the design space of the IBII tests it was necessary to develop a parametric simulation tool in ABAQUS/Explicit. This was used to select experimental parameters such that the reflected tensile stress pulse was sufficiently high to cause fracture without damaging the material with the initial compressive stress wave. Simulations were also used to generate a set of kinematic fields based on a known input constitutive behaviour to verify the VFM identification routines. As part of this work, a new set of special optimised virtual fields were developed to isolate the interlaminar elastic modulus, E_{33} from the other orthotropic stiffness parameters. A key outcome from the first phase of the work was the integration of simulations into an image deformation framework to rigorously quantify the experimental uncertainties in the IBII test resulting from spatial and temporal smoothing, lighting intensity, imaging resolution, frame rate, and camera grey-level noise. An experimental campaign with 20 interlaminar specimens demonstrated that the proposed test configuration was able to provide consistent measurements of the interlaminar stiffness parameters and tensile failure stress from the same test. An average interlaminar elastic modulus of 10.3 GPa was identified across all 1-3 plane specimens using reconstructed stress-strain curves, and 10.5 GPa using the new reduced special optimised virtual fields approach. This represents an increase between 30-33% compared to quasi-static values, at strain rates on the order $3.5{\times}10^3$ s^{-1}. The average tensile failure stress over all specimens was measured to be 115 MPa at peak average strain rates on the order $7{\times}10^3$ s^{-1}, corresponding to an increase of approximately 129%, compared to quasi-static values.

The second phase of the project was aimed at understanding the limitations of the experimental setup, and validity of the two-dimensional assumption required to use full-field measurements for material characterisation. Using synchronised ultra-high speed imaging combined with full-field measurements from both sides of the sample, it was possible to identify cases where the assumption of uniform through-thickness behaviour was not satisfied. The results showed that when the waveguide and projectile were misaligned between 0.8-1.2°, a bending wave was introduced into the sample after the wave reached the free edge. This non-uniform loading through-the-thickness was shown to have a substantial effect on stiffness identified from individual tests (difference between faces up to 20%), but a lesser effect over several samples (difference between average identifications was at most 4%, with COV = 3-4%). Follow-up experiments with a single camera showed a significant improvement in consistency for measurements of the interlaminar stiffness and failure stress at strain rates on the order of $3{\times}10^3$ s^{-1}. Scatter on interlaminar failure stress measurements (COV = 6.6%) were much improved compared to results from the first phase of the project (COV = 21%). These tests were compared with back-to-back measurements to estimate the bias introduced by the three-dimensional loading on stiffness and failure stress measurements. The average stiffness measured across all samples that were subjected to three-dimensional loading was biased by at most 4%. The effect on failure stress was much larger as the bending stress was not captured by the linear stress-gauge reconstructions on each face, causing failure stress to be underestimated by 30% on average. This emphasises the importance of two-dimensional loading for accurate failure stress measurements. An additional outcome of this second phase of the work was the establishment of diagnostics for detecting

issues with three-dimensional loading from single-sided measurements.

The third phase of this work presented the design and experimental validation of an IBII test to measure the interlaminar shear modulus. A simple short-beam shear configuration was used to activate the interlaminar shear behaviour, with specimen geometry and pulse length selected using a simulation design study in ABAQUS/explicit. A new set of special optimised virtual fields were developed for the direct identification of the shear modulus from heterogeneous maps of strain and acceleration. A separate image deformation framework was successfully implemented to quantify the uncertainty associated with the identification of the shear modulus from limited camera spatial resolution, smoothing, and grid rotation. Measurements of the interlaminar shear modulus from an experimental test campaign were made with impressive consistency (COV $\leq$ 3%) at strain rates on the order of 1.5×10^3 s^{-1}, which is beyond the capabilities of existing tests methods.

This project has demonstrated the potential of new test methods based on full-field measurements for measuring interlaminar properties at strain rates where current techniques are unreliable. While spatial resolution of available cameras imposes some restrictions on the complexity of specimen design, the capability of full-field measurements will only increase as ultra-high-speed camera technology improves. This will vastly open up the design space, providing exciting opportunities to consider other configurations (thinner samples, different specimen geometries, notches, holes, *etc.*) for identifying multiple stiffness parameters from a single test and potentially begin populating failure envelopes at high strain rates. This information is not currently available at the strain rates considered here, and would be an invaluable advancement for improved high-strain-rate modelling of composite materials. The design framework developed in this work will facilitate the exploration of a new set of high-strain-rate IBII tests for more complete material characterisation.

7.4 Contributions

This work has lead to five journal articles, two awards in international student paper competitions and 10 international conference papers, five journal articles (three published, two in preparation/review), and two awards in international student paper competitions. The details are provided below along with a summary of the author's contributions to each manuscript.

Journal papers

1. **J. Van Blitterswyk**, L. Fletcher, F. Pierron, The effect of out-of-plane loading on the image-based inertial impact (IBII) test, *To be submitted to Strain*, 2019.

   Contributions: Responsible for preparing specimens (*e.g.:* specimen manufacturing and grid deposition), conducting experiments, developing improved alignment procedure, and full processing of experimental images. Primary author of manuscript.

2. **J. Van Blitterswyk**, L. Fletcher, F. Pierron, An image-based inertial impact (IBII) test for measuring the interlaminar shear moduli of composites, *To be submitted to Journal of Dynamic Behavior of Materials*, 2019.

   Contributions: Responsible for simulations (*e.g.:* test design, image deformation), preparing specimens (*e.g.:* specimen manufacturing and grid deposition), conducting experiments, developing data analysis procedures and full processing of experimental images. Primary author of manuscript.

3. **J. Van Blitterswyk**, L. Fletcher, F. Pierron, Image-based inertial impact test for composite interlaminar tensile properties, *Journal of Dynamic Behavior of Materials*; 4, pp. 543-572, 2019, doi: 10.1007/s40870-018-0175-1.

   Contributions: Responsible for simulations (*e.g.:* test design, image deformation), preparing specimens (*e.g.:* specimen manufacturing and grid deposition), conducting experiments, image processing and data analysis. Primary author of manuscript.

4. L. Fletcher, **J. Van Blitterswyk**, F. Pierron, A novel image-based inertial impact (IBII) test for the transverse properties of unidirectional composites at high strain rates, *Journal of Dynamic Behavior of Materials*; 5, pp. 65-92, 2019, doi:10.1007/s40870-019-00186-y.

   Contributions: Developed reduced special optimised virtual fields routine for identification of the transverse stiffness and assisted with experimental testing. Manuscript contributions include: writing up description of theory and implementation for reduced special optimised virtual fields routine, and revision of manuscript drafts.

5. **J. Van Blitterswyk**, L. Fletcher, F. Pierron, Interlaminar mechanical properties of polymer matrix fibre composites at high strain rates: a review, *Advanced Experimental Mechanics*; 2, pp. 3-28, 2017, doi: 10.11395/aem.2.0_3.

   Contributions: Conducted review and analysis of literature. Primary author of manuscript.

Open-access reports

1. L. Fletcher, **J. Van Blitterswyk**, F. Pierron, A manual for conducting image-based inertial impact (IBII) tests, 2019, doi:doi:10.5258/SOTON/P0015.

Contributions: Development of reduced special optimised virtual fields for stiffness identification, development of experimental alignment procedure and best practices, image processing (edge data reconstruction methodology, grid method processing). Manuscript contributions include: write up theory for reduced special optimisation routine, image processing routine, description of code structure and review of manuscript drafts.

International student paper competition awards

1. **Awarded 1st prize**: J. Van Blitterswyk[1], L. Fletcher, F. Pierron, Image-based inertial impact tests for composite interlaminar tensile properties , *13th International Conference on Advances in Experimental Mechanics (BSSM) - Young Stress Analyst Competition*, 29-31 Aug. 2018.
2. **Awarded 3rd prize**: J. Van Blitterswyk, L. Fletcher, F. Pierron, A novel image-based impact (IBI) test for high strain rate interlaminar tensile properties of fibre-reinforced polymer matrix composites, *2018 SEM Annual Conference - International Student Competition*, 4-7 June 2018.

International conference papers and presentations

1. J. Van Blitterswyk, L. Fletcher, F. Pierron, Advancing the image-based inertial impact test for high strain rate interlaminar properties using synchronised ultra-high-speed-cameras, *14th International Conference on Advances in Experimental Mechanics (BSSM)*, 10-12 Sept. 2019.
2. J. Van Blitterswyk, L. Fletcher, F. Pierron, Advancing the image-based inertial impact test for high strain rate interlaminar properties using synchronised ultra-high-speed cameras, *2019 SEM Annual Conference*, 3-6 June 2019.
3. L. Fletcher, J. Van Blitterswyk, F. Pierron, Combined shear / tension testing of fibre composites at high strain rates using an image-based inertial impact test, *EPJ Web of Conferences, DYMAT 2018*; 183, 02041, 2018, doi: 10.1051/epjconf/201818302041.
4. J. Van Blitterswyk, L. Fletcher, F. Pierron, An image-based inertial impact test for high strain rate interlaminar shear properties of fibre-reinforced polymer matrix composites, *13th International Conference on Advances in Experimental Mechanics (BSSM)*, 29-31 Aug. 2018.
5. L. Fletcher, J. Van Blitterswyk, L. Fletcher, F. Pierron, Off-Axis Testing of Fibre Composites at high Strain Rates using an Image-Based Inertial Impact Test, *13th International Conference on Advances in Experimental Mechanics (BSSM)*, 29-31 Aug. 2018.
6. F. Pierron, F.M. Davis, L.F. Fletcher, X. Régal, R. Seghir, J. Van Blitterswyk, Novel image-based inertial high strain rate tests: an overview, *13th International Conference on Advances in Experimental Mechanics (BSSM)*, 29-31 Aug. 2018.
7. J. Van Blitterswyk, L. Fletcher, F. Pierron, High strain rate tensile testing of fibre reinforced polymer composites using an image-based inertial impact test, *European Conference on Composite Materials (ECCM)*, 24-28 June 2018.

[1] Underlined name denotes the presenter of the paper

8. J. Van Blitterswyk, L. Fletcher, F. Pierron, High strain rate interlaminar shear testing of fibre-reinforced composites using an image-based inertial impact test, *2018 SEM Annual Conference*, 4-7 June 2018.

9. J. Van Blitterswyk, L. Fletcher, F. Pierron, Design of a photomechanical test to measure the high strain rate through-thickness tensile strength of composites, *12th International Conference on Advances in Experimental Mechanics (BSSM)*, 29-31 Aug. 2017.

10. L. Fletcher, J. Van Blitterswyk, F. Pierron, Inertial impact method for the transverse and through-thickness tensile strengths of composites at high strain rates, *2017 SEM Annual Conference*, 12-15 June 2017.

Bibliography

[1] M.R. Wisnom. The role of delamination in failure of fibre-reinforced composites. *Philosophical Transactions of the Royal Scoiety A*, 370:1850–1870, 2012.

[2] F. Hélénon, M.R. Wisnom, S.R. Hallett, and R.S. Trask. Numerical investigation into failure of laminated composite T-piece specimens under tensile loading. *Composites Part A: Applied Science and Manufacturing*, 43(7):1017–1027, 2012.

[3] K. Zimmermann, D. Zenkert, and M. Siemetzki. Testing and analysis of ultra thick composites. *Composites Part B: Engineering*, 41(4):326–336, 2010.

[4] Airbus. Airbus' new centre wing box design holds great promise for future aircraft, https://www.airbus.com/newsroom/news/en/2017/01/airbus-new-centre-wing, 2017.

[5] G.C. Jacob, J.F. Fellers, S. Simunovic, and J.M. Starbuk. Energy absorption in polymer composites for automotive crashworthiness. *Journal of Composite Materials*, 36(7):813–850, 2002.

[6] K. Mahadevan, P. Liang, and J. Fekete. Effect of strain rate in full vehicle frontal crash analysis. *SAE Paper*, No. 2000-0, 2000.

[7] R.H. Mao, S.A. Meguid, and T.Y. Ng. Transient three dimensional finite element analysis of a bird striking a fan blade. *International Journal of Mechanics and Materials in Design*, 4:79–96, 2008.

[8] J. Harding and L. Dong. Effect of strain rate on the interlaminar shear strength of carbon-fibre-reinforced laminates. *Composites Science and Technology*, 51:347–358, 1994.

[9] T. Yokoyama and K. Nakai. High strain-rate compressive characteristics of laminated composites in the through-thickness direction. In *SEM X International Congress & Exposition on Experimental & Applied Mechanics*, pages 1–8, Costa Mesa, California, USA, 7-10 June, 2004.

[10] N.K. Naik, A. Asmelash, V.R. Kavala, and V. Ch. Interlaminar shear properties of polymer matrix composites: Strain rate effect. *Mechanics of Materials*, 39, 2007.

[11] K. Nakai and T. Yokoyama. Through-thickness tensile strength of carbon/epoxy laminated composites under impact loading. In *16th International Conference on Experimental Mechanics*, Cambridge, UK, 7-11 July, 2014.

[12] R. Gerlach, C.R. Siviour, N. Petrinic, and J. Wiegand. Experimental characterisation and constitutive modelling of RTM-6 resin under impact loading. *Polymer*, 49(11):2728–2737, 2008.

[13] J. Van Blitterswyk, L. Fletcher, and F. Pierron. Characterisation of the interlaminar properties of composites at high strain rates: a review. *Advanced Experimental Mechanics*, 2(June):3–28, 2017.

[14] H.L. Gowtham, J.R. Pothnis, G. Ravikumar, and N.K. Naik. Dependency of dynamic interlaminar shear strength of composites on test technique used. *Polymer Testing*, 42:151–159, 2015.

[15] R. Olsson. A survey of test methods for multiaxial and out-of-plane strength of composite laminates. *Composites Science and Technology*, 71(6):773–783, 2011.

[16] W.R. Broughton. Through-thickness testing. In *Mechanical Testing of Advanced Fibre Composites (Hodgkinson J.M. ed.)*, chapter 8. 2000.

[17] Y. He, A. Makeev, and B. Shonkwiler. Characterization of nonlinear shear properties for composite materials using digital image correlation and finite element analysis. *Composites Science and Technology*, 73:64–71, 2012.

[18] W. Cui, T. Liu, J. Len, and R. Ruo. Interlaminar tensile strength (ILTS) measurement of woven glass/polyester laminates using four-point curved beam specimen. *Composites Part A: Applied Science and Manufacturing*, 27(11):1097–1105, 1996.

[19] A. Makeev, P. Carpentier, and B. Shonkwiler. Methods to measure interlaminar tensile modulus of composites. *Composites Part A: Applied Science and Manufacturing*, 56:256–261, 2014.

[20] J.S. Charrier, F. Laurin, N. Carrere, and S. Mahdi. Determination of the out-of-plane tensile strength using four-point bending tests on laminated L-angle specimens with different stacking sequences and total thicknesses. *Composites Part A: Applied Science and Manufacturing*, 81:243–253, 2016.

[21] W.W. Chen. Experimental methods for characterizing dynamic response of soft materials. *Journal of Dynamic Behaviour of Materials*, 2:2–14, 2016.

[22] Z. Li and J. Lambros. Determination of the dynamic response of brittle composites by the use of the split Hopkinson pressure bar. *Composite Science and Technology*, 59:1097–1107, 1999.

[23] G.T. Grey III. Mechanical testing and evaluation (ASM International). In *ASM Handbook Volume 8*, pages 462–476. 2000.

[24] B.A. Gama, S.L. Lopatnikov, and J.W. Gillespie. Hopkinson bar experimental technique: A critical review. *Applied Mechanics Reviews*, 57(4):223, 2004.

[25] J.E. Field, S.M. Walley, W.G. Proud, H.T. Goldrein, and C.R. Siviour. Review of experimental techniques for high rate deformation and shock studies. *International Journal of Impact Engineering*, 30:725–775, 2004.

[26] R. Moulart, F. Pierron, S. R. Hallett, and M. R. Wisnom. Full-field strain measurement and identification of composites moduli at high strain rate with the virtual fields method. *Experimental Mechanics*, 51(4):509–536, 2011.

[27] F. Pierron and P. Forquin. Ultra-high-speed full-field deformation measurements on concrete spalling specimens and stiffness identification with the virtual fields method. *Strain*, 48(5):388–405, 2012.

[28] F. Pierron, H. Zhu, and C. R. Siviour. Beyond Hopkinson's bar. *Philosophical transactions of the Royal Society A*, 372:20130195, 2014.

[29] H. Zhu. *A novel methodology for high strain rate testing using full-field measurements and the virtual fields methods.* PhD thesis, University of Technology of Troyes, France, 2015.

[30] B. Koohbor, A. Kidane, W.-Y. Lu, and M.A. Sutton. Investigation of the dynamic stress–strain response of compressible polymeric foam using a non-parametric analysis. *International Journal of Impact Engineering*, 91:170–182, 2016.

[31] L. Fletcher, J. Van Blitterswyk, and F. Pierron. Combined shear/tension testing of fibre composites at high strain rates using an image-based inertial impact test. In *EPJ Web of Conferences, DYMAT 2018*, volume 183, page 02041, 2018.

[32] L. Fletcher and F. Pierron. An image-based inertial impact (IBII) test for tungsten carbide cermets. *Journal of Dynamic Behavior of Materials*, 4:481–504, 2018.

[33] S.H. Yoon, M. Winters, and C.R. Siviour. High strain-rate tensile characterization of EPDM rubber using non-equilibrium loading and the virtual fields method. *Experimental Mechanics*, 56(1):25–35, 2016.

[34] S.H Yoon and C.R. Siviour. Application of the virtual fields method to rubbers under medium strain rate deformation using both acceleration and traction force data. *Journal of Dynamic Behavior of Materials*, 3(1):12–22, 2017.

[35] P. Forquin and B.B. Lukić. On the processing of spalling experiments. Part I: identification of the dynamic tensile strength of concrete. *Journal of Dynamic Behavior of Materials*, 4:34–55, 2018.

[36] B.B Lukić, D. Saletti, and P. Forquin. On the processing of spalling experiments. Part II: identification of concrete fracture energy in dynamic tension. *Journal of Dynamic Behavior of Materials*, 4:56–73, 2018.

[37] L. Fletcher, J. Van Blitterswyk, and F. Pierron. A novel image-based inertial impact (IBII) test for the transverse properties of unidirectional composites at high strain rates. *Journal of Dynamic Behavior of Materials*, 5:65–92, 2019.

[38] J. Van Blitterswyk, L. Fletcher, and F. Pierron. Image-based inertial impact test for composite interlaminar tensile properties. *Journal of Dynamic Behavior of Materials*, 4:543–572, 2018.

[39] M. Rossi and F. Pierron. On the use of simulated experiments in designing tests for material characterization from full-field measurements. *International Journal of Solids and Structures*, 49:420–435, 2012.

[40] P. Lava, S. Cooreman, S. Coppieters, M. De Strycker, and D. Debruyne. Assessment of measuring errors in DIC using deformation fields generated by plastic FEA. *Optics and Lasers in Engineering*, 47(4-7):747–753, 2009.

[41] F. Pierron and M. Grédiac. Identification of the through-thickness moduli of thick composites from whole-field measurements using the Iosipescu fixture: theory and simulations. *Composites: Part A*, 31:309–318, 2000.

[42] M. Grédiac, E. Toussaint, and F. Pierron. Special virtual fields for the direct determination of material parameters with the virtual fields method. 2—Application to in-plane properties. *International Journal of Solids and Structures*, 39:2707–2730, 2002.

[43] F. Pierron and S. Avril. Inverse problems in experimental solid mechanics. *Experimental Mechanics*, 39, 2007.

[44] B. Bouette, C. Cazeneuve, and C. Oytana. Effect of strain rate on interlaminar shear properties of carbon/epoxy composites. *Composites Science and Technology*, 45:313–321, 1992.

[45] S.R. Hallett, C. Ruiz, and J. Harding. The effect of strain rate on the interlaminar shear strength of a carbon/epoxy cross-ply laminate: comparison between experiment and numerical prediction. *Composite Science and Technology*, 59:749–758, 1999.

[46] J.W. Gillespie, B.A. Gama, C.E. Cichanowski, and J.R. Xiao. Interlaminar shear strength of plain weave S2-glass/SC79 composites subjected to out-of-plane high strain rate compressive loadings. *Composite Science and Technology*, 65:1891–1908, 2005.

[47] R. Gerlach, C.R. Siviour, J. Wiegand, and N. Petrinic. In-plane and through-thickness properties, failure modes, damage and delamination in 3D woven carbon fibre composites subjected to impact loading. *Composites Science and Technology*, 72:397–411, 2012.

[48] K. Nakai and T. Yokoyama. Dynamic stress – strain properties of carbon/epoxy laminated composites in through-thickness direction: tension and compression. In *The 9th International Symposium on Impact Engineering*, Tainan, Taiwan, 5-9 September, 2016.

[49] R.J. Davis. High strain rate tensile testing. In *Tensile Testing, 2nd Edition*, pages 251–263. 2004.

[50] R. Gerlach, C. Kettenbeil, and N. Petrinic. A new split Hopkinson tensile bar design. *International Journal of Impact Engineering*, 50:63–67, 2012.

[51] R. Gerlach, C.R. Siviour, J. Wiegand, and N. Petrinic. The strain rate dependent material behavior of S-GFRP extracted from GLARE. *Mechanics of Advanced Materials and Structures*, 20(7):505–514, 2013.

[52] A. Gilat, T.E. Schmidt, and A.L. Walker. Full field strain measurement in compression and tensile split Hopkinson bar experiments. *Experimental Mechanics*, 49:291–302, 2009.

[53] S.A. Novikov and A.V. Chernov. Determination of the spall strength from measured values of the specimen free surface velocity. *Zhurnal Prikladnoi Mekhaniki i Teknicheskoi Fiziki*, 23(703-705), 1982.

[54] A. Gilat, R.K. Goldberg, and G.D. Roberts. Strain rate sensitivity of epoxy resin in tensile and shear loading. *Journal of Aerospace Engineering*, 20(2):75–89, 2007.

[55] K. S. Vecchio and F. Jiang. Improved pulse shaping to achieve constant strain rate and stress equilibrium in split-Hopkinson pressure bar testing. *Metallurgical and Materials Transactions A: Physical Metallurgy and Materials Science*, 38(11):2655–2665, 2007.

[56] R. Ravichandran and S. Ghatuparthi. Critical appraisal of limiting strain rates for compression testing of ceramics in a split Hopkinson pressure bar. *Journal of the American Ceramic Society*, 77.1:263–267, 1994.

[57] B.A. Gama, J.W. Gillespie, H. Mahfuz, R.P. Raines, A. Haque, S. Jeelani, T.A. Bogetti, and B.K. Fink. High strain-rate behavior of plain-weave S-2 glass/vinyl ester composites. *Journal of Composite Materials*, 35(13), 2001.

[58] Z. Song, Z. Wang, H. Ma, and H. Xuan. Mechanical behavior and failure mode of woven carbon/epoxy laminate composites under dynamic compressive loading. *Composites: Part B*, 60:531–536, 2014.

[59] H. Zhao and G. Gary. On the use of SHPB techniques to determine the dynamic behavior of materials in the range of small strains. *International Journal of Solids and Structures*, 33(23):3363–3375, 1996.

[60] M.Z. Shah Khan and G. Simpson. Mechanical properties of a glass reinforced plastic

naval composite material under increasing compressive strain rates. *Materials Letters*, 45:167–174, 2000.

[61] L. Shen, Y. Li, and Z. Wang. Experimental investigation of the effect of strain rate on the compression behavior of 3D E-glass fiber-reinforced composites. *Applied Mechanics and Materials*, 174-177:1528–1532, 2012.

[62] O. Akil, U. Yıldırım, M. Güden, and I.W. Hall. Effect of strain rate on the compression behaviour of a woven fabric S2-glass fiber reinforced vinyl ester composite. *Polymer Testing*, 22:883–887, 2003.

[63] M. Guden, U. Yildirim, and I.W. Hall. Effect of strain rate on the compression behavior of a woven glass fiber/SC-15 composite. *Polymer Testing*, 23:719–725, 2004.

[64] M.V. Hosur, J. Alexander, U.K. Vaidya, and S. Jeelani. High strain rate compression response of carbon/epoxy laminate composites. *Composite Structures*, 52:405–417, 2001.

[65] M. Pankow, A. Salvi, A.M. Waas, C.F. Yen, and S. Ghiorse. Split Hopkinson pressure bar testing of 3D woven composites. *Composites Science and Technology*, 71:1196–1208, 2011.

[66] R.A. Govender, L.A. Louca, A. Pullen, A.S. Fallah, and G.N. Nurick. Determining the through-thickness properties of thick glass fiber reinforced polymers at high strain rates. *Journal of Composite Materials*, 46(10):1219–1228, 2012.

[67] N.K. Naik, V. Ch, and V.R. Kavala. Hybrid composites under high strain rate compressive loading. *Materials Science and Engineering A*, 498:87–99, 2008.

[68] S.-C. Woo and T.-W. Kim. High strain-rate failure in carbon/Kevlar hybrid woven composites via a novel SHPB-AE coupled test. *Composites Part B*, 97:317–328, 2016.

[69] V. L. Tagarielli, G. Minisgallo, A. J. Mcmillan, and N. Petrinic. The response of a multi-directional composite laminate to through-thickness loading. *Composites Science and Technology*, 70:1950–1957, 2010.

[70] R. Kapoor, L. Pangeni, A. K. Bandaru, S. Ahmad, and N. Bhatnagar. High strain rate compression response of woven Kevlar reinforced polypropylene composites. *Composites Part B*, 89:374–382, 2016.

[71] J.M. Lifshitz and H. Leber. Response of fiber-reinforced polymers to high strain-rate loading in interlaminar tension and combined tension/shear. *Composite Science and Technology*, 58(9):987–996, 1998.

[72] J.L. Medina and Harding J. The effect of strain rate on the through-thickness tensile stiffness and strength properties of fibre-reinforced epoxy composites. *Journal de Physique IV*, 10:275–280, 2000.

[73] W. Hufenbach, A. Langkamp, M. Gude, C. Ebert, A. Hornig, S. Nitschke, and H. Böhm. Characterisation of strain rate dependent material properties of textile reinforced thermoplastics for crash and impact analysis. *Procedia Materials Science*, 2:204–211, 2013.

[74] N.K. Naik, P. Yernamma, N.M. Thoram, R. Gadipatri, and V.R. Kavala. High strain rate tensile behavior of woven fabric E-glass/epoxy composite. *Polymer Testing*, 29:14–22, 2010.

[75] W. Hufenbach, A. Hornig, B. Zhou, A. Langkamp, and M. Gude. Determination of strain rate dependent through-thickness tensile properties of textile reinforced thermo-

plastic composites using L-shaped beam specimens. *Composites Science and Technology*, 71(8):1110–1116, 2011.

[76] G. Y. Cui and C. Ruiz. Through-thickness failure of laminated carbon/epoxy composites under combined stresses. *Composites Science and Technology*, 53:253–258, 1995.

[77] J. Harding and Y. L. Li. Determination of interlaminar shear strength for glass/epoxy and carbon/epoxy laminates at impact rates of strain. *Composites Science and Technology*, 45:161–171, 1992.

[78] W. Hufenbach, A. Langkamp, A. Hornig, and C. Ebert. Experimental determination of the strain rate dependent out- of-plane shear properties of textile-reinforced composites. In *ICCM 17*, pages 1–9, 2009.

[79] T. Yokoyama and K. Nakai. Evaluation of interlaminar shear strength of a unidirectional carbon/epoxy laminated composite under impact loading. In *Journal de Physique IV*, volume 122, pages 1–5, 2006.

[80] Y. Kondo, K. Takubo, H. Tominaga, R. Hirose, N. Tokuoka, Y. Kawaguchi, Y. Takaie, A. Ozaki, S. Nakaya, F. Yano, and T. Daigen. Development of HyperVision HPV-X high-speed video camera, 2013.

[81] T.G. Etoh. A high-speed video camera of 4,500 fps. *Journal of the Institution of Television Engineers*, 46(5):543, 1992.

[82] G.T. Etoh, C. Vo Le, Y. Hashishin, N. Otsuka, K. Takehara, H. Ohtake, T. Hayashida, and H. Maruyama. Evolution of ultra-high-speed CCD imagers. *Plasma and Fusion Research*, 2:S1021, 2007.

[83] P. L. Reu and T. J. Miller. The application of high-speed digital image correlation. *The Journal of Strain Analysis for Engineering Design*, 43(May):673–688, 2008.

[84] F. Pierron. Ultra-high speed imaging, http://photodyn.org/tools/ultra-highspeed-%0Acamera, 2017.

[85] http://www.cordin.com Cordin. Framing camera systems, 2018.

[86] Madhu S. Kirugulige, Hareesh V. Tippur, and Thomas S. Denney. Measurement of transient deformations using digital image correlation method and high-speed photography: application to dynamic fracture. *Applied Optics*, 46(22):5083, 2007.

[87] V. Tiwari, M.A. Sutton, and S.R. Mcneill. Assessment of high speed imaging systems for 2D and 3D deformation measurements: methodology development and validation. *Experimental Mechanics*, 47:561–579, 2007.

[88] F. Pierron, R. Cheriguéne, P. Forquin, R. Moulart, M. Rossi, and M. A. Sutton. Performances and limitations of 3 ultra high-speed imaging cameras for full-field deformation measurements. *Applied Mechanics and Materials*, 70:81–86, 2011.

[89] W.F.F. Kosonocky, Y. Guang, Y. Chao, R.K.K. Kabra, X. Liansheng, J.L.L. Lawrence, V. Mastrocolla, F.V.V. Shallcross, and V. Patel. 360/Spl Times/360-element very-high-frame-rate burst image sensor. *Digest of Technical Papers - IEEE International Solid-State Circuits Conference*, (5):182–183, 1996.

[90] T.G. Etoh, D. Poggemann, A. Ruckelshausen, A. Theuwissen, G. Kreider, H.O. Folkerts, H. Mutoh, Y. Kondo, H. Maruno, K. Takubo, H. Soya, K. Takehara, T. Okinaka, Y. Takano, T. Reisinger, and C. Lohmann. A CCD image sensor of 1 Mframes/s for

continuous image capturing 103 frames. *Digest of Technical Papers - IEEE International Solid-State Circuits Conference*, (February):2–5, 2002.

[91] T.G. Etoh, V.T.S. Dao, H.D. Nguyen, K. Fife, M. Kureta, M. Segawa, M. Arai, and T. Shinohara. Progress of ultra-high-speed image sensors with in-situ CCD storage. In *Progress of Ultra-high-speed Image Sensors with In-situ CCD Storage*, 2011.

[92] K.A. Stetson. A review of speckle photography and interferometry. *Optical Engineering*, 14(5):145482, 1975.

[93] D. Post and B. Han. Moiré interferometry. In *Handbook of Experimental Solid Mechanics*, pages 1–27. Springer, 2008.

[94] T.H. Jeong. Basic principles and applications of holography. *Fundamentals of Photonics*, pages 381–417, 2008.

[95] H. Schreier, J.J. Orteu, and M.A. Sutton. *Image correlation for shape, motion and deformation measurements*. Springer, 2009.

[96] M. Grédiac, F. Sur, and B. Blaysat. The grid method for in-plane displacement and strain measurement: a review and analysis. *Strain*, 52(3):205–243, 2016.

[97] W.C. Wang, C.H. Hwang, and S.Y. Lin. Vibration measurement by the time-averaged electronic speckle pattern interferometry methods. *Applied Optics*, 35(22):4502–9, 1996.

[98] Y. Li, I. Yamaguchi, and J. Kato. ESPI vibration fringe enhancement by laser diode wavelength modulation. *Proceedings of SPIE 1553*, Laser Inte(January):150–159, 1991.

[99] M.A. Sutton, W.J. Wolters, W.H. Peters, W.F. Ranson, and S.R. Mcneill. Determination of displacements using an improved digital correlation method. *Image and Vision Computing*, 1(3):133–139, 1983.

[100] B. Pan, L. Yu, and D. Wu. High-accuracy 2D digital image correlation measurements with bilateral telecentric lenses: error analysis and experimental verification. *Experimental Mechanics*, 53:1719–1733, 2013.

[101] B. Pan, Z. Lu, and H. Xie. Mean intensity gradient: An effective global parameter for quality assessment of the speckle patterns used in digital image correlation. *Optics and Lasers in Engineering*, 48:469–477, 2010.

[102] M. A. Sutton, J. H. Yan, V. Tiwari, H. W. Schreier, and J. J. Orteu. The effect of out-of-plane motion on 2D and 3D digital image correlation measurements. *Optics and Lasers in Engineering*, 46:746–757, 2008.

[103] M. Badaloni, M. Rossi, G. Chiappini, P. Lava, and D. Debruyne. Impact of experimental uncertainties on the identification of mechanical material properties using DIC. *Experimental Mechanics*, 55:1411–1426, 2015.

[104] M. Rossi, P. Lava, F. Pierron, D. Debruyne, and M. Sasso. Effect of DIC spatial resolution, noise and interpolation error on identification results with the VFM. *Strain*, 51(3):206–222, 2015.

[105] X. Gu and F. Pierron. Towards the design of a new standard for composite stiffness identification. *Composites: Part A*, In Press, 2016.

[106] H. Koerber, J. Xavier, and P.P. Camanho. High strain rate characterisation of unidirectional carbon-epoxy IM7-8552 in transverse compression and in-plane shear using digital image correlation. *Mechanics of Materials*, 42:1004–1019, 2010.

[107] Y. Surrel. Design of algorithms for phase measurements by the use of phase stepping. *Applied optics*, 35(1):51–60, 1996.

[108] F. Sur and M Grédiac. Influence of the analysis window on the metrological performance of the grid method. *Journal of Mathematical Imaging and Vision*, 56(3):472–498, 2016.

[109] C. Badulescu, M. Grédiac, J.D. Mathias, and D. Roux. Investigation of the grid method for accurate in-plane strain measurement This. *Experimental Mechanics*, 49(6):841–854, 2009.

[110] Q. Kemao. Applications of windowed Fourier fringe analysis in optical measurement: a review. *Optics and Lasers in Engineering*, 66:67–63, 2015.

[111] M. Grédiac and F. Sur. Effect of sensor noise on the resolution and spatial resolution of displacement and strain maps estimated with the grid method. *Strain*, 50(1):1–27, 2014.

[112] E.M.C Jones and M.A. Iadicola. A Good Practices Guide for Digital Image Correlation Standardization, Good Practices, and Uncertainty Quantiication Committee. Technical report, 2018.

[113] S. Avril and F. Pierron. General framework for the identification of constitutive parameters from full-field measurements in linear elasticity. *International Journal of Solids and Structures*, 44:4978–5002, 2007.

[114] E. Pagnacco, A. Moreau, and D. Lemosse. Inverse strategies for the identification of elastic and viscoelastic material parameters using full-field measurements. *Materials Science and Engineering A*, 452-453:737–745, 2007.

[115] G. Geymonat and S.E. Pagano. Identification of mechanical properties by displacement field measurement: a variational approach. *Meccanica*, 38:535–545, 2003.

[116] J. Molimard, R. Le Riche, A. Vautrin, and J.R. Lee. Identification of the four orthotropic plate stiffnesses using a single open-hole tensile test. *Experimental Mechanics*, 45(5):404–411, 2005.

[117] D. Claire, F. Hild, and S. Roux. A finite element formulation to identify damage fields: The equilibrium gap method. *International Journal of Numerical Methods in Engineering*, 62:189–208, 2004.

[118] J. Cugnoni, T. Gmü, and A. Schorderet. Inverse method based on modal analysis for characterizing the constitutive properties of thick composite plates. *Computers and Structures*, 85:1310–1320, 2007.

[119] H. Leclerc, J.-N. Périé, S. Roux, and F. Hild. Integrated digital image correlation for the identification of mechanical properties. In *Computer Vision/Computer Graphics Collaboration Techniques. MIRAGE*, pages 161–171, Berlin, Heidelberg, 2009. Springer.

[120] L. Le Magorou, F. Bos, and F. Rouger. Identification of constitutive laws for wood-based panels by means of an inverse method. *Composites Science and Technology*, 62(4):591–596, 2002.

[121] J. Peirs, P. Verleysen, W. Van Paepegem, and J. Degrieck. Determining the stress-strain behaviour at large strains from high strain rate tensile and shear experiments. *International Journal of Impact Engineering*, 38:406–415, 2011.

[122] J. Kajberg, K.G. Sundin, L.G. Melin, and P. Ståhle. High strain-rate tensile testing and viscoplastic parameter identification using microscopic high-speed photography. *International Journal of Plasticity*, 20(4-5):561–575, 2004.

[123] K. Genovese, L. Lamberti, and C. Pappalettere. Mechanical characterization of hyperelastic materials with fringe projection and optimization techniques. *Optics and Lasers in Engineering*, 44:423–442, 2006.

[124] G. Besnard, F. Hild, and S. Roux. Finite-element displacement fields analysis from digital images: Application to Portevin-Le Châtelier bands. *Experimental Mechanics*, 46:789–803, 2006.

[125] F. Pierron and M. Grédiac. *The virtual fields method: extracting constitutive mechanical parameters from full-field deformation measurements*. Springer, 2012.

[126] M. Grédiac, F. Pierront, S. Avrilt, and E. Toussaint. The virtual fields method for extracting constitutive parameters from full-field measurements: a review. *Strain*, 42:233–253, 2006.

[127] S. Avril, M. Grédiac, and F. Pierron. Sensitivity of the virtual fields method to noisy data. *Computational Mechanics*, 34:439–451, 2004.

[128] A. Giraudeau, B. Guo, and F. Pierron. Stiffness and damping identification from full field measurements on vibrating plates. *Experimental Mechanics*, 46(6):777–787, 2006.

[129] S. Avril, M. Bonnet, A.-S. Bretelle, M. Grédiac, F. Hild, P. Ienny, F. Latourte, D. Lemosse, S. Pagano, E. Pagnacco, and F. Pierron. Overview of identification methods of mechanical parameters based on full-field measurements. *Experimental Mechanics*, 48:381–402, 2008.

[130] T. G. Etoh and H. Mutoh. An image sensor of 1 Mfps with photon counting sensitivity. *26th International Congress on High-Speed Photography and Photonics*, 5580:301–307, 2005.

[131] F. Pierron and L. Fletcher. Generalized stress-strain curves for IBII tests on isotropic and orthotropic materials. *Journal of Dynamic Behavior of Materials*, 5:180–193, 2019.

[132] E. Clarkson, T. Valliappan, and D. Tan. CYTEC (Formerly Advanced Composites Group) MTM45-1/ 12K AS4 145gsm 32%RW unidirectional qualification statistical analysis report FAA special project number SP3505WI-Q test panel fabrication facility. Technical report, National Institute for Aerospace Research (NIAR), Tulse, OK, 2016.

[133] J.L. Piro and M. Grédiac. Producing and transferring low-spatial-frequency grids for measuring displacement fields with moiré and grid methods. *Experimental Techniques*, 28(4):23–26, 2004.

[134] Surrel Y. The Grid Method (GM), http://photodyn.org/wp-content/uploads/2016/03/Report_UniversityPrintCentre_2.pdf. 2018.

[135] Surrel Y. The Grid Method (GM), http://photodyn.org/wp-content/uploads/2016/03/Report_UniversityPrintCentre.pdf. 2018.

[136] L. Fletcher, J. Van Blitterswyk, and F. Pierron. A manual for conducting image-based inertial impact (IBII) tests. pages 1–57, 2019.

[137] M.A. Herráez, D.R. Burton, M.J. Lalor, and M.A. Gdeisat. Fast two-dimensional phase-unwrapping algorithm based on sorting by reliability following a noncontinuous path. *Applied optics*, 41(35):7437–7444, 2002.

[138] P. Wang, F. Pierron, and O.T. Thomsen. Identification of material parameters of PVC foams using digital image correlation and the virtual fields method. *Proceedings of the Society for Experimental Mechanics, Inc.*, 53(6):1001–1015, 2013.

[139] E. Toussaint, M. Greiac, and F. Pierron. The virtual fields method with piecewise virtual fields. *International Journal of Mechanical Sciences*, 48(3):256–264, 2006.

[140] B. Lukić, D. Saletti, and P. Forquin. Use of simulated experiments for material characterization of brittle materials subjected to high strain rate dynamic tension. *Philosophical transactions of the Royal Society A*, 375:20160168, 2017.

[141] N.R. Brodnik, C.J. Hsueh, and M.T. Johnson. A nonconstraining templated powder grid for measurement of strain. *Strain*, In press, 2018.

[142] F. Pierron. Saint-Venant effects in the Iosipescu specimen. *Composite Materials*, 32(22):1986–2015, 1998.

[143] H. Zhu and F. Pierron. Exploration of Saint-Venant's principle in inertial high strain rate testing of materials. *Experimental Mechanics*, 56(1):3–23, 2016.

[144] B. Karp and D. Durban. Saint-Venant's principle in dynamics of structures. *Applied Mechanics Reviews*, 64(2):020801, 2011.

[145] ASTM International. ASTM D5379 / D5379M-12, standard test method for shear properties of composite materials by the V-notched beam method, 2012.

[146] F. Pierron and A. Vautrin. Accurate comparative determination of the in-plane shear modulus of T300/914 by the iosipescu and 45° off-axis tests. *Composites Science and Technology*, 52(1):61–72, 1994.

[147] Addis Kidane and H L Gowtham Niranjan K Naik. Strain Rate Effects in Polymer Matrix Composites Under Shear Loading : A Critical Review. *Journal of Dynamic Behavior of Materials*, 3(1):110–132, 2017.

[148] Seghir R., Pierron F., and Fletcher L. Image-based stress field reconstruction in complex media. In *Residual Stress, Thermomechanics and Infrared Imaging, Hybrid Techniques and Inverse Problems, Volume 7*, pages 101–104, 2019.

[149] A. Leygue, R. Seghir, J. Réthoré, M. Coret, E. Verron, and L. Stainier. Non-parametric material state field extraction from full field measurements. *Computational Mechanics*, 64(2):501–509, 2019.

[150] A. Marek, F.M. Davis, and F. Pierron. Sensitivity-based virtual fields for the non-linear virtual fields method. *Computational Mechanics*, 60(3):409–431, 2017.

[151] A. Marek, F.M. Davis, M. Rossi, and F. Pierron. Extension of the sensitivity-based virtual fields to large deformation anisotropic plasticity. *International Journal of Material Forming*, 12(3):457–476, 2019.

[152] H. Chalal, S. Avril, F. Pierron, and F. Meraghni. Experimental identification of a nonlinear model for composites using the grid technique coupled to the virtual fields method. *Composites Part A*, 37:315–325, 2006.

[153] A. Guigue, L. Fletcher, R. Seghir, and F. Pierron. IBII test for high strain rate tensile testing of adhesives. In *Dynamic Behavior of Materials, Volume 1, Conference Proceedings of the Society for Experimental Mechanics Series*, pages 301–305. Springer International Publishing, 2018.

Appendices

Appendix A

Literature Survey Tables

Table A.1: Summary of published studies on strain rate effects of interlaminar compressive properties of fibre-reinforced polymer composites. Notes: Constituent materials listed in the format: 'fibre/matrix'. Material labels are included in '( )' for association with Fig. 2.5 - Fig. 2.7. Quasi-static: italic typeface; high strain rate: regular typeface; test method: electro-mechanical load frame (EMLF), hydraulic load frame (HLF), high-speed load frame (HSLF), split Hopkinson pressure bar (SHPB); specimen geometry (in '[ ]'): R = rectangular/cubic specimens, C = cylindrical specimens

Reference	Material	Test [Specimen]	Strain Rate (s^{-1})	Notes
Yokoyama T. & Nakai K. (2004) [9]	carbon/epoxy pre-preg. ($[0/90]_s$): T700S/2500 (CFRP-PP) carbon/epoxy 2D plain weave: T300B/2500 (CFPR-W) glass/epoxy 2D plain weave: E-2/2500 (GFRP-W)	*EMLF* (*Instron 4505*) [*C-stack*] Compression SHPB [C]	0.002 – 1,510	Dynamic stress equilibrium is not achieved during the early stages of the test. Authors study influence of strain rate on secant modulus instead. Reinforcement architecture has a greater influence on the compressive properties with exception to compressive strength. Strain rate sensitivity attributed to viscoelastic nature of the epoxy resin. carbon/epoxy pre-preg: increase in elastic modulus (+105%), decrease in failure strength (-30%), and failure strain (-11%) at 1,510 s^{-1}; carbon/epoxy 2D weave: increase in elastic modulus (+143%), decrease in strength (-6%), and decrease in ultimate strain (-17%) at 1,510 s^{-1}; glass/epoxy 2D weave: increase in elastic modulus (+60%), increase in strength (+15%), and decrease in ultimate strain (-9%) at 1,510 s^{-1}.
Song Z. *et al.* (2014) [58]	carbon/epoxy 2D satin weave: T300-3/– (GFRP-W)	*HLF* (*MTS 810*) [*C*] Compression SHPB [C]	500 – 1,100	High strain rate stress-strain curves are affected by dispersion. Consistency of test questionable as strength decreases significantly only at 800 s^{-1}. No explanation for this behaviour is provided. Elastic modulus increases (qualitatively) up to 1,100 s^{-1}, and strength decreases up to 800 s^{-1} (-37%) before increasing at 1,100 s^{-1} (+11%). Ultimate strains decrease between -62% at 800 s^{-1} and -42% at 1,100 s^{-1}.

Naik N.K. *et al.* (2008) [67]	carbon/epoxy 2D satin weave: –/– (CFRP-W) E-glass/epoxy 2D plain weave: –/– (GFRP-W) E-glass/epoxy 2D satin weave: –/– (GFRP-W) carbon 2D satin weave & E-glass 2D plain weave/epoxy: –/– (HYBRID-W)	Compression SHPB [C]	1,275 & 1,503	Quasi-static properties not provided. Stress wave attenuation attributed to offset in force between input and transmitter bar. Inertia effects present during entire loading sequence. Transmitter bar peak force used as conservative estimate for computing stress in specimen. Elastic modulus estimated using strain and stress at peak stress. Slight increase in elastic modulus (+7%), strength increases (+46%), and ultimate strain increases (+25%) at 1,503 s^{-1} relative to 1,275 s^{-1}.
Hosur M.V. *et al.* (2001) [64]	carbon/epoxy pre-preg.($[0/90]_s$): PANEX 33/APCM LLC (DA 4518) (CFRP-PP)	*LF not spec.* [*R*] Compression SHPB [R]	82, 164, 817	Quasi-static strain estimated using crosshead displacement corrected for compliance. Higher quasi-static ultimate strains attributed to greater time for stress redistribution. Incident pulse generated by SHPB is highly non-uniform (significant dispersion suspected). Samples at 82 s^{-1} did not fail with SHPB, therefore, strength at quasi-static conditions cannot be compared. Elastic modulus increases at 82 s^{-1} (+30%), followed by a decrease with increasing strain rate to 817 s^{-1} (+12%). Strength increases (+19% at 817 s^{-1} relative to 82 s^{-1}), but lower compared to quasi-static values. Failure strain increases (+19% at 817 s^{-1} relative to 82 s^{-1}), but are lower than quasi-static values.
Woo S.-C. & Kim T.-W. (2016) [68]	carbon & kevlar/epoxy 2D twill weave: T300/Kevlar49/– (HYBRID-W)	Compression SHPB [C]	1,007, 1,485, 1,941	Low transmission of the input pulse through the specimen (10-12% at 1,485 s^{-1} and 1,941 s^{-1}). Therefore, low signal-to-noise ratio on stress measurement (noise in stress-strain curves). Material behaves in a more brittle manner at high strain rates. Acoustic emission signals were analysed to identify the onset of failure, and damage progression within the specimen. Effect of strain rate on modulus was not reported. Strength increases (+80% at 1,941 s^{-1}), and ultimate strain decrease (-15% at 1,941 s^{-1}).

Kapoor R. *et al.* (2016) [70]	kevlar/polypropylene 2D plain weave: Kevlar 29/MAg-PP (Not included in figures)	Compression SHPB [C]	1,370, 2,005, 2,538, 3,239, 3,440, 4,264	Possibly the first paper to report on the high strain rate through-thickness properties for kevlar/thermoplastic resin composites. Specimens have very low aspect ratio (L/D = 0.1-0.3). Reliable measurements were not possible with the thinnest specimens. Elastic modulus increases (+245% at 4,264 s^{-1} relative to 1,370 s^{-1}), strength increases (+196% at 4,264 s^{-1} relative to 1,370 s^{-1}), and ultimate strain increases (+134%). Significant increase in ultimate strain due to ductile behaviour of thermoplastic matrix. Toughness increases in a non-linear manner (+808% at 4,264 s^{-1} relative to 1,370 s^{-1}).
Gama B. *et al.* (2001) [57]	S-2 glass/vinyl ester 2D plain weave: –/– (GFRP-W)	*LSLF* (*Instron - not spec.*) [*R*] Compression SHPB [R]	200 - 1600	Strains measured directly from specimens using strain gauges. Input pulse from SHPB highly non-uniform. Strain measured by strain gauges mounted on the specimen is used until unloading, then SHPB theory used. High levels of dispersion make stress-strain curves uninformative. 'Non-linear' strains are defined to account for parasitic strains from dispersion. Specimens may not reach quasi-static stress equilibrium prior to failure. Effect of strain rate on modulus not reported. Strength increases (+38% at 1,125 s^{-1}) before reaching an approximately asymptotic value at higher strain rates. Ultimate strain increases (+98% at 1,125 s^{-1}), but with high uncertainty.
Govender R. *et al.* (2011) [66]	glass/vinyl ester 2D plain weave: E-glass 24 oz./Derakane 8084 (GFRP-W)	*EMLF* (*Zwick Universal*) [*C*] Compression SHPB [C]	510	Cross head displacement used to estimate strain due to concerns about strain gauge alignment. Small specimens prevented the use of extensometers. Effect of strain rate on modulus not reported as quasi-static stress equilibrium was not achieved until late in the test. Strength initially increases (+13% at 510 s^{-1}) but decreases with increasing strain rate (+4% at 1,800 s^{-1}). Slight reduction in ultimate strain (-5%).

Gerlach R. *et al.* (2012) [47]	carbon/epoxy 3D weave: (Tenax HTS/HTA)/RTM-6 (3D-W)	*EMLF* (*not spec.*) *HLF* (*Itm.* s^{-1}) [*R*] Compression SHPB [R]	0.004 - 6,000	Strain was measured using a laser extensometer for quasi-static tests. At intermediate strains digital speckle photography was used. Modified direct impact SHPB used for high strain rate testing. Compression stress-strain response at high strain rates shows some waviness due to dispersion. Strength measured as maximum stress before unstable failure. Tangent modulus (measured at 300 MPa) increases (+43% at 6,000 s^{-1}). Negligible strain rate effect on strength.
Shah Khan M.Z. & Simpson G. (2000) [60]	carbon/epoxy 2D plain weave: DF1400/Synolite 0288-T 1 resin (CFRP-W)	*HLF* [*R*]	0.001 - 10	Quasi-static strains estimated using crosshead displacement corrected for compliance. Hydraulic load frame used to load at intermediate strain rates. Strength and ultimate strain taken at point of maximum stress. Inconsistent failure modes thought to contribute to scatter in measured ultimate parameters. Elastic modulus increases (+25% at 10 s^{-1}), strength increases (+21% at 10 s^{-1}), and strain increases (+11% at 10 s^{-1}). Significant scatter in all measured parameters (up to ± 25%, 12% and 33% for elastic modulus, strength and ultimate strain, respectively).
Shen *et al.* (2012) [61]	glass/vinyl ester 3D weave: E-glass/ML-506 (3D-W)	*HLF* (*MTS 810*) [*R*] Compression SHPB [R]	0.001 - 1,200	Hydraulic load frame used to test at quasi-static and intermediate strain rates. Stress strain curves are very non-linear and exhibit very large increase in the tangent modulus (defined above 0.025 strain). Unclear how many specimens were tested. Unrealistically high effect of strain rate on the tangent modulus suggests specimens are not in a state of stress equilibrium. Tangent modulus increases (+350% at 1,200 s^{-1}) with very high uncertainty (± 79%). Strength increases (+8% at 1,200 s^{-1}) and ultimate strain decreases (-50% 1,200 s^{-1}).

Akil *et al.* (2003) [62]	glass/vinyl ester 2D weave: S-2 glass/– (GFRP-W)	*HLF* (*not spec.*) [*R,C*] Compression SHPB [C]	0.001 - 900	Tangent modulus, fitted to later region of 'linear' response and used to estimate elastic modulus. Strain rate sensitive behaviour attributed to viscoelastic properties of the matrix. Consistent shear failure mode between quasi-static and high strain rate tests. Tangent modulus increases (+79% at 900 s^{-1}) with high uncertainty (± 26%), strength increases (+29%at 900 s^{-1}), and ultimate strain decreases slightly (-6% at 900 s^{-1}).
Pankow *et al.* (2011) [65]	glass/epoxy 3D weave: Z-fibre/SC-15	*HLF* (*not spec.*) [*R*] Compression SHPB [C]	QS - 1750	Used 2D DIC performed with high speed camera to measure strain on the specimen. Poor spatial and temporal resolution results in high error (> 5% strain). No details provided on the DIC setup. High strain rate tests suffer from high levels of dispersion (oscillations in stress-strain response). This introduces uncertainty in strength and ultimate strain measurements. Effect of strain rate on modulus not reported quantitatively. Strain rate appears to have negligible effect on elastic modulus. Strength increases relative to quasi-static values (+11% at 1,750 s^{-1}) but not strain rate sensitive (within scatter). Ultimate strains increase relative to quasi-static values (+20% at 1,750 s^{-1}) but also not strain rate sensitive (within scatter).
Guden *et al.* (2004) [63]	glass/epoxy 2D weave: S-2 glass/ SC-15	*EMLF* (*Shimadzu AG-I*) [*C*] Compression SHPB [C]	0.0001 - 1,100	Compressive modulus computed using linear region of stress-strain curve at 4% strain. Strain rate limited to 1,100 s^{-1}, above which quasi-static stress equilibrium could not be achieved prior failure. Consistent shear failure mode between quasi-static and high strain rate tests. Elastic modulus increases (+70% at 1,100 s^{-1}), strength increases (+53% at 1,100 s^{-1}), ultimate strain decreases slightly with increasing strain rate (-3% at 1,100 s^{-1}).

Table A.2: Summary of published studies on strain rate effects of interlaminar tensile properties of fibre-reinforced polymer composites. Notes: Constituent materials listed in the format: 'fibre/matrix'. Material labels are included in '( )' for association with Fig. 2.8 - Fig. 2.10. Quasi-static: italic typeface; high strain rate: regular typeface; test method: electro-mechanical load frame (EMLF), hydraulic load frame (HLF), high-speed load frame (HSLF), split Hopkinson pressure bar (SHPB); specimen geometry (in '[ ]'): W = waisted, D = dog-bone, L = L-shaped/curve beam, O = off-axis, C = cylindrical specimens

Reference	Material	Test [Specimen]	Strain Rate (s^{-1})	Notes
Nakai K. & Yokoyama T. (2014), (2016) [11, 48]	carbon/epoxy pre-preg. ([0], $[0/90]_s$): T700S/2521, T700S/2500 (CFRP-PP)	*EMLF* (*Instron 5500R*) [*W*] Tension SHPB [C-W]	0.02 – 60	Waisted specimens were bonded to magnesium alloy end caps using DP-460 epoxy. Strains under quasi-static and high strain rate loading were measured using strain gauges. Specimen appears to be in a state of quasi-static stress equilibrium for much of the test. Strains computed using SHPB overestimate true strains due to non-uniform deformation of the gauge region. Effect of strain rate on elastic modulus not reported. Strength increases more for the cross-ply layup compared to the unidirectional layup (+130% at 50 s^{-1} ($[0/90]_s$), +77% at 50 s^{-1} ($[0]_s$)), and ultimate strain increases more for the cross-ply layup compared to the unidirectional layup (+31% at 50 s^{-1} ($[0/90]_s$), -10% at 50 s^{-1} ($[0]_s$)). Large uncertainty in strength (up to ± 51% for $[0/90]_s$ and ± 18% for $[0]_s$ at 50 s^{-1}) and ultimate strains (up to ± 61% for $[0/90]_s$ and ± 43% for $[0]_s$ at 50 s^{-1}).

Lifshitz J. & Leber H. (1998) [71]	carbon/epoxy pre-preg.: AS4/3502 ($[0]_s$) (CFRP-PP) glass/epoxy 2D plain weave: NEMA/ASTM G-10 (GFRP-W)	Tension SHPB [C-W-O]	127-195	Tension, shear and combined tension-shear behaviour was studied using two types of specimens. Waisted specimens were used for tension, and off-axis waisted specimens were used for tension/shear loading. Off-axis specimens were formed by bonding two halves together. Bonded specimens very difficult to machine from CFRP and the results had too much scatter to be meaningful. Specimens bonded to incident and transmitter bars (Hyson adhesive). Oscillations in stress-strain response and erratic shape close to failure thought to be a result of micro crack formation. Strains measured using strain gauges. No quasi-static ultimate strains reported. Elastic modulus increases (+41% for carbon/epoxy at 195 s^{-1}, +7% for glass/epoxy at 127 s^{-1}). Strength increases for the carbon/epoxy laminate (+36% at 195 s^{-1}), but decreases for the glass/epoxy laminate (-14% at 127 s^{-1}).
Naik N.K. *et al.* (2010) [74]	glass/epoxy 2D plain weave: E-glass/LY556 (GFRP-W)	*LF not spec.* [*C-W*] Tension SHPB [C-W]	140 – 400	Specimens bonded to end tabs which fit inside incident and transmitter bars. Authors claim specimen reach quasi-static stress equilibrium; however, plots of reaction forces do not appear equal during loading. Strength increases significantly when compared to quasi-static values (+88% at 390 s^{-1}). The influence of strain rate on strength is much lower within the range of high strain rates considered (+11% at 390 s^{-1} relative to 145 s^{-1}).

Gerlach R. *et al.* (2013) [51]	S2-glass/epoxy pre-preg.: –/FM94 (cut from GLARE sheets) (GFRP-PP)	*EMLF* (*not spec.*) [*C-W*] Tension SHPB [C-W]	5 x 10^{-4}, 10, 200	Attempts to measure interlaminar strength from GLARE plates. Specimens bonded directly to incident and transmitter bars. Due to the small effective gauge length (2 mm), no meaningful strain measurements could be performed using digital speckle photography. Large scatter in through-thickness direction attributed to inconsistent failure modes and variation in manufacturing the GLARE plates. Effect of strain rate on elastic modulus and ultimate strain not reported. Strength increased (+45% (± 105%)) at 200 s^{-1}.
Hufenbach W. *et al.* (2013) [73]	glass/epoxy 2D weave: (MKF & Twintex) (GFRP)	Tension SHPB [D,L]	5 x 10^{-4} - 400	Large scatter in SHPB tension tests attributed to reinforcement architecture. Authors conclude that SHPB is not suitable for testing coarse textile architectures. Varying levels of compaction in L-shaped beam specimens resulted in unacceptable scatter (results not reported). Effects of strain rate on modulus not reported. Increasing strength (+93% at 400 s^{-1}) with approximately constant strain at failure (within scatter: -75% – +87% at 44 s^{-1} to -87% –+ 639% at 400 s^{-1}).
Govender R. *et al.* (2011) [66]	glass/vinyl ester 2D plain weave: E-glass 24 oz./Derakane 8084 (GFRP-W)	Compression SHPB-spall [C]	1,800	No quasi-static values reported due to consistent failure within the grips. A spall test was used to measure tensile strength. Pulse time-shifting used to estimate forces in the specimen at failure. A high speed camera was used to qualitatively monitor the failure. The effect of strain rate on the elastic modulus and ultimate strain were not reported. The average strength was 125 MPa (std. dev. = 21.2 MPa). Authors compare this to the strength quoted by the epoxy manufacturer (76 MPa) to conclude that the material likely exhibits a significant sensitivity to strain rate.

Gerlach R. *et al.* (2012) [47]	carbon/epoxy 3D weave (Tenax HTS/HTA)/RTM-6 (3D-W)	*EMLF* (*not spec.*) [*cross*] *HLF* (*Itm.* s^{-1}) [*CROSS*] Compression SHPB [CROSS]	0.004 - 11,000	Cross-specimens used to introduce load without edge effects for 3D reinforcement. Specimens loaded in compression with a SHPB using U-shaped fixture. Specimen geometry and fixture made non-contact measurements prohibitive. Stress state not uniform due to small fillets between cross arms. Influence of strain rate on elastic modulus and ultimate strain not reported. Strength generally increases (+84% – +94%) with increasing strain rate, but with high scatter (± 60%).
Hufenbach W. (2011) [75]	glass/polypropylene 2D plain weave: Twintex TPP 60 745 (GFRP-W)	*EMLF* (*ZWICK Z250*) [*L*] HSLF (INSTRON VHS 160/20) [L]	10^{-4} - 7	3D DIC used on L-shaped beam specimens. Significant scatter in the optical measurements attributed to the coarse textile surface pattern. Heterogeneous strain fields through thickness. Strains averaged over subsets. Limited measurement resolution at intermediate strain rates (HS camera resolution). Effect of strain rate on modulus and ultimate strain not reported. Strength increases significantly (+204% at 1 s^{-1} and +171% at 7 s^{-1}).

Medina J. & Harding J. (2000) [72]	carbon/epoxy pre-preg.: T300/924 (CFRP-PP) carbon/epoxy 2D plain weave: Fibredux 924C/833 (CFRP-W) R-glass/epoxy 2D plain weave: Fibredux 924G/20982 (GFRP-W)	*LF not spec.* [*W-C*] Tension SHPB [W-C]	5 - 940	Waisted specimens bonded to steel end caps. Strain gauges occasionally failed before the specimen, or were positioned off of the failure plane. Longitudinal strain gauge shows persistent oscillations in strain. Results show that reinforcement architecture has larger influence than fibre material. Poisson's ratio doubled when glass fibres used compared to carbon fibres. carbon/epoxy pre-preg: Tensile modulus increases with strain rate (+31%), tensile strength increases (+12%), and tensile strain also increases (+22%); carbon/epoxy 2D plain weave: Tensile modulus increases with strain rate (+7%), tensile strength increases (+37%), and tensile strain also increases (+63%); glass/epoxy 2D plain weave: Tensile modulus decreases with strain rate (-13%), tensile strength increases (+40%), and tensile strain also increases (+65%).

Table A.3: Summary of published studies on strain rate effects of interlaminar shear properties of fibre-reinforced polymer composites. Notes: Constituent materials listed in the format: 'fibre/matrix'. Material labels are included in '( )' for association with Fig. 2.11 - Fig. 2.13. Quasi-static: italic typeface; high strain rate: regular typeface; test method: electro-mechanical load frame (EMLF), hydraulic load frame (HLF), high-speed load frame (HSLF), split Hopkinson pressure bar (SHPB); specimen geometry (in '[ ]'): SBS = short beam shear (3 point bend), I = notched/unnotched shear test, R = rectangular/cubic specimens, O = off-axis, T = thin-walled tube, SL = single lap-shear joint, DL = double lap-shear joint

Reference	Material	Test [Specimen]	Strain Rate (s^{-1})	Notes
Naik N.K. *et al.* (2007) [10]	carbon/epoxy 2D plain-weave: –/– (CFRP-W), E-glass/epoxy 2D plain weave: –/– (GFRP-W)	*LF not spec.* [*SL*] Torsion SHPB [T] Compression SHPB [SL]	496 – 1,000	Single lap and tubular specimens considered at high strain rates. Viscoelastic behaviour of matrix and less time for damage propagation responsible for increase in shear strength. Post failure microscopy of tubular specimens reveals features associated with a pure shear stress state. Shear stress may not be constant due to the fabric and different properties within the specimen thickness. Wall thickness set at 3 mm since thinner walls gave inconsistent results (thought to be a result of manufacturing defects). No quasi-static ultimate strains provided. Modulus estimated by stress and strain at point when quasi-static stress equilibrium was thought to be achieved. carbon/epoxy 2D plain weave: Increase in modulus (+38%), increase in strength (+69%) and increase in ultimate strain (+41%) at 1,000 s^{-1} relative to 496 s^{-1}; glass/epoxy 2D plain weave: Increase in modulus (+29%), increase in strength (+67%) and increase in ultimate strain (+35%) at 1,000 s^{-1} relative to 576 s^{-1}.

Harding J. & Dong L. (1994) [8]	carbon/epoxy pre-preg.: T800/924 ([0], [0/90], [± 45]) (CFRP-PP)	*LF not spec.* [*DL*] Tension SHPB [DL]	275 – 332	Scatter is so large that the experiments cannot be considered as proof of a strain rate dependence. Improved specimen design required if strength values are to be accepted with confidence. Normal stress plays a significant role in the failure process as shown by micrographs of failure surfaces. Influence of strain rate on shear modulus not reported. carbon/epoxy pre-preg. [0] (1-3): shear strength increases (+26%) and ultimate shear strain decreases (-16%) at 275 s^{-1}. carbon/epoxy pre-preg. [0/90] (2-3): shear strength increases (+39%) and ultimate shear strain decreases (-16%) at 332 s^{-1}. carbon/epoxy pre-preg. [± 45] (1-3): shear strength increases (+38%) and ultimate shear strain decreases (-22%) at 281 s^{-1}.
Hufenbach W. *et al.* (2009) [78]	glass/polypropylene hybrid yarn: MKF 3D weave (3D-W) & Twintex 2D weave (GFRP-W)	*HSLF* (*INSTRON VHS 160/20*) [I]	6 x 10^{-3} - 60	Lightweight Iosipescu fixture used to reduce the effects of frame inertial. High speed cameras used for visual analysis of damage and failure processes. Approximately equal interlaminar shear strength for both composites. Low failure stress and strain levels (Twintex in 1-3 plane) make the measurements noisy and unreliable. Influence of strain rate on shear modulus not reported. MKF (2-3): shear strength increases (+6%) up to 6 s^{-1}, followed by a decrease (-18%) at 60 s^{-1}, and ultimate shear strain decreases (-13%) at 60 s^{-1}. Twintex (2-3): shear strength increases (+41%) and ultimate shear strain increases (+18%) at 60 s^{-1}. Twintex (1-3): shear strength trends unclear (range between -35% at 6 s^{-1} and +35% at 60 s^{-1}) and ultimate shear strain increases (+118%) at 60 s^{-1}.

Hufenbach W. *et al.* (2013) [73]	glass/polypropylene hybrid yarn: MKF 3D weave (3D-W)	*HSLF* (*INSTRON VHS 160/20*) [I]	5 x 10^{-4} - 60	Lightweight Iosipescu fixture used to reduce the effects of frame inertial. Used previously up to 60 s^{-1} [78]. Highly non-linear shear response at all strain rates. Influence of strain rate on shear modulus not reported. Shear strength increases (+83% at 3 s^{-1}), and negligible effect on ultimate shear strain (within scatter: +21% ± 57%).
Gowtham H.L. *et al.* (2015) [14]	E-glass/epoxy 2D plain weave: –/LY556(HY951 Hardener) (GFRP-W)	Torsion SHPB [T] Compression SHPB [SL]	192 – 457 (T) 300 – 1500 (SL)	Quasi-static testing performed only for torsion specimens (details not reported). Quasi-static torsional simulations performed to assess possible stress concentrations in tubular specimens. Single-lap and tubular specimens compared using two SHPBs. Lower strength measured with thin-walled specimens thought to be a result of variations in stiffness and stress along the radial, and circumferential directions. Effect of strain rate on shear modulus and ultimate shear strain not reported. Interlaminar shear strength increases (+56% at 457 s^{-1}) for tubular specimens and increases (+11% at 1,500 s^{-1}) for single-lap specimens.
Gerlach R. *et al.* (2012) [47]	carbon/epoxy 3D weave: (Tenax HTS/HTA)/RTM-6 (3D-W)	*EMLF* (*not spec.*) [*I - dbl. notch*] Compression SHPB [I - dbl. notch)]	0.004 - 11,000	Two binder volume fractions considered (3% and 6%). Tubular specimens not practical for 3D weaves due to the arrangement and wide spacing of reinforcement. A double-notch shear specimen was adopted. Average shear strength is higher in the 2-3 plane compared to the 1-3 plane. Inadequate resolution and accuracy of optical shear strain measurements (digital speckle photography). Large scatter in strength measurement attributed to stress concentrations at notches. Influence of strain rate on shear modulus and ultimate strain not reported. Shear strength increases in the 1-3 plane (+52% (3 % binder) and +37% (6 % binder)) and increases in the 2-3 plane (+34% (3 % binder) and +31% (6 % binder)) at 11,000 s^{-1}.

Yokoyama T. & Nakai K. (2006) [79]	carbon/epoxy pre-preg.: T700/2521 ([0]) (CFRP-PP)	*EMLF* (*Instron 5500R*) [*I, SBS*] Compression SHPB [I - dbl. notch)]	0.02 - 780	Similar results are obtained when the notched shear specimens are loaded in tension and compression. Strength values from notched specimens agree well with the short beam shear (SBS) tests. Compressive normal stresses around notches thought to reduce effect of stress concentrations. Effect of strain rate on shear modulus and ultimate shear strain not reported. Negligible effect of strain rate on interlaminar shear strength up to 780 s^{-1}.
Bouette B. *et al.* (1992) [44]	carbon/epoxy pre-preg.: T300/5208 ([0])(CFRP-PP)	*EMLF* (*LF not spec.*) [SL] *HLF* (*LF not spec.*) (*Itm.* s^{-1}) [*SL*] Tension SHPB [SL, DL]	0.001 - 1,000	Two specimens were designed using FEA: one permitting the determination of the shear modulus, and the other (double lap shear specimen) permitting measurement of the shear strength (1-3 plane). Only values for single-lap specimens reported. Strain measured using strain gauges on the specimen. Authors emphasize that strength values must be interpreted with caution due to tensile normal stresses ends of the overlap. Maintaining shorter overlap length reduces peel stresses. Effect of strain rate on ultimate shear strain not reported. Negligible change in shear modulus or interlaminar shear strength up to 1,000 s^{-1} (within experimental scatter).

Hallett S.R. *et al.* (1999) [45]	carbon/epoxy pre-preg.: T300/914 ($[0/90]_s$) (CFRP-PP)	*LF not spec.* [*SL (Z)*] Compression SHPB [SL (Z)]	5 x 10^{-4} - 800	Z-shaped single-lap specimens used. Shear strain measured directly using ± 45° rosette strain gauge. High speed photography (Cordin) used to observe failure mechanisms. Linear regression fit used to estimate shear modulus from stress-strain curve (noise and oscillations in curve). Too much scatter on shear strength values to resolve strain rate dependency. Failure found to initiate near the notches, suggesting that the stress concentration may dominate the failure. Shear modulus increases (+41% at 700 s^{-1}) but with high scatter (± 34%). Negligible effect on shear strength (within experimental scatter) at 450 s^{-1} and 700 s^{-1}. Ultimate shear strain increases (+27% at 700 s^{-1}) but with high scatter (± 20% at 450 s^{-1} and ± 12% at 700 s^{-1}).
Gillespie J. et al (2005) [46]	S-2 glass/epoxy 2D weave (15x15 and 5x5) – /SC79 (GFRP-W)	*LF not spec.* [*R-O*] Compression SHPB [R-O]	QS - 1,000	Out-of-plane off-axis specimens loaded in compression to obtain shear strength. Off-axis angles considered include: 0°, 15°, 30°, 45°, 60°, 75°, and 90°. An 'R-value' criterion (based on relative difference between reaction forces) was to determine which tests were likely contaminated by inertial effect (limits strain rate to < 600 s^{-1}). A strain rate dependent failure criterion was identified based on experimental results. Effect of strain rate on shear modulus and ultimate shear strain not reported. Interlaminar shear strength found to increase (+134%) at 985 s^{-1}.

Harding J. & Li Y.L. (1992) [77]	carbon/epoxy pre-preg. ([0]): T300-3000A/Ciba-Geigy XD 927 (CFRP-PP) E-glass/epoxy 2D plain weave: –/Ciba-Geigy XD 927 (CFPR-W) hybrid carbon-glass/epoxy: T300-3000A/Ciba-Geigy XD 927, –/Ciba-Geigy XD 927 (GFRP-W)	*LF not spec.* (*Instron*) [*DL*] Tension SHPB [DL]	QS - 1,600	Shear strains and shear modulus were not measured. Load cell displacement used to infer an apparent shear strain. No sensitivity to fibre volume fraction or ply layup for the same material. Problems arose with hybrid specimens as a result of a discontinuity in elastic properties (different types of reinforcing plies) on either side of the failure plane. Finite element simulations show significant normal stresses at the ends of the overlap. Stress concentrations thought to dominate failure initiation in the specimens. carbon/epoxy pre-preg: increase in failure strength (+73%) at 1,600 s^{-1} but with high scatter (± 27%); glass/epoxy 2D weave: increase in strength (+111%) at 1,600 s^{-1} but with high scatter (± 56%); hybrid glass/epoxy: increase in strength (+37%) at 1,600 s^{-1} but with high scatter (± 31%).

Appendix B

Supporting Information - Chapter 5

Table B.1: Parameters used to generate synthetic images for each camera - interlaminar IBII tension/compression test

	HPV-X Camera	**HPV-X2 Camera**
Synthetic Image Parameters		
Pitch size, p (mm)	0.337	
Grid sampling (pixels)	7	
Grey level noise (% of dyn. range)	0.36	0.79
Mean grid contrast (% of dyn. range)	37	43
Grid contrast amplitude (full) (% of dyn. range)	26	28

Table B.2: Grid method processing parameters and measurement performance for interlaminar IBII tension/compression test

	HPV-X Camera	**HPV-X2 Camera**
Displacement calculation		
Pitch size, p (mm)	0.337	
Grid sampling (pixels)	7	
Analysis window	Bi-triangular	
Analysis window size, $2p$ (pixels, mm)	14, 0.674	
Edge data reconstruction [38]	Linear fit over 7 pixels	
Strain calculation		
Calculation method	Central difference	
Smoothing window	Gaussian	
Window width, standard deviation σ (pixels, mm)	10, 0.48	18, 0.86
Virtual strain gauge size ($4\sigma + 2p$) (pixels, mm)	54, 2.60	86, 4.14
Acceleration calculation		
Calculation method	Double central difference	
Smoothing window	3rd-order Savitsky-Golay	
Window size (frames)	11	11
Measurement uncertainties		
Displacement (μm)	0.3	0.4
(pixel)	0.006	0.008
(pitch)	p/1,000	p/850
Strain (μm·m^{-1})	46	56
Acceleration ($\times 10^5$ $m \cdot s^{-2}$)	5.1	8.4

Appendix C

Supporting Information - Chapter 6

Table C.1: Summary of parameters used to generate synthetic images for processing parameter optimisation - interlaminar IBII shear test

Image Parameter	Value
Pitch size, p (mm)	0.337
Grid sampling (pixels)	7
Grey level noise (% of dyn. range)	0.30
Mean grid contrast (% of dyn. range)	37
Grid contrast amplitude (full) (% of dyn. range)	26

Table C.2: Grid method processing parameters and measurement performance for interlaminar IBII shear test

Displacement calculation	
Pitch size, p (mm)	0.337
Grid sampling (pixels)	7
Analysis window	Bi-triangular
Analysis window size, $2p$ (pixels, mm)	14, 0.674
Edge data reconstruction [38]	Linear fit over 7 pixels
Strain calculation	
Calculation method	Central difference
Smoothing window	Gaussian
Window width, standard deviation σ (pixels, mm)	6, 0.29
Virtual strain gauge size (4σ +1 + $2p$) (pixels, mm)	39, 1.88
Acceleration calculation	
Calculation method	Double central difference
Smoothing window	3rd-order Savitsky-Golay
Window size (frames)	5
Measurement uncertainties	
Displacement (μm)	0.4
(pixel)	0.008
(pitch)	$p/850$
Strain (μm·m^{-1})	75
Acceleration ($\times 10^5$ $m \cdot s^{-2}$)	5.8